Dissertation
submitted to the
Combined Faculties of Natural Sciences and for Mathematics
of the Ruperto-Carola University of Heidelberg, Germany
for the degree of
Doctor of Natural Sciences

presented by:
Dipl. Phys. Reza Shaiganfar
born in: Sanandaj/Iran

Oral examination:
26.11.2012

Estimation of NO_x Emissions from megacities using mobile MAX-DOAS and satellite observations

Referees:
Prof. Dr. Ulrich Platt
Prof. Dr. Heinz Friedrich Schöler

Zusammenfassung

Der Fokus dieser Studie liegt auf der Quantifizierung von NO_x Emissionen. Wir charakterisierten und quantifizierten die vertikalen integrierten NO_2-Konzentration (VCDs) und NO_x Emissionen durch mobile MAX-DOAS-Messungen und Satellitenbeobachtungen. Die mobilen Messungen werden auf Kreisen um Megacities durchgeführt. Die gesamten NO_x Emissionen von verschiedenen Megacities werden durch MAX-DOAS Beobachtungen, kombiniert mit meteorologischen Daten, bestimmt. In dieser Studie wurden verschiedene Korrekturverfahren entwickelt, die erstmals die quantitative Bestimmung der NO_x Emissionen aus mobilen MAX-DOAS Beobachtungen erlaubten. OMI Satelliten-Beobachtungen wurden ebenso für die Schätzung von NO_x Emissionen verwendet, die abgeleitete Emissionen im Sommer sind in der gleichen Größenordnung wie die abgeleiteten Emissionen aus MAX-DOAS. Auch VCDs von mobilen MAX-DOAS und OMI wurden verglichen. Gute Übereinstimung wurde für die Sommer Daten gefunden, aber schlechtere im Winter. Die abgeleiteten Emissionen aus mobilen MAX-DOAS Beobachtungen sind Saison-abhängig mit 145% höheren Werten im Winter. Wir vergliechen ebenso die NO_2 VCDs und NO_x Emissionen mit CHIMERE-Modelergebnissen und Inputemissionen. Gute Übereinstimmung wurde für den Sommer gefunden, im Winter aber sind die NO_2 VCDs und NO_x Emissionen, bestimmt aus den MAX-DOAS Messungen, um 35% und 45% höher als die entsprechenden Werte des CHIMERE-Modellls.

Abstract

The focus of this study is on the quantification of NO_x emissions. We characterized and quantified vertically integrated NO_2 concentrations (VCDs) and NO_x emissions by using mobile MAX-DOAS and satellite observations. The mobile MAX-DOAS observations are conducted on different circles around megacities. From the combination of MAX-DOAS observations with meteorological data, total NO_x emissions from different megacities were estimated. In this thesis, several correction methods were developed, which allowed for the first time the quantitative determination of NO_x emissions from mobile MAX-DOAS observations. OMI satellite observations were also used for estimation of NO_x emissions, and were found to be very similar to the obtained emissions from MAX-DOAS in summer. Also VCDs from mobile MAX-DOAS and OMI were compared. Good agreement was found for summer, but worse agreement for winter. The obtained emissions from mobile MAX-DOAS are season-dependent with 145% higher in winter. We also compared the NO_2 VCDs and NO_x emissions with CHIMERE model results and input emissions. Good agreement was found for summer, but in winter the NO_2 VCDs and NO_x emissions derived from MAX-DOAS are about 35% and 45% higher than from CHIMERE respectively.

Contents

1 Introduction

Megacities are localized, heterogeneous and variable sources of various air pollutants, having great impact on air quality and ultimately on the composition of the atmosphere. The impact of megacities and large air pollution on local, regional and global air quality should be analyzed and the feedback among the megacity air quality on local and regional climate change should be quantified.

Megacities: Emissions, urban, regional and Global Atmospheric POLlution and climate effects, and Integrated tools for assessment and mitigation "(MEGAPOLI)" was a three year cooperative project. The main MEGAPOLI objectives were.

1. To assess the impact of megacities and large air pollution hot-spots on local, regional and global air quality.
2. To quantify feedbacks among megacity air quality, local and regional climate, and global climate change.
3. To develop improved integrated tools for prediction of air pollution in megacities.

At present, there are about 20 cities worldwide with a population of about 10 million or more, and 30 with a population exceeding 7 million. It is expected that these numbers grow considerably in the near future. Such coherent urban areas with more than about 5 million people are usually called megacities (Mahura & Baklanov (2011)). In Europe there are six major population centers which clearly qualify as megacities:

Paris, the Rhine-Ruhr region, the po Valley, Moscow, Istanbul and London.

In atmospheric chemistry the term NO_x is used for the total concentration of NO plus NO_2. During daylight NO and NO_2 are in equilibrium with the ratio $\frac{NO}{NO_2}$ determined by the intensity of sunshine (which converts NO_2 to NO) and the concentration of ozone (which reacts with NO to give back NO_2). NO and NO_2 are also central to the formation of tropospheric ozone.

NO_x is naturally produced by lightning, fires, emission from soils, but the major fraction comes from fossil fuel combustion and biomass burning due to anthropogenic activity.

Nitrogen oxides are among the most important trace gases in the atmosphere. Nitrogen oxides are key substances involved in some chemical reactions and catalytic cycles which destroy ozone in the stratosphere, and provide a way to produce tropospheric ozone.

In this work satellite and ground based observations were used. The satellite data are used to characterize megacity pollution levels and outflow plumes, as well as to evaluate the regional and global models. Satellites provide long time series with global cover, which is an important advantage to study these measurements. From the satellite observations the link from local to regional and global scales can be made. Especially the impact of important sources like megacities on the surrounding areas and also over longer distances can be studied.

The Multi-Axis Differential Optical Absorption Spectroscopy (MAX-DOAS) is a measurement technique that observes scattered sunlight under different elevation angles between zenith and horizon. Using different elevation angles give us the possibility to derive the vertical distribution of trace gases and aerosols.

The DOAS observations in the open atmosphere using sunlight (Passive DOAS) is used to obtain the trace gas concentrations (slant column densities) in the atmosphere. From the measured trace gas concentrations, the vertical column densities of the trace gas can be determined. By using an instrument (MAX-DOAS) on a mobile platform, a horizontal integration in addition to vertical integration of the tropospheric trace gas concentrations can be determined. If a pollutant source (megacity in this study) is encircled by a mobile MAX-DOAS, the emission of the emitted molecules in the closed area can be determined from the vertical column densities of the molecules and the wind speed within the trace gas layer.

The obtained vertical column densities (VCDs) from mobile MAX-DOAS can be compared to satellite data and also model data. In this study, OMI tropospheric vertical column densities are compared to the tropospheric VCDs from mobile MAX-DOAS.

The first measurement campaign of the MEGAPOLI project was the Paris campaign. Paris was selected, because it is a very concentrated European urban pollution hot spot surrounded by rural areas.
The estimated emissions from mobile MAX-DOAS are compared to emissions from the

CHIMERE model and derived from OMI tropospheric VCDs and the EDGAR model.

The mobile MAX-DOAS method was carried out also in New Delhi to estimate the emissions of Delhi and comparison to satellite data.

In addition to the above mentioned measurements, some stationary measurements were executed in the CINDI campaign and at Greater Noida (India).

2 Atmospheric Chemistry

The earth's atmosphere mainly consists of 78 % nitrogen, 20 % oxygen and low percentage of argon and other gases. The trace gases represent less than 1 % of the atmosphere. Many of the existing trace gases in the atmosphere can be observed by spectroscopic methods, while these gases absorb and scatter the sun light. A known technique to evaluate the atmospheric trace gases and aerosols is DOAS. All the observed trace gases in this study are introduced in this chapter.

2.1 Chemistry

In the atmosphere, different gases other than N_2, O_2, Ar and H_2O exist at low concentrations and are called trace gases. These gases affect the ozone layer, greenhouse effect, smog and environmental issues.

Chemical species are emitted to the atmosphere by a variety of sources. Some of these sources, such as fossil fuel combustion, originate from human activity and are called anthropogenic. Others, originate from natural processes of biological organisms and are called biogenic. Still others, such as volcanoes, originate from non-biogenic natural processes (Jacob, 1999).

2.1.1 Ozone

The existence of a high altitude ozone layer was detected by one of the first solar UV spectral measurements. Ozone is the most important trace constituent in the stratosphere, which is qualitatively explained by the CHAPMAN mechanism (Jacob, 1999). The ozone layer originates from the photolysis of atmospheric O_2, which happens at high altitude.

$$O_2 + h\nu \rightarrow O + O \quad (\lambda < 240nm) \tag{2.1}$$

These O atoms are in triplet state and highly reactive; they react with the O_2 molecules in the presence of a third molecule M (O_2 or N_2) to produce ozone.

$$O + O_2 + M \rightarrow O_3 + M \tag{2.2}$$

and also:

$$O_3 + h\nu \rightarrow O_2 + O \quad (\lambda < 320nm) \tag{2.3}$$

With a lower energy, ozone will be photolyzed back to O_2 but this reaction is much slower than the forward reaction namely O_2 to ozone.

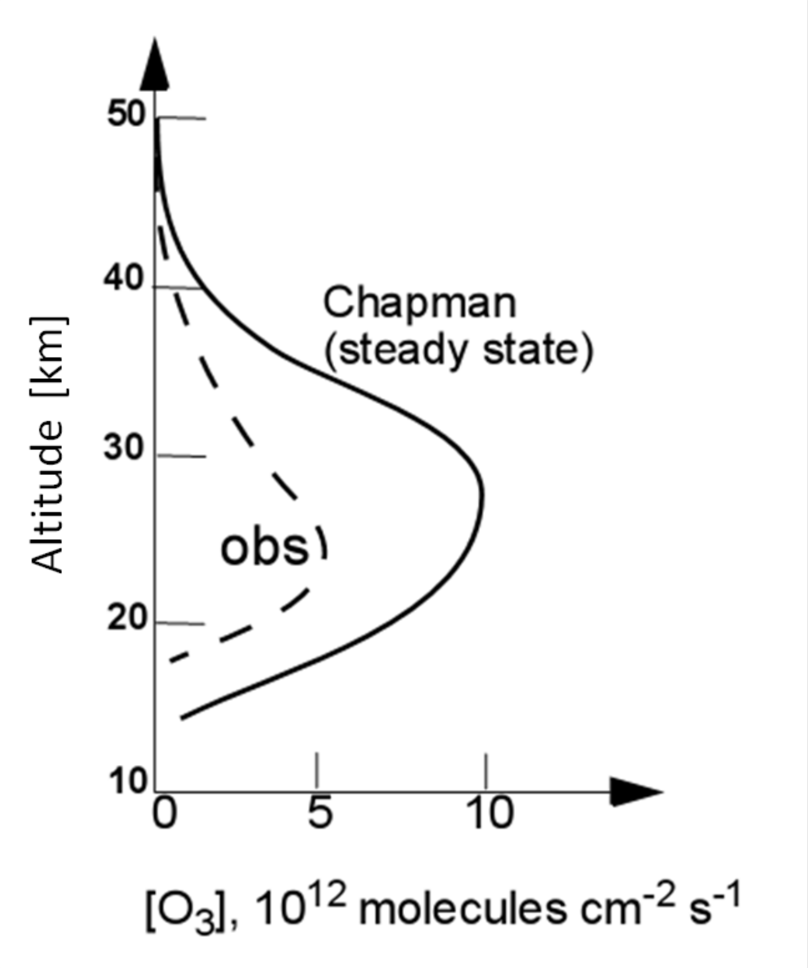

Figure 2.1: Calculated and observed vertical profiles of Ozone concentrations, (Jacob, 1999). The discrepancy between observation and calculated Ozone is because of additional sinks for Ozone, which were not included in the Chapman mechanism.

Most of earth's atmospheric ozone is stratospheric (see figure 2.1) and absorbs most solar ultraviolet radiations.

A small fraction of stratospheric ozone can be transported to the troposphere, during this transport, OH radicals are produced in the tropopause (Jacob, 1999). Tropospheric ozone can be produced also by the oxidation of CO and hydrocarbons in the presence of nitrogen oxides. Nitrogen oxides acts as a source of tropospheric ozone in urban areas.
High concentrations of surface tropospheric ozone are toxic to human and vegetation, since

O_3 oxidizes biological substances. The tropospheric ozone causes inflammation in the human lungs, heart problems and maybe death, it is an important greenhouse gas too.

2.1.2 Nitrogen Oxides

Nitrogen oxides ($NO_x : NO_2 + NO$) are one of the most important components in the atmosphere, which are produced in combustion processes, mainly through fossil fuel combustion or the direct combination of atmospheric oxygen and nitrogen at high temperatures. Lightning is a natural nitrogen oxide source (direct combination of oxygen and nitrogen). Microbial processes in soil are a small fraction of the natural source of nitrogen oxides.
Power plants and motor vehicles play an important role for NO_x emissions. Natural sources as agricultural and biomass burning emit ammonia, others like nitrate and ammonium salts are secondary products from NO, NO_2 and ammonia (ammonium NH_4^+ ion is an important component of the tropospheric aerosol).

The primary pollutant (directly emitted) as nitrogen oxides is mostly nitric oxide (NO) and a small fraction is nitrogen dioxide.
NO is oxidized by ozone in the atmosphere, on a time scale of several minutes. The nitrogen oxides are rapidly inter converted to each other during the daytime.
In the stratosphere NO reacts rapidly with O_3 to produce NO_2, which photolyzes back to NO. This rapid exchange between NO and NO_2 is called a null cycle:

$$\begin{aligned} NO + O_3 &\rightarrow NO_2 + O_2 \\ NO_2 + h\nu &\rightarrow NO + O \\ O + O_2 + M &\rightarrow O_3 + M \end{aligned} \tag{2.4}$$

In the stratosphere, the natural source of NO_x is N_2O that is destroyed by photolysis. Nitrous oxide (N_2O) is a very stable molecule, which does not react in the troposphere, and is transported directly to the stratosphere. There, it is photolysed:

$$N_2O + h\nu \rightarrow N_2 + O(^1D) \tag{2.5}$$

$$N_2O + O(^1D) \rightarrow 2NO \tag{2.6}$$

The main part of the atmospheric mass is in the troposphere. The troposphere extends from the surface to 8-18 km altitude depending on latitude and season.
The reaction 2.4 regenerates NO and produces an O_3 molecule, which can undergo photolysis and produce additional OH radicals. These and related reactions are responsible for a chain cycle and determine the abundance of NO_x in the atmosphere.
The principal sink of NO_x is oxidation to HNO_3. During the day NO_x is oxidized to HNO_3

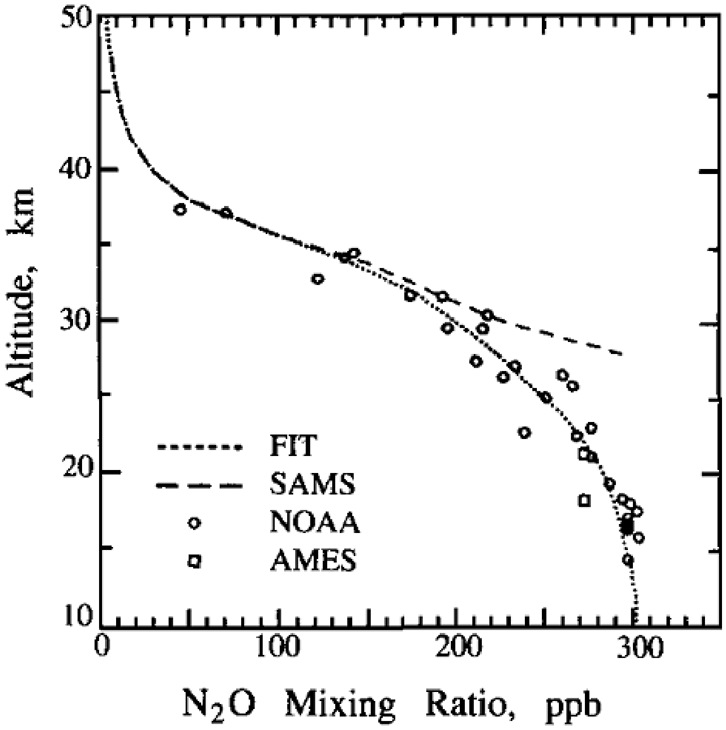

Figure 2.2: Vertical profile of N_2O over the tropics (Seinfeld & Pandis, 2006).

by the strong radical oxidant:

$$NO_2 + OH + M \rightarrow HNO_3 + M \tag{2.7}$$

The existence of OH radicals is limited to daytime, because there is no $O(^1D)$ (O atom in an excited singlet state) to oxidize H_2O during night:

$$O(^1D) + H_2O \rightarrow 2OH \tag{2.8}$$

At high temperatures, nitric oxide can be produced from oxygen and nitrogen, e.g. lightning that can reach extremely high temperatures.
Nitrate radicals dominate the night time chemistry, such radicals are formed from the reaction of ozone with nitrogen dioxide. Nitrate radicals react with nitrogen dioxide and form dinitrogen pentoxide, which is a reservoir of nitrate. The sink process of nitric oxides at night time is:

$$NO_2 + O_3 \rightarrow NO_3 + O_2 \tag{2.9}$$

$$NO_3 + NO_2 + M \rightarrow N_2O_5 + M \tag{2.10}$$

$$N_2O_5 + H_2O \overset{aerosol}{\rightarrow} 2HNO_3 \tag{2.11}$$

Nitric acid can be rapidly absorbed by cloud droplets, soil or vegetation. Deposition removes HNO_3 in the troposphere, therefore it is not an effective reservoir for NO_x. Other nitrogen oxides are removed rather slowly compared to nitric acid, and may be transported several hundreds of kilometer before they are converted to nitric acid or nitrates.

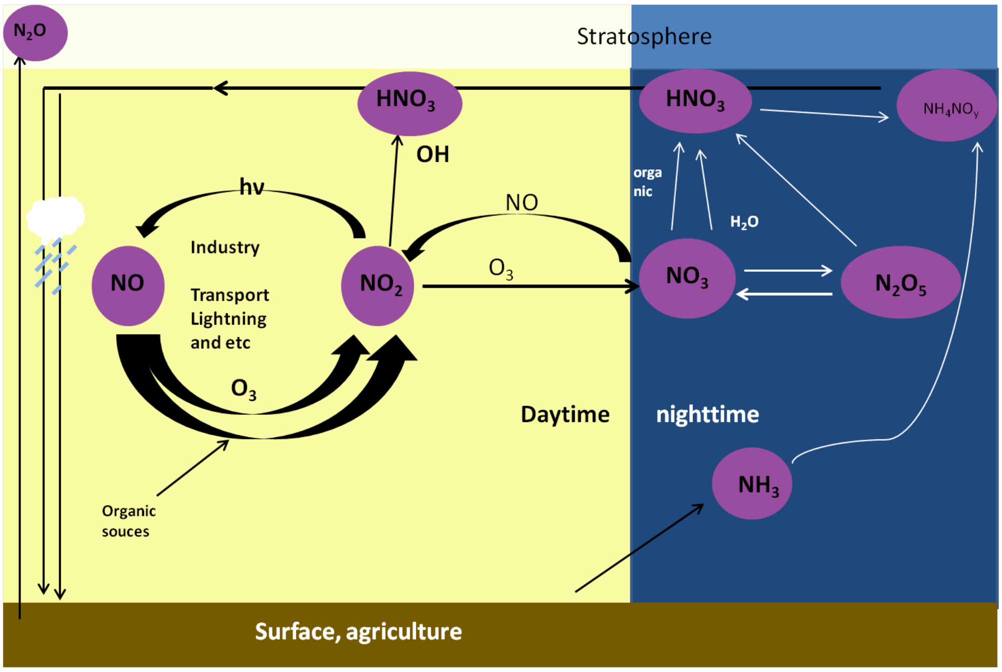

Figure 2.3: An overview about tropospheric nitrogen oxides chemistry during day and night.

Photochemical oxidation of carbonyl compounds produces PAN (Peroxyacetylnitrate) in the troposphere in the presence of NO_x. PAN is not very soluble in water, and by thermal decomposition can regenerate nitrogen oxides:

$$PAN \overset{heat}{\rightarrow} CH_3C(O)OO + NO_2 \tag{2.12}$$

The lifetime of PAN depends strongly on temperature: at 295 K it is 1 hour and at 250 K several months (Jacob, 1999). Therefore PAN can play different roles in the lower and upper troposphere, as a reservoir for long-range transport of nitrogen oxides in the troposphere. A reaction, which produces nitrogen dioxide, is in the presence of HO_2 radicals. The oxidation of CO in the atmosphere by OH radicals produce HO_2 radicals:

$$HO_2 + NO \rightarrow NO_2 + OH \tag{2.13}$$

In the troposphere, under low NO_x limit, the production rate of O_3 increases linearly with the NO concentration and independent from the CO level. In the high NO_x limit, the produced O_3 increases linearly with CO and HO_x, and it decreases with increasing NO_x

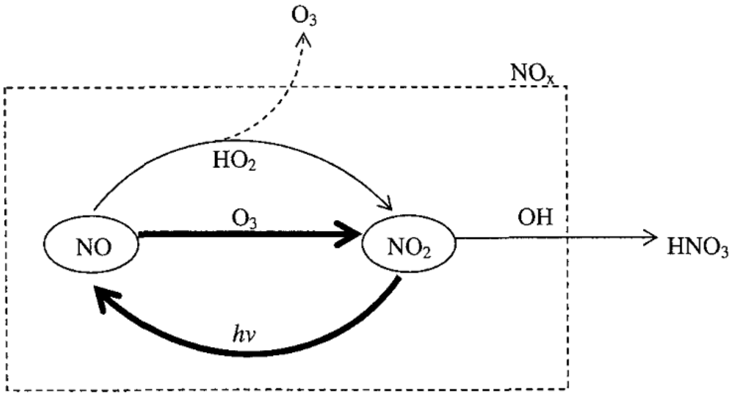

Figure 2.4: Important atmospheric reactions including nitrogen species (Seinfeld & Pandis, 2006).

(Seinfeld & Pandis, 2006).

2.1.3 Formaldehyde

HCHO is an organic compound. It is colorless and flammable. Formaldehyde can be directly emitted into the atmosphere by combustion of fuels in cars and oil refineries as a product of incomplete combustion. Formaldehyde can also be formed in the atmosphere by photochemical oxidation of reactive volatile organic compounds (VOC). The oxidation of isoprene from vegetation is a source of secondary formaldehyde production.

The hydroxyl radicals react with oxidable gases in the atmosphere. Methane is a source of formaldehyde:

$$CH_4 + OH \rightarrow CH_3 + H_2O \tag{2.14}$$

The methyl radicals react virtually instantaneously with oxygen to yield the methyl peroxy radicals (Seinfeld & Pandis, 2006):

$$CH_3 + O_2 + M \rightarrow CH_3O_2 + M \tag{2.15}$$

Under tropospheric conditions, the methyl peroxy radical (CH_3O_2) reacts with NO_x and HO_2 radicals, which from the reaction with NO yields methoxy radical, CH_3O. The methoxy radical reacts with oxygen that gives formaldehyde:

$$CH_3O + O_2 \rightarrow HCHO + HO_2 \tag{2.16}$$

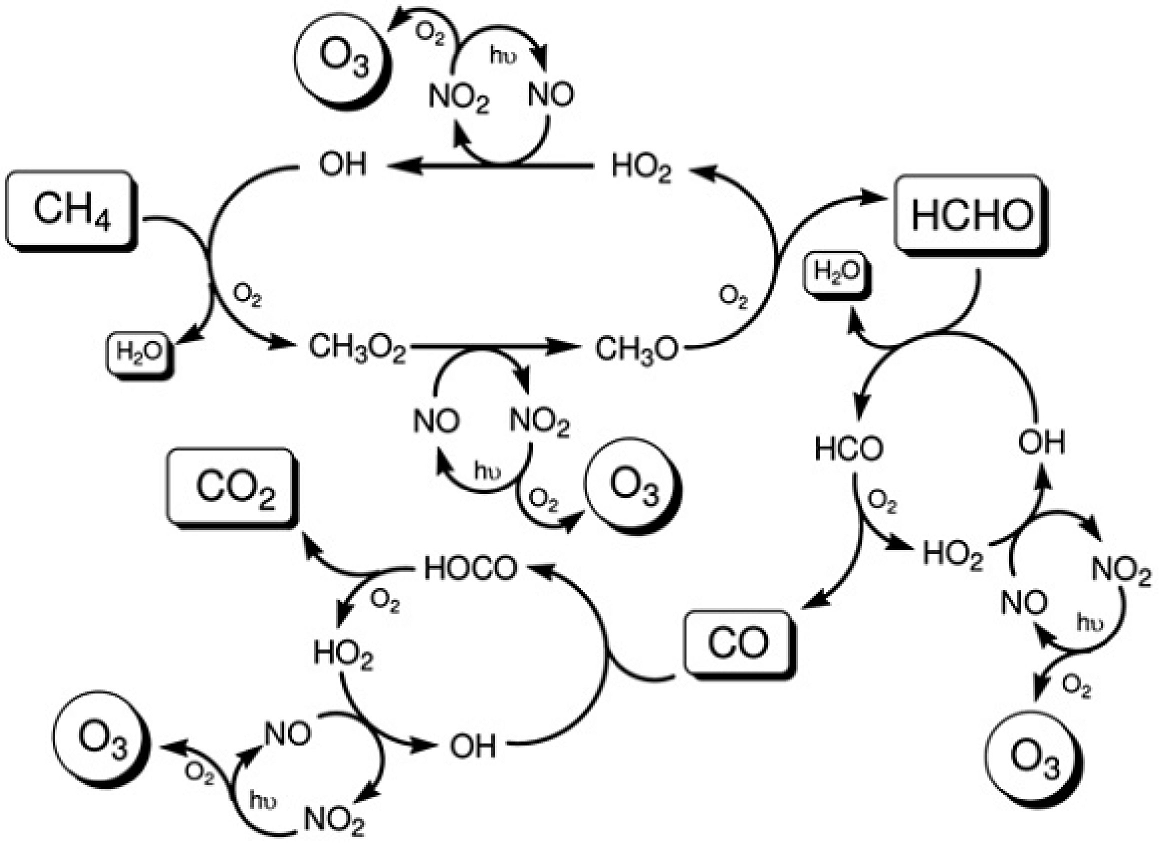

Figure 2.5: The schematic shows the methan oxidation and formaldehyde formation (Jenkin *et al.* (2008)).

The reaction of CH_3O_2 with HO_2 forms the methyl hydoperoxide (CH_3OOH), which can photolyze or react with OH and produce HCHO. These reactions have different reaction rates.
Formaldehye photolysis in the atmosphere:

$$\begin{aligned} HCHO + h\nu &\rightarrow CO + H_2 \\ HCHO + OH &\overset{O_2}{\rightarrow} HO_2 + CO + H_2O \end{aligned} \tag{2.17}$$

or reacts with the OH radical and produces CO.
Formaldehyde plays an important role in the chemistry of the troposphere. The oxidation of most hydrocarbons produces formaldehyde. Biomass burning and biogenic emissions are important sources of formaldehyde.

2.1.4 HONO

Nitrous acid is a weak and monobasic acid, which is formed by a heterogeneous reaction over night in the troposphere, and is a reservoir for HO_x and NO_x. Nitrous acid is formed heterogeneously on surfaces in the presence of water and nitrogen dioxide.

$$H_2O + 2NO_2 \rightarrow HONO + HNO_3 \tag{2.18}$$

Another source of HONO is the direct emission from the combustion of diesel engines. Nitrous acid dissociates by photolysis at sunrise.

$$HONO + h\nu \rightarrow OH + NO \tag{2.19}$$

2.1.5 Sulfur dioxide

Sulfur dioxide is a toxic gas with a pungent, irritating smell, which is mostly released by volcanoes and in various industrial processes. The combustion of sulfur containing fuels (coal and oil) results in the emission of SO_2. In the atmosphere, OH oxidizes sulfur dioxide and produces sulfuric acid:

$$SO_2 + OH + M \rightarrow HSO_3 + M \tag{2.20}$$

$$HSO_3 + O_2 \rightarrow SO_3 + HO_2 \quad half\ a\ day \tag{2.21}$$

$$SO_3 + H_2O + M \rightarrow H_2SO_4 + M \quad half\ a\ day \tag{2.22}$$

Another way to produce sulfuric acid is in clouds by dissolution of sulfur dioxide in cloud droplets (Jacob, 1999). The lifetime of sulfur oxide based on the OH reaction is about one week.

2.1.6 Glyoxal

Glyoxal is an organic compound with the formula CHOCHO. Glyoxal is an important product of the OH reaction with aromatic compounds. Most of glyoxal is formed by isoprene oxidation.

2.1.7 O_4

Oxygen dimer measurements can be applied to determine the average light path through the atmosphere, which is helpful to obtain information about the clouds and aerosols.
O_4 can be measured by DOAS, which is important for the atmospheric radiative transfer.

3 Differential Optical Absorption Spectroscopy (DOAS)

Absorption spectroscopy is an important method to study the chemical composition of gases in the atmosphere.

Differential optical absorption spectroscopy (DOAS) (Platt & Stutz, 2008) is a practical method to detect the concentration of different trace gases in the open atmosphere.

3.1 Radiative transfer in the atmosphere

In the atmosphere, the transfer of solar radiation is determined by scattering and absorption processes.

Through absorption processes, radiation is removed from the radiation field and converted into some other form of energy. Elastic scattering changes the direction of propagation of an individual photon, but not its energy. Such scattering on air molecules is called Rayleigh scattering and on aerosols particles Mie scattering.

Inelastic scattering (the energy is changed) is caused by Raman scattering.

3.1.1 Rayleigh Scattering

Elastic scattering is caused by air molecules, if the direction of photons change but without any energy transfer.

The Rayleigh scattering cross-section is given by (Lord Rayleigh, 1899):

$$\sigma(\lambda) \approx \frac{\sigma_0}{\lambda^4} \tag{3.1}$$

where λ denotes the wavelength of the photon. The Rayleigh phase function is given by:

$$\phi(cos(\theta)) = \frac{3}{4}(1 + cos^2(\theta)) \tag{3.2}$$

θ is the scattering angle.

3.1.2 Mie Scattering

This scattering is an elastic scattering defined as the interaction of light with matter of dimensions comparable to the wavelength of the incident radiation (Mie, 1908). For this kind of scattering, there is a weaker wavelength dependency compared to Rayleigh scattering.

3.1.3 Raman scattering

Inelastic scattering processes change the energy of the photon. Energy can be transfered from photons to the molecules (Stockes line), vice versa (Anti-Stockes). The term rotational Raman scattering is used if only the rotational excitation is affected (Platt & Stutz, 2008).

3.1.4 Absorption Processes

The Lambert-Beer'law is the basis of many present quantitative trace gas analytical methods in the atmosphere and the laboratory. The law was discovered by Pierre Bouguer before 1729. It is often mis-attributed to Johann Heinrich Lambert, who cited Bouguer's Essai d'Optique sur la Gradation de la Lumiere (Claude Jombert, Paris, 1729), and even quoted from it, in his Photometri in 1760. Much later, August Beer extended the exponential absorption law in 1852 to include the concentration of solutions in the absorption coefficient.

Radiation is absorbed by molecules in the atmosphere (trace gases and aerosols). The radiance will be reduced by the amount dI after traversing an absorbing layer of the thickness ds:

$$dI(\lambda) = -I(\lambda)\sigma(\lambda)Nds \quad , \tag{3.3}$$

where $\sigma(\lambda)$ is the absorption cross section of the absorbor, and N is the number of absorbing molecules per volume.
Integration of the formula 3.3 yields:

$$ln(\frac{I_0}{I}) = \sigma(\lambda)\int_0^L Nds \quad , \tag{3.4}$$

where I_0 denotes the initial radiance and L the thickness of the layer. We can use $S = \int_0^L Nds$ in the formula, and D as optical density and ϵ is the absorption coefficient:

$$dD = \epsilon(\lambda)ds \tag{3.5}$$

With these steps, the radiance traversing the absorbing layer is:

$$I_L(\lambda) = I_0e^{-\sigma(\lambda)S} = I_0(\lambda)e^{-D} \quad , \tag{3.6}$$

which is known as Beer-Lambert Law.

3.2 Ground based observations

The absorption of photons by atmospheric molecules changes the state of the molecules by causing electronical, vibrational and rotational transitions. The absorption cross section is characteristic for the absorbing molecules.
The absorption of radiation by matter is described by the Beer-Lambert Law .
The emitted light with an intensity $I_0(\lambda)$ passes through a volume (open atmosphere) with absorbers (trace gases and aerosols). From the reduced intensity $I(\lambda)$, we can derive information about these absorption and scattering processes.
The optical density is defined as:

$$D = ln(\frac{I_0}{I}) = \int_0^L \sum_j \sigma(\lambda)_j c_j dl, \tag{3.7}$$

where σ_j is the absorption cross sections and c_j is the gas concentration:

$$\begin{aligned} c &= \frac{D}{\sigma(\lambda)L} \\ &or \\ SCD &== \frac{D}{\sigma(\lambda)L}, \end{aligned} \tag{3.8}$$

where SCD is the slant column density of an atmospheric trace gas, which is the concentration integrated over the light path in the atmosphere.

3.2.1 Passive DOAS

Passive DOAS means that natural light sources (sun or moon, extraterrestrial) are used as light source. The relatively simple experimental setup is an advantage of passive DOAS.

3.2.2 MAX-DOAS

The Multi-Axis Differential Optical Absorption Spectroscopy (MAX-DOAS) is a measurement technique that observes scattered sunlight under different elevation angles between zenith and horizon (Leser *et al.* (2003); Van Roozendael *et al.* (2003); Hönninger *et al.* (2004); Wagner *et al.* (2004)). Using different elevation angles give us the possibility to derive the vertical distribution of trace gases.

3.2.3 Correction of the spectra

The MAX-DOAS spectra have to be corrected before the analysis. These spectra have to be corrected by offset and dark current spectra, which are recorded by the same instrument.

3.2.3.1 Offset

The analogue-digital converter transforms the signals to digital form, and before this step, an offset is added to the measured spectra to avoid negative signals. Therefore this offset has to be subtracted from the spectra. The corrected spectrum can be obtained by:

$$I_{corr} = I_{meas} - \frac{N_{meas}}{N_f} O_f \tag{3.9}$$

I_{corr} is the corrected spectrum.
O_f is the Offset spectrum.
N_{meas} is the number of scans of the measured spectrum, N_f is the number of scans of the Offset spectrum and I_{meas} is the intensity of the measured spectrum.
An offset spectrum is a measured spectrum with a high number of scans and a short integration time.

3.2.3.2 Dark Current

This is the signal measured by the detector without illumination. This effect is caused by thermal excitation. The probability of this excitation is proportional to the Boltzmann function. To reduce the dark current signals, detectors are usually cooled to a constant temperature. The corrected spectrum can be obtained by:

$$I_{corr} = I_{meas} - \frac{t_{meas}}{t_{DC}} I_{DC}, \tag{3.10}$$

where I_{meas} is the intensity of the measured spectrum.

where the t_{meas} and t_{DC} are the integration times of measured and dark current spectrum. I_{DC} represents the dark current spectrum, which is a measured spectrum with one scan and a long integration time.

3.2.4 DOAS Retrieval

The measured spectra can be analyzed using the DOAS method (Platt & Stutz, 2008). Several trace gas absorption cross sections as well as a Fraunhofer reference spectra, a Ring spectrum and a polynomial (order 2-5) are included in the spectral fitting process by means of a least squares fitting routine.
The DOAS analysis is based on the separation of slow and fast varying spectral structures (Platt & Stutz, 2008). The Levenberg-Marquordt Algorithm (LMA) (Levenberg, 1944) is used in the fitting retrieval. The LMA is a combination of linear and non-linear fitting processes. During the fitting process the difference between the measured spectrum $I(\lambda)$ and simulated spectrum F is minimised:

$$\sum_i (ln(I_i(\lambda)) - F_(i))^2 \longrightarrow min \tag{3.11}$$

The simulated spectrum can be shown in this form: $F = \sum \sigma(\lambda) SCD$, and $\sigma(\lambda)$ represents the absorption cross sections. The difference between the first term (optical depth of the measured spectrum) and the second term (the simulated spectrum) is the residual, which should be minimized.

The output of the spectral analysis is the so called slant column density (SCD), the integrated trace gas concentration along the light path through the atmosphere.

3.2.4.1 Ring Effect

Inelastic Raman scattering in the atmosphere causes a reduction of the optical density of Fraunhofer lines. Because of this reduction, a correction has to be applied during the spectral analysis. Light intensity scattered into a passive DOAS instrument can be written as (Platt & Stutz, 2008) and (Solomon *et al.* , 1987):

$$I_{meas} = I_{Rayleigh} + I_{Mie} + I_{Raman} = I_{elastic} + I_{Raman} \tag{3.12}$$

If we rewrite this equation:

$$\begin{aligned} ln(I_{meas}) &= ln(I_{elastic}) + ln(1 + \frac{I_{Raman}}{I_{elastic}}) \\ &\approx ln(I_{elastic}) + \frac{I_{Raman}}{I_{elastic}} \quad , \end{aligned} \tag{3.13}$$

where the last ratio of the Raman and the elastic part of the intensity is defined as Ring spectrum:

$$I_{Ring} = \frac{I_{Raman}}{I_{elastic}} \tag{3.14}$$

The Ring spectrum is included as pseudo-absorber in the DOAS retrieval.

3.2.4.2 Stratospheric correction

From the MAX-DOAS observations, the total column of a trace gas can be obtained, the total column can be separated into tropospheric and stratospheric parts. Our focus in this study is the tropospheric part.

To obtain the SCD from MAX-DOAS observations, two different spectra are required, the measured one $I(\lambda)$ and the solar reference spectrum $I_0(\lambda)$, which is usually from the zenith direction.

The SCD is the sum of the troposphere and the stratosphere:

$$SCD_{meas} = SCD_{trop} + SCD_{strat} \tag{3.15}$$

The result of the DOAS retrieval is the difference between the SCDs of the measured spectrum and the Fraunhofer reference spectrum SCD_{ref}, since the Fraunhofer reference spectrum also contains atmospheric trace gas absorptions. This DSCD (differential slant column density) can be written as:

$$DSCD_{meas} = SCD_{meas} - SCD_{ref} \tag{3.16}$$

For the Fraunhofer reference spectrum usually a spectrum with small trace gas absorption is chosen. For trace gases, for which the stratospheric part can be comparable to or smaller than the tropospheric part, an assumption is feasible that the stratospheric absorption is the same in all spectra taken during one elevation sequence. (Wagner *et al.* , 2010):

$$\begin{aligned} DSCD_{meas}(\alpha) &= SCD_{trop}(\alpha) + SCD_{strat} - SCD_{trop}(ref) - SCD_{strat} \\ &= SCD_{trop}(\alpha) - SCD_{trop}(ref) = DSCD_{trop}(\alpha) \quad , \end{aligned} \tag{3.17}$$

where $DSCD_{trop}(\alpha)$ is the tropospheric differential slant column density for the elevation angle α, which contains only tropospheric absorption signals.

For the spectra in this equation, the same Frauhofer reference spectrum is used.

3.2.4.3 Determination of the tropospheric vertical column density

The vertical column density is defined as the concentration of a trace gas vertically integrated over the entire extent of the atmosphere. The airmass factor (AMF) (Solomon *et al.* , 1987) is defined as:

$$AMF = \frac{SCD}{VCD} \quad , \tag{3.18}$$

where AMF is the proportionality factor between the observed slant column density and the vertical column.
For a slant viewing geometry, the absorption paths through the lower atmosphere can become rather large. MAX-DOAS observations are especially sensitive to tropospheric trace gases. From the combination of observations at several elevation angles, also information on vertical trace gas profile can be obtained (Hönninger & Platt, 2002) and (Wagner *et al.* , 2007).

The accuracy of the airmass factor calculations directly affects the accuracy of the vertical column densities. For many applications, the AMF is retrieved from radiative transfer simulations (Solomon *et al.* , 1987). The tropospheric AMF is defined as:

$$AMF_{trop}(\alpha) = \frac{SCD_{trop}(\alpha)}{VCD_{trop}} \tag{3.19}$$

We can rewrite this equation as:

$$\begin{gathered}
\frac{SCD_{trop}(\alpha)}{AMF_{trop}(\alpha)} = \frac{DSCD_{trop}(\alpha) + SCD_{trop}(ref)}{AMF_{trop}(\alpha)} \\
DSCD_{trop}(\alpha) = AMF_{trop}(\alpha)VCD_{trop} - AMF_{trop}(ref)VCD_{trop} \\
VCD_{trop} = \frac{DSCD_{trop}(\alpha)}{AMF_{trop}(\alpha) - AMF_{trop}(ref)}
\end{gathered} \tag{3.20}$$

$$VCD_{trop} = \frac{DSCD_{trop}(\alpha)}{DAMF_{trop}(\alpha)} \quad , \tag{3.21}$$

where $DAMF_{trop}(\alpha) = AMF_{trop}(\alpha) - AMF_{trop}(ref)$.

3.2.4.3.1 Geometrical approximation for ground based observations

In many cases, we can use an approximation for the airmass factor, the so called geometric approximation (Brinksma *et al.* , 2008). The tropospheric airmass factor can be described by:

$$AMF_{trop} \approx \frac{1}{sin(\alpha)} \tag{3.22}$$

Thus the tropospheric vertical column density can be determined as:

$$VCD_{trop} = \frac{DSCD_{trop}(\alpha)}{\frac{1}{sin(\alpha)} - \frac{1}{sin(ref)}}, \tag{3.23}$$

This equation can be rewritten as:

$$VCD_{trop} = \frac{DSCD_{trop}(\alpha)}{\frac{1}{sin(\alpha)} - 1}, \tag{3.24}$$

if a Fraunhofer reference spectrum measured at zenith is used. The geometric approximation can usually be applied only for high elevation angles.

3.2.4.3.2 Mobile MAX-DOAS observations

The determination of the tropospheric vertical column density is more difficult for mobile MAX-DOAS observations. Because of the movement of the platform, the trace gas concentrations can considerably change during one measurement sequence.

The tropospheric VCD can be obtained from two measurements:

$$\begin{aligned} VCD_{trop} &= \frac{SCD_{meas}(\alpha) - SCD_{strat}(\alpha)}{AMF_{trop}(\alpha)} \\ &= \frac{DSCD_{meas}(\alpha) + SCD_{ref} - SCD_{strat}(SZA)}{AMF_{trop}(\alpha)} \\ &= \frac{DSCD_{meas}(\alpha) + DSCD_{offset}}{AMF_{trop}(\alpha)} \end{aligned} \tag{3.25}$$

The SCD_{ref} and $SCD_{strat}(SZA)$ are usually unknown. While SCD_{ref} is constant, $SCD_{strat}(SZA)$ depends on the solar zenith angle. For high SZA, this dependency is large, but for low SZA it is usually negligible. We add both terms:
$DSCD_{offset}(SZA) = SCD_{ref} - SCD_{strat}(SZA)$.
If we use the equations 3.21 and 3.25, we get:

$$DSCD_{offset}(SZA) = \frac{AMF_{trop}(ref)DSCD_{meas}(\alpha) - AMF_{trop}(\alpha)DSCD_{meas}(ref)}{AMF_{trop}(\alpha) - AMF_{trop}(ref)} \tag{3.26}$$

This term can be derived from a single pair of measurements from one elevation sequence. To minimize the effect of the moving platform, we apply this method to all measurements:

$$DSCD_{offset}(t_i) = \frac{AMF_{trop}(ref,t_i)DSCD_{meas}(\alpha,t_i) - AMF_{trop}(\alpha,t_i)DSCD_{meas}(ref,t_i)}{AMF_{trop}(\alpha,t_i) - AMF_{trop}(ref,t_i)}, \tag{3.27}$$

and finally we find:

$$DSCD_{offset}(t) = \frac{\sum_1^N SCD_{ref}(t_i)}{N} - SCD_{strat}(t_i) \quad , \tag{3.28}$$

where N is the number of measurements. We can fit now a polynomial as a function of time to $DSCD_{offset}(t)$.

3.2.5 Mini-MAX-DOAS

The Mini-MAX-DOAS instrument is a fully automated, light weighted spectrometer ($13cm \times 19cm \times 14cm$) designed for the spectral analysis of scattered sunlight (Bobrowski *et al.* , 2003). It consists of a sealed aluminium box containing the entrance optics, a fibre coupled spectrograph and the controlling electronics. A stepper motor mounted outside the box rotates the whole instrument to control the elevation of the viewing angle (angle between the horizontal and the viewing direction). The entrance optics consists of a quartz lens of focal length f = 40 mm coupled to a quartz fibre bundle which leads the collected light into the spectrograph (field of view is 1.2°). The light is dispersed by a crossed Czerny-Turner spectrometer (USB2000+, Ocean Optics Inc.) with a spectral resolution of 0.7 nm over a spectral range from 320 - 460nm. A one-dimensional CCD (Sony ILX511, 2048 individual pixels) is used as detector. Before the signal is transferred to the 16 bit analog to digital converter, an electronic offset is added. After conversion, the signal is digitally transmitted to PC via USB cable.
For mobile MAX-DOAS observations, a mini MAX-DOAS instrument was mounted on the roof of a car.

3.3 Remote Sensing from Space

Passive UV/vis satellite remote sensing instruments are detecting the reflected sunlight from the earth and scattered back from the atmosphere.
Typical viewing geometries are Nadir and Limb. In Nadir geometry the instrument looks perpendicular down to the earth. In Limb geometry light scattered from the earth's rim is used. Satellites are the best devices to measure the global distribution trace gases, and study the transport of pollutions.

3.3.1 GOME

The Global Ozone Monitoring Experiment (GOME) (Burrows *et al.* , 1999), a UV-vis spectrometer was launched onboard the ERS-2 in 1995 by the European Space Agency (ESA). It was designed for monitoring ozone, but from GOME also the information about other trace gases, like $NO_2, SO_2, HCHO, BrO\ and\ OClO$ can be obtained.

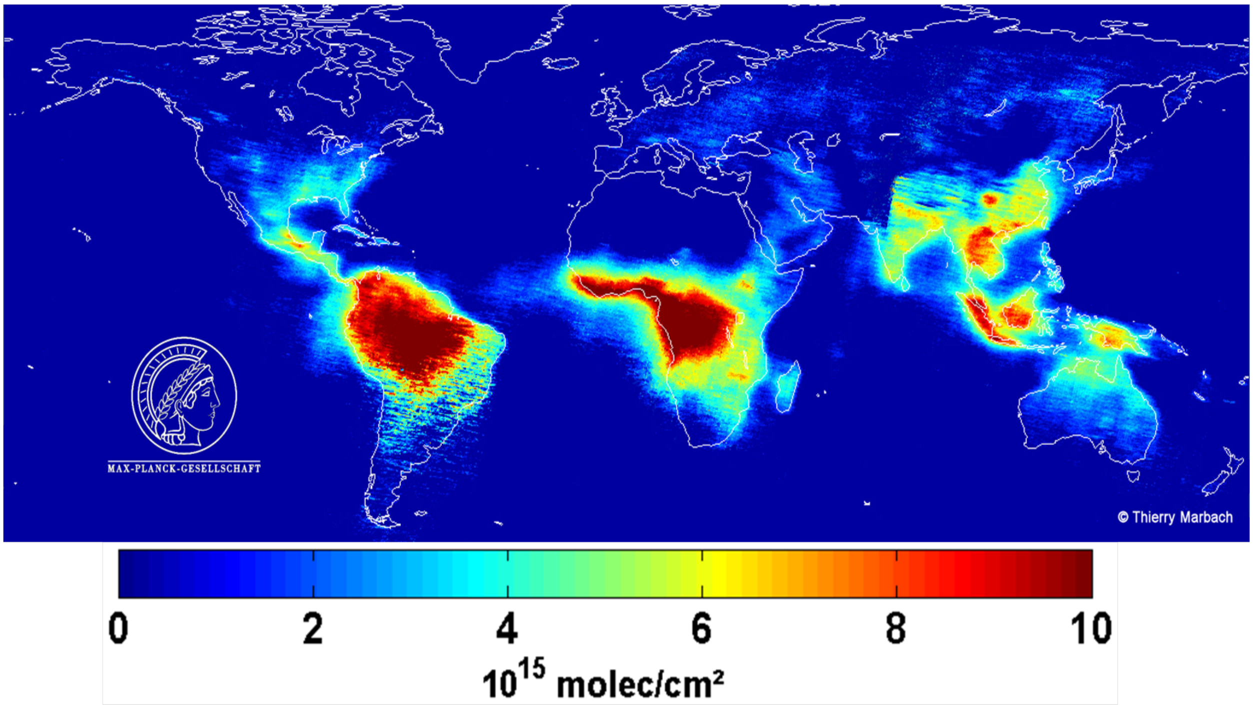

Figure 3.1: 7,5 year mean of Formaldehyde tropospheric column density (1996 to June 2003) derived from GOME observations (only measurements with less than 20 % cloud cover) (ref: `http://joseba.mpch-mainz.mpg.de/hcho.htm`).

The average of the tropospheric column densities of formaldehyde from 1996 to 2003 from GOME observations is shown in figure 3.1.

3.3.2 SCIAMACHY

SCIAMACHY: the SCanning Imaging Absorption SpectroMeter for Atmospheric CHartography was launched in March 2002 onboard the ESA satellite ENVISAT. The solar radiation transmitted, backscattered and reflected from the atmosphere is observed at relatively high resolution over the range 240 nm to 1700 nm, and in selected regions between 2000 nm and 2400 nm (Bovensmann *et al.* , 1999). Different atmospheric trace gases can be observed by SCIAMACHY in two different viewing geometries, Limb and Nadir.

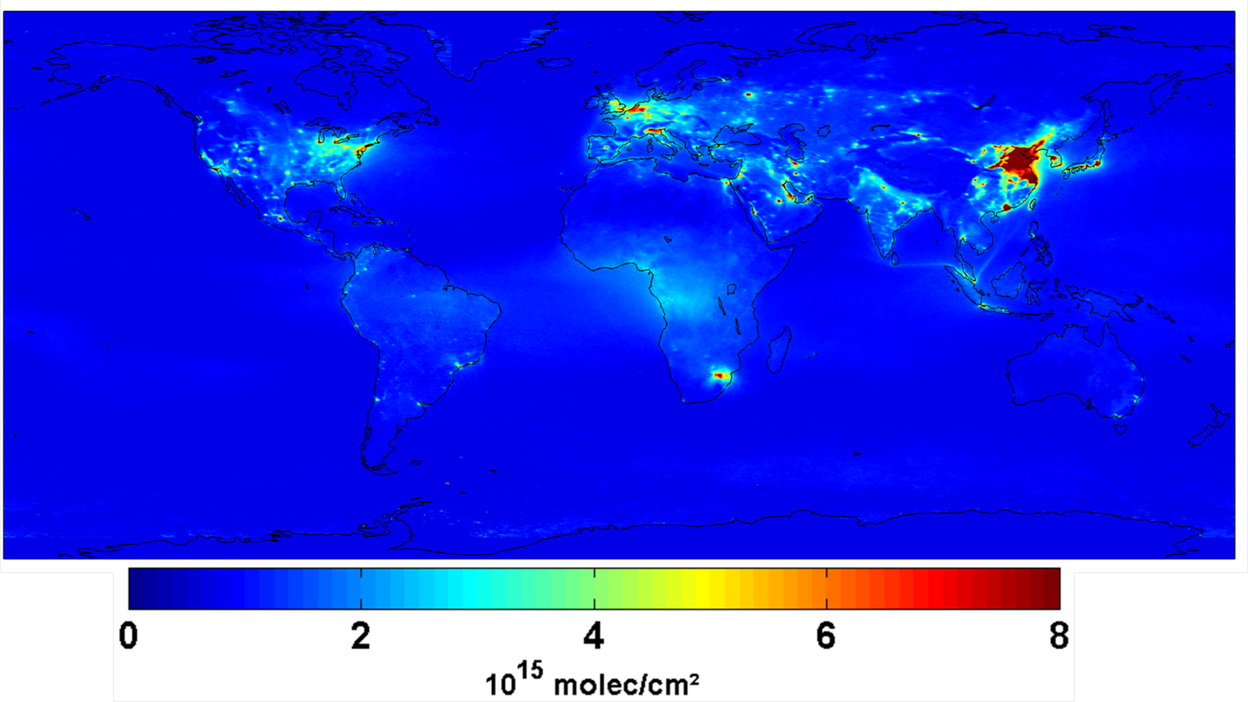

Figure 3.2: Average tropospheric NO_2 vertical column densities from 2003 to 2010 from SCIAMACHY observations and with 30 % cloud restriction(Ref.: Steffen Beirle personal communication).

An example from SCIAMACHY observations is shown in figure 3.2, which is the average of the tropospheric vertical column densities of nitrogen dioxide from 2003 to 2010.

3.3.3 The Ozone Monitoring Instrument (OMI)

The ozone monitoring instrument (OMI) was launched in July 2004 onboard the EOS-AURA satellite of NASA. The Aura spacecraft circulates in a 98.2° inclination, sun-synchronous polar orbit at 705 km altitude, with a local afternoon equator crossing time at 13:45 (ascending node), providing 14 orbits a day.

OMI is a UV/VIS (range from 270 to 500 nm) nadir viewing imaging solar backscatter

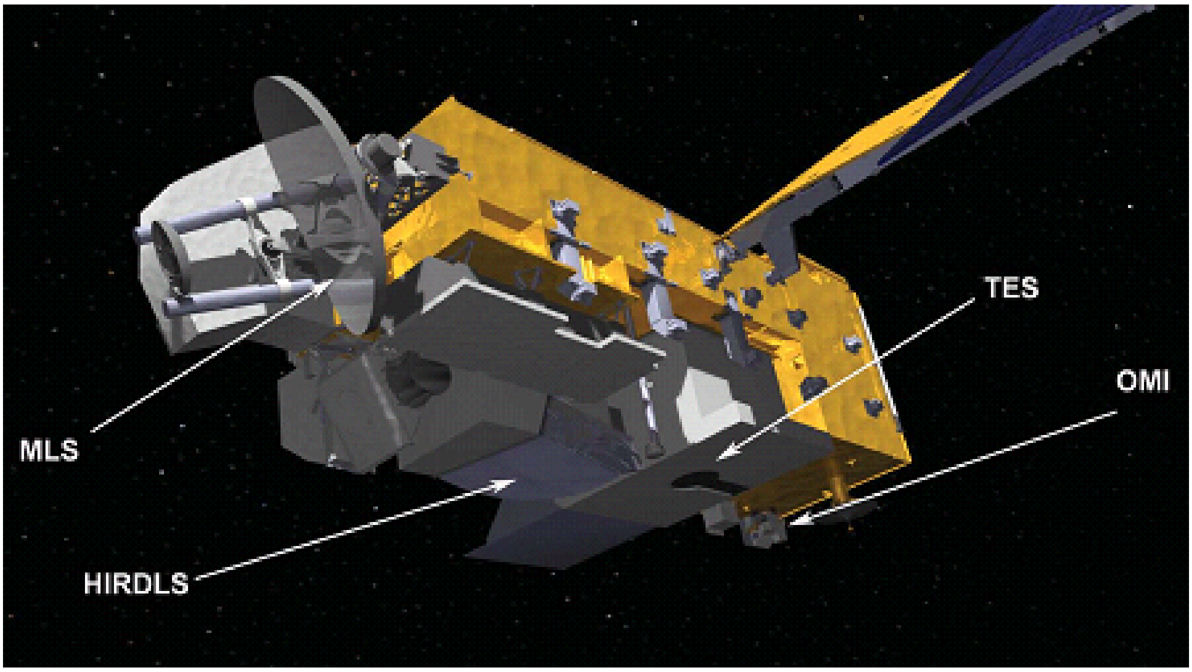

Figure 3.3: This model shows the EOS-Aura satellite with different instruments including OMI (Schoeberl *et al.* , 2004).

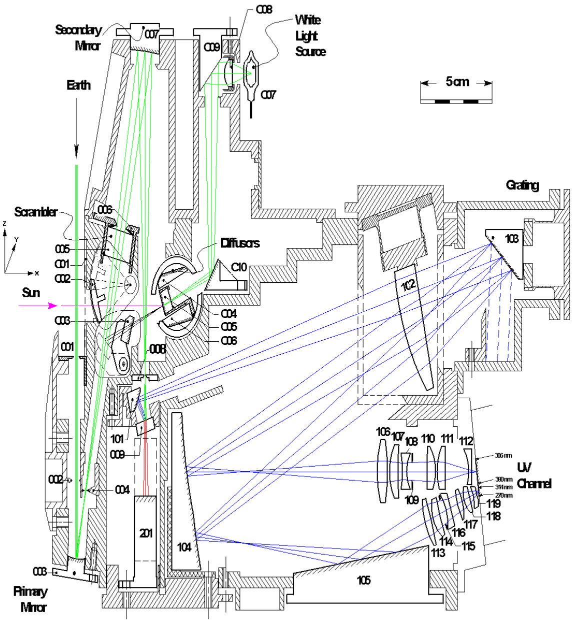

Figure 3.4: Optical layout, UV OMI telescope with light paths and optical elements (`http://www.knmi.nl/omi/research/instrument/optic.php?tag=full`).

spectrograph, which provides near-global coverage in one day with a spatial resolution of 13×24 km^2 (Levelt *et al.* , 2006). OMI measures various parameters for stratospheric and tropospheric chemistry, including ozone (column and profile), nitrogen dioxide, sulfur diox-

ide, formaldehyde, UV-B radiation at the surface, aerosol and cloud properties etc. OMI has been equipped with two two-dimensional CCD detectors, which record a complete spectrum in one direction with a 114° field of view, distributed over 60 discrete viewing angles.
OMI's wide field of view corresponds to a 2600 km wide spatial swath on the earth surface for one orbit, enough to obtain a complete global coverage in one day. The exposure time of the CCD-camera measures 2s, corresponding to a spatial sampling of 13 km along track (2 s×6.5 km/s, the latter being the orbital velocity projected onto the earth surface).
Across track the size of an OMI pixel varies with viewing zenith angle from 24 km in the nadir to approximately 128 km for the extreme viewing angles of 57° at the edges of the swath (Boersma *et al.* , 2007).

In figure 3.3, the instruments (including OMI) onboard EOS-AURA satellite are shown. The optical elements and light paths from UV OMI telescope is displayed in figure 3.4.

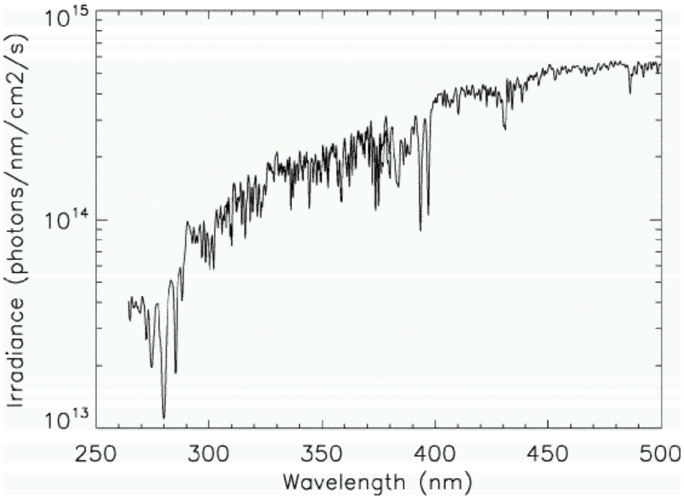

Figure 3.5: Measured solar spectrum (over quartz volume diffuser with binning factor eight from row 33) (orbit 3207, 20.02.205) (Dobber *et al.* , 2006)

In figure 3.5, a typical Fraunhofer spectrum is shown.

4 Estimation of Megacities Emissions

Various air pollutants impact air quality and ultimately climate and megacities are important sources of air pollutants. Urban areas with more than 5 million people are usually called megacities. They emit different harmful substances to the atmosphere, which can have local, regional and global effects.
In this chapter, we introduce, how the emission of a megacity can be estimated from mobile MAX-DOAS observations.

4.1 Emission from the encircled area

With mobile MAX-DOAS observations, a horizontal integration can be obtained, in addition to vertical integration of the tropospheric trace gas concentrations. Such observations allow to determine the complete flux F of trace gas molecules from the encircled area.
The transport of a conserved quantity (mass, energy, electric charge and air molecules) can be described by continuity equation. If one of these quantities flows through a surface, we can define a flux of the quantity. The differential form of a general continuity equation is written so:

$$\frac{\partial \varphi}{\partial t} + \vec{\nabla}.\vec{f} = \sigma \tag{4.1}$$

f: flux.
φ: the ratio of infinitesimal particles to the volume $\varphi = \frac{dq}{dV}$ (q: quantity of particles and V: volume; $q = \int \phi dV$).
t: time.
σ: the generation of particles per unit volume per unit time. As source or generation, if $\sigma > 0$, and sink, if $\sigma < 0$.

If we apply this continuity equation for nitrogen dioxide molecules, which are flowing over the megacity, we can describe the flowing of the molecules per unit area and time as flux of NO_2.
If we integrate the equation 4.1 over the volume: $\int \frac{dq}{dt} dv + \int \nabla . f dv = \int \sigma dV$
We assume that the amount of the molecules inside our closed volume is constant and does

not change during the encircling, therefore $\frac{dq}{dt}$ can be neglect.

$$\begin{aligned}\int \nabla.f dv &= \int \sigma dV \\ \oint_S \vec{f}.\vec{n} dS &= \int \sigma dV,\end{aligned} \tag{4.2}$$

where the flux of the emitted molecules in the closed area can be written from the VCD's of molecules and the wind speed within the trace gas layer.
The total emissions from the encircled area are determined from the following equation (Ibrahim *et al.* , 2010), where the wind speed and direction are required.

$$\begin{aligned}F &= \oint_S VCD(s)\vec{w}.\vec{n} ds \\ &= \sum_i VCD_i w_i sin(\beta_i) ds\end{aligned} \tag{4.3}$$

Here $\vec{n}$ indicates the normal vector parallel to the earth's surface and orthogonal to the driving direction at the position s of the driving route; $\vec{w}$ is the wind vector within the trace gas layer at the location of the mobile MAX-DOAS. The total flux entering and leaving the encircled area can be determined, if the emission sources are completely encircled. In simple cases, the integrated total emission flux of the encircled area is just the difference between the influx and the out-flux. In figure 4.1, an example of such observations is illustrated. The colored points indicate the vertical column densities from mobile MAX-DOAS. The related wind vectors are shown in the same figure (4.1), and from the equation 4.3, the flux for every measured point can be determined, which provides, the in-flux close to the blue points (low values) and out-flux close to the red points (high values).

Usually, there are gaps in the measurements, which can be caused by different reasons like instrumental problems (connection the instrument to the computer) etc. To determine the associated uncertainty, a simple method is applied: in the first calculation, we determine the total emissions clockwise, and in the second calculation counter-clockwise. From both calculations, we determine the average emissions and the corresponding uncertainties.

The flux from the equation 4.3 can be used for different trace gases. One of the applications is the determination of NO_x emissions from MAX-DOAS observations, but because we measure only NO_2 and not NO, we have to apply some corrections, to determine the NO_x emissions.

Lifetime correction: If we have a constant (not too low) wind speed and constant direction over our interested area, a correction factor for the effect of a limited atmospheric lifetime can be determined. Without suitable conditions (e.g. low or calm wind or winds variable with time and space), such cases are complicated and require the use of atmospheric model

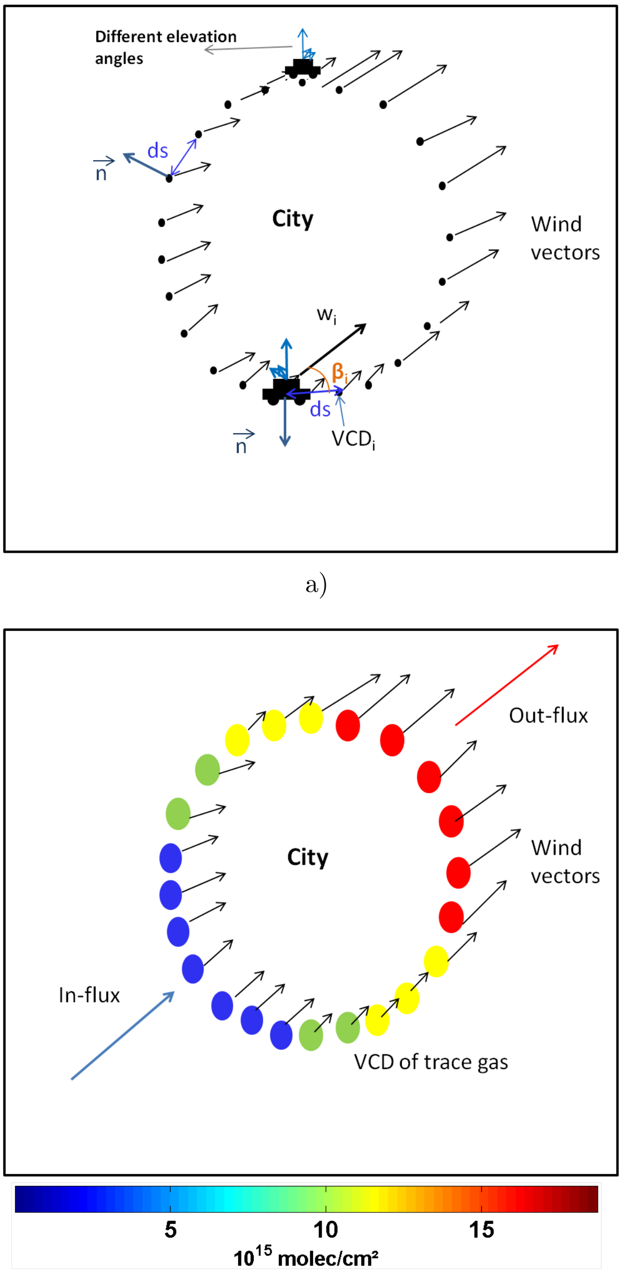

a)

b)

Figure 4.1: a) The mobile MAX-DOAS is encircling the city counterclockwise. b) The colored points indicate VCD's of a trace gas (like NO_2) with related wind vectors.

simulations. The lifetime correction factor can be given as:

$$c_\tau = e^{\frac{t}{\tau}} = e^{\frac{\frac{r}{w}}{\tau}} \tag{4.4}$$

Here t is the ratio of the radius r of the driving circle and w is the related wind speed.

Chemical transformation factor: Rapid chemical reactions can change the partitioning of the emitted species. In the NO_x emission case, most of NO_2 was primarily emitted as NO. The partitioning of these molecules depends on the ozone concentration and the NO_2 photolysis rate. The atmospheric concentrations of the emitted species can be changed by processes, which are fast compared to the transport time between the emission source and the location of the measurement. Thus the measured trace gas concentration represents only a fraction of the emitted trace gas abundance (Ibrahim *et al.* , 2010). The chemical transformation factor can be written as:

$$c_L = \frac{[NO_x]}{[NO_2]} \tag{4.5}$$

Typical values of c_L derived from model simulations are in the range of 1.3 to 1.46 . With both correction factors, the whole NO_x emission from the encircled area is:

$$F_{NO_x} = c_L.c_\tau.F_{NO_2} \tag{4.6}$$

4.2 Up-scaling of the encircled area to the whole megacity

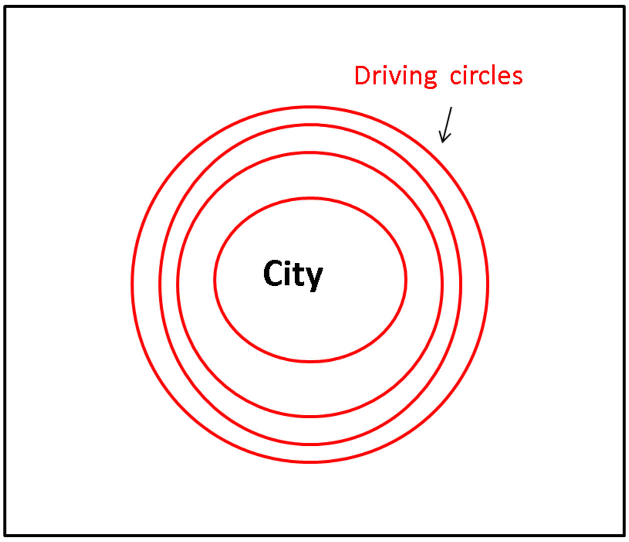

Figure 4.2: The red circles are the driving routes by mobile MAX-DOAS, which should be upscaled to the black box. Here, the black box is defined as the whole ”megacity”.

The results from the last equation are representative only for the emissions from the encircled area. If we want to compare our emissions to different emission inventories and between different days of measurements with different circles; (see figure 4.2), the mobile MAX-DOAS emissions have to be up-scaled to a greater area which is defined here as ”megacity”.

In figure 4.2, the red circles indicate the different driving routes, and the estimated emissions from these different orbits should be upscaled to the black box, which is here defined as megacity.

For the up-scaling, different proxies can be used like e.g. the EDGAR (Emission Database for Global Atmospheric Research) emission inventory, population density, measured night time lights etc.
A) EDGAR emission inventories: we used the EDGAR inventory version 4.1 for 2005 (see (Olivier *et al.* , 1998)); European commission, 2010. Note that the spatial resolution of this data set is rather coarse (0.1°).
B) Population density: we used data on the population density (obtained from CIESIN, GWPv3, 2010, `http://sedac.ciesin.columbia.edu/gpw/global.jsp`) with a spatial resolution of 2.5 arc minutes.
C) Radiances of night time measurements: we apply the distribution of night-time lights measured from satellite (NOAA, National geophysical Data Center, 2006, `http://www.ngdc.noaa.gov/dmsp/download_radcal.html`, (Ziskin *et al.* , 2010)) with a spatial resolution of 0.5 arc minutes.

In chapter 5, we used all these three proxies to up-scale the encircled emissions; but in the chapter 6, we used only the radiances of night time measurements. For Paris the choice of the proxy is not critical, because of its concentric shape.

5 New Delhi NO_x Emissions

This chapter is based on Shaiganfar *et al.* (2011).

Delhi, home of 19 million people, second largest metropolitan city (`http://www.indiaonlinepages.com/population/delhi-population.html/`), is located in the Indo-Gangetic plains in India. The growing population and human activities increase the atmospheric pollution which is e.g. the cause of the dense fog, smog and haze during winter season (December and January) every year ((Singh *et al.* , 2004); (Singh *et al.* , 2005); (Ramanathan & Ramana, 2005); (Ramanathan *et al.* , 2005); (Gautam *et al.* , 2007)). In the years 2005 and 2006, about 4.8 million vehicles were in operation in Delhi. In the last three decades the atmospheric trace gas and aerosol loading has increased in the Indo-Gangetic plains due to intense urbanization, anthropogenic activities, industrial growth and energy demand. Especially in the northern part of India, the pollutants swing in the Indo-Gangetic basin depending upon the meteorological conditions. The sources of atmospheric pollutants are localized and heterogeneous and depended on season ((Gurjar *et al.* , 2004); (Goyal *et al.* , 2006)).

To study of atmospheric pollutants, performed a measurement campaign in the greater Delhi area. The campaign had two purposes: first to determine the total NO_x emissions of the Delhi area and second to validate satellite observations.

5.1 Mobile MAX-DOAS Measurements

The mobile MAX-DOAS observations were carried out in April 2010 (some days) and 2 days in January 2011. The telescope was mounted parallel to the driving direction, pointing backward (April) or forward (January). The start was at Greater Noida to Delhi and around the city. In figure 5.1, the driving routes are shown.

A mini MAX-DOAS instrument mounted on a car, was used (see section 3.2.5). The sequence of elevation angles was chosen to: 1×90°, 5×22°, 1×45°, 5×22° and the duration of an individual measurement was about 60s. For the measurements on 15 January 2011, an elevation angle of 30° was set up instead of 22° during April 2010. The temperature setpoint of the mini MAX-DOAS was 15° C in April and 5° C in January. A handy GPS (GPS-Logger: HOLUX, m.247) was used to track the coordinates of the route along which

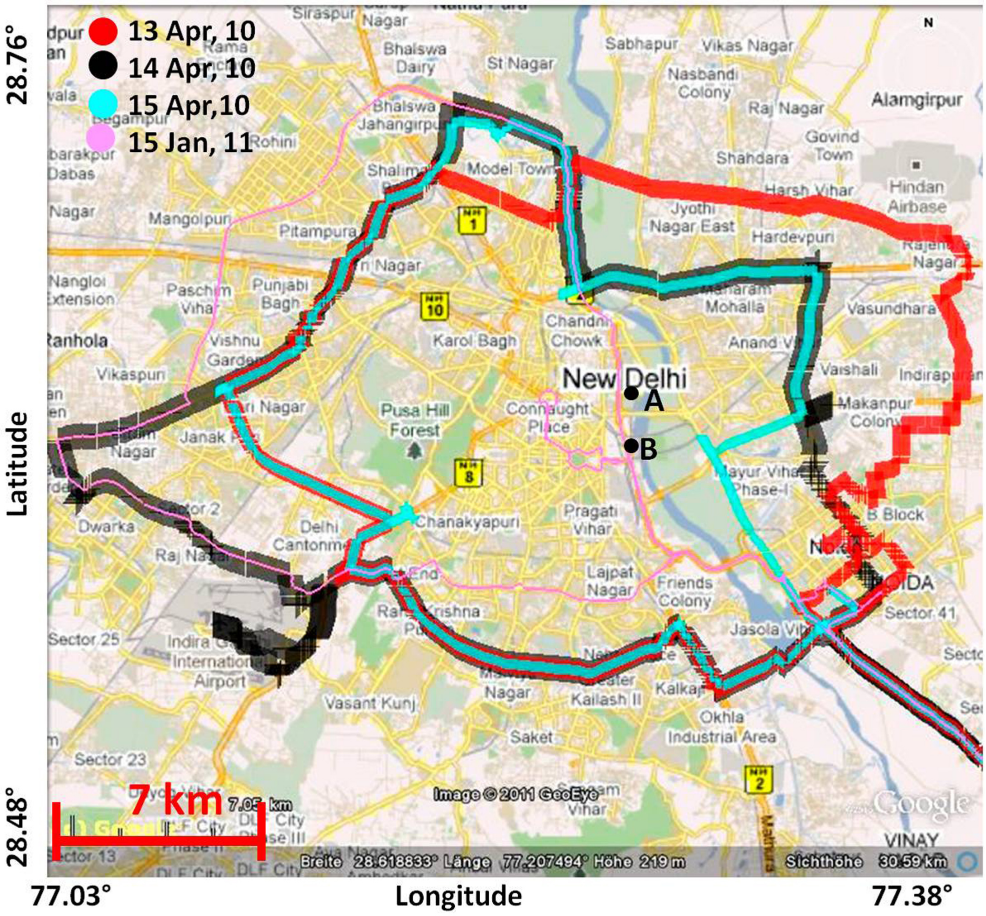

Figure 5.1: Different driving routes around Delhi. The points A and B indicate the locations of two power plants Rajghat Power Station and Pragati Gas Power Station, respectively.

the observations were made.

During some days of this campaign, whole circles around the city were possible, namely 13, 14 and 15 April 2010 and 15 January 2011. All the days in April were cloud free. The aerosol optical depth derived from MODIS satellite was found in the range of 0.2-0.5 at 550 nm (data taken from AERONET data energy tool, `http://aeronet.gsfc.nasa.gov/cgi-bin/bamgomas_interactive`). On 15 January 2011, the AOD was found to be only 0.1 in the afternoon. During the start of the measurements at 11 am, the AOD might be higher, but we do not have any estimate due to non availability of MODIS aerosol data. The range of AOD is consistent with those measured by AERONET in Delhi for January and April 2009 (see `http://aeronet.gsfc.nasa.gov/`). They are also consistent with those reported in the study of (Satheesh *et al.* , 2011) for the city of Bangalore and of (Rehman *et al.* , 2011) for the city of Kanpur. In April 2010 the wind direction was mostly north-westerly, and the temperature was found in the range 35 - 45°C. On 15 January 2011 the wind is found to be westerly and temperature to vary in the range 15 - 20°C. The time to complete one full circle around the route (see figure 5.1) took about 3 to 5 hours. In contrast to MAX-DOAS

observations at fixed locations, during car MAX-DOAS observations we have used rather high elevation angles to avoid shades from nearby obstacles (e.g. buildings or trees). From such high elevation angles usually no profile information can be retrieved, but we can obtain the total tropospheric trace gas column density.
MAX-DOAS measurements are also affected by aerosols and clouds. A detailed investigation of aerosol effects is performed for New Delhi (section 5.1.1). Measurements at high elevation angles are less affected by aerosols than observations at more low elevation angles.

The measured spectra are analyzed using the DOAS method (see chapter 3). A wavelength range 435-456 nm was selected for the analysis. Several trace gas absorption cross sections (NO_2 at 298 K (Vandaele *et al.* , 1996), H_2O at 298 K (Rothman *et al.* , 2005), Glyoxal at 296 K (Volkamer *et al.* , 2005), O_3 at 243 K (Bogumil *et al.* , 2003), O_4 at 296 K (Hermans *et al.* , 1999) as well as a Fraunhofer reference spectrum, a Ring spectrum (calculated from the Fraunhofer spectrum) and a polynomial of third order) were included in the spectral fitting process, using the WinDOAS software (Fayt & Van Roozendael, 2001). The wavelength calibration was performed based on a high resolution solar spectrum (Kurucz *et al.* , 1984). A typical fit result is shown in figure 5.2. Note that from all fitted trace gases, for the Delhi measurements only the NO_2 and H_2O absorptions were above the detection limit for most measurements.

From the spectral analysis, also the uncertainty of the retrieved SCD can be determined, for the NO_2 analysis, it is typically $< 15\%$.
We have considered 22° elevation angles for measurements in April 2010 but 30° for January 2011. We considered DSCDs with RMS of residuals smaller than 2.5×10^{-3}.
The tropospheric VCD can be obtained from the SCD (see section 3.2.4.3) using a geometric airmass factor (AMF). The tropospheric AMF were found to be 2.67 and 2 for elevation angles of 22° and 30°, respectively. Depending on the aerosol load, cloud condition and vertical trace gas profile, the true AMF can show substantial deviations from the geometric approximation. However, NO_2 is generally located near the surface; therefore the deviations for our measurements are expected to be small.

5.1.1 Effect of aerosols on the measurements

The geometric approximation for the tropospheric AMF (see equation 3.22) is only valid if the light path through the trace gas layer of interest can be well approximated by a simple geometric path. This assumption is usually fulfilled for shallow trace gas layers and low aerosol loads, since the observed light is typically scattered from above the trace gas layer. But in the presence of high aerosol extinction, a substantial fraction of the observed light might be scattered from inside the trace gas layer and the geometric approximation is not appropriate for the complete trace gas layer.

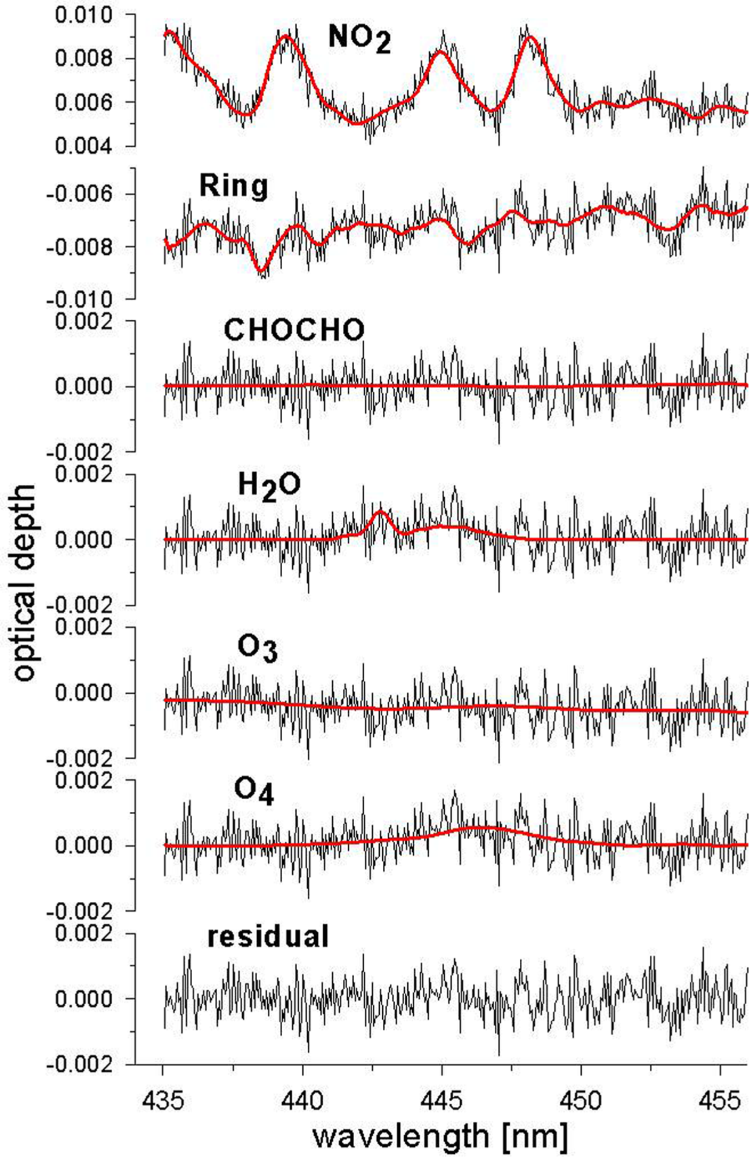

Figure 5.2: Typical result of DOAS fit. Shown are the cross sections scaled by the respective absorptions of the measured spectrum (black).

Depending on the elevation angle and the amount and properties of the aerosols, scattering inside the trace gas layer may either increase (for high elevation angles) or decrease (for lower elevation angles) the true AMF compared to the geometric approximation (Wagner *et al.* , 2004). Thus, the true tropospheric trace gas VCD will be either over- or underestimated. We have quantified these deviations from the geometric approximation using the Monte Carlo radiative transfer model McARTIM (Deutschmann *et al.* , 2010) for various aerosol scenarios and NO_2 layer heights (see figure 5.3).

For these sensitivity studies the aerosol optical parameters were chosen as follows: single scattering albedo: 0.95 and asymmetry parameter: 0.68 (Dubovik *et al.* , 2002). To investigate the effect of different aerosol optical properties we performed similar sensitivity studies as in figure 5.3, but for different values of the single scattering albedo and the asymmetry

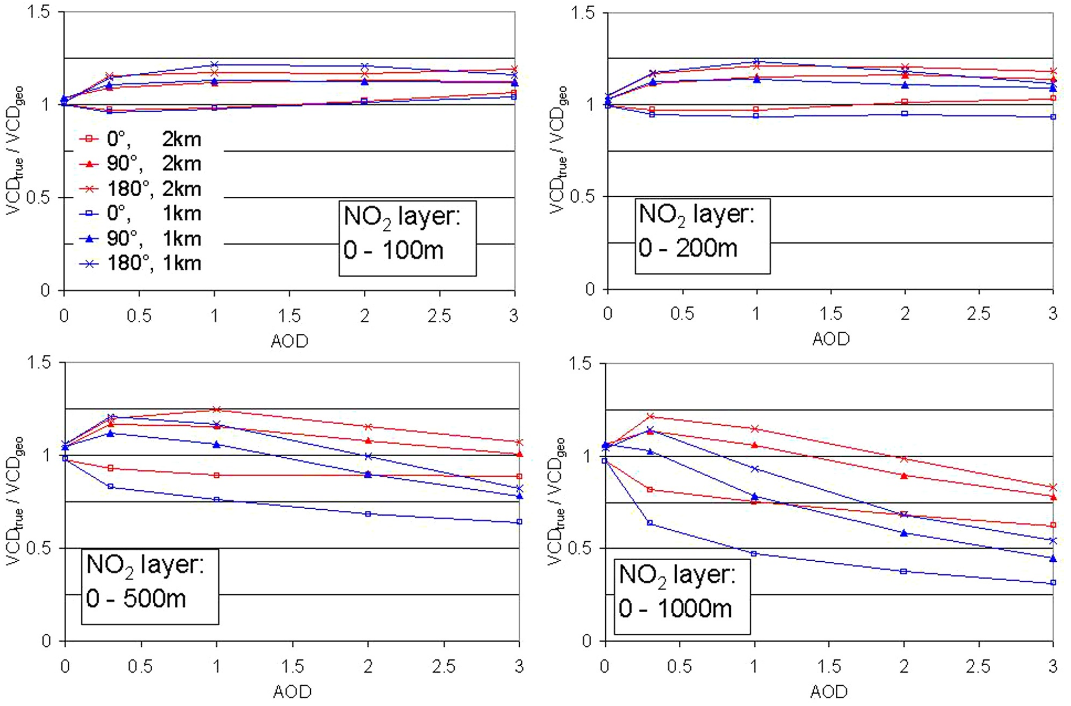

Figure 5.3: Relative deviation of the true tropospheric VCDs (derived from radiative transfer simulations) from the geometric VCD for different trace gas layer heights, aerosol optical depth, aerosol layer heights and relative azimuth angles (i.e. the difference of the azimuth angles of the sun and the viewing direction at the telescope). Calculations are performed for an elevation angle of 22°; the results for an elevation angle of 30° (not shown) are similar.

parameter. The differences to the results in figure 5.3 are small compared to the effects of the aerosol optical depth and the NO_2 and aerosol layer heights. The most important result of these simulation studies is that for NO_2 layer heights $<$ 500m and for moderate aerosol optical depth (about <1), the deviations from the geometric approximation are found to be in the order of up to 20% (see results for elevation angle of 22° in figure 5.3). For measurements at an elevation angle of 30° (15 January 2011) similar results are found (not shown). Here it is important to note that recent MAX-DOAS measurements indicated that the height of the NO_2 layer is typically systematically lower than the mixing layer height. For example, MAX-DOAS observations in Milan in September 2003 (Wagner *et al.* , 2011) show rather low NO_2 layer heights typically <500m. Interestingly, for these measurements the layer heights for HCHO and aerosols were found to be systematically higher. These findings can be understood by a) the rather short lifetime of NO_x compared to aerosols and b) the fact that HCHO and aerosols might even be formed when air masses are lifted up, while NO_x is gradually destroyed. Even for measurements downwind of strong NO_x emission sources like at Cabauw, The Netherlands, NO_2 layer heights of the order of 500m or below were often found (Piters *et al.* , 2011). These findings indicate that usually the NO_2 profile is probably systematically lower than the mixing layer height.

As shown in figure 5.3, the relative azimuth angle between the viewing direction and the sun position has a systematic effect on the sensitivity of the MAX-DOAS measurements. In general, measurements with relative azimuth angles close to zero tend to underestimate the true NO_2 VCD, while measurements at larger relative azimuth angles tend to overestimate the true NO_2 VCDs. This systematic dependence on the relative azimuth angle is found for all combinations of NO_2 layer heights and aerosol properties (although with different amplitudes).
Future studies might explicitly consider this azimuth dependence if tropospheric trace gas VCDs are retrieved from MAX-DOAS observations using high elevation angles (from 15° until higher elevation angles).

For simplicity, in this study, we only applied an azimuth dependent correction for measurements with strongly enhanced NO_2 VCDs (see figure 5.4), because they have the strongest influence on the derived emission estimate. For this correction we assumed a NO_2 layer height of 500m and an aerosol layer height of 2000m. With this simple correction we took already into account part of the variability shown in figure 5.3.

Remaining error due to the dependence of the AMF on the NO_2 profile, aerosol layer height and aerosol optical properties is estimated to about 20%. Here it is interesting to note that the possible presence of uplifted aerosol layers (Babu *et al.* , 2011) has only negligible influence on the NO_2 AMF.

The error in the spectral retrieval is of the order of 15% (see section 2.3). Thus, we estimate the total error in the retrieved tropospheric NO_2 VCD to be about 25%.

5.1.2 Estimation of NO_x emissions

The total NO_x emission from the encircled area are determined from the equation 4.3. This integral is evaluated for the MAX-DOAS measurements around Delhi.
The distance between two measurements is taken as the geometric difference between the locations at the beginning of two successive measurements. From the same segment, the angle between the driving route and the wind direction is calculated.

Wind fields are taken from analyses of the European Centre for Medium-Range Weather Forecasts (ECMWF, full scientific and technical documentations are found from the website `http://www.ecmwf.int/research/ifsdocs/CY33r1/index.html`).
We considered wind speeds up to 1000m and weighted them by an assumed exponentially decreasing NO_x profile with a scale height of 500m. Since the strongest changes in wind speed and direction occur below about 200m altitude, the exact scale height of the assumed NO_x profile has only little influence on derived effective wind speed and direction. The wind

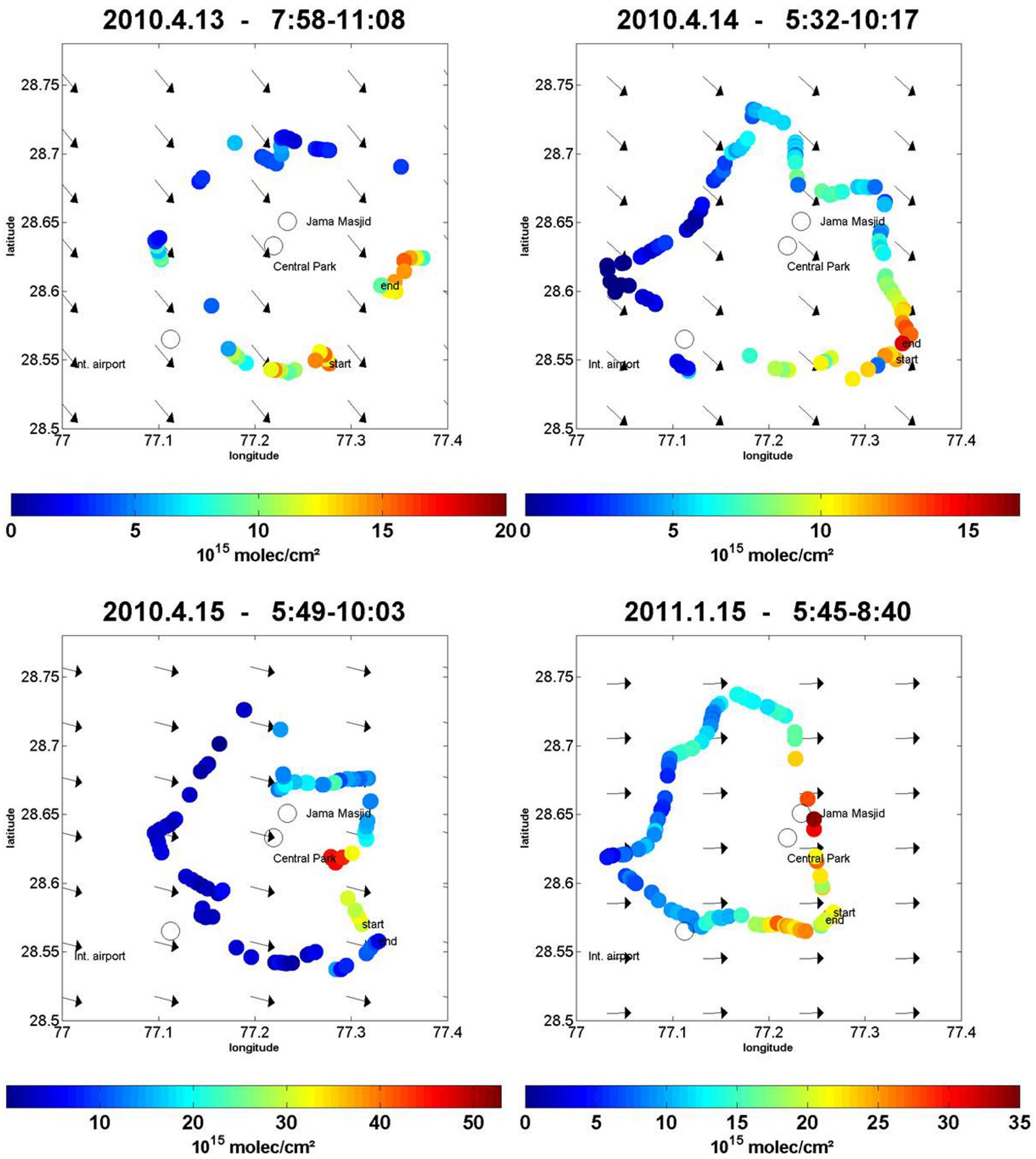

Figure 5.4: Tropospheric NO_2 VCDs derived from mobile MAX-DOAS observations around Delhi on different days. The arrows indicate the average wind direction.

data are linearly interpolated in time to match the MAX-DOAS measurements.

We estimate the uncertainty of the flux estimation due to the choice of wind fields by a) varying the scale height of the assumed NO_x profile by 200m (causing variations within 12%), and b) taking the closest ECMWF output times at 6 and 12 UTC instead of interpolating (causing variations within 10% except for January 15, where the wind fields at 12 UTC have changed significantly, whereas the measurements were taken close to 6 UTC). Overall, we estimate the error due to wind fields as 15%.

The measured NO_2 VCDs together with the wind fields for the four measurement days are shown in figure 5.4. In general, the highest values of NO_2 VCDs are found at the lee side of the city, as expected.

On some days, due to instrument problems, gaps along the driving route occurred; this was mainly due to disturbances caused by uneven road conditions. Due to such problems, NO_2 data are missing at some locations, which has contributed to the larger uncertainties in the estimation of the total emissions. We estimate these uncertainties in a simple way: in a first calculation, we determine the total emissions clockwise, in a second calculation counter-clockwise. In both cases, the NO_2 VCD from the last measurements at the beginning of the gap is considered as the true value for the whole gap. From both calculations, we determine the average emissions and the corresponding uncertainties.

To determine the total NO_x emission from Delhi, we used equation 4.6. The chemical transformation factor, the ratio of NO_x to NO_2 in the polluted layer, in urban pollution conditions during daytime; c_L (see equation 4.5) is about 1.32 (Seinfeld & Pandis, 2006) with an uncertainty of about 10%. c_τ (see equation 4.4) describes the ratio of the measured NO_x and the originally emitted NO_x. Assuming a typical urban plume daytime NO_x lifetime of 5 hours (Spicer, 1982) and taking into account the wind speed of the individual days, using equation 4.4, we found c_τ in the range of 1.09 - 1.18 with uncertainties of about ±10 % (assuming uncertainties of the lifetime of ±2h).

Correction factors: for the azimuth dependence of the AMF were applied for the measurements with the highest NO_2 VCDs along the driving routes. These correction factors were calculated for the exact solar zenith angle, solar azimuth angle and viewing direction under the assumption of a NO_2 layer height of 500m and an aerosol layer height of 2000m (see the previous section). The respective correction factors reach from 0.84 to 0.9.

The total NO_x emissions from within the circles on the different days are shown in figure 5.5. Here the error bars show the uncertainties due to missing data at some locations (green) or total uncertainties (black). The total NO_x emissions are found to be similar for the different days within the range of uncertainties between 1.3 - $1.9.10^{25}$ molecules per second.

It should be noted that especially close to strong emission sources, part of the emitted NO might not be quickly converted to NO_2 if the NO mixing ratios locally exceed those of O_3. In such cases complete establishment of the $\frac{NO_2}{NO}$ steady state will eventually take place only after ambient air has mixed with the emitted plume (Ibrahim *et al.* , 2010). However, for our study such effects can be neglected: First, according to the study of (Gurjar *et al.* , 2004) the relative contributions from power plants to the total NO_x emissions is small (below 10%). Thus even if the emissions from power plants were systematically underestimated, the effects

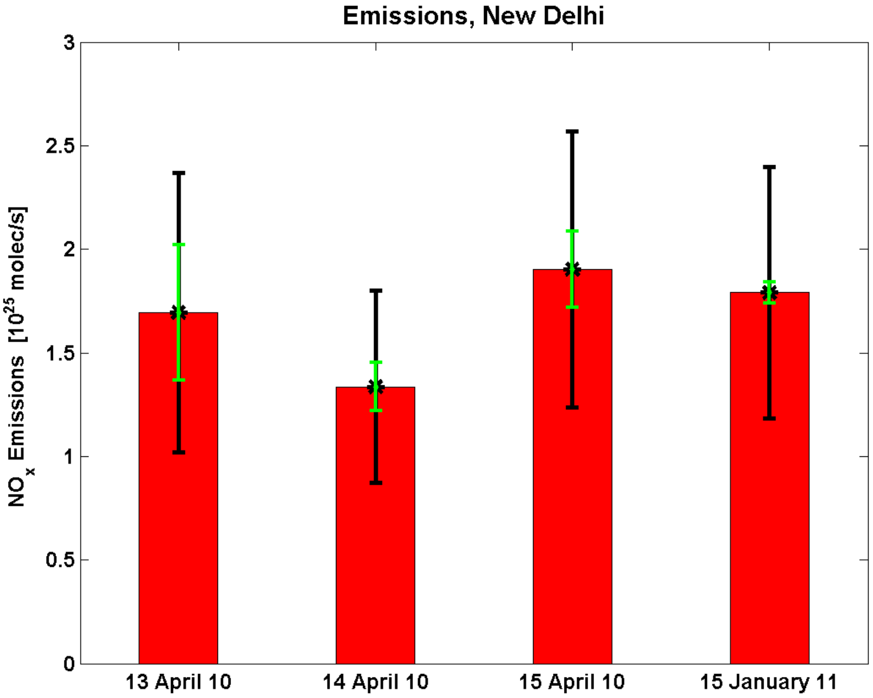

Figure 5.5: NO_x emissions obtained from the car MAX-DOAS measurements for the surrounded areas. The green error bars indicate the uncertainties related to the gaps in the measurements; the black error bars represent the total uncertainty.

on the total emissions would be small.

In addition we estimated the plume extension and the respective NO_x mixing ratios at the location of the car MAX-DOAS measurements according to the atmospheric stability. We considered the actual wind direction and speed and the distance between the car MAX-DOAS measurements and power plants (see figure 5.1) for the different days. On 13th and 14th of April the dilution of the plumes was very effective and NO_x mixing ratios at the location of the car MAX-DOAS measurements were below the O_3 mixing ratios of the ambient air. On 15th of April, the NO_x mixing ratios at the location of the car MAX-DOAS measurements are similar to the O_3 mixing ratios of the ambient air and conversion of part of the emitted NO_x might be hindered. However, on that day the determined emissions are even larger than on the two previous days. On 15th of January 2011 the driving route did not surround the power plants. From the overall good consistency of the results for the different days we conclude that the possible limited conversion efficiency of NO_x to NO_2 close to strong emission sources does not play an important role for our study.

The NO_x emissions for the different days (figure 5.5) only reflect the emissions from the encircled areas. In order to make these results comparable within each other and to existing emission inventories, the results have to be up-scaled to the greater Delhi area (bounded in the region indicated in figure 5.1, latitude 28.5°N to 28.77°N and longitude 77.0°E to 77.4°E).

For the up-scaling, we used different proxies for the spatial distribution of the NO_x emissions across the considered area. First, we use the EDGAR emission inventory (version 4.1 for 2005, see Olivier *et al.* (1998); European commission, 2010), but the spatial resolution of this data set is rather coarse (0.1°). Second, we use data on the population density (obtained from CIESIN, GWPv3, 2010, `http://sedac.ciesin.columbia.edu/gpw/global.jsp`) with a spatial resolution of 2.5 arc minutes. Third, we apply the distribution of night-time lights measured from satellite during night (NOAA, National geophysical Data Center, 2006, `http://www.ngdc.noaa.gov/dmsp/download_radcal.html`, (Ziskin *et al.* , 2010)) with a spatial resolution of 0.5 arc minutes. The respective maps of the different proxies, together with the driving routes of the different days are shown in figure 5.6 . For all selected proxies the encircled areas include a substantial fraction of the total Delhi emissions (between 30 and 50%), but a slightly larger fraction lies still outside of these circles (see Table 5.1).

day	fraction based on EDGAR emission density	fraction based on population density	fraction based on night-time lights
13 April 2010	43%	45%	42%
14 April 2010	49%	42%	43%
15 April 2010	42%	35%	35%
13 January 2010	36%	29%	33%

Table 5.1: Fraction of the EDGAR NO_x emissions, population, and light within the surrounded areas for the different days.

Surprisingly, the calculated fractions using the different proxies are found to be quite similar, that gives us confidence of our up-scaling procedure to determine the total emissions of the selected area. Figure 5.7 summarises the total NO_x emissions using the different proxies; it also includes the corresponding NO_x emissions from the EDGAR data base and a study by (Gurjar *et al.* , 2004).

Error of	due to	13 April 2010	14 April 2010	15 April 2010	15 January 2011
SCD	Spectral analysis	15%	15%	15%	15%
VCD	Geometric Approximation	20%	20%	20%	20%
NO_2 flux	Wind fields	15%	15%	15%	15%
	Measurement gaps	21%	8%	9%	1%
NO_x flux	c_L	10%	10%	10%	10%
Lifetime	c_τ	10%	10%	10%	10%
New Delhi emissions	Upscaling	10%	10%	10%	10%
Total	Square root of quadratic sum	40%	35%	35%	34%

Table 5.2: Uncertainties of the different steps of the emission estimate.

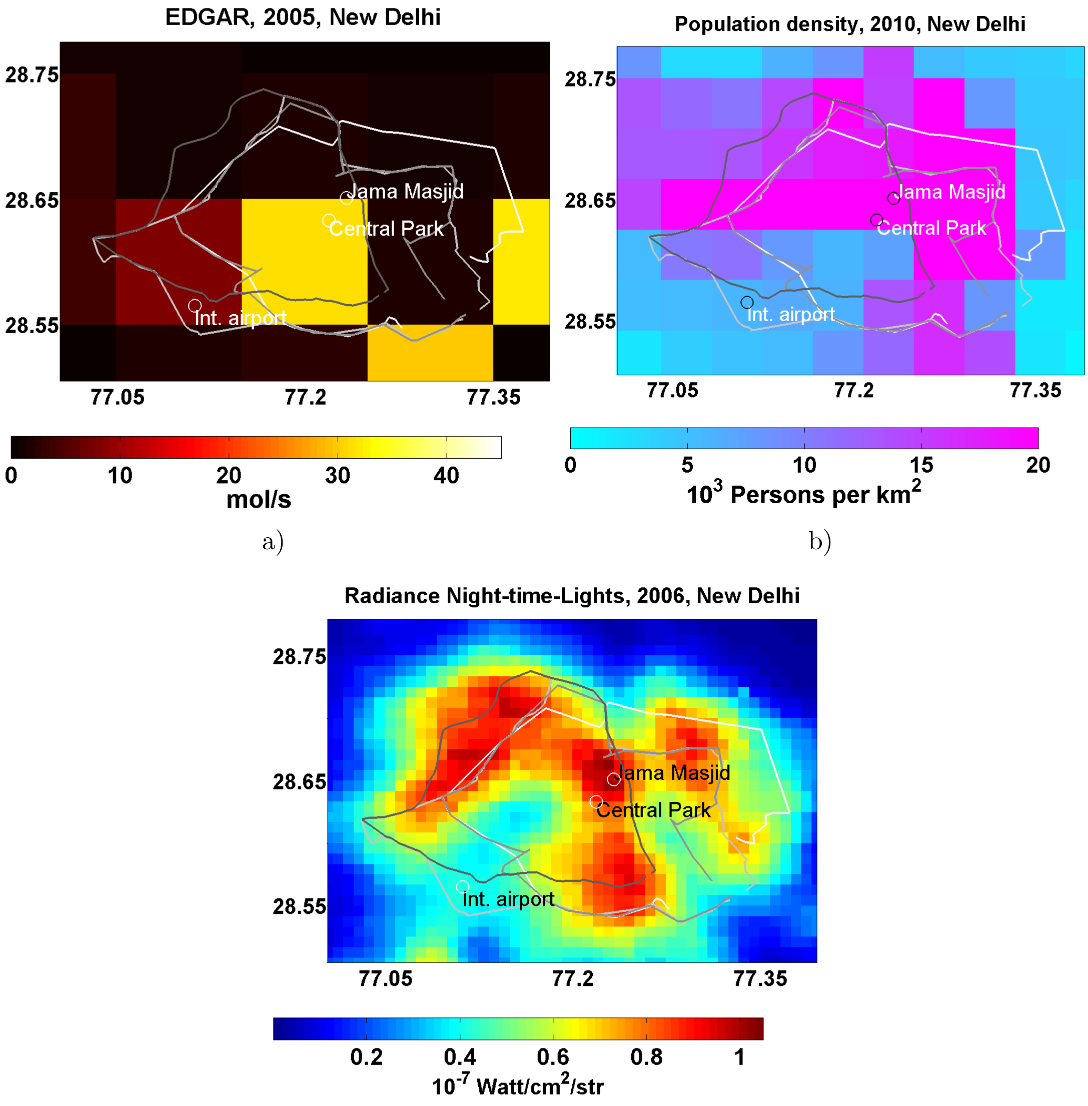

a)

b)

c)

Figure 5.6: Spatial distribution of the NO_x emissions from the EDGAR data base (a), of the population density (b), and the night-time lights (c) for the selected Delhi area. Also shown are the driving routes for the different days

Compared to these emission estimates, our results are found to be mostly lower, indicating that the existing emission inventories might overestimate the true emissions. However, it should be taken into account that our results represent only the conditions during a few measurements, while the other inventories are annual averages. Unfortunately, it seems that currently no information on the seasonality (and on the diurnal variation) of the NO_x emissions is available, which could be used to upscale our emission estimates to the annual average. Unfortunately, existing time series of the NO_x mixing rations at the surface (Guttikunda, 2009) can not be directly used for this purpose, because they not only represent the NO_x emissions but also variations of the mixing layer height and NO_x lifetime, which also vary with season. In figure 5.7 also the NO_x emission estimates from OMI satellite obser-

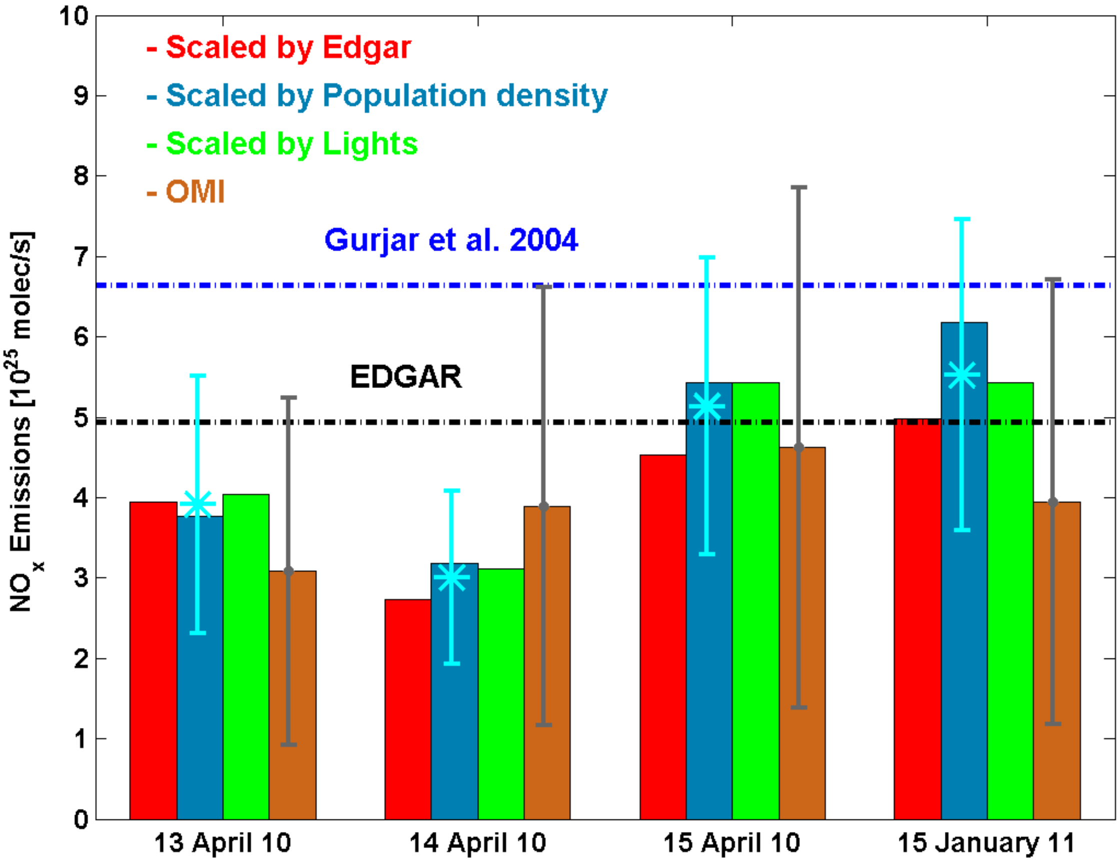

Figure 5.7: Comparison of the up-scaled NO_x emissions from the mobile MAX-DOAS measurements (using different proxies) and existing emission estimates. The cyan points show the mean emission estimate for each day with the respective total error, as explained in Table 5.2. The brown columns show emission estimates derived from OMI observation (see section 5.1.3).

vations are included, which are mostly slightly lower than those from the car MAX-DOAS measurements.
Table 5.2 lists the different errors of the derived NO_x emissions. If we assume these errors to be independent, we obtain total uncertainties of about 40 %.

5.1.3 Comparison with OMI satellite data

We compare the results from the mobile MAX-DOAS measurements to OMI satellite observations in two ways. First, we determine emission estimates for Delhi from the satellite observations and compare them to the respective emissions derived from the mobile MAX-DOAS observations. Second we compare the NO_2 VCDs derived from mobile MAX-DOAS directly to the satellite observations. We use the DOMINO product, v1.02, `http://www.temis.nl/airpollution/no2.html`, see (Boersma *et al.* , 2007).

Satellite observations can be directly used to estimate emission (e.g. (Leue *et al.* , 2001); (Martin *et al.* , 2003); (Beirle *et al.* , 2011)). By integration of the tropospheric NO_2 VCD from satellite observations across a selected area, the total number of NO_2 molecules in the volume above that area can be determined. With the knowledge of the mean NO_x lifetime the corresponding emissions can then be simply derived by the following formula:

$$F_{NO_x} = c_L \frac{\int VCD_{NO_2} dA}{\tau} \tag{5.1}$$

The area over which the satellite measurements are integrated has to be chosen carefully. First, it should include the emission source of interest. Second, it should not be significantly influenced by other strong sources from outside or inside the selected area. Third, it should be large enough to contain most of the emitted NO_x, which is advected from the source. In practice this means that the distance between the emission source and the borders of the selected area should be larger than the product of the wind speed and the NO_x lifetime. Like for the determination of the NO_x emissions from the mobile MAX-DOAS observations we assume the NO_x lifetime to about 5 hours. According to wind speeds on the selected days between 3 and 9 $\frac{m}{s}$ this results in a minimum distance between 50 km and 160 km.

It is interesting to note that in contrast to the mobile MAX-DOAS measurements the uncertainty of the derived NO_x emissions using equation 6.1 is directly proportional to the uncertainty of the assumed NO_x lifetime. While an uncertainty of ± 2 hours leads to an uncertainty of about $\pm 10\%$ for the NO_x emission estimate from mobile MAX-DOAS measurements, it leads to $\pm 40\%$ for the NO_x emission estimate from satellite observations.

In figure 5.8 the spatial distributions of the tropospheric NO_2 VCDs observed by OMI around Delhi are shown for the four days on which the NO_x emissions were determined from mobile MAX-DOAS measurements. Also shown is the area (red rectangle) over which the satellite NO_2 VCDs are integrated. Since the wind was blowing from mainly westerly directions (see figure 5.4), we chose the area to include large parts of the downwind plume in easterly and southerly directions. On all days the pollution outflow from Delhi is clearly visible in the satellite images.

The next step is to estimate the 'background' NO_2 VCDs at the side of the inflow into the city. This 'background' NO_2 VCD is then subtracted from the tropospheric NO_2 VCDs before equation 5.1 is applied. We determined the 'background' NO_2 VCD from the closest OMI measurements at the inflow side, which were not yet affected by the emissions from the city.
The NO_x emissions from Delhi derived with this method are also shown in figure 5.7 They are typically slightly lower than those derived from the mobile MAX-DOAS measurements for the same days. However, the uncertainties of this method are rather large (about 70%). Several sources contribute to the total uncertainty: the exact choice of the area over which

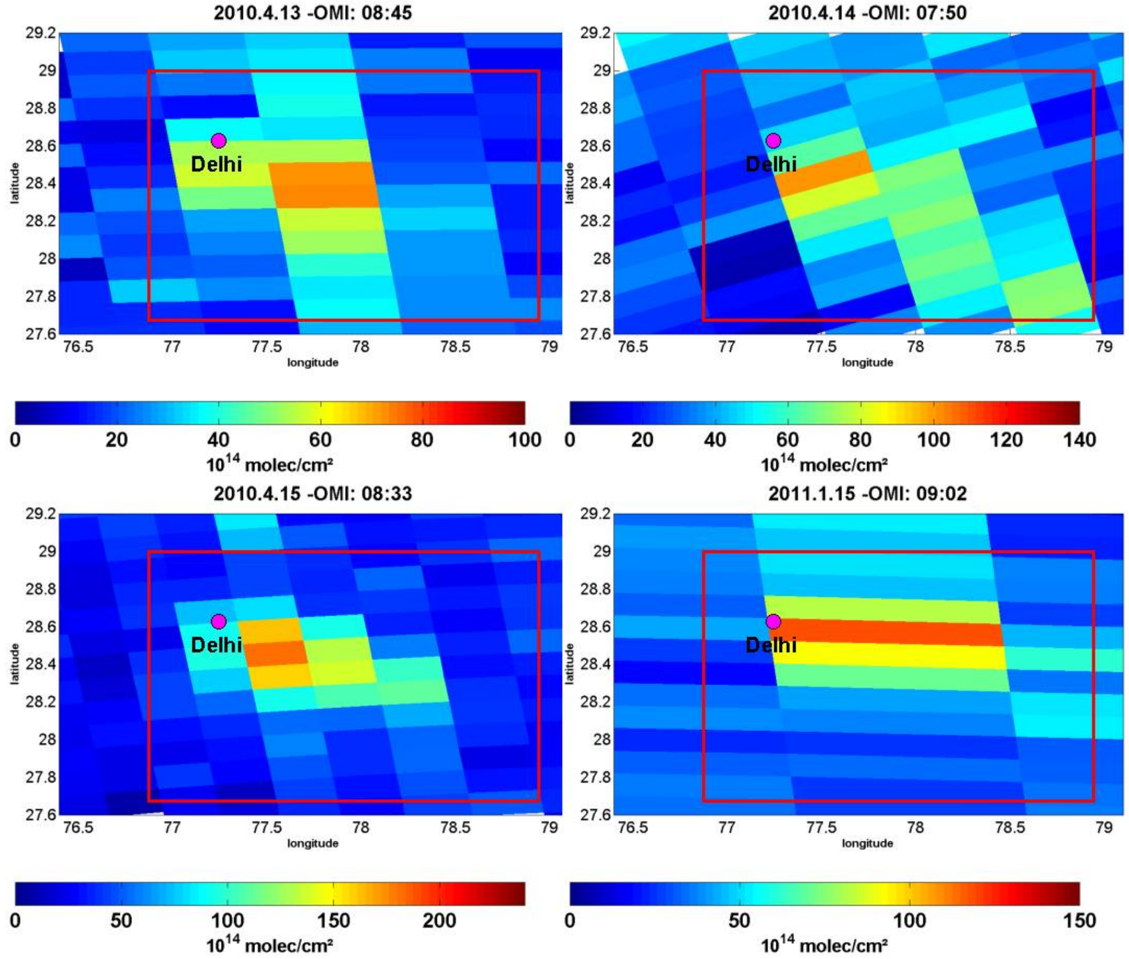

Figure 5.8: Tropospheric NO_2 VCD measured by OMI around Delhi for the four days, for which the NO_x emissions were obtained from the mobile MAX-DOAS measurements. The outflow from the city is clearly visible and follows the wind patterns (see figure 5.4). For the determination of the NO_x emissions the satellite observations inside the red rectangle were considered. Note the different color scales.

the satellite measurements are integrated leads to uncertainties of about 40%. We determined this uncertainty by sensitivity studies varying the selected area. In a similar way we determined the uncertainties related to the determination of the 'background' NO_2 VCD to about 15%. The uncertainties of the satellite VCDs are about 35%. Finally, the errors caused by the uncertainties of the assumed NO_x lifetime are about 40%.

5.1.4 Validation of OMI measurements using mobile MAX-DOAS measurements

Validation of tropospheric trace gas products from satellite observations is a challenging task for several reasons. First, since satellites measure the vertically integrated tropospheric column density, observations of in-situ surface concentrations can not be directly used for validation purposes. Even if vertical profiles are available from aircraft measurements (Heland *et al.* , 2002) or balloon soundings (Sluis *et al.* , 2010), they are often not representative for the whole spatial extent of the satellite ground pixel, which is typically of the order of several hundreds of km^2 or more. Similar arguments hold for observations of the integrated tropospheric column measurements e.g. from MAX-DOAS observations at fixed locations (Brinksma *et al.* , 2008).

Here it is important to note that close to strong emission sources like megacities, where the validation of tropospheric satellite products is of highest importance, the largest variability and strongest gradients are typically found (Chen *et al.* , 2009).

Information about the spatial variability across a satellite ground pixel can be obtained from mobile measurements like mobile MAX-DOAS observations (e.g. Volkamer *et al.* (2006); Wagner *et al.* (2010)), thus we also use the tropospheric NO_2 VCDs obtained during our measurement campaigns in Delhi for the validation of the simultaneous observations of the tropospheric NO_2 VCDs from the OMI instrument. We selected OMI satellite observations (Levelt & Noordhoek, 2002), because the ground pixel sizes are much smaller ($13 \times 26 km^2$ in nadir geometry) compared to observations from SCIAMACHY and GOME-2.
One important aspect of tropospheric satellite observations is the use of a-priori information on the (relative) trace gas profile. For the DOMINO tropospheric NO_2 product from OMI observations profile data from model simulations (TM4) are used for that purpose. The specific choice of the NO_2 profile has a strong effect on the retrieved NO_2 VCD, since the sensitivity of the satellite observations strongly depends on altitude (Boersma *et al.* , 2011). One particular critical aspect of the use of model data is that the spatial resolution of the model (2° latitude and 3° longitude) is much coarser than the spatial scales of tropospheric NO_2 field close to strong emission sources (Heckel *et al.* , 2011). Thus for model grid cells including strong emission sources the average NO_2 profile must necessarily be a compromise between those over the source regions and those of the outflow and inflow regions.

Figure 5.9 shows the comparison of the tropospheric NO_2 VCDs on 14 April 2010 from mobile MAX-DOAS and OMI observations. On that day, OMI observes Delhi at relatively slant viewing angles, and the ground pixel sizes are rather large. Thus, the mobile MAX-DOAS observations cover only relatively small fractions of the individual ground pixels. Nevertheless, in both data sets the same general distribution of NO_2 is observed: highest values of NO_2 are found in the south east, which is consistent with the wind direction on that day (north-westerly wind, see figure 5.4). The mobile MAX-DOAS observations reveal much finer spatial patterns with stronger spatial gradients, which are not resolved from the OMI data.

The comparison of the tropospheric NO_2 VCDs for 15 April 2010 is shown in figure 5.10. On that day the OMI observations were made almost vertically (nadir geometry), and the satellite pixels are much smaller compared to 14 April 2010. Both satellite ground pixels over

Delhi are well covered by the mobile MAX-DOAS observations and similar spatial patterns were observed in both data sets. Again, the mobile MAX-DOAS observations resolve details on a much finer scale.

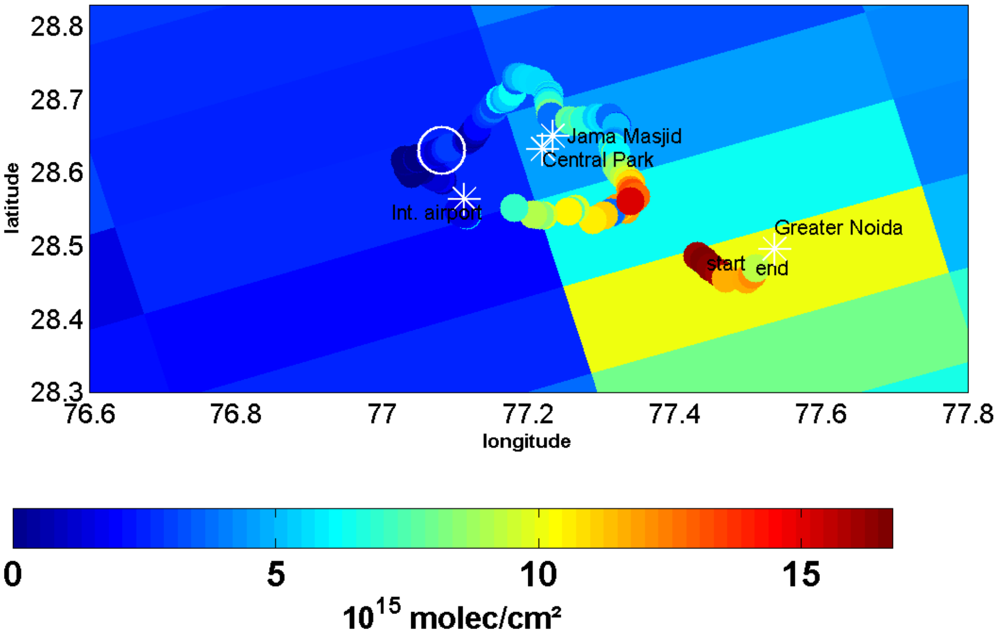

Figure 5.9: Comparison of the tropospheric NO_2 VCDs on 14 April 2010 measured from OMI and mobile MAX-DOAS. MAX-DOAS observations were carried out between 5:20 and 10:57 UT; OMI overpass was at 7:50 UT. The large circle indicates MAX-DOAS observations during the OMI overpass.

Figure 5.11 shows another validation example from 16 January 2011, when MAX-DOAS observations were carried out along a route from Delhi to Agra (about 225 km). Like in the previous examples the general distribution of the tropospheric NO_2 VCD is found to be similar in both data sets with the highest values at or close to Delhi. An interesting finding is that OMI underestimates the high values over Delhi, but overestimates the low values over rural regions along the route from Delhi to Agra.

Figure 5.12 shows a correlation analysis of all mobile MAX-DOAS observations (during April 2010 and January 2011) and the coincident OMI satellite data (blue points). Here, all MAX-DOAS observations within an OMI ground pixels were averaged. The error bars indicate the OMI error and the standard deviation of the MAX-DOAS observations, respectively. Using these errors, we performed an orthogonal regression (Cantrell, 2008).
A reasonable correlation (coefficient of determination $r^2 = 0.48$) is found, but the slope (0.38) deviates strongly from unity. In contrast, the ratio of the average of all OMI VCDs $(5.7 \pm 2.7 \cdot 10^{15}\ \frac{molec}{cm^2})$ to the average of the MAX-DOAS observations $(8.5 \pm 4.4 \cdot 10^{15}\ \frac{molec}{cm^2})$ is 0.77, and the average of the individual ratios is even 1.07.

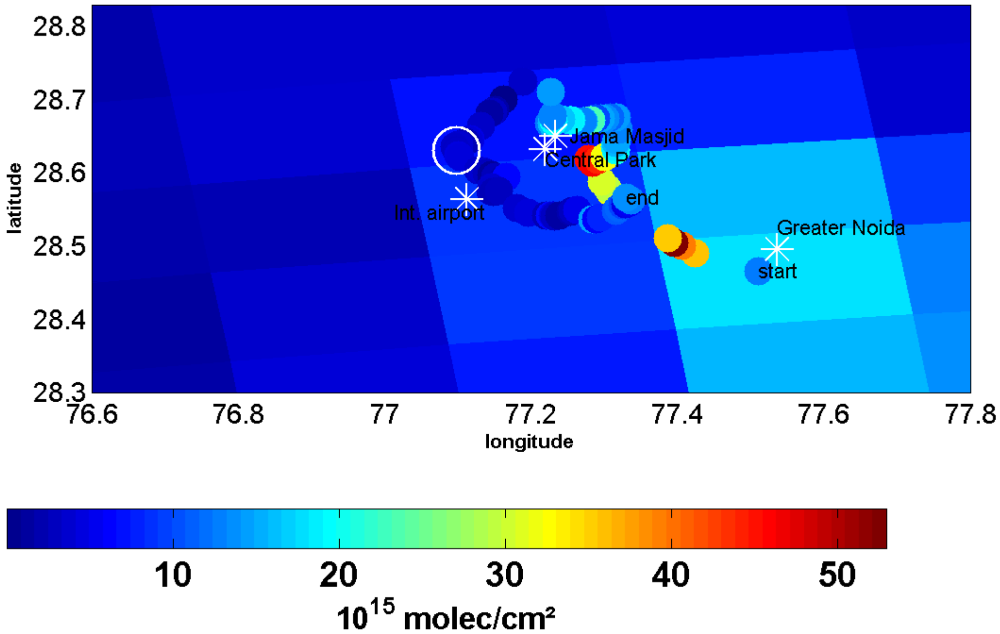

Figure 5.10: Comparison of the tropospheric NO_2 VCDs on 15 April 2010 measured from OMI and mobile MAX-DOAS. MAX-DOAS observations were carried out between 5:05 and 10:06 UT; OMI overpass was at 8:33 UT. The large circle indicates MAX-DOAS observations during the OMI overpass.

In order to investigate the effect of limited spatial sampling in the presence of strong gradients in more detail, a second comparison was made including only observations, for which the mobile MAX-DOAS observations cover large fractions of the OMI pixels (at least 50% in east-west direction (defined by the most eastern and most western MAX-DOAS observation within the OMI pixel) like e.g. shown in figure 5.10, which shows a good coverage of OMI pixels). Only five measurements fulfilled this criterion. If only these observations are considered, a better correlation (coefficient of determination $r^2 = 0.79$) is obtained, but the results of the orthogonal regression are almost unchanged.

A general finding of this comparison is that over polluted sites the OMI tropospheric NO_2 VCDs are systematically smaller than those from the mobile MAX-DOAS measurements, while for areas with low pollution levels the opposite behaviour is found.

The underestimation of high tropospheric NO_2 VCDs by OMI might be partly caused by the shielding of the surface-near NO_2 by aerosols. Here it should, however, be noted that the (effective) cloud fractions for the OMI observations used in our study are found to be very low: 2.3% on average for all observations; <1.2% for the sub-set of OMI pixels, which are well covered by the mobile MAX-DOAS observations. Thus, effects of cloud shielding is considered to be negligible here. Part of the underestimation might also be related to differences between the true (relative) NO_2 height profiles and those assumed in the satellite retrieval. If e.g. the assumed profiles contain a smaller fraction close to the surface compared to the true profiles, the respective tropospheric AMFs overestimate the true tropospheric AMFs,

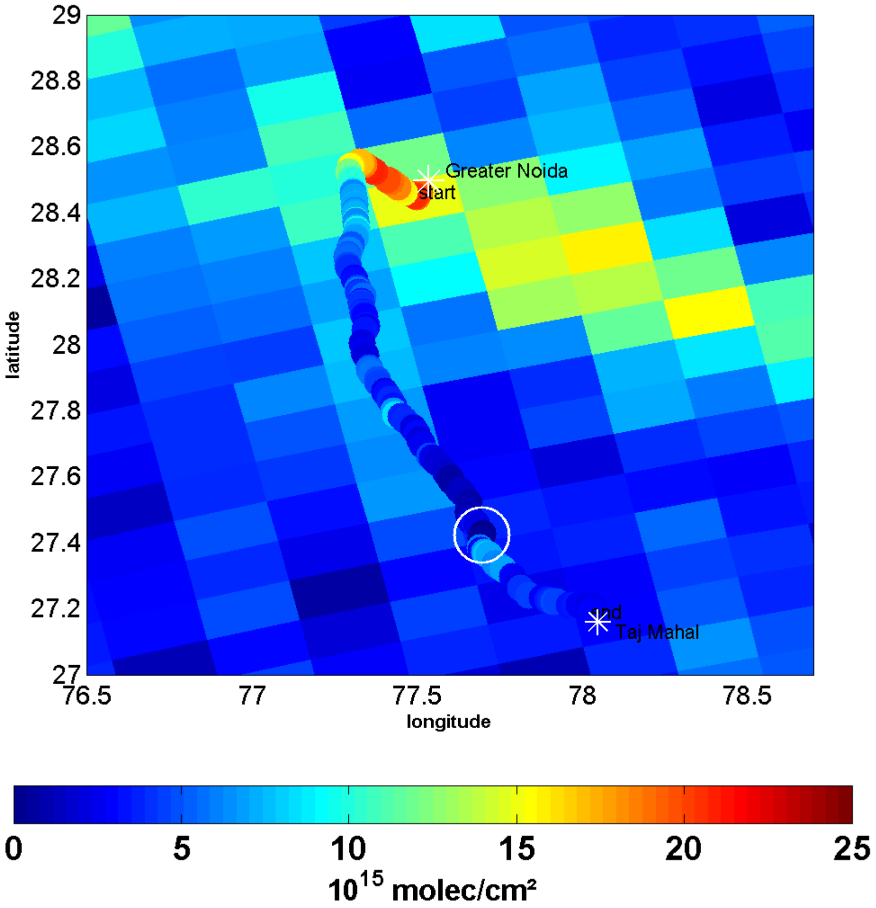

Figure 5.11: Comparison of the tropospheric NO_2 VCDs on 16 January 2011 measured from OMI and mobile MAX-DOAS from New Delhi to Agra (Taj Mahal). MAX-DOAS observations were carried out between 4:33 and 9:05 UT; OMI overpass was at 8:06 UT. The large circle indicates MAX-DOAS observations during the OMI overpass.

and consequently, the retrieved tropospheric NO_2 VCDs underestimate the true tropospheric NO_2 VCDs (Boersma *et al.* , 2009). Of course also the uncertainties of the car MAX-DOAS measurements might contribute to the deviations, but especially for NO_2 profiles with low layer heights, the uncertainties of the mobile MAX-DOAS measurements are smaller than for the satellite observations.

Different conclusions can be drawn for the less polluted areas. Here the OMI tropospheric NO_2 VCDs probably overestimate the true NO_2 VCDs, because the NO_2 profile assumed for the retrieval probably overestimates the NO_2 concentrations close to the surface. But for less polluted regions, also the uncertainties of the mobile MAX-DOAS observations probably substantially contribute to the discrepancies between both data sets. Because of the larger fraction of the NO_2 at higher altitudes the uncertainties of the mobile MAX-DOAS observations become larger than for measurements close to strong emission sources (see figure 5.3). Moreover, for the measurements between Delhi and Agra on 15th January 2011 the car

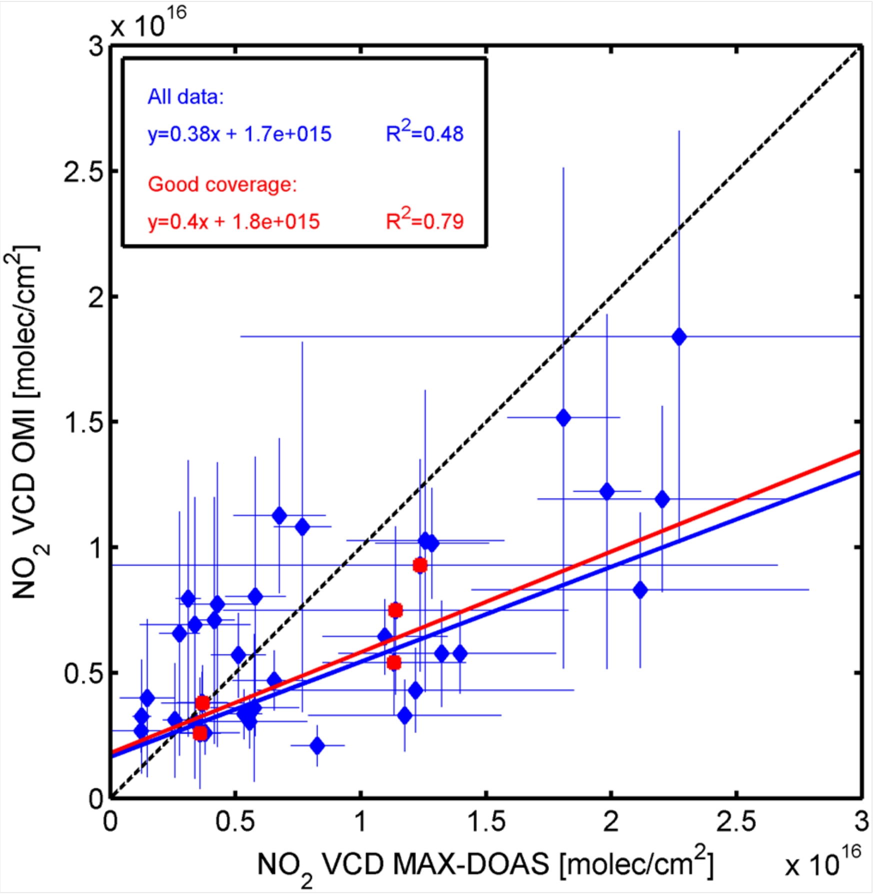

Figure 5.12: Correlation analysis of OMI and car MAX-DOAS observations of the tropospheric NO_2 VCD during April 2010 and January 2011. Blue dots represent all coincident measurements; red dots represent measurements where the OMI ground pixels were mostly covered (at least 50% in east-west dimension) by the mobile MAX-DOAS measurements (like in figure 5.9).

MAX-DOAS observations might systematically underestimate the true tropospheric NO_2 VCD, because the relative azimuth angle is close to zero for large parts of the driving route (figure 5.3).

It should be noted that existing validation studies show quite controversial results: studies based on in-situ observations (at the surface or from aircraft) and LIDAR observations indicate that the troposheric NO_2 VCD (DOMINO, v1.02) derived from OMI observations is biased high ((Boersma *et al.* , 2011), (Hains *et al.* , 2010) and reference therein). In contrast, studies based on MAX-DOAS observations ((Brinksma *et al.* , 2008); (Celarier *et al.* , 2008)) indicate that the troposheric NO_2 VCD derived from OMI is biased low. The latter results are in agreement with the findings of our validation study.

5.2 Formaldehyde from mobile MAX-DOAS

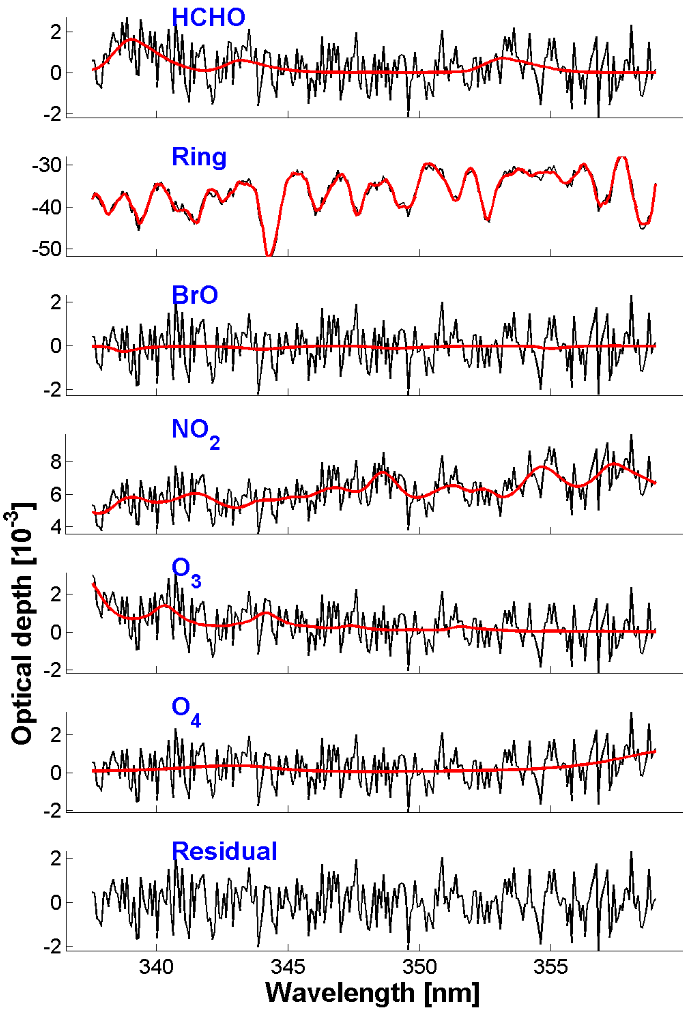

Figure 5.13: A typical example of the HCHO analysis from April 15, 2010, at 08:25 (UTC time). Shown are the fitted trace gas cross sections (red) scaled by the respective absorptions of the measured spectrum (black).

Formaldehyde is one of the important pollutants in the troposphere and plays an important role in air quality. Formaldehyde can be directly emitted or formed in the atmosphere as secondary product by photochemical oxidation of reactive volatile organic compounds in polluted areas.
From the New Delhi mobile MAX-DOAS observations, also formaldehyde can be evaluated.

The evaluation of Formaldehyde with closest reference to the spectrum was performed for the fit-window: 337.5-359 nm. Three absorption peaks of HCHO exist in this fit-range. Several trace gas absorption cross sections are applied: HCHO at 298 K (Meller & Moortgat, 2000), NO_2 at 294 K (Vandaele *et al.* , 1998), O_3 at 241 K (Bogumil *et al.* , 2003), O_4 (Greenblatt *et al.* , 1990), BrO at 228 K (Wilmouth *et al.* , 1999), as well as a Fraunhofer reference spectrum, which were determined from averaging of every last and next zenith measurements

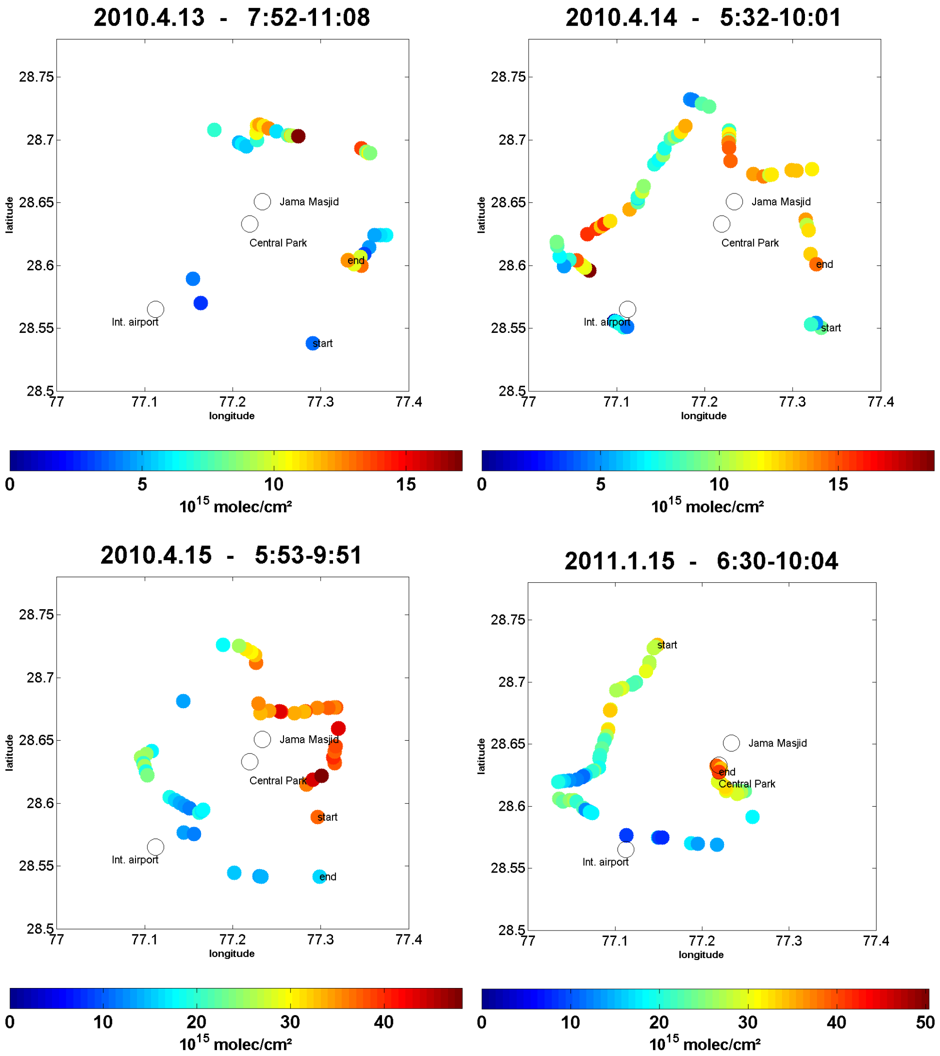

Figure 5.14: Tropospheric formaldehyde VCDs for different days from mobile MAX-DOAS measurements.

and Ring spectrum calculated from the averaged Fraunhofer reference. A polynomial of fifth order was included in the fitting procedure. The measured spectra and the O_4 cross section were allowed to be shifted against the reference spectrum. The wavelength calibration was performed based on a high resolution solar spectrum (Kurucz *et al.* , 1984).

A typical formaldehyde fit result is shown in figure 5.13 for 15th of April 2010 at 08:25 (UTC time) from a spectrum with an elevation angle of 22°.

We consider for the formaldehyde analysis the spectra with 22° elevation angles for April 2010 and 30° for January 2011. In figure 5.14, the tropospheric formaldehyde VCDs are shown from different days, on which we encircled New Delhi with the mobile MAX-DOAS instrument. Measurements with RMS of the residuals smaller than 1.5×10^{-3} are considered in figure 5.14.

The tropospheric VCD are obtained from the SCD (see section 3.2.4.3) using a geometric airmass factor (AMF). The observations from April 2010 with 22° elevation angles are used to determine the tropospheric vertical column densities shown in figure 5.14, while observations at 30° elevation angles are used for January 15, 2011.

Generally, the high values of HCHO could not be well found at the lee sides of the city, as expected. In figure 5.14, there are more gaps in the results in comparison to NO_2 (see figure 5.4). This is caused by a smaller RMS threshold for formaldehyde, namely $RMS_{HCHO} = 0.6 RMS_{NO_2}$.

The comparison of the figures 5.14 and 5.4, shows that for April 14, 2010, we find high values for HCHO at the inflow, while we found lower values at the outflow. This situation is similar for 13 of April. The plume positions of nitrogen dioxide and formaldehyde are rather similar for April 15, 2010 and January 15, 2011.

5.3 Summary

The Mobile MAX-DOAS observations were performed in the greater Delhi area during April 2010 and January 2011. The aims of the measurements were first the determination of the total NO_x emissions of the greater Delhi area and second the validation of satellite observations.
The total NO_x emissions were derived from observations along closed circles around the city. Since the MAX-DOAS observations encircled only part of the entire Delhi area, we had to up-scale our results. For that purpose we used three different proxies: the spatial distribution of a) the NO_x emissions from the EDGAR emission inventory, b) the population density, and c) the light intensity observed from satellite during night. Although the first two proxies have rather coarse spatial resolution, the up-scaled results using the three proxies agree well (within 20%). Two additional corrections were applied to account for the partitioning of NO and NO_2 and for the limited lifetime of NO_x (leading to destruction of part of the emitted NO_x between the locations of the emission source and the observation). The overall uncertainty of our emission estimate is about 40%, taking into account measurement uncertainties and uncertainties of the various assumptions. From four measured circles around Delhi (three during April 2010 and one in January 2011) an average NO_x emission of $4.4 \times 10^{25} \ \frac{molecules}{s}$ was derived. The results from the four days were found to agree within 40%.

Our NO_x emission estimate is slightly lower than NO_x emissions from the EDGAR data base (v4.1) ($4.94 \times 10^{25} \ \frac{molecules}{s}$) and substantially lower than from a recent study by (Gurjar

et al. , 2004) (6.42×10^{25} $\frac{molecules}{s}$). However, no exact agreement should be expected, because our measurements represent short periods during two months of two contrast seasons (winter and summer), whereas the values from emission inventories are annual averages.
We estimated also NO_x emissions from Delhi using OMI satellite observations on the same days as for the mobile MAX-DOAS measurements. These emissions are slightly smaller than those from the mobile MAX-DOAS measurements.

The MAX-DOAS observations were also used for the validation of tropospheric OMI NO_2 VCDs. We chose OMI observations because of its relatively small pixel sizes. In general, similar spatial patterns are found in both data sets, but with a much finer spatial resolution in the mobile MAX-DOAS data. The comparison of absolute values show overall a fair agreement. However, over highly polluted regions the OMI observations are systematically smaller than the mobile MAX-DOAS measurements. Most probably, this difference is caused by the a-priori vertical NO_2 profile assumed in the OMI retrieval. In less polluted regions, OMI tropospheric NO_2 VCDs are larger than those from mobile MAX-DOAS observations, but under such conditions large part of the differences might be also caused by the errors of the mobile MAX-DOAS observations.

Formaldehyde could be also analyzed from the New Delhi mobile MAX-DOAS observations. Tropospheric vertical column densities of HCHO were determined from the measured SCDs using a geometric airmass factor. Surprisingly, high values of formaldehyde were not found at the lee sides as for NO_2. Because of many gaps and ambiguous results, the formaldehyde emissions did not estimated.

6 Paris Campaigns

Megacities: Emissions, urban, regional and Global Atmospheric POLlution and climate effects, and Integrated tools for assessment and mitigation "(MEGAPOLI)" was a three year cooperative project (`http://megapoli.dmi.dk/`).
The main MEGAPOLI objectives were: first, to assess the impact of megacities and large air pollution hot-spots on local, regional and global air quality. Second, to quantify feedbacks among megacity air quality, local and regional climate, and global climate change. Third, to develop improved integrated tools for prediction of air pollution in megacities (Mahura & Baklanov (2011)).
The first measurement campaign of the MEGAPOLI project was a campaign at Paris. Paris is a densely populated European urban pollution hot spot surrounded by rural areas.

Paris is the largest metropolitan area in Europe with a population of around 11 million people. The city and surroundings are located in a flat terrain. The city is located on the river Seine, at the heart of the Île-de-France region.
The typical Western European oceanic climate (the North Atlantic current) affects the climate of Paris.
Within the MEGAPOLI project we performed MAX-DOAS measurements using an instrument mounted on a car. From such observations, the total Paris emissions can be estimated. Validation of satellite measurements was also one of our tasks for the Paris campaigns.

We participated in 2 measurement campaigns in Paris (summer 2009 from June 30 to July 31 and winter 2010 from January 13 to February 15). We used mobile Multi-Axis-Differential Optical Absorption Spectroscopy (Max-DOAS) (see (Hönninger *et al.* , 2004), (Wagner *et al.* , 2010), (Ibrahim *et al.* , 2010) and (Shaiganfar *et al.* , 2011)) during both campaigns to quantify the NO_x emissions of the Paris megacity. The instrument was mounted on a car roof and measurements were performed on orbits around Paris. In combination with wind data, the total emission from the encircled area was determined.

6.1 Mobile MAX-DOAS Instrument

The mini MAX-DOAS was mounted on the roof of a car (see section 3.2.5 and figure 6.1), the instrument is shown from different sides. In figure 6.2, a typical spectrum from our mini MAX-DOAS instrument is presented. The sequence of elevation angles was chosen to:

Figure 6.1: The mini MAX-DOAS instrument mounted on a car shown from different directions. The instrument is looking at 22° elevation angle.

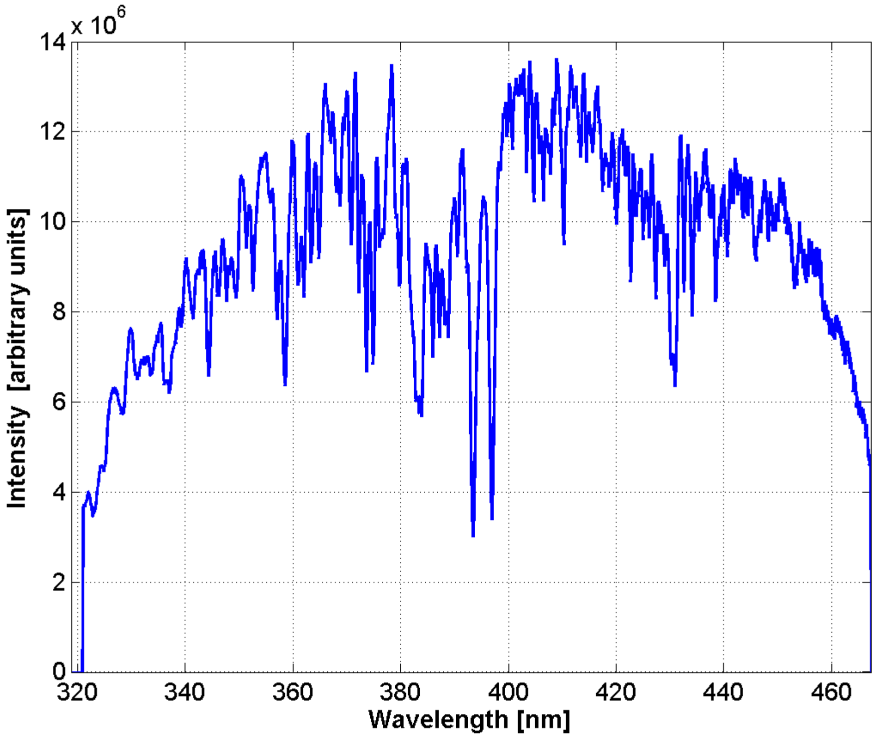

Figure 6.2: A typical spectrum from the mini MAX-DOAS instrument.

1×90°, 5×22°, 1×45°, 5×22° and the duration of an individual measurement was about 60s.

6.2 Overview of the campaigns

The summer campaign took place from June 30, 2009 until July 31, 2009. The winter campaign took place from January 14, 2010 to February 15, 2010. We drove with the instrument in three different ways around Paris.
1. Small circles: périphérique.
2. Middle circles: A86 (highway).
3. Outer circles: a combination of A104, N104 (N: country road), A86 and some small routes between them.
In figure 6.3, these three pattern are shown.

In the summer campaign, a GPS logger (GPS-Receiver CR4, connected to the Notebook by a USB cable) was used to track the coordinates of the route along where the observations were made; but during the winter campaign, a handy GPS (HOLUX m247) was applied.

The measured spectra were analyzed using the DOAS method (discussed in chapter 3). A wavelength range 420-460 nm was selected for the analysis. A few trace gas absorption cross

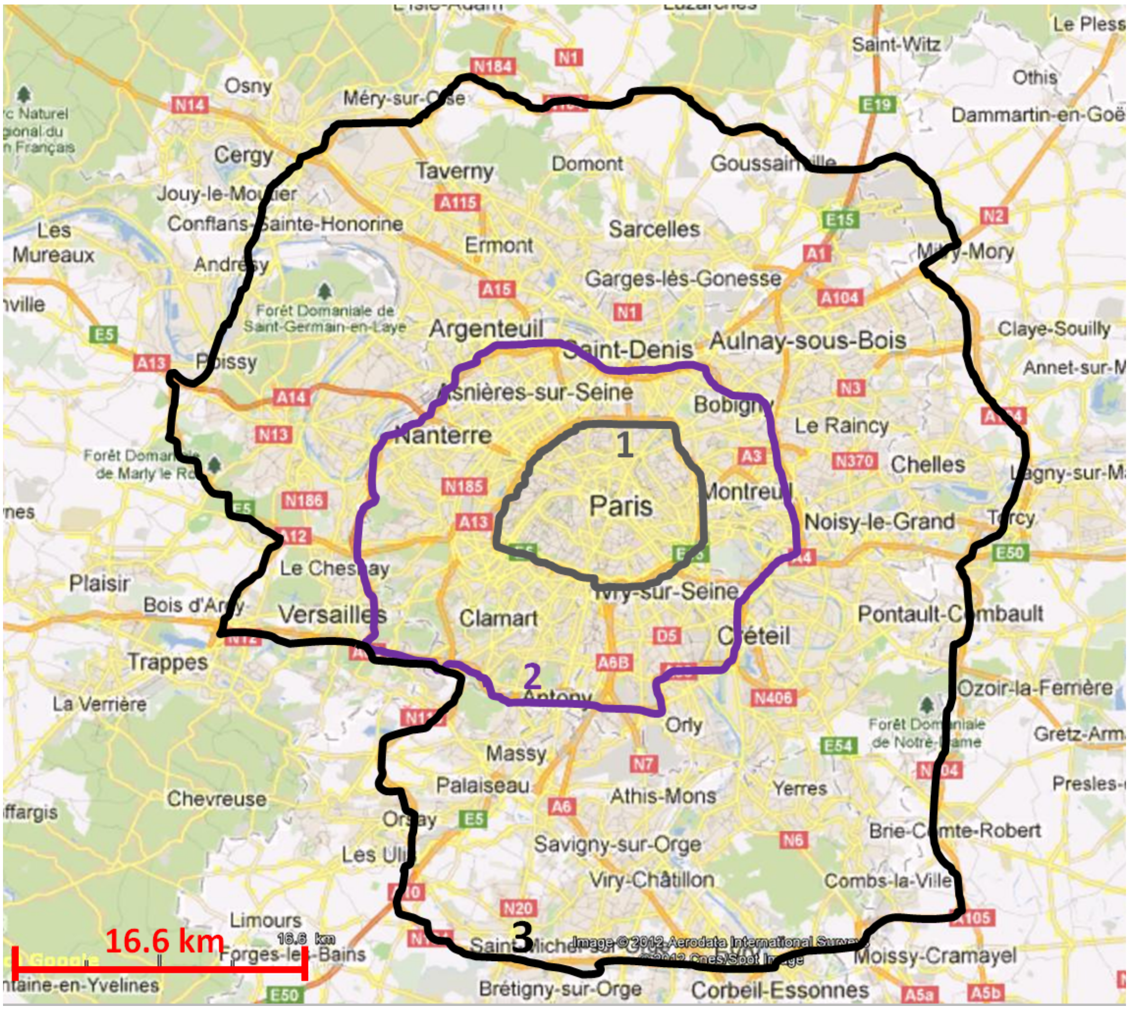

Figure 6.3: The three defined orbits. 1. périphérique (small circle), 2. middle and finally 3. outer orbit.

sections (NO_2 at 298 K (Vandaele *et al.* , 1996), H_2O at 298 K (Rothman *et al.* , 2005), Glyoxal at 296 K (Volkamer *et al.* , 2005), O_3 at 243 K (Bogumil *et al.* , 2003), O_4 at 296 K (Hermans *et al.* , 1999) as well as a Fraunhofer reference spectrum, a Ring spectrum (calculated from the Fraunhofer spectrum) and a polynomial of third order) were included in the spectral fitting process, using the WinDOAS software (Fayt & Van Roozendael, 2001). The wavelength calibration was performed based on a high resolution solar spectrum (Kurucz *et al.* , 1984).

6.3 NO_2 Results

The output of the spectral analysis is the slant column density (SCD), the integrated trace gas concentration along the light path through the atmosphere. From the spectral analysis, also the uncertainty of the retrieved SCD can be determined, for the NO_2 analysis it is less

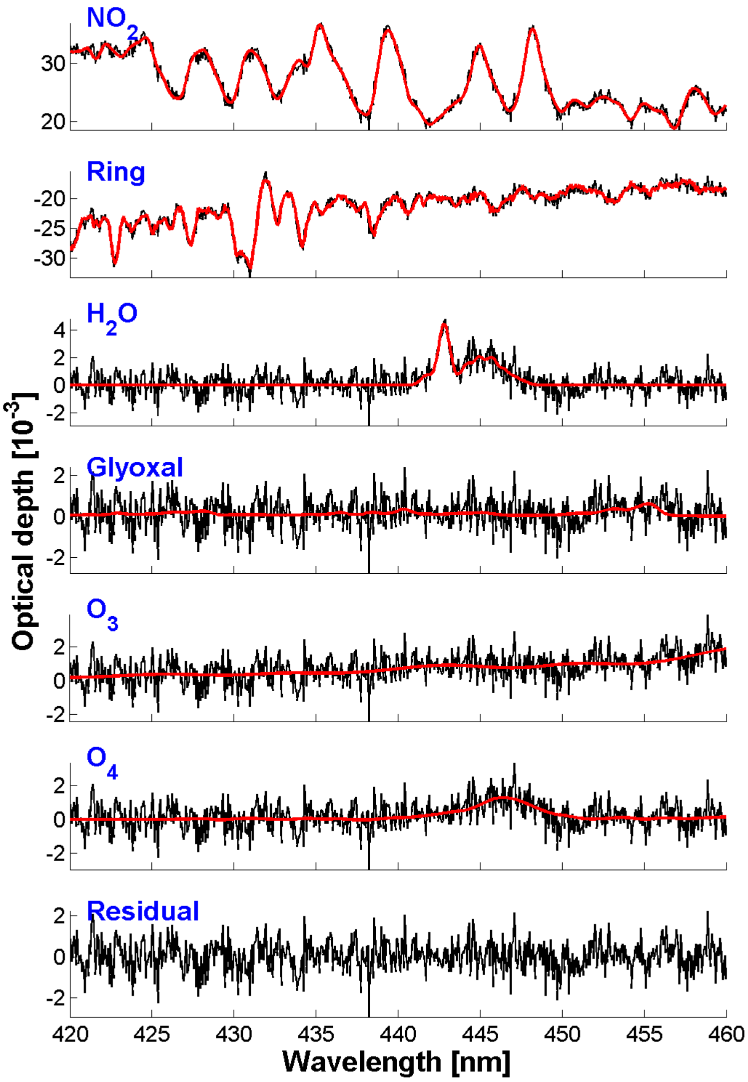

Figure 6.4: Typical result of a DOAS fit. Shown are the fitted trace gas cross sections (red) scaled by the respective absorption of the measured spectrum (black).

than 15%.
The NO_2 DSCDs with RMS of the residuals smaller than 2.5×10^{-3} are used for further processing.

The tropospheric VCD can be obtained from the SCD (see section 3.2.4.3) using the geometric airmass factor (AMF). The observations with 22° elevation angles are used to determine the tropospheric vertical column densities.

The tropospheric vertical column densities (TVCDs) of NO_2 together with wind vectors for some days are shown in figure 6.5. Generally, the high values of NO_2 are found at the lee sides of the city, as expected. We drove counterclockwise around Paris with approximately 3 hours driving time per orbit.

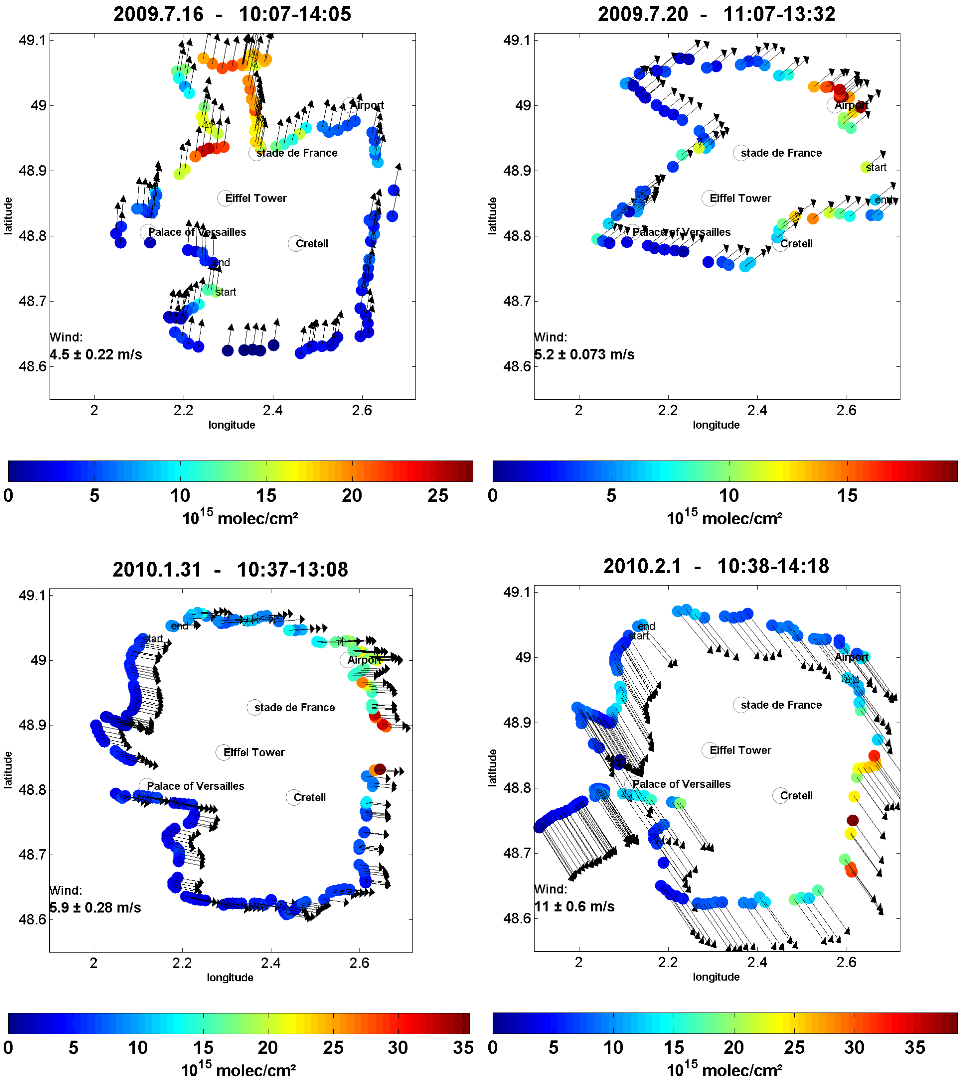

2009.7.16 - 10:07-14:05

2009.7.20 - 11:07-13:32

2010.1.31 - 10:37-13:08

2010.2.1 - 10:38-14:18

Figure 6.5: Tropospheric NO_2 VCDs for different days of the Paris campaigns with associated wind vectors, in summer and winter.

There are some gaps in MAX-DOAS VCD orbits (figure 6.5) caused by different reasons, the main one was occasional disconnection between the instrument and the computer.

The wind speed and direction might vary considerably during the measurements on a given day. In general, the wind speed had a larger fluctuation in winter. The wind data are taken from MATEO data, which is the meteorological input data for CHIMERE chemistry transport model (hourly wind data in 3×3 km^2 horizontal resolution).

The effective wind speed and direction were determined by averaging wind data from different levels between the ground and 1000 m. They were weighted by an exponentially

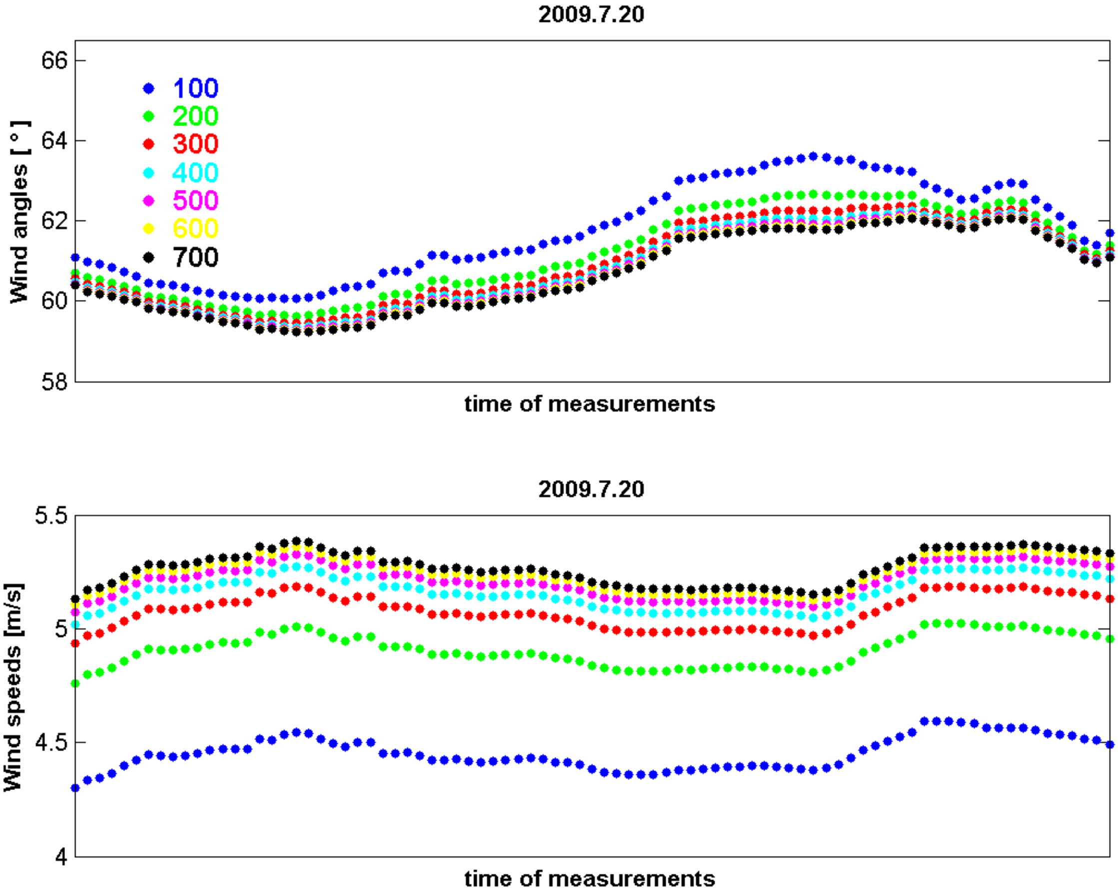

Figure 6.6: Average wind speeds and angles from ground up to 1000m weighted by exponentially decreasing NO_2 profiles with scale heights from 100 to 700m. Time of measurements: 11:07-13:32.

decreasing NO_2 profile with scale heights between 100 and 700 m. In figure 6.6 the resulting wind components for July 20 are shown. From these data, the wind speed and direction for every measurement point are determined.
The wind speed for a scale height of 100 m (blue dotted line in figure 6.6) is lower than the other wind speeds, but the differences are not so large. The NO_2 profile during winter is usually lower compared to summer. In the following we used scale heights of 500 m for summer and 300 m for winter respectively.

6.4 Estimation of NO_x Emissions from Paris

The total NO_x emission from the encircled area can be calculated from equation 4.3. The distance between two measurements is the geometric difference between the locations at the end of two successive measurements; also the angle between the wind vector and the driving direction (distance vector) can be determined for every measured VCD by mobile MAX-

DOAS instrument.

The wind data with $3 \times 3 \ \ km^2$ resolution were temporally and spatially linear interpolated to match the time and location of an observation point.

For determination of the total NO_x emissions, 2 correction factors have to be applied: for lifetime and chemical transformations (see the equations 4.4 and 4.5).

NO_2 lifetimes for the urban plume during daytime of about 5 hours for the summer time and 15 hours for the winter time were used (Martin *et al.* , 2003). The uncertainty of this correction factor is less than ± 0.1 by assuming an ± 2 hours uncertainty of the lifetime.

The chemical transformation factor for urban pollution during daytime was determined from the CHIMERE model. It was determined from the surface concentrations of NO and NO_2 for the locations with the highest pollution level of the individual days.
In figure 6.7, the horizontal distribution of NO_2 and vertical distributions of NO and NO_2 are shown for July 21, 2009.

The total encircled NO_x emissions from different days during summer and winter seasons are shown in figure 6.8, the error bars show the uncertainties caused by missing data (gaps) at some locations.

We compare the encircled emissions from summer and winter. The winter emissions (blue bars in figure 6.8a) are higher compared to the summer emissions (red bars). The average emission (blue line in figure 6.8a) is about three times higher than the average emission in summer (red line in the same figure).
Note that from all measurements (figure 6.8b), we selected the results in figure 6.8a, which fulfilled the following two conditions:
1. The error bars based on missing data are smaller than 1×10^{25} molec/s.
2. The wind speeds (in average) are higher than 4 m/s.
15 days from 23 fulfilled these conditions.

The orbits of different days are rather different. These variations make the comparison of emissions between each other and with other data difficult. Therefore these emissions have to be up-scaled to a defined area for Paris namely covering a latitude range from 48.57°N to 49.11°N and a longitude range from 1.9°E to 2.7°E.

For the up-scaling, we considered different proxies for the spatial distribution of the NO_x emissions across the considered area: EDGAR emission inventory, population density and the distribution of night time radiances (lights) measured from satellite (NOAA). Because of the high spatial resolution 0.5 arc minutes of the night-time radiances, we used this proxy

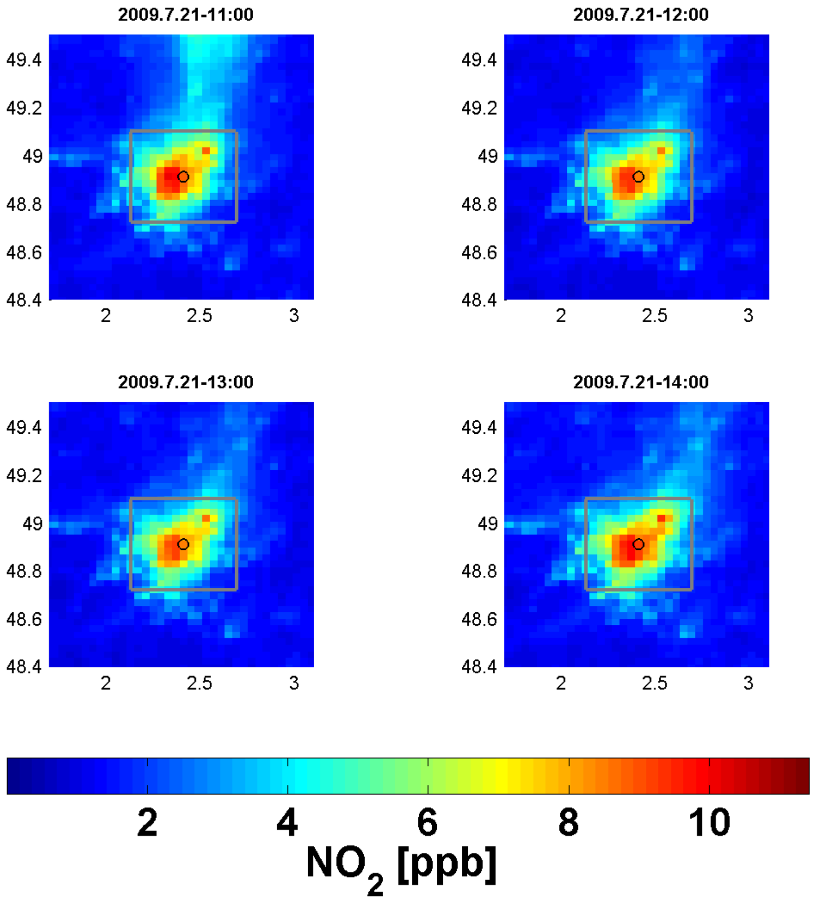

a)

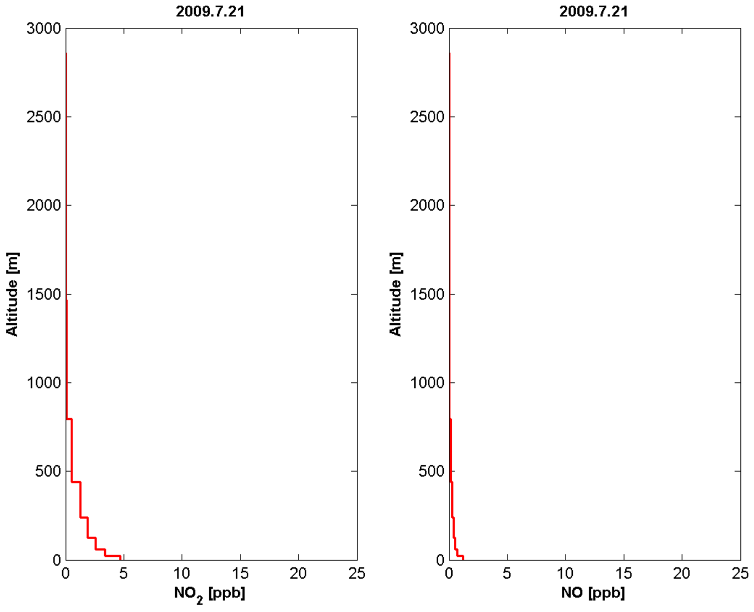

b)

Figure 6.7: a): Horizontal distributions of the NO_2 concentration (lowest layer) for selected times.
b): Concentration profiles of NO_2 and NO for the areas with the highest mixing ratios on July 21, 2009.

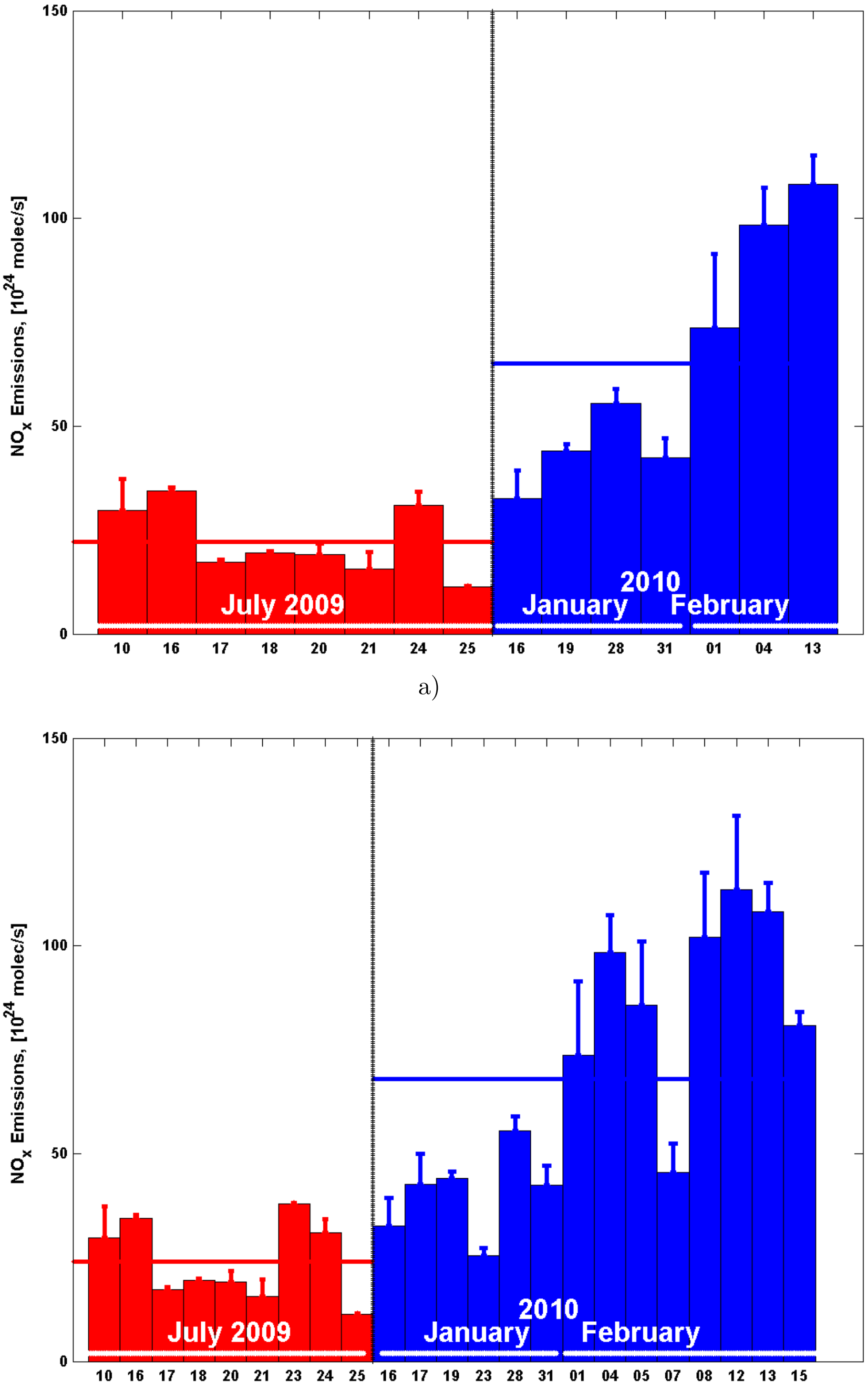

a)

b)

Figure 6.8: NO_x emissions determined for the encircled areas. a) These days fulfilled two conditions: 1. The error bars based on missing data are smaller than 1×10^{25} molec/s. 2. The wind speeds (in average) are higher than 4 m/s.
b) All days without any conditions.

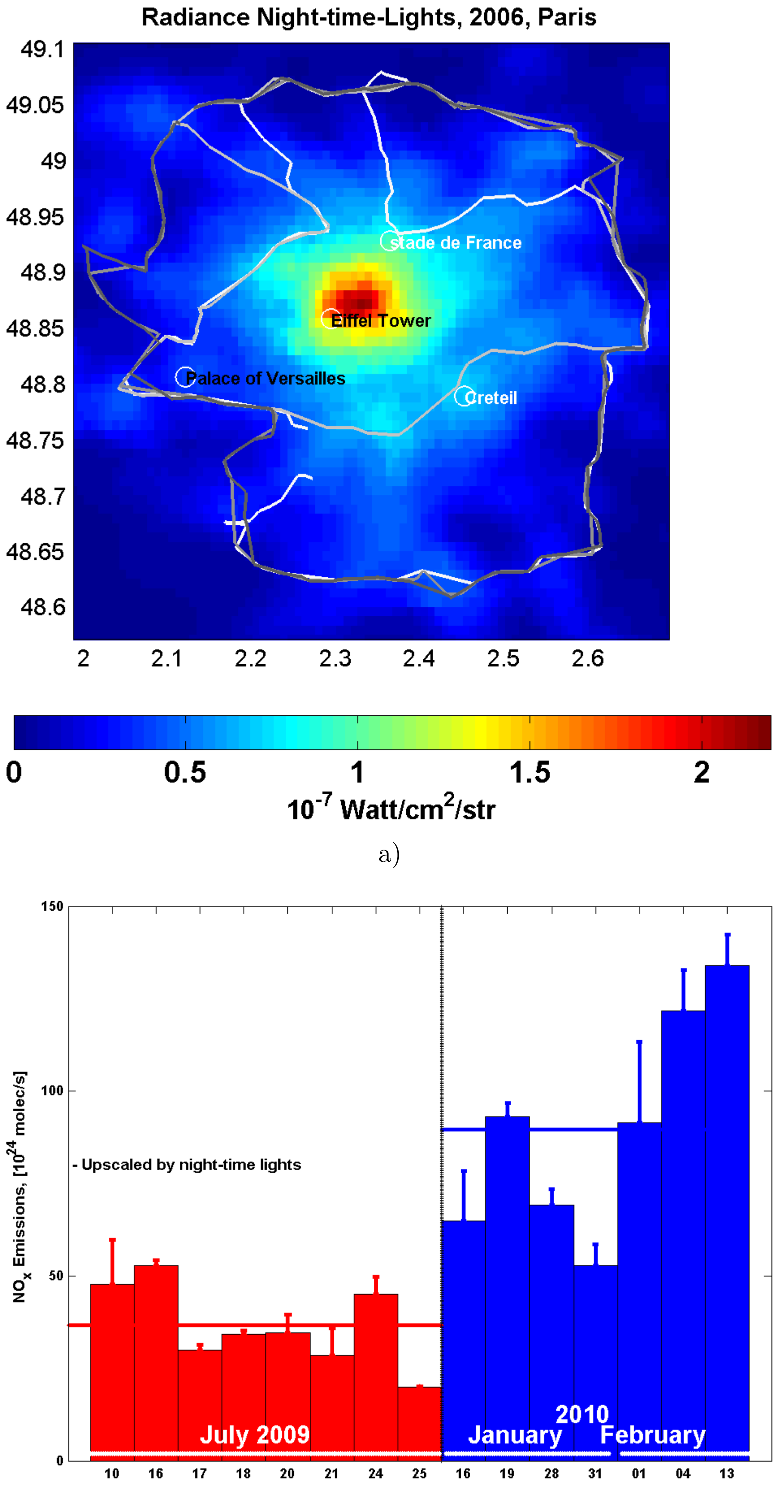

a)

b)

Figure 6.9: a) Spatial distribution of the night-time lights for the selected area. Different routes (2 days in summer and 2 days in winter) are shown.
b) The upscaled emissions from mobile MAX-DOAS using night-time lights (see the figure in part a).

Table 6.1: The correction factors, which are used for Paris campaigns.

Day of measurements	Chemical transformation factor	lifetime correction factor	upscaling factor
2009.07.10	1.32	1.20	1.60
2009.07.16	1.32	1.34	1.53
2009.07.17	1.32	1.15	1.74
2009.07.18	1.32	1.15	1.76
2009.07.20	1.32	1.31	1.82
2009.07.21	1.32	1.13	1.82
2009.07.24	1.32	1.16	1.46
2009.07.25	1.32	1.38	1.74
2010.01.16	1.44	1.02	1.99
2010.01.19	1.44	1.07	2.11
2010.01.28	1.44	1.06	1.25
2010.01.31	1.44	1.07	1.24
2010.02.01	1.44	1.04	1.24
2010.02.04	1.44	1.08	1.24
2010.02.13	1.44	1.08	1.24

for the upscaling (the results for all three proxies are rather similar). A map of this proxy is shown in figure 6.9a.

In the Table 6.1, different correction factors are shown (for chemical transformation factor (averaged values), lifetime correction factor and upscaling factor), these parameters are used to yield the Paris NO_x emissions.
The up-scaled emissions are shown in figure 6.9b. The difference between summer and winter emissions is still perceivable. The average of summer emissions is shown as a red line in figure 6.9b, and the average of winter emissions is indicated by the blue line. The ratio of averaged emissions (winter to summer) is 2.45.

These upscaled emissions can be compared to different emission inventories, and even, the mobile MAX-DOAS upscaled emissions are comparable to each other for different days and seasons.

6.4.1 Effect of aerosols on the measurements

For the tropospheric AMF a geometric approximation can be used: the light paths through the trace gas layer of interest is approximated by simple geometric paths. This assumption is valid if the aerosol concentrations are low. But if in the case of high aerosol concentrations, geometric approximation deviates from the true tropospheric AMF.

Table 6.2: The azimuth correction factors.

Day	RAA°	c_{az}	c_{az}	c_{az}	c_{az}	c_{az}	c_{az}
		NO_2 profile 0-500m	NO_2 profile 0-500m	NO_2 profile 0-100m	NO_2 profile 0-100m	NO_2 profile 0-200m	NO_2 profile 0-200m
		aerosol profile 0-1km	aerosol profile 0-2km	aerosol profile 0-1km	aerosol profile 0-2km	aerosol profile 0-1km	aerosol profile 0-2km
2009.07.10	103	1.09	1.09	1.08	1.06	1.09	1.09
2009.07.16	68	1.05	1.06	1.06	1.04	1.07	1.07
2009.07.17	90	1.09	1.09	1.08	1.06	1.09	1.09
2009.07.18	106	1.09	1.09	1.08	1.06	1.09	1.09
2009.07.20	125	1.1	1.1	1.09	1.07	1.095	1.095
2009.07.21	99	1.09	1.09	1.08	1.06	1.09	1.09
2009.07.24	129	1.1	1.1	1.09	1.07	1.095	1.095
2009.07.25	100	1.09	1.09	1.08	1.06	1.09	1.09
2010.01.16	66	1.05	1.06	1.06	1.04	1.07	1.07
2010.01.19	37	0.96	1	1.01	1.01	1.01	1.02
2010.01.28	27	0.95	0.99	1.01	1	1	1.01
2010.01.31	39	0.96	1	1.01	1.01	1.01	1.02
2010.02.01	26	0.96	1	1.01	1.01	1.01	1.02
2010.02.04	65	1.05	1.06	1.06	1.04	1.07	1.07
2010.02.13	66	1.05	1.06	1.06	1.04	1.07	1.07

The true tropospheric AMF are determined using the Monte Carlo radiative transfer model McARTIM (Deutschmann *et al.* , 2010) for different aerosol and NO_2 layer heights. The following aerosol optical parameters are used: single scattering albedo: 0.95 and asymmetry parameter: 06 (see appendix D.1.2 and figure E.1).

Three NO_2 layer heights (box profiles upper boundaries at 100 m, 200 m and 500 m for box profiles) and two aerosol layer heights (box profiles upper boundaries at 1 km and 2 km; box profiles) are applied in the calculations. The applied elevation angle is 22°. The aerosol optical depth derived from AERONET webpage (level 2.0 at 500 nm) are rather low for Paris, for July 2009: 0.18, for January 2010: 0.15 and finally February 2010: 0.13 (data taken from the LIDAR in Paris `http://aeronet.gsfc.nasa.gov/cgi-bin/type_one_station_opera_v2_new?site=Paris&nachal=0&year=17&month=6&aero_water=0&level=3&if_day=0&if_err=0&place_code=10&year_or_month=0`).
The azimuth dependent correction factors are shown in the table 6.2 for different scenarios. Because of low aerosol extinction, the azimuth correction factors are as expected close to one and the highest deviation is about 4% and the average of these deviations is about 2%, which is negligible in comparison to other affects. Therefore we do not apply this correction factor in this study.

6.4.2 TNO emission inventories

Anthropogenic emission inventories (year, 2005) for Europe are provided for the MEGAPOLI project. The TNO European inventory as well as the megacities inventories are bottom-up emission inventories using data at the city scale and national scale, respectively (Kuenen *et al.* , 2010). The emission grids refer to down-scaled emissions. Selected air pollutants consist of 10 source categories.
The resolution of these emission inventories is 0.125° longitude×0.1667° latitude.

Table 6.3: Description of source categories maintained in the gridded emission data (Kuenen *et al.* , 2010). SNAP is an index to distinguish the source category.

SNAP	Description
1	Power generation
2	Residential commercial and other combustion
3	Industrial combustion
4	Industrial process emission
5	Fossil fuel production
6	Solvent and product use
7	Road transport 7.1 Road transport Gasoline 7.2 Road transport Diesel 7.3 Road transport LPG 7.4 Non-exhaust (Evaporation) 7.5 Non-exhaust (brake, tire and road wear)
8	Other mobile sources
9	Waste treatment and disposal
10	Agriculture

The NO_x emission provided by TNO shows a good agreement with inventories from AirParif (`http://www.airparif.asso.fr/pages/emissions/emisidf`), AirParif has set up emission inventory for the Ile-de-France region, that has been made available for the MEGAPOLI project for the year 2005 (Kuenen *et al.* , 2010).

In figures 6.10 and 6.11, different TNO emission sources are shown for the Paris area for July 2005 and January and February 2005, respectively. Dependent on the source of emissions, the emissions have different resolutions.
The emissions in winter are higher than in summer (see figures 6.11 and 6.10).

6.4.3 Chemistry transport Model CHIMERE

The CHIMERE model (Schmidt *et al.* , 2001) has been developed since 1997 by IPSL (Institute Pierre Simon Laplace) and INERIS (Institut National de l'Environnement Industriel

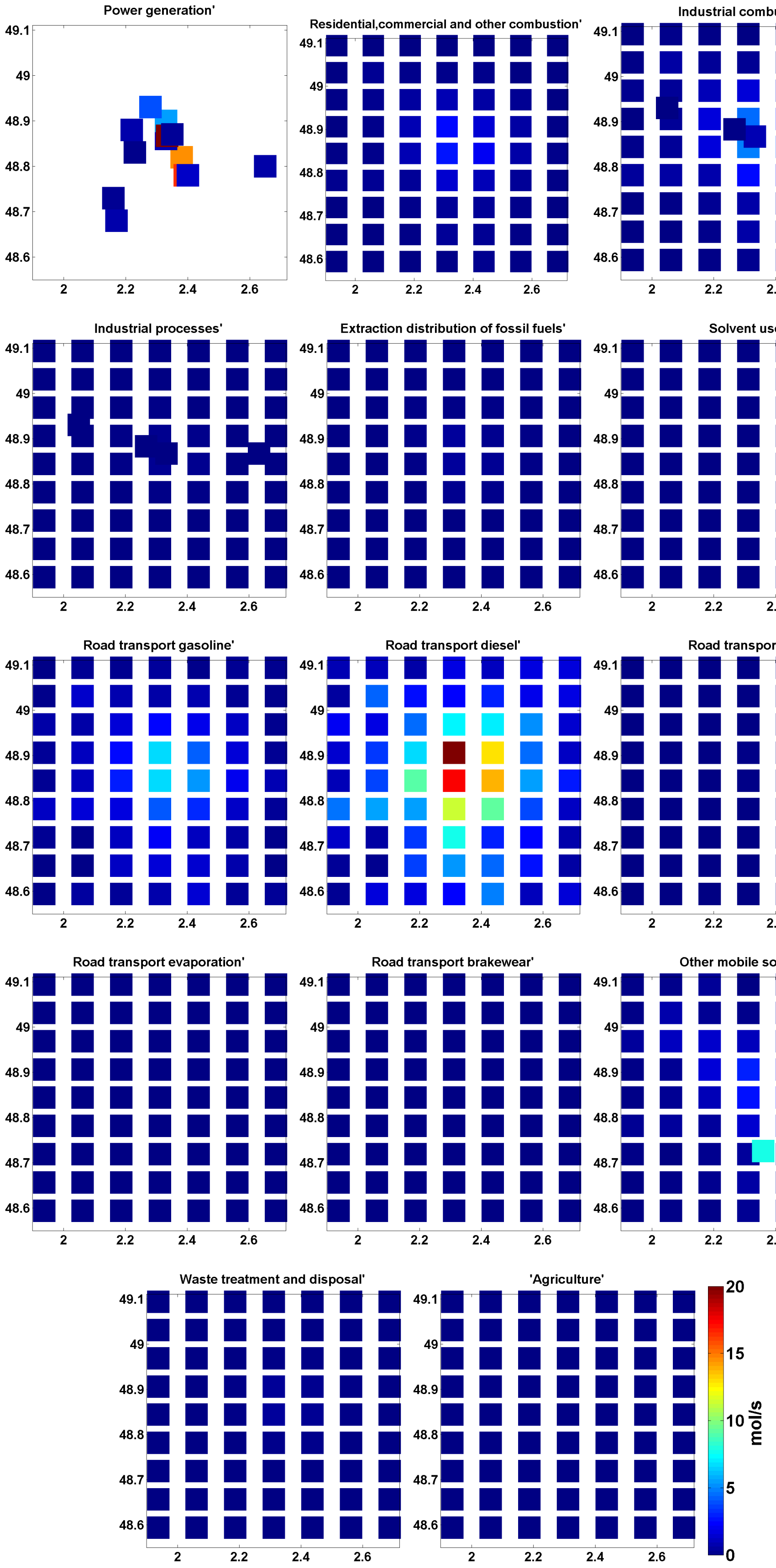

Figure 6.10: Different NO_x emission sources described by the TNO inventory for July 2005.

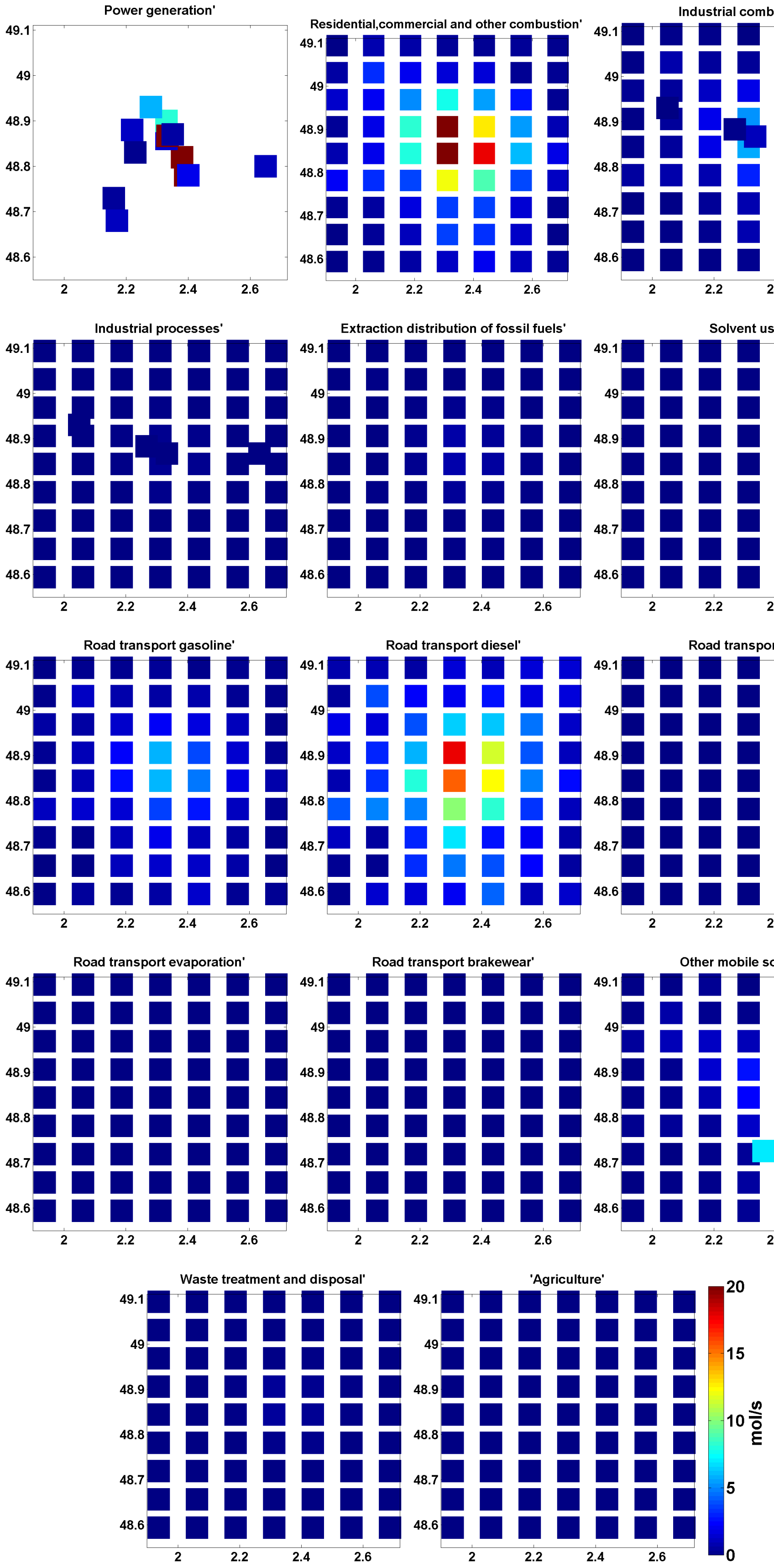

Figure 6.11: Different NO_x emission sources described by the TNO inventory for Winter (January and February) 2005.

et des Risques). This chemistry transport model is used to produce daily forecasts of ozone, trace gases and aerosols and other pollutants and for long term simulation, which can be done in different resolutions.
The model is based on the mass continuity equation for the concentration of chemical species in every box of a given grid. The CHIMERE model needs input data like meteorological data, boundary conditions, land-use and emissions.

Mateo data (MM5 model) are used for meteorological input variables; INCA (INteraction between Chemistry and Aerosols) for gas species, GOCART (GOddard Chemistry Aerosol Radiation and Transport) for aerosols as source for boundary and initial conditions; GLCF (Global Land Cover Facility) global land-use database for land-use data (Petetin *et al.* , 2011).

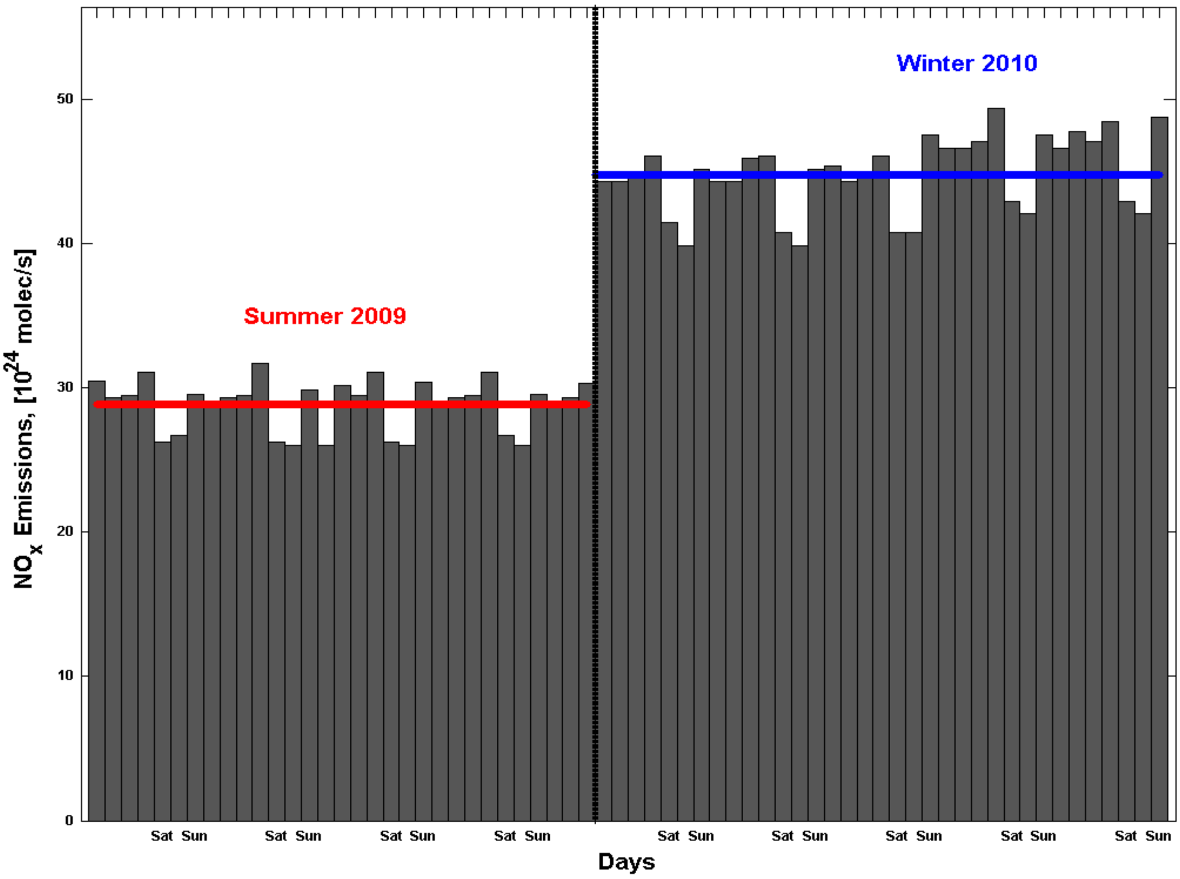

Figure 6.12: Daily averaged NO_x emissions from the TNO inventory for Paris: summer data are from June 30, 2009 to July 30, 2009 and winter data from January 12 to February 15, 2010.

The selected domain has eight vertical layers, from ground to about 5 km, with decreasing vertical resolution with altitude.
For input emissions, MEGAPOLI MC inventories were used, which are obtained from TNO inventories.

In figure 6.12, times series of daily averaged NO_x emissions are shown, obtained from the

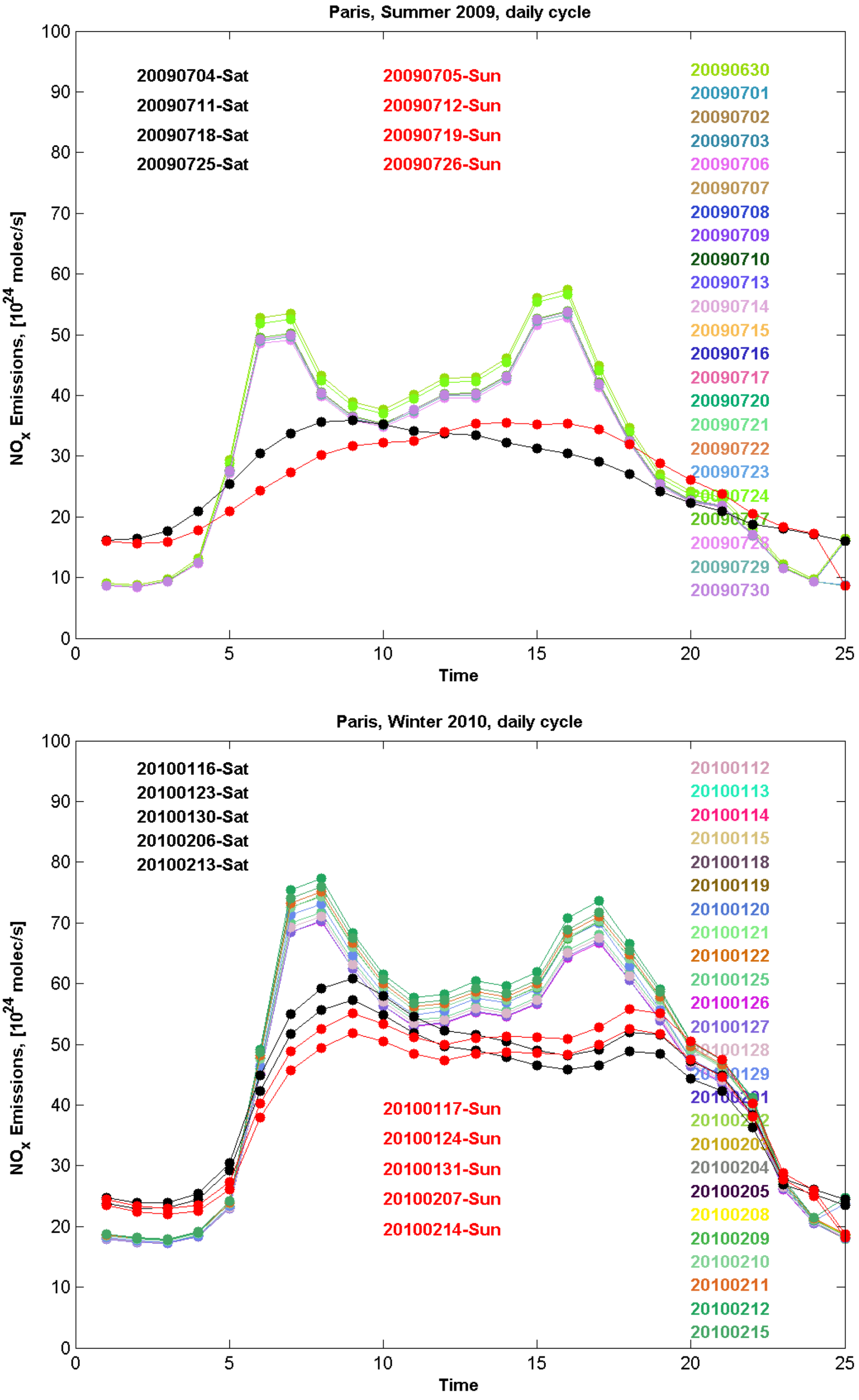

Figure 6.13: Diurnal cycle of the NO_x emissions from the TNO inventory for Paris during summer and winter campaigns.

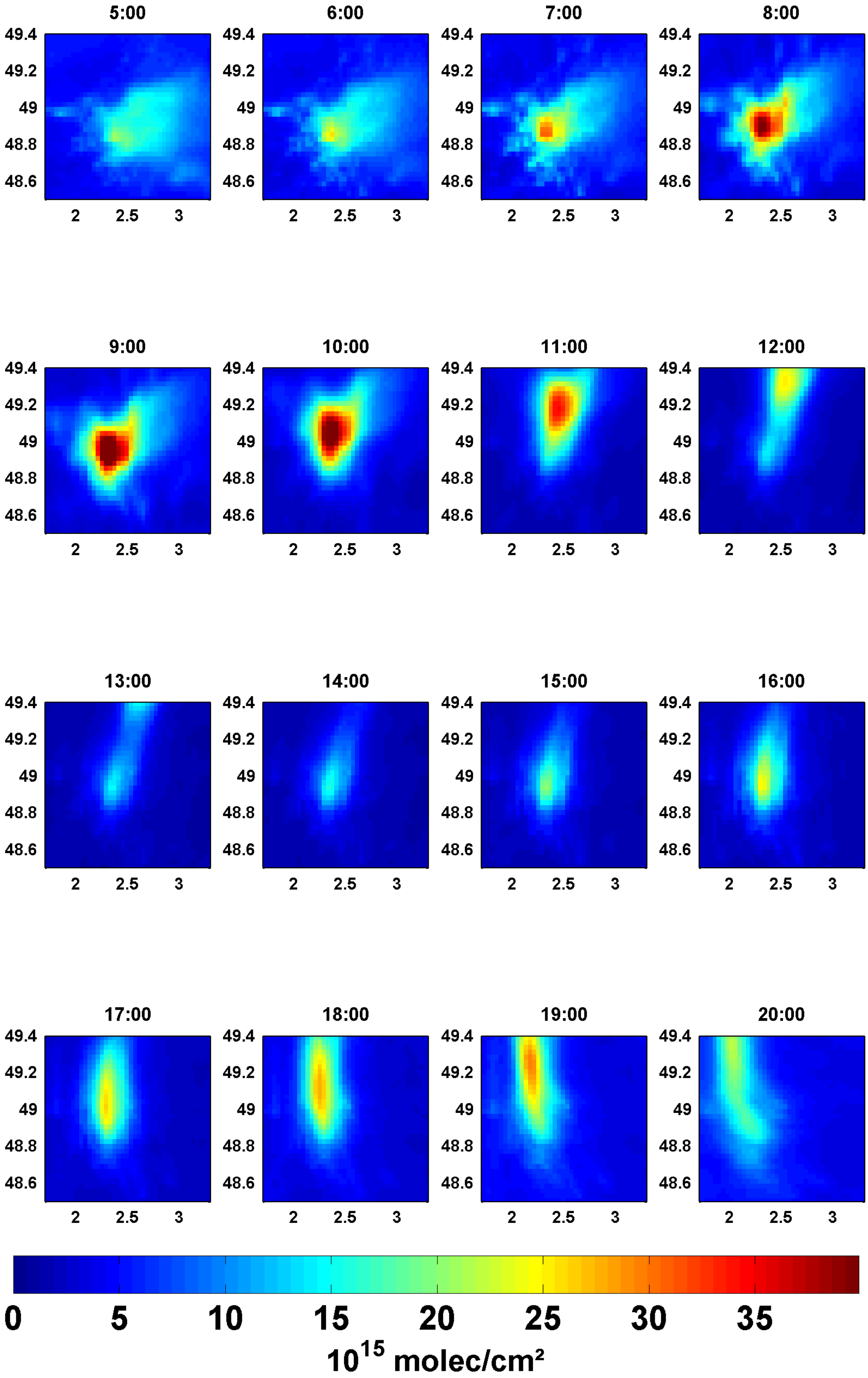

Figure 6.14: Vertical column densities of NO_2 from July 16, 2009. The CHIMERE model data are shown for different times in a day.

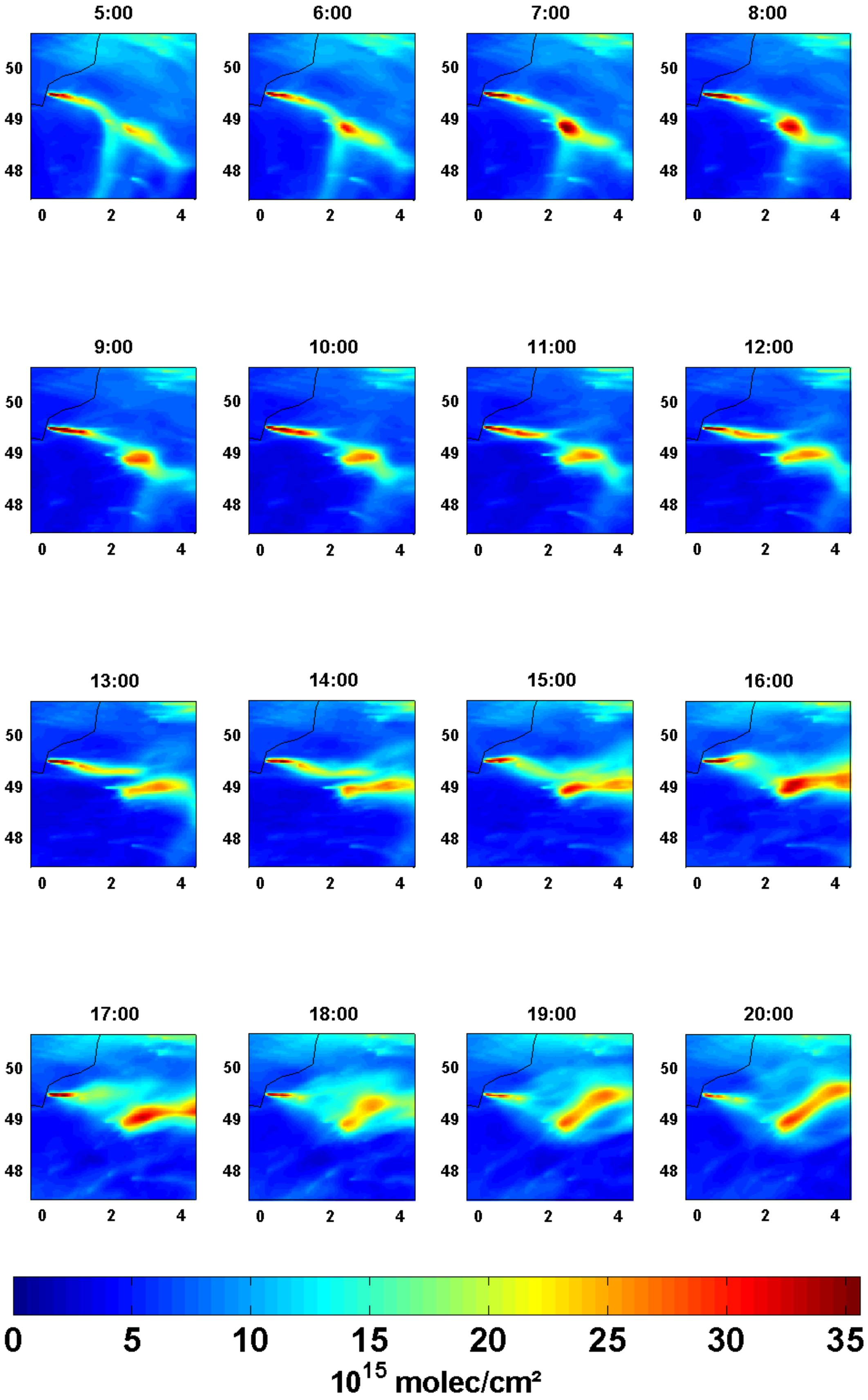

Figure 6.15: Vertical column densities of NO_2 from January 31, 2010. The CHIMERE model data are shown for different times in a day.

TNO inventories for the Paris area covered by the mobile MAX-DOAS measurements. The red line indicates the average for the summer period and the blue line that for winter period. The winter emissions are about 55% higher than the summer emissions.

Because of less activity at the weekend, lower values are found for the weekend. Such a weekly cycle can be seen for summer and winter time. Such weekly cycle was also found by satellite observations (Beirle, 2004). There is one interesting exception in summer with low emissions ($2.6 \times 10^{25}\ \frac{molec}{s}$) for July 14, which is the Bastille day (14 Juillet-Fête Nationale).

In figure 6.13, diurnal cycles of the NO_x emissions from the TNO inventory are shown for the time intervals of the summer and winter campaigns. The diurnal cycles are rather separated in three categories, workdays (various colors), Saturdays (black) and Sundays (red). The emissions at weekend show more a smooth curve, while for the workdays, they emphasize two peaks, first in the morning and second in the afternoon.

NO_2 Vertical column densities from the CHIMERE model are shown in figure 6.14 for July 16, 2009. The temporal resolution of the CHIMERE model data is hourly. In figure 6.14, the shape and position of the plume are variable and displayed from 5:00 in the morning to 20:00 in the evening. Emission of NO_2 from the city, transport of the plume and also conversion to NO can be seen from this figure.

NO_2 vertical column densities for January 31 in 2010 are shown in figure 6.15. Here a bigger area is shown, because the size of the plume is larger than in summer. The absolute values do not change on this day, but the plume is transported. Much of NO_x exist in winter as NO, because there is not enough ozone to convert.

6.4.3.1 Estimation of NO_x emissions using the CHIMERE model

In order to verify our algorithm for the determination of NO_x emissions from mobile MAX-DOAS observations, we applied the same algorithm to the NO_2 data from the CHIMERE model. From the comparison of the derived emissions and the input emissions of the model, the accuracy of the algorithm can be quantified.

The CHIMERE model data are simulated in $3 \times 3\ km^2$ spatial resolution. We linearly interpolate the CHIMERE data in time and space to match the locations and times of the MAX-DOAS data.

In figure 6.16, the comparison between the results from mobile MAX-DOAS (colored circles) and the interpolated CHIMERE model data (colored squares) is shown. This example from July 20, 2009, shows a good agreement between measurements and model. High values of NO_2 are found in the area of the airport at the north east side of the city. For this day, a

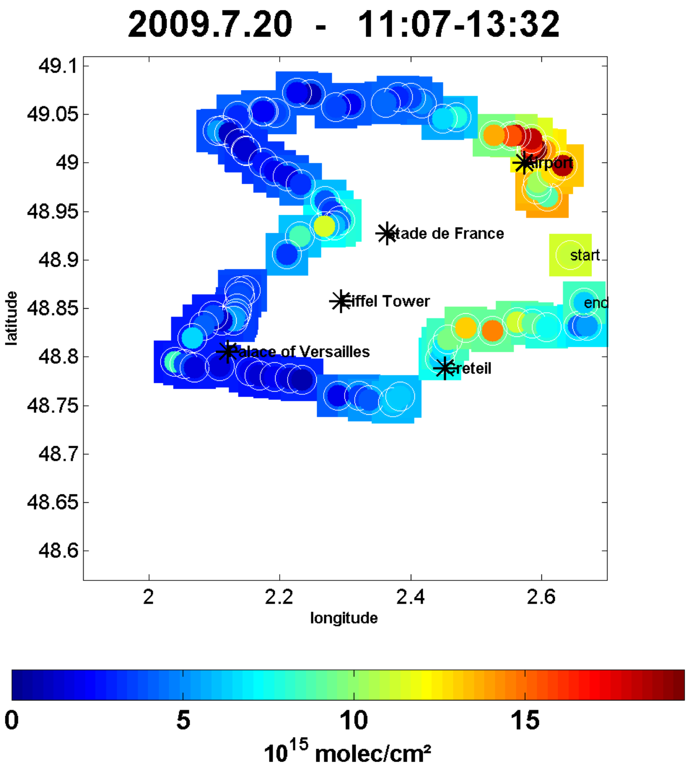

Figure 6.16: Tropospheric vertical column densities from mobile MAX-DOAS (colored circles) and CHIMERE (colored squares).

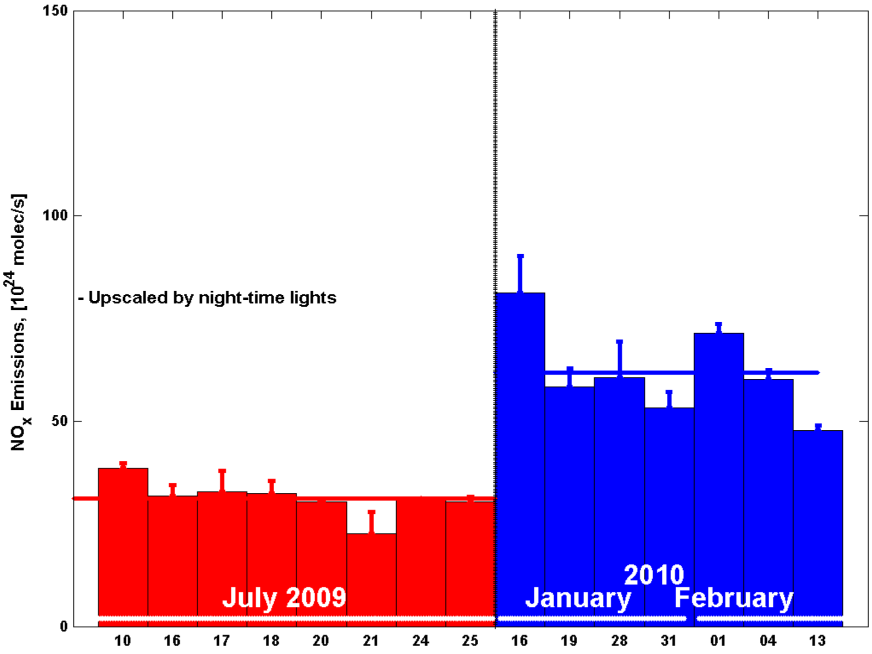

Figure 6.17: The emissions derived from the CHIMERE model (upscaled by night-time lights).

correlation coefficient r^2 of 0.74 could be found between CHIMERE and mobile MAX-DOAS vertical column densities.

From the encircled area, the emissions can be estimated by using again the equation 4.3. But now the VCD values were obtained from CHIMERE. The same wind data and correction factors were used as for the mobile MAX-DOAS.

In figure 6.17, the emissions for Paris are shown as derived from CHIMERE data. We refer to these emissions as CHIMERE output emissions in the following. The red line shows the average emissions in summer, while the blue one shows the average emissions in winter, which is about twice the average of the summer emissions.

Now it is interesting to compare the derived emissions with those used as input for the model. The respective ratios are shown in figure 6.18 (top).
The expected value of this ratio is one. Most of these ratios in figure 6.18 (top) are indeed close to 1. Deviations of the expected value (1) might be caused by two reasons:
First, the effective NO_x lifetime in the CHIMERE model might deviate from that assumed in the retrieval algorithm for the output emissions.
Second, the diurnal variation of the input emissions might play an important role. This influence is studied in the following.

In figure 6.18 (middle and bottom), the ratios of the CHIMERE output emissions to the TNO emissions (Input emission) are studied as a function of time.
The input emissions are averaged from TNO inventories for the time of the MAX-DOAS measurements.

To investigate the influence of the diurnal variation of the NO_x emissions, we calculated the input emissions for different periods of the day. We begin from 6 hours before the orbit time, and increase it by one hour up to the actual orbit time.
This means, if we began to measure at 09:00 with a total measurement duration of 3 hours (example, 2009.07.10), the input emissions were first calculated from 3' clock in the morning. First input emission is averaged from 3:00 to 6:00. Second: from 4:00 to 7:00. Third: from 5:00 to 8:00. Fourth: from 6:00 to 9:00. Fifth: from 7:00 to 10:00. Sixth: from 8:00 to 11:00 and finally the last one from 9:00 to 12:00. Note that, the output emissions do not change at all.
The corresponding ratios are shown in figure 6.18 (middle and bottom). In general, the influence of the diurnal cycle of the input emissions is of the order of 10 %.

We conclude that larger deviations of the ratio from 1 must be caused by different reasons, most probably by a different effective NO_x lifetime in the model than assumed in determination of the output emissions.

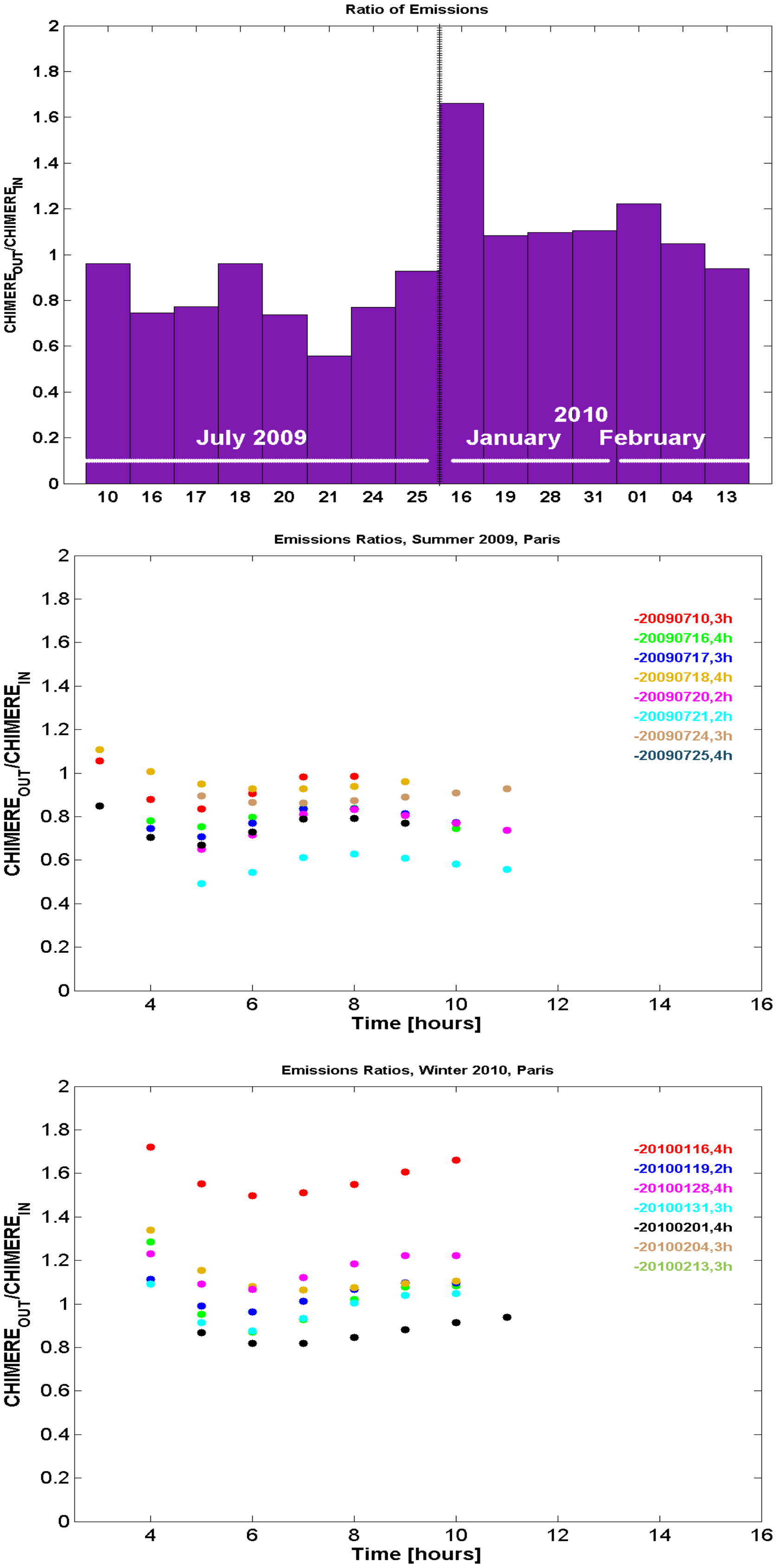

Figure 6.18: Top: ratios of input and output emissions of CHIMERE (chemistry transport model). Middle and bottom: ratios of input and output emissions with input emission as a function of time (see text).

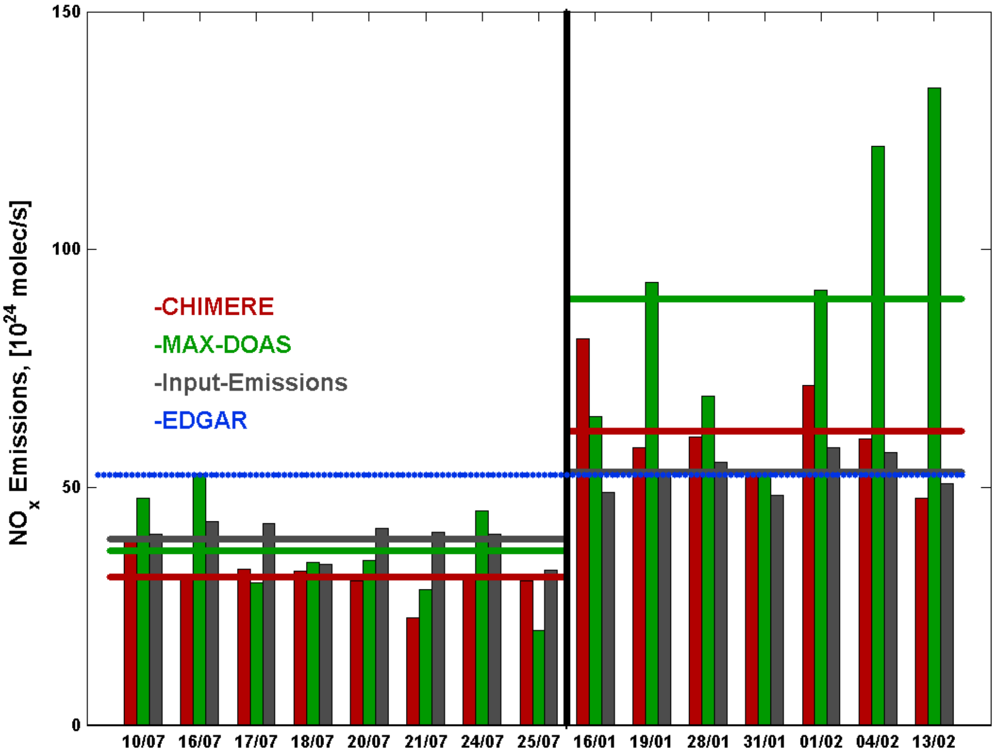

Figure 6.19: The comparison of emissions from mobile MAX-DOAS, CHIMERE, Input emissions and EDGAR. The colored lines represent the average emissions.

In figure 6.19, the output emissions from CHIMERE and mobile MAX-DOAS are compared. Also included (in gray) are TNO emission inventories, which are applied as input emissions for the CHIMERE model. The colored lines show averaged emissions, separated for summer and winter. The gray, green, red and blue lines represent respectively: TNO inventories (input emissions), mobile MAX-DOAS, CHIMERE average emissions and EDGAR emission. We use the EDGAR emission inventory (version 4.1 for 2005, see (Olivier *et al.* , 1998); European commission, 2010), with a spatial resolution of 0.1°. The EDGAR inventory is almost as large as the input emissions in winter.

As already seen in figure 6.18, the input emissions into the CHIMERE model and CHIMERE output emissions are mostly similar. In summer, also the MAX-DOAS emissions are similar (17 % higher on average than CHIMERE), while in winter, the average MAX-DOAS emissions is about 45 % higher than CHIMERE. The average input emissions is about 26 % higher than CHIMERE in summer, but in winter, it is 16 % less than the average CHIMERE emissions.

The comparison of tropospheric vertical column densities of mobile MAX-DOAS and CHIMERE is shown in figure 6.20. The average tropospheric vertical column densities from CHIMERE and from mobile MAX-DOAS, for summer time are almost the same. For winter time, the average tropospheric vertical column densities from mobile MAX-DOAS is 35 % higher than

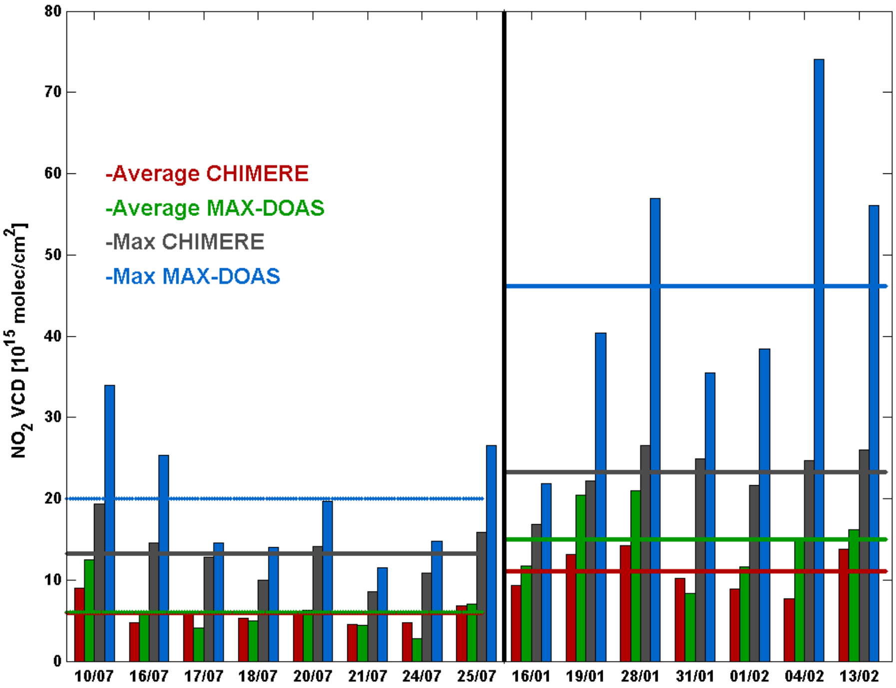

Figure 6.20: The comparison of tropospheric vertical column densities of mobile MAX-DOAS and CHIMERE.

from CHIMERE.

The maximum values of the different days (in figure 6.20) are shown in gray and blue, respectively, for CHIMERE and mobile MAX-DOAS. The difference between the averages of max values in winter is higher than in summer. These differences between CHIMERE and MAX-DOAS can be mainly attributed to the limited spatial resolution of the CHIMERE model (3km in North-South and East-West direction).
It is interesting to note that the relative deviations between CHIMERE and MAX-DOAS in winter are similar for the comparison of vertical column densities (VCDs) and emissions.

The ratios of VCDs are shown in figure 6.21 (top), and at the bottom the ratio of MAX-DOAS emissions to CHIMERE are shown.

6.4.3.2 Correlation between mobile MAX-DOAS and CHIMERE

The spatial correlation between measurements and model is an important measure to quantify the agreement between both data sets. We compared the tropospheric vertical column densities from mobile MAX-DOAS (measurements) to the tropospheric vertical column densities from the CHIMERE model data. For this purpose, the CHIMERE data are spatially and temporally interpolated to match the MAX-DOAS data.

In figure 6.22, the tropospheric vertical column densities from mobile MAX-DOAS are shown with associated CHIMERE TVCDs for different days in summer and winter from the Paris campaigns. In general good agreement of the relative patterns is found, but MAX-DOAS data are usually higher at the lee sides compared to CHIMERE model data.

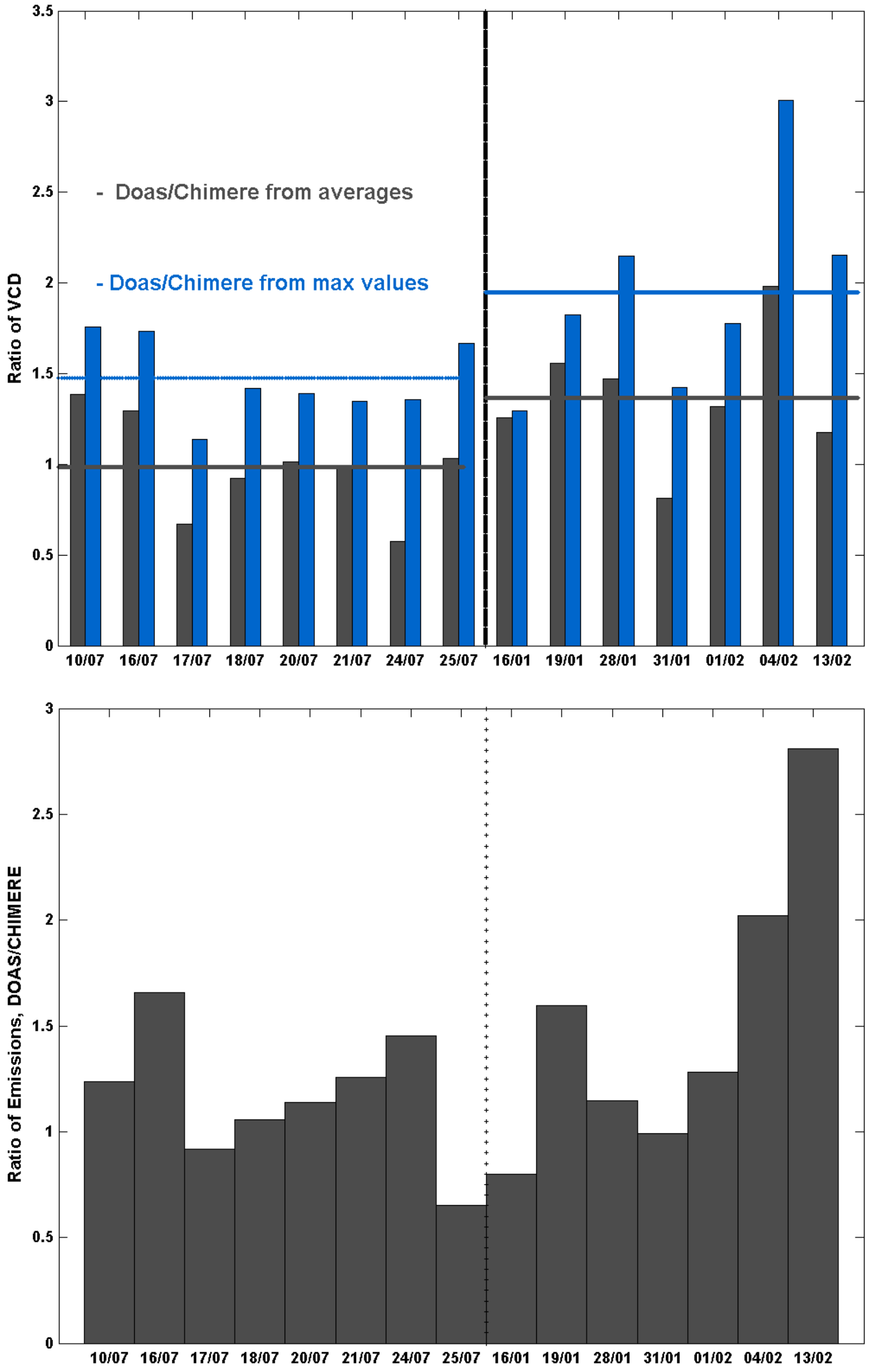

Figure 6.21: Top: Ratios of MAX-DOAS and CHIMERE VCDs. Bottom: Ratios of MAX-DOAS and CHIMERE emissions.

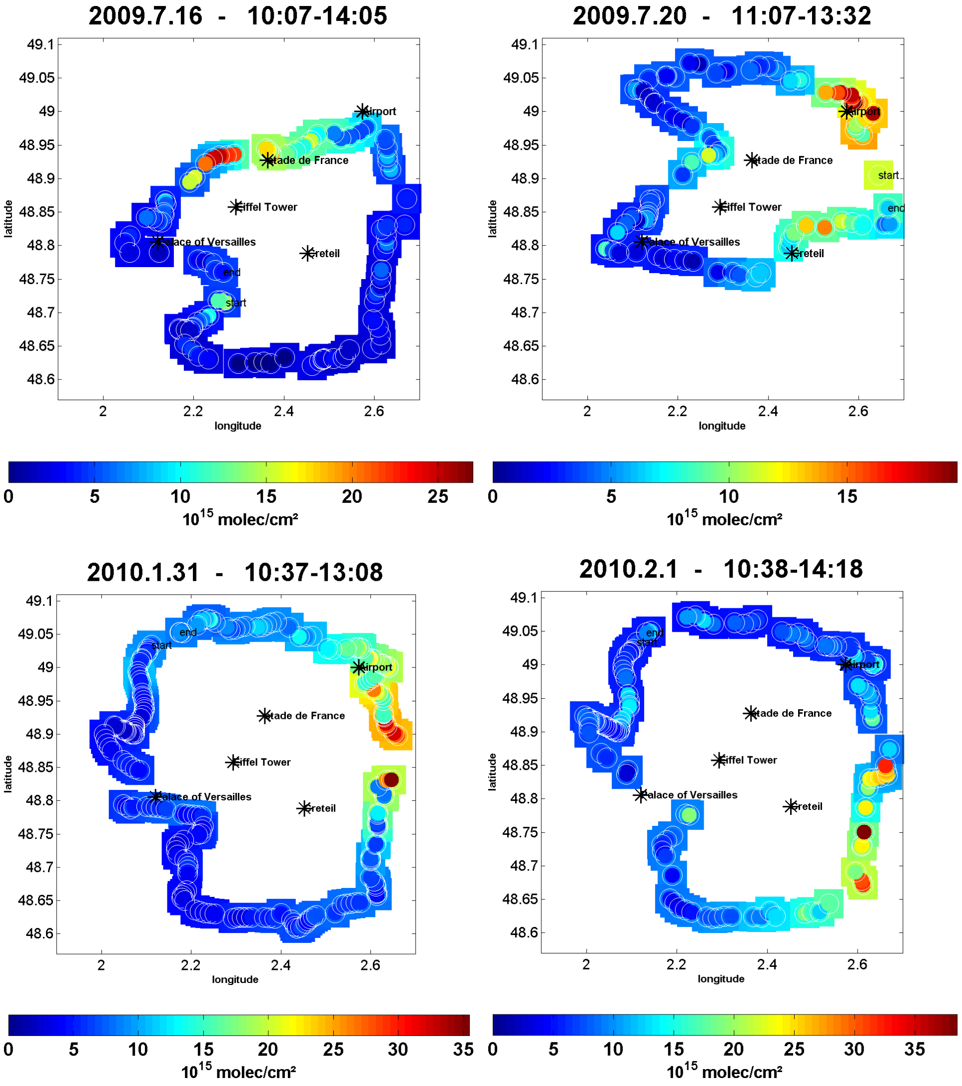

Figure 6.22: NO_2 tropospheric vertical column densities from mobile MAX-DOAS (colored circles) and the CHIMERE model (colored squares) for four days in Paris.

The averages of NO_2 tropospheric vertical column densities from the encircled area are compared in figure 6.20. While the seasonal averages show rather good agreement, the maximums show larger discrepancies. The ratios of VCDs are shown in figure 6.21. For the daily averages, the lowest ratio is from July 24, 2009 and highest from February 4, 2010. This day has the highest ratio of max values too, but the lowest ratio of maximum values is from July 17, 2009.

The different spatial resolutions of the CHIMERE model and mobile MAX-DOAS are probably responsible for the different maximum values, because the CHIMERE VCDs are averaged in a 3×3 km^2 grid.

The spatial correlations of the daily data with related slopes are shown in figure 6.23. The variation of the results is rather high. The red points represent the correlation coefficients

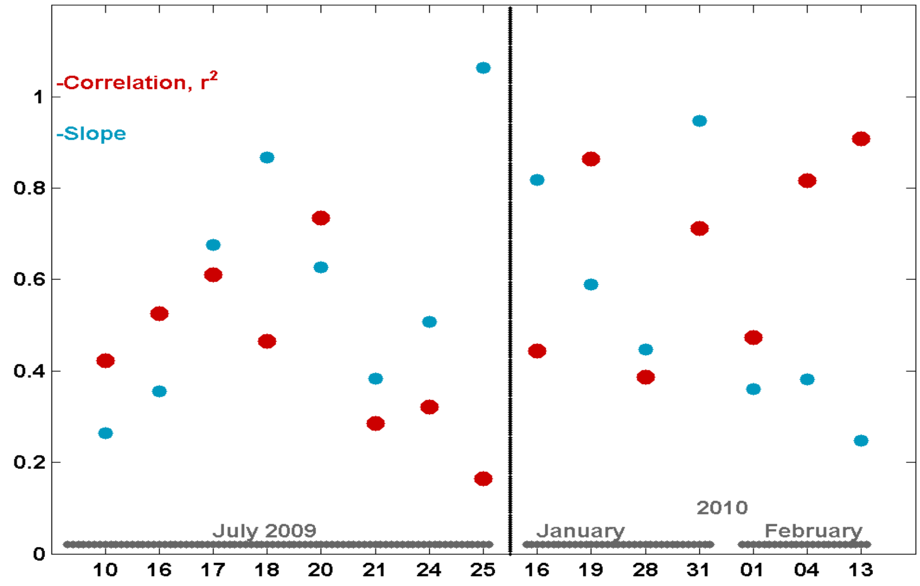

Figure 6.23: Correlation coefficients between mobile MAX-DOAS and CHIMERE VCDs.

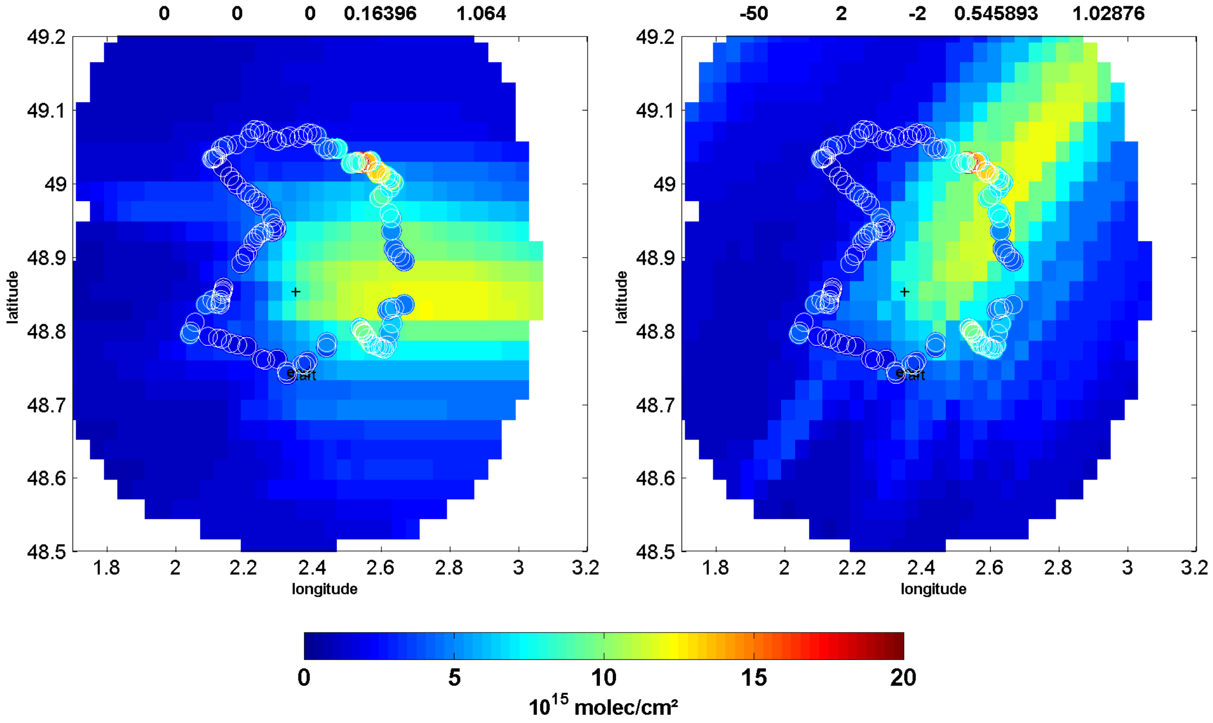

Figure 6.24: The tropospheric NO_2 VCDs from MAX-DOAS and CHIMERE for July 25, 2009. The left figure shows the original VCDs. The right figure shows the CHIMERE data after rotation and shifts have been applied. The numbers on top of the figures represent rotation, shift in east-west, shift in north-south direction, correlation coefficient r^2 and slope respectively.

r^2 between MAX-DOAS and CHIMERE VCDs and the blue points the slopes between measurement and model. An orthogonal linear regression fit was used to obtain the correlation coefficients and slopes.

The two days July 25, 2009 and February 13, 2010 (see figure 6.23) are more extreme cases, for the other days the correlations and slopes are much closer.
In several cases, it is obvious that a low correlation results just from a slight miss-match of the patterns.

In figure 6.24 (left), the mobile MAX-DOAS vertical column densities are shown in colored circles and the CHIMERE vertical column densities in colored boxes, the patterns of high NO_2 values from measurements and model do not match, and the plume would have to be shifted to reach a better correlation between MAX-DOAS and CHIMERE. So we investigated how rotations or shifts of the model data affect the correlation.

The comparison of mobile MAX-DOAS vertical column densities to the CHIMERE VCDs is shown in figure 6.24 for July 25, 2009, the left one represents the comparison without any change of the data, whereas the right figure represents the comparison after a rotation of 50° and a 2 pixels shift of the model in east-west direction and a 2 pixels shift in north-south direction. The numbers on top of the figures represent respectively rotation, shift in east-west, shift in north-south direction, correlation coefficient r^2 and slope. The original correlation was 0.16. After rotation and shift, we reached 0.55, but the slope does not change so much.

A similar example for winter (January 28) is shown in figure 6.25. On this day only small variations of the model data lead to a large improvement of the correlation.

The combination of rotation and shift can be rather complicated, therefore we consider both changes separately.
In figure 6.26, maximum correlations between mobile MAX-DOAS and CHIMERE VCDs are shown. These correlations can be reached, if the rotation, transport in east-west or transport in north-south direction is made to the CHIMERE model data. All correlations are higher than original (without changes). Exception July 25, 2009, all new correlations in summer are larger than 60 % and for winter larger than 70%.

6.5 Comparison of OMI satellite observations to mobile MAX-DOAS measurements

In this chapter, we compare ground based measurements to satellite data. First, we compare the retrieved emissions from OMI observations to the respective emissions obtained from the mobile MAX-DOAS observations. Second, we directly compare the NO_2 VCDs derived from

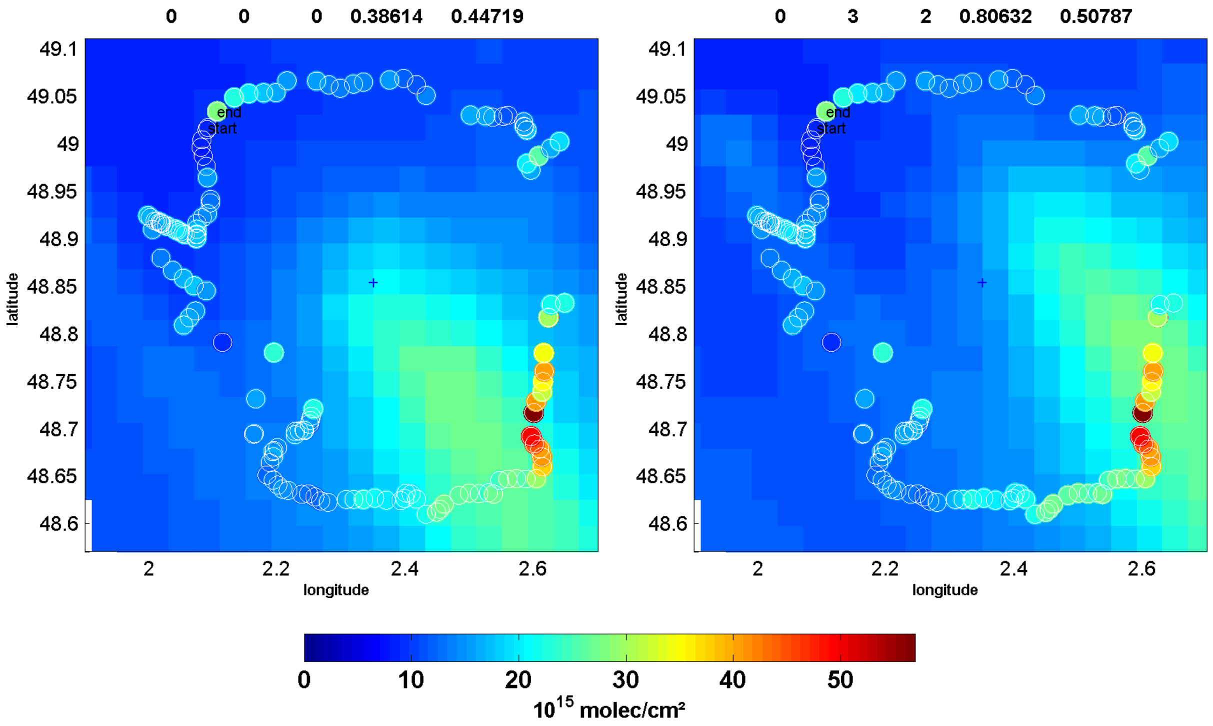

Figure 6.25: The tropospheric NO_2 VCD from MAX-DOAS and CHIMERE for January 28, 2010. The left figure shows the original VCDs. The right figure shows the CHIMERE data after rotation and shifts have been applied. The numbers on top of the figures represent rotation, shift in east-west, shift in north-south direction, correlation coefficient r^2 and slope respectively.

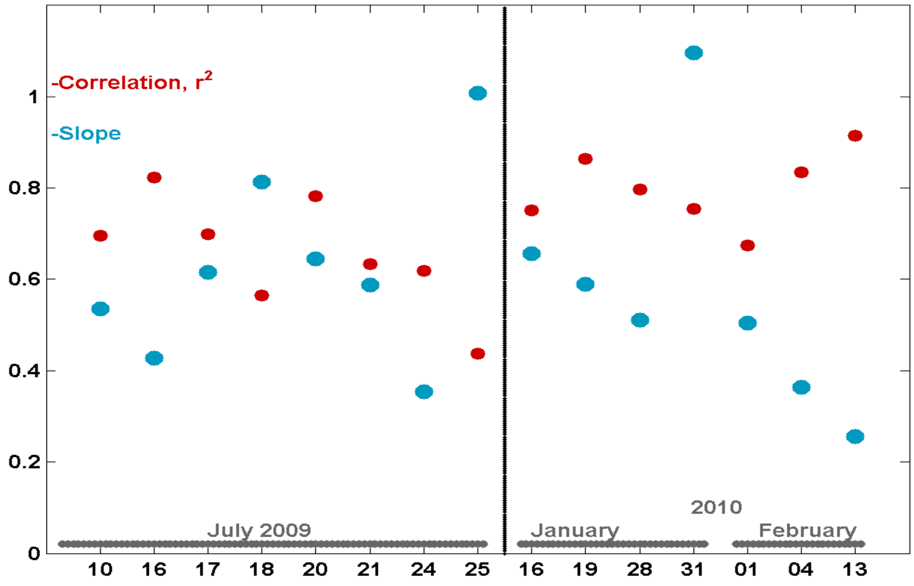

Figure 6.26: Correlation coefficients between mobile MAX-DOAS and CHIMERE VCDs after rotation or transportation.

mobile MAX-DOAS to the satellite VCD from OMI. We use the DOMINO product, version 1.0.2 and version 2.0, `http://www.temis.nl/airpollution/no2.html`, see Boersma *et al.* (2007).

6.5.1 Comparison of emissions

Satellite observations can be used to estimate emission (e.g. Leue *et al.* (2001); Martin *et al.* (2003); Beirle *et al.* (2011); Shaiganfar *et al.* (2011)). By integration of the tropospheric NO_2 VCD from satellite observations across a selected area, the total number of NO_2 molecules in the volume above that area can be determined. With the knowledge of the mean NO_x lifetime the corresponding emissions can then be simply derived by the following formula:

$$F_{NO_x} = c_L \frac{\int VCD_{NO_2} dA}{\tau} \tag{6.1}$$

The area over which the satellite measurements are integrated has to be chosen carefully. First, it should include the emission source of interest. Second, it should not be significantly influenced by other strong sources from outside the selected area. Third, it should be large enough to contain most of the emitted NO_x, which is advected from the source. In practice this means that the distance between the emission source and the borders of the selected area should be larger than the product of the wind speed and the NO_x lifetime. Like for the determination of the NO_x emissions from the mobile MAX-DOAS observations we assume the NO_x lifetime to about 5 hours for summer and 15 hours for winter.

It is interesting to note that in contrast to the mobile MAX-DOAS measurements the uncertainty of the obtained NO_x emissions using equation 6.1 is directly proportional to the uncertainty of the assumed NO_x lifetime. While an uncertainty of ± 2 hours leads to an uncertainty of less than $\pm 10\%$ for the NO_x emission estimate from mobile MAX-DOAS measurements, it leads to 40% for the NO_x emission estimate from satellite observations in summer.

There are two versions of OMI satellite data for NO_2 products, which we used: version 1.0.2 and version 2.0. Many days during the campaigns in Paris, we had cloudy days or even snow in winter. Such conditions reduce the coverage of satellite observations over Paris. By skipping these days only a few days with good satellite coverage were left.

Three days in summer fulfill these conditions: July 16, 20 and 21, 2009. Other days with limited satellite coverage are included in appendix B.1.2.

In figure 6.27, two different tropospheric NO_2 vertical column density products from OMI observations are shown: version 1.0.2 and version 2.0 for July 16 2009. Because of some changes in the algorithm in version 2.0 (Boersma *et al.* , 2011), the NO_2 VCDs from version

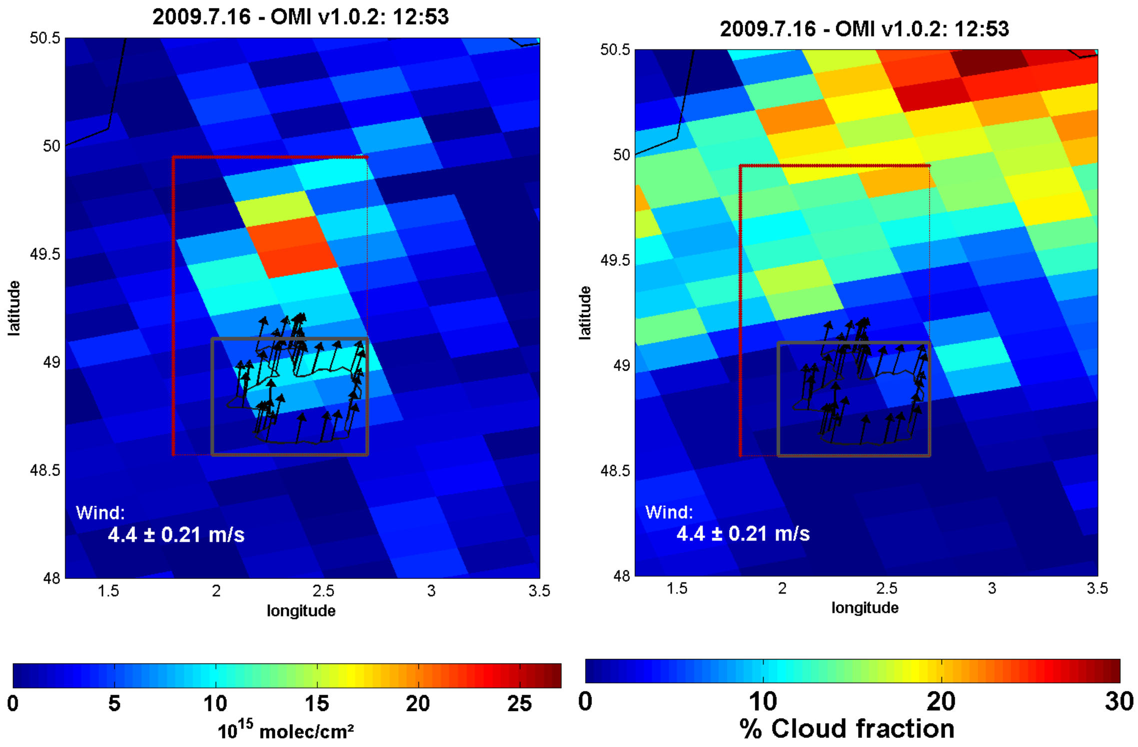

2009.7.16 - OMI v1.0.2: 12:53

2009.7.16 - OMI v1.0.2: 12:53

a) The tropospheric vertical column densities from OMI satellite version 1.0.2.

b) The cloud fraction from version 1.0.2.

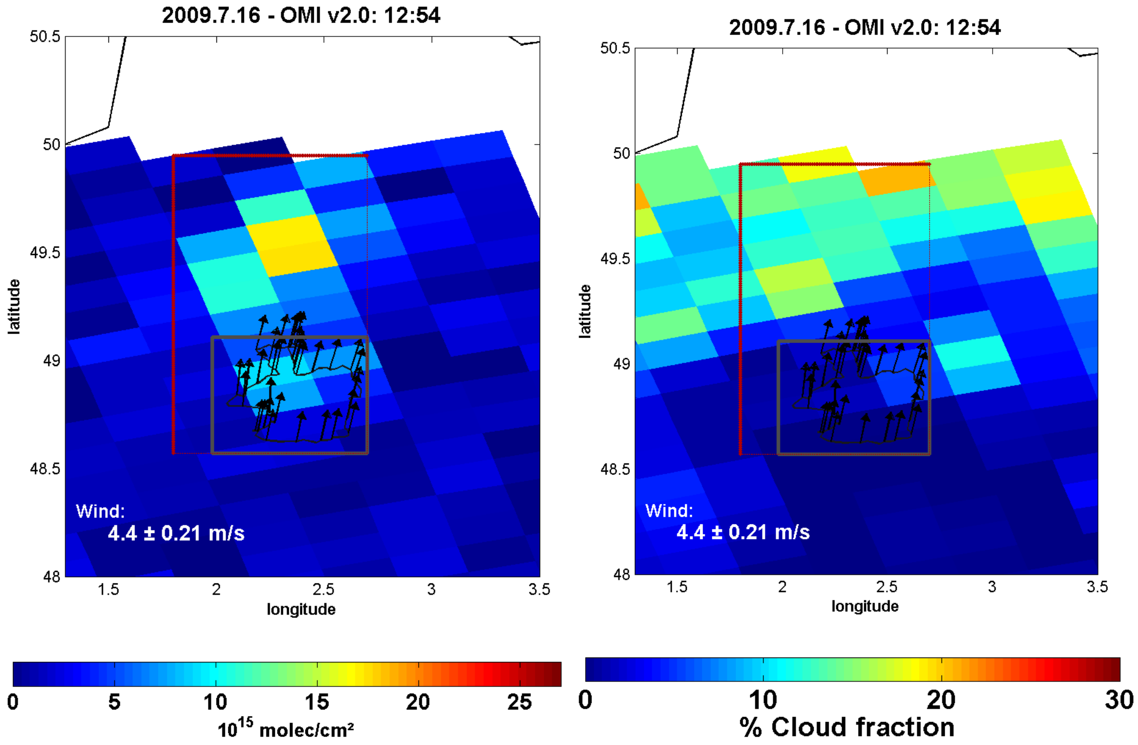

2009.7.16 - OMI v2.0: 12:54

2009.7.16 - OMI v2.0: 12:54

c) The tropospheric vertical column densities from version 2.0.

d) The cloud fraction from version 2.0.

Figure 6.27: The comparison of tropospheric NO_2 VCDs from MAX-DOAS with two different versions of OMI data for July 16, 2009 (left). The related cloud fractions (right) and wind vectors are shown. The red boxes are selected areas for the estimation of emission from OMI data.

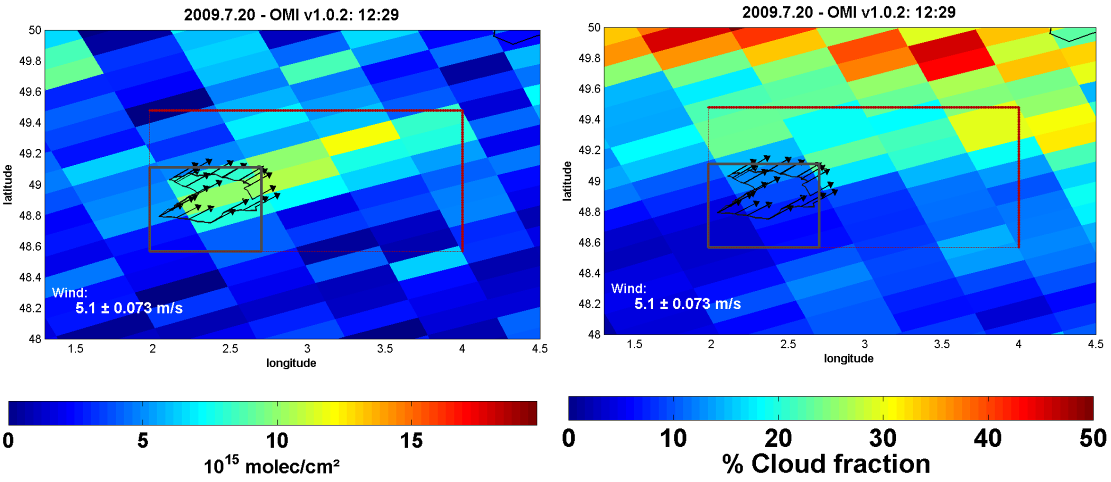

a) The TVCDs from OMI satellite version 1.0.2 b) The cloud fraction from version 1.0.2

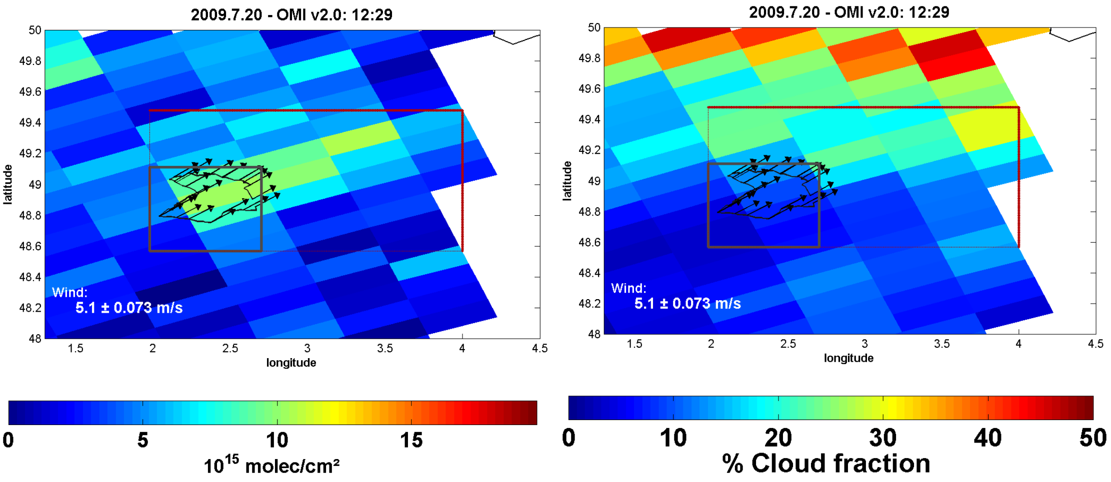

c) The TVCD from version 2.0 d) The cloud fraction from version 2.0

Figure 6.28: The comparison of tropospheric NO_2 VCDs from MAX-DOAS with two different versions of OMI data for July 20, 2009 (left). The related cloud fractions (right) and wind vectors are shown. The red boxes are selected areas for the estimation of emission from OMI data.

1.0.2 are rather different than those of version 2.0.

Also shown (in the gray boxes) are the driving routes of the MX-DOAS observations. The red box is used for emission estimation from the OMI data. The related wind arrows are also shown in the figure 6.27, the transport of the NO_2 plume by the wind can be well seen. The difference between OMI satellite product version 1.0.2 and version 2.0 can be also seen in figure 6.28. However the differences are smaller than in figure 6.27.

For July 21 (figure 6.29), there is only one version of OMI data (v1.0.2) available. The NO_2 plume is widely distributed. High values are found up to more than 100 km in north direction.

Because of the difference of the tropospheric NO_2 vertical column densities between both

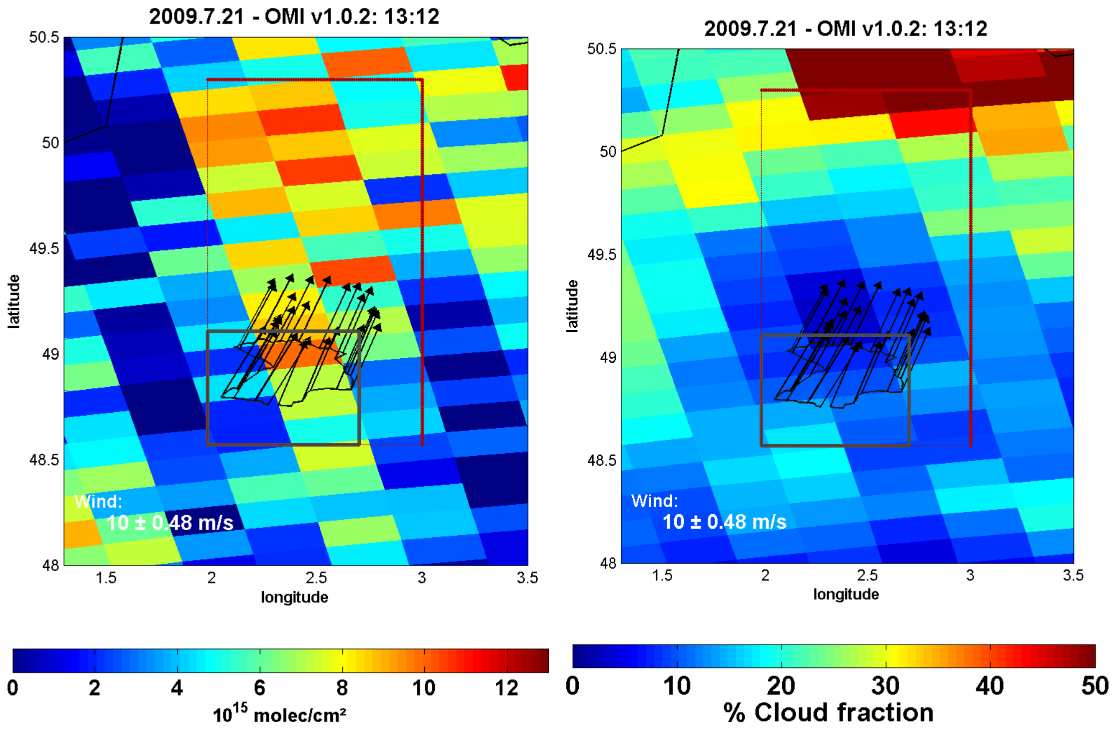

a) The TVCDs from OMI satellite version 1.0.2 b) The cloud fraction from version 1.0.2

Figure 6.29: The comparison of tropospheric NO_2 VCDs from MAX-DOAS with a version of OMI data for July 21, 2009 (left). The related cloud fraction (right) and wind vectors are shown. The red boxes are selected areas for the estimation of emission from OMI data.

OMI versions, the estimated emissions are not the same for every day by using the equation 6.1.

For July 16, we obtained $6.51 \times 10^{25} molec/cm^2$ for version 1.0.2 and $4.52 \times 10^{25} molec/cm^2$ by using version 2.0.

In figure 6.30, a comparison of emissions obtained from mobile MAX-DOAS, the two versions of OMI and the CHIMERE model data for three days during summer 2009 is shown.

There are some more days with good OMI satellite coverage. However on these days, the NO_2 plume from Paris was not well defined. Thus no emission estimations from OMI were possible.

The obtained emissions from OMI are in good agreement with the estimated emissions from mobile MAX-DOAS and CHIMERE model.

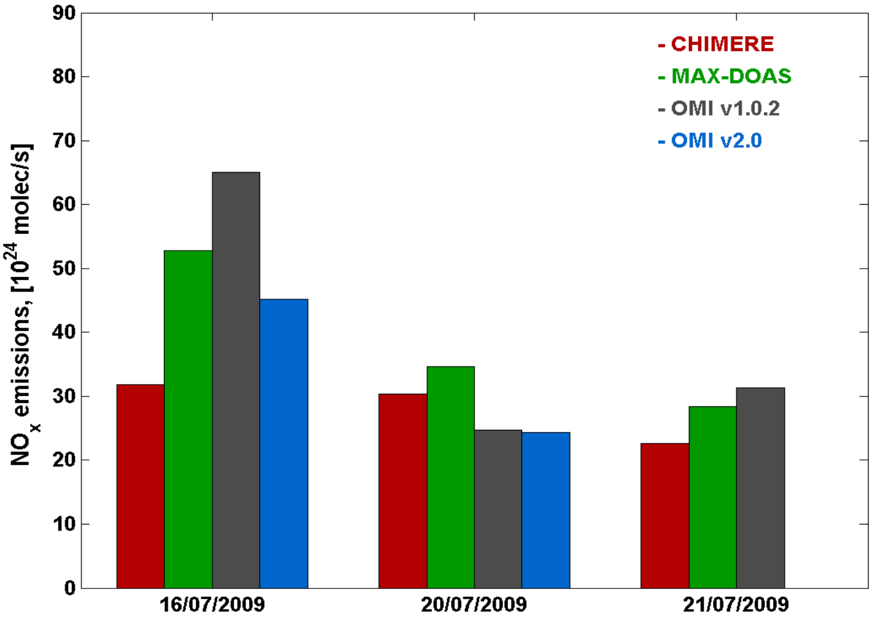

Figure 6.30: Comparison of NO_x emissions between the CHIMERE model data, mobile MAX-DOAS and the two versions of OMI.

6.5.2 Validation of OMI satellite observations by mobile MAX-DOAS measurements

Validation of tropospheric trace gas products from satellite observations is a challenging task for several reasons. First, since satellites measure the vertically integrated tropospheric column density, observations of in-situ surface concentrations can not be directly used for validation purposes. Even if vertical profiles are available from aircraft measurements (Heland *et al.* , 2002) or balloon soundings (Sluis *et al.* , 2010), they are often not representative for the whole spatial extent of the satellite ground pixel, which is typically of the order of several hundreds of km^2 or more. Similar arguments hold for observations of the integrated tropospheric column measurements e.g. from MAX-DOAS observations at fixed locations (Brinksma *et al.* , 2008). Here it is important to note that close to strong emission sources like megacities, where the validation of tropospheric satellite products is of highest importance, the largest variability and strongest gradients are typically found (Chen *et al.* , 2009).
Information about the spatial variability across a satellite ground pixel can be obtained from mobile measurements like mobile MAX-DOAS observations (e.g. (Volkamer *et al.* , 2006); (Wagner *et al.* , 2010)), thus we also use the tropospheric NO_2 VCDs obtained during our measurement campaigns in Paris for the validation of the simultaneous observations of the tropospheric NO_2 VCDs from the OMI instrument.

We selected OMI satellite observations (Levelt & Noordhoek, 2002), because the ground pixel sizes are much smaller ($13 \times 26 km^2$ in nadir geometry) compared to observations from SCIAMACHY and GOME-2. One important aspect of tropospheric satellite observations is the use of a-priori information on the (relative) trace gas profile. For the DOMINO tropo-

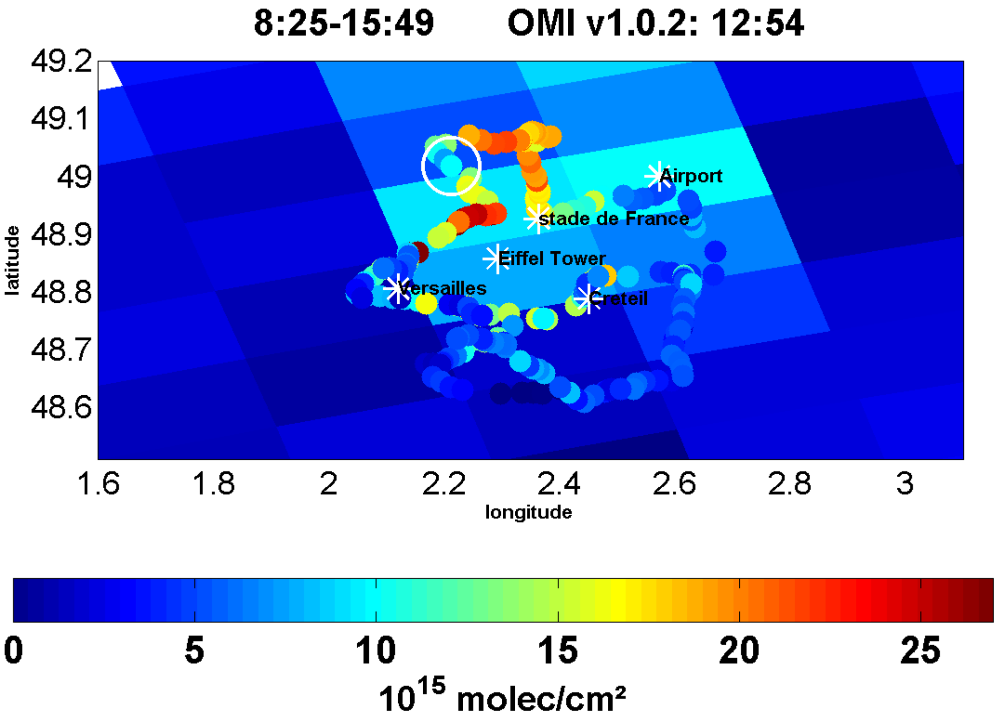

a) OMI data, version 1.0.2.

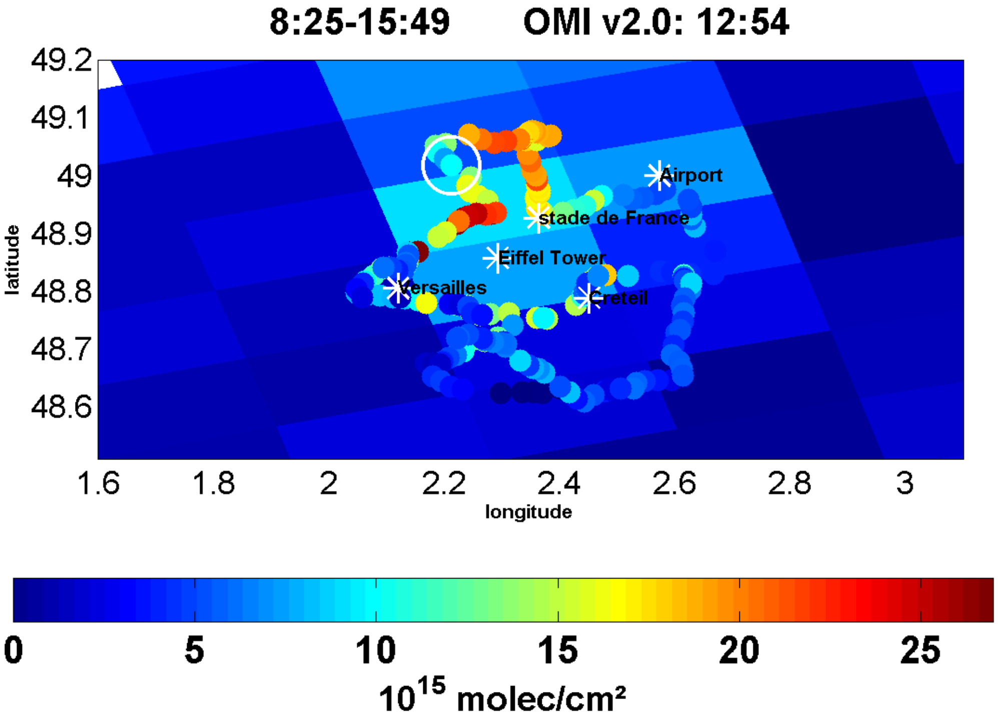

b) OMI data, version 2.0.

Figure 6.31: The comparison of OMI satellite data to mobile MAX-DOAS for July 16, 2009.

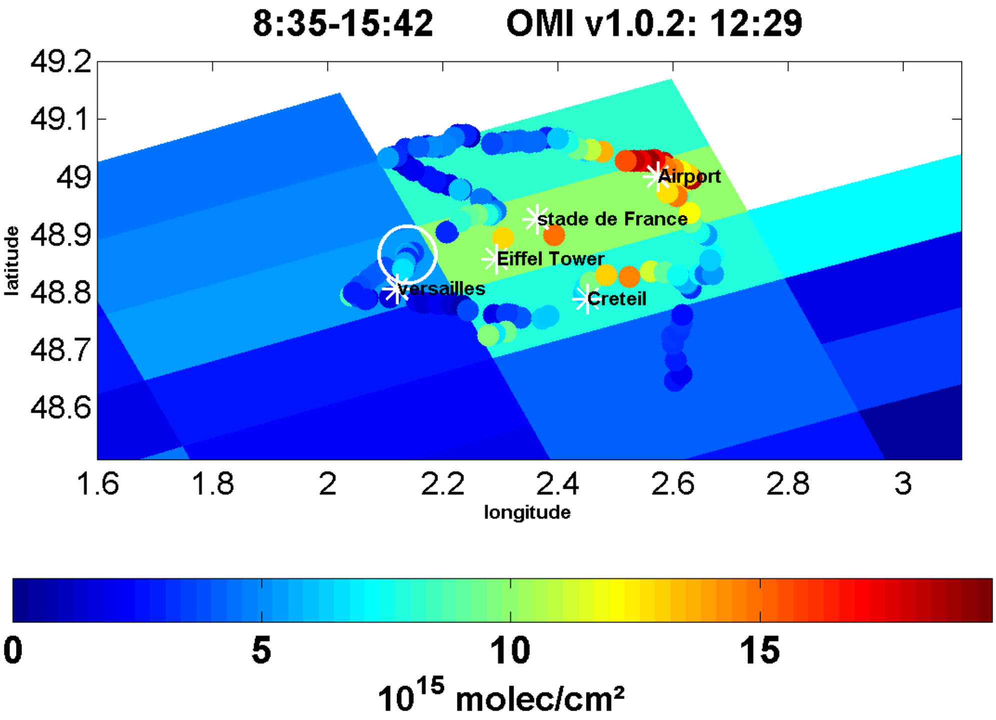

a) OMI version 1.0.2.

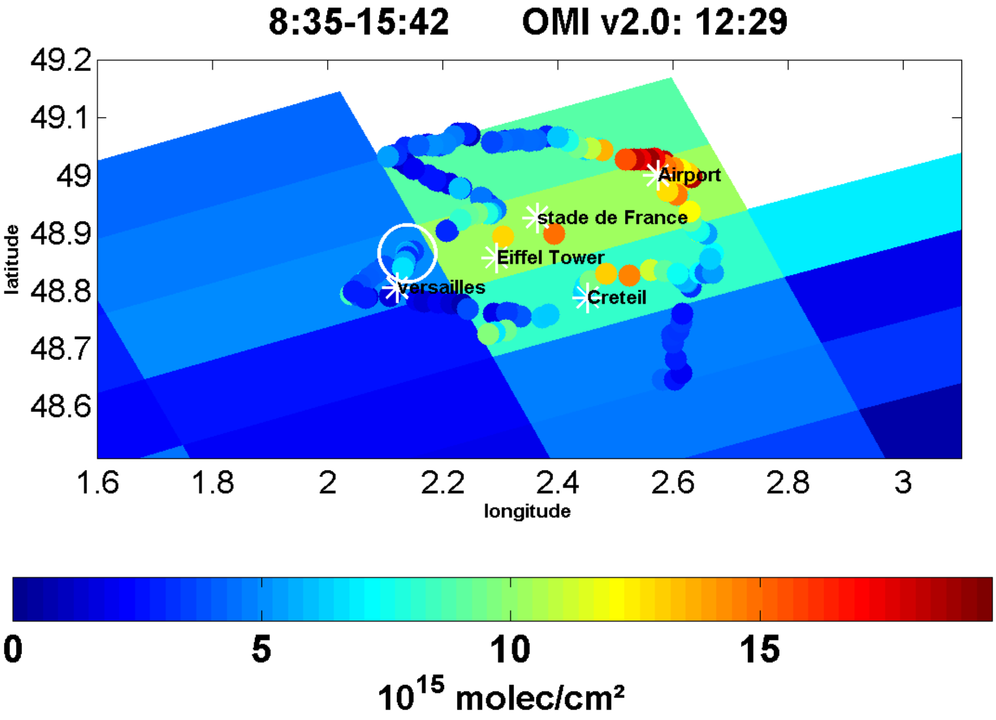

b) OMI version 2.0.

Figure 6.32: The comparison of OMI satellite data to mobile MAX-DOAS for July 20, 2009.

spheric NO_2 product from OMI observations profile data from model simulations (TM4) are used for that purpose (Boersma *et al.* , 2007). The specific choice of the NO_2 profile has a strong effect on the retrieved NO_2 VCD, since the sensitivity of the satellite observations strongly depends on altitude (Boersma *et al.* , 2011).

In figure 6.31, the NO_2 tropospheric vertical column densities from mobile MAX-DOAS (the colored circles) are compared to the OMI satellite data (background) for July 16, 2009. In part a is the OMI satellite data from version 1.0.2, whereas we used version 2.0 of OMI data in part b. The white circle indicates the location of the MAX-DOAS measurements during the overpass time, here 12:54 (UTC time).

For July 20, 2009, the comparison of nitrogen dioxide from OMI observations to mobile MAX-DOAS is shown in figure 6.32. Again, the white circle indicates the location of the MAX-DOAS measurements during the overpass time of OMI (12:29).
In figure 6.32, there are some missing pixels from OMI data due to clouds.

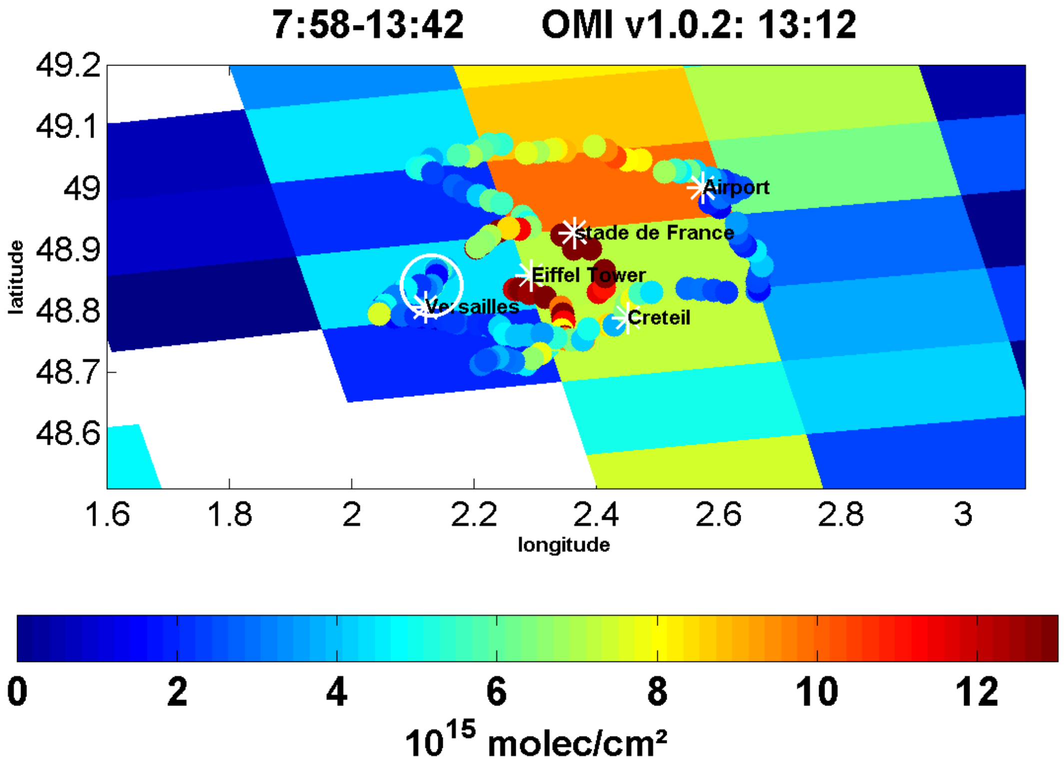

Figure 6.33: The tropospheric vertical column densities comparison from OMI satellite data (version 1.0.2) to mobile MAX-DOAS for July 21, 2009.

For July 21, 2009, only OMI version 1.0.2 is available (figure 6.33).
The overpass of OMI coincides with MAX-DOAS observations at the Château de Versailles (the white circle in the figure 6.33). The high values in the center are from measurements in

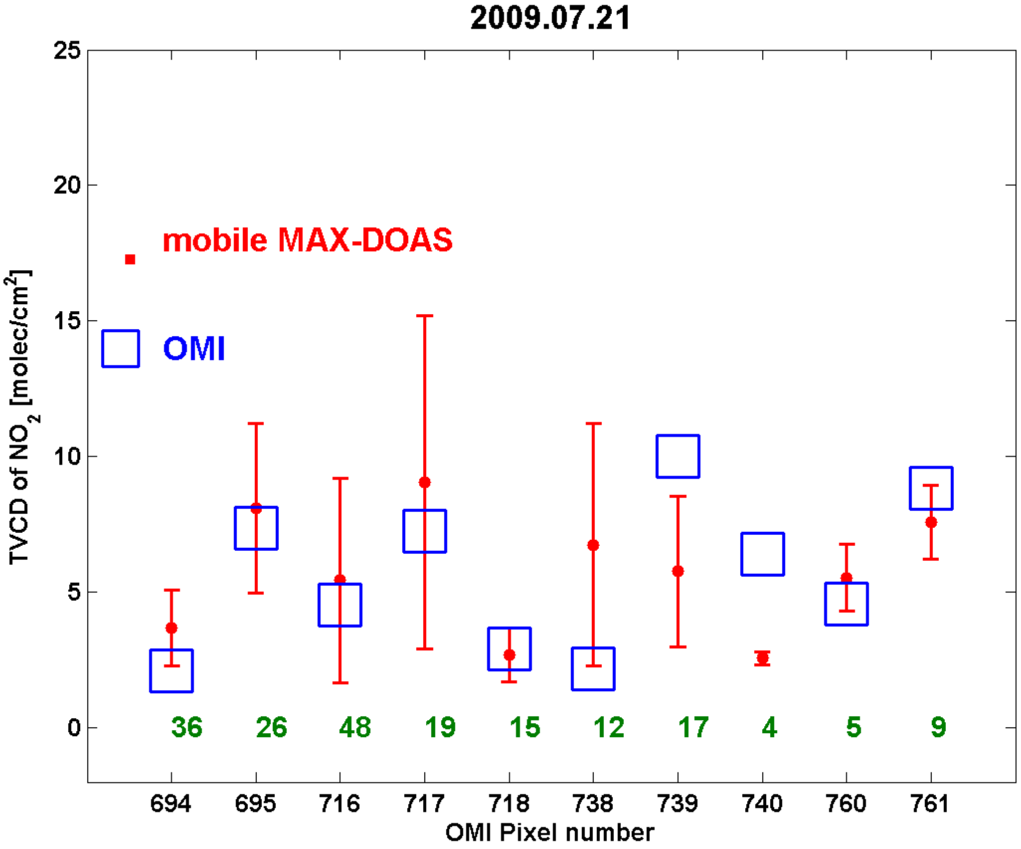

Figure 6.34: Comparison of the NO_2 VCD from OMI for individual pixels with average values of mobile MAX-DOAS within the pixel. The green numbers show the numbers of MAX-DOAS measurements. The numbers at the x-axis indicate the pixel number of the OMI data. The error bars present the standard deviation of the mobile MAX-DOAS.

the early morning.

In figure 6.34, tropospheric vertical column densities of NO_2 from OMI are compared to the average TVCDs of NO_2 from mobile MAX-DOAS within the individual OMI pixels for July 21, 2009. The green numbers show the number of measurements per OMI-pixel. The error bars represent the standard deviation of mobile MAX-DOAS in the pixel, most values agree within the error bars.

In figure 6.35, we compared all existing OMI observations from version 2.0 to the related mobile MAX-DOAS VCDs. Because of snowy pixels, there are high errors for some of the winter data in figure 6.35 left.
To assure a meaningful comparison between mobile MAX-DOAS VCDs and OMI VCDs, several restrictions are applied.
1. Cloud fraction less than 30 %.
2. Number of mobile MAX-DOAS measurements per pixel more than 10.

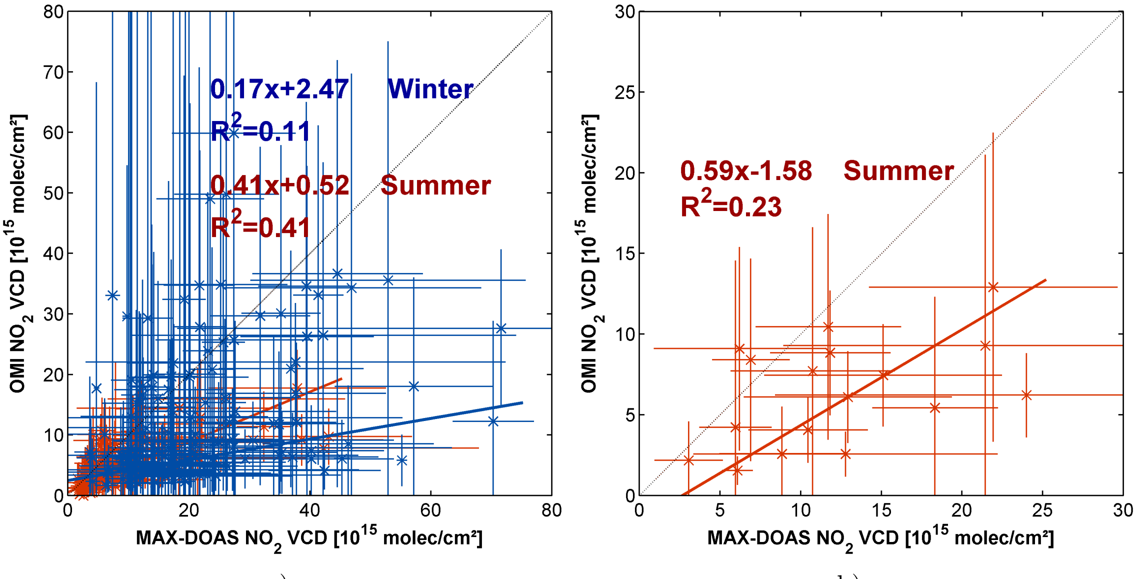

a) b)

Figure 6.35: The correlation of OMI satellite vertical column densities (version 2.0) to mobile MAX-DOAS VCDs, for all days in summer and winter. Left: correlation for all OMI pixels. Right: correlation for a subset of OMI pixels by using the restrictions, described in the text.

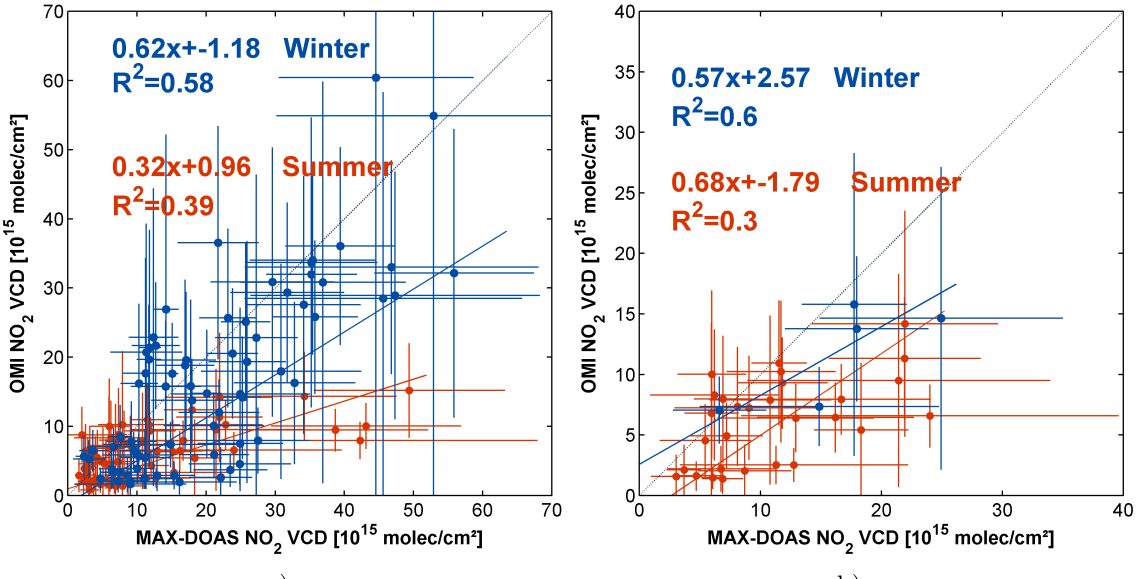

a) b)

Figure 6.36: The correlation of OMI satellite vertical column densities (version 1.0.2) to mobile MAX-DOAS VCDs, for all days in summer and winter. Left: correlation for all OMI pixels. Right: correlation for a subset of OMI pixels by using the restrictions, described in the text.

3. Coverage of OMI pixel in east west direction by mobile MAX-DOAS > 35 %.
4. OMI pixels without snow and ice are used.

The right figure 6.35 shows the resulting correlation using these conditions. For summer, we obtained a worse correlation but a higher slope, while for winter no observations fulfilled these conditions.

This study is made also with the OMI vertical column densities, version 1.0.2. The figure 6.36 left shows the correlation without any conditions, whereas the right one is with the mentioned restrictions. Again, we found a smaller correlation but a slope closer to unity for the summer data. For the winter data, only 5 points remained but without a big change in slope and correlation.

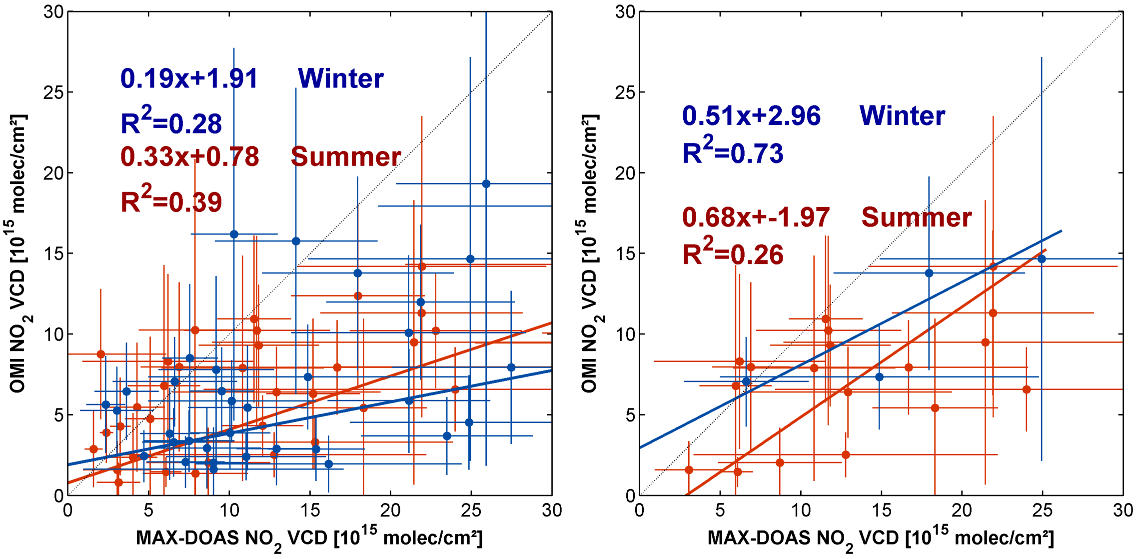

a) b)

Figure 6.37: Correlation analyses between OMI satellite vertical column densities (version 1.0.2) to mobile MAX-DOAS VCDs. In contrast to figure 6.36, only OMI observations were used, for also version 2.0 data were available. Left: correlation for all OMI pixels. Right: correlation for a subset of OMI pixels by using the restrictions, described in the text.

In figure 6.37, the correlations between mobile MAX-DOAS VCDs to OMI VCDs version 1.0.2 are shown. In contrast to figure 6.36, only OMI observations were used, for also version 2.0 data were available. The correlation of 0.39 (left) without restrictions is equal to the summer correlation in figure 6.36, but the winter correlation is much lower than the correlation in figure 6.36. In part b, we applied the conditions, described before. Again we found a worse correlation (but same slope) as in figure 6.36b for summer, but a comprehensive improvement for winter with a correlation of 0.73.

Figure 6.38 shows the same data as figure 6.35, but now only data are shown, for which also

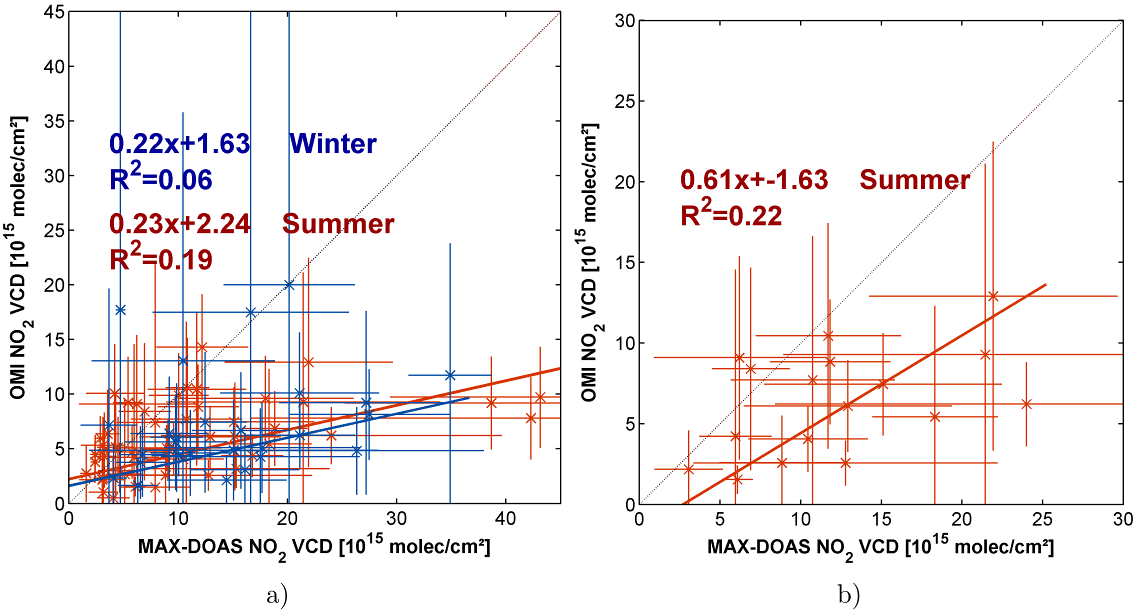

a) b)

Figure 6.38: Second case of correlation between OMI satellite vertical column densities (version 2.0) to mobile MAX-DOAS VCDs. In contrast to figure 6.35, only OMI observations were used, for also version 1.0.2 data were available. Left: correlation for all OMI pixels. Right: correlation for a subset of OMI pixels by using the restrictions, described in the text.

version 1.0.2 data exist. For all data (left) worse correlation compared to figure 6.35 is found for summer and winter. In part b, we applied the conditions described before. We obtained a slight improvement for summer, but no data remains for winter as before for version 2.0.

In the next step, additional restrictions are applied:
1. Cloud fraction less than 30 %.
2. Number of measurements per pixel more than 30.
3. Coverage of OMI pixel in east west direction more than 60 %.
4. Standard deviation of MAX-DOAS VCDs less than 5×10^{15} $molec/cm^2$.
5. OMI pixels without snow and ice are used.

In figure 6.39, the correlation between mobile MAX-DOAS and OMI VCDs with the additional restrictions are shown. All results are very similar.

Generally, high correlations and slopes close to unity are found. For winter, because of weather conditions, no data remain.

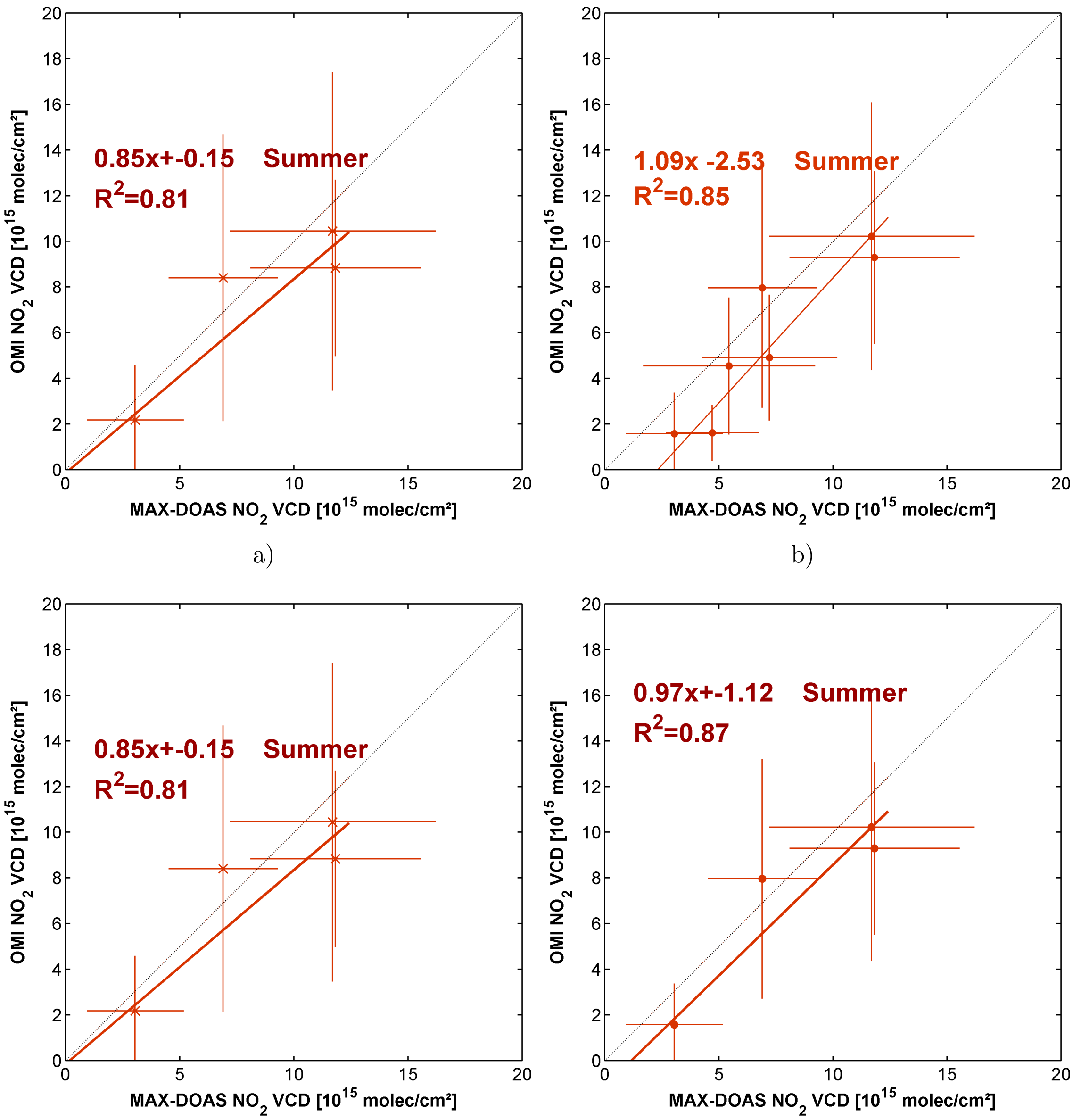

a) b)

c) d)

Figure 6.39: Correlation analyses between MAX-DOAS and OMI VCDs with additional restrictions. a) OMI VCDs version 2.0 with all existing days. b) OMI VCDs version 1.0.2 with all existing days. c) OMI VCDs version 2.0, if version 1.0.2 data are available. d) OMI VCDs version 1.0.2, if version 2.0 data are available.

6.6 Formaldehyde Results

Formaldehyde is an important pollutant in the troposphere and plays a significant role in air quality. Formaldehyde can be directly emitted or formed in the atmosphere as secondary product by photochemical oxidation of reactive volatile in polluted areas.

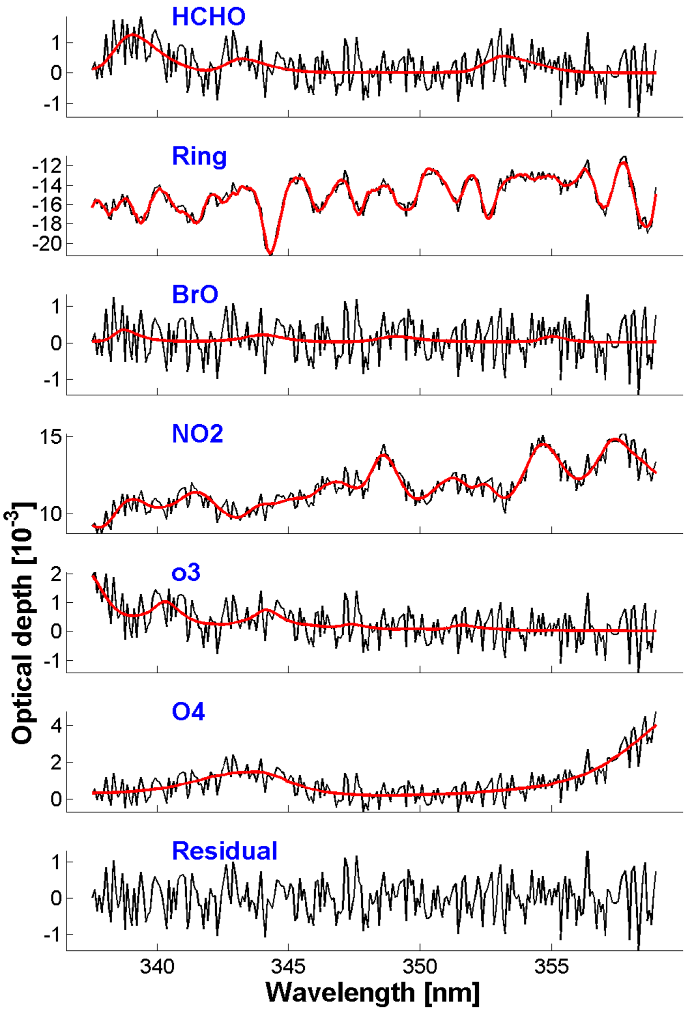

Figure 6.40: An example of the HCHO analysis from July 16, 2009, at 12:22 (UTC time). Shown are the fitted trace gas cross sections (red) scaled by the respective absorption of the measured spectrum (black).

From the mobile MAX-DOAS observations in Paris, also formaldehyde can be obtained. . The evaluation of Formaldehyde with closest reference (using more than one Fraunhofer reference for one day) to the spectrum was performed for the fit-window: 337.5-359 nm. Three absorption peaks of HCHO exist in this selected fit-range. The following trace gas absorption cross sections are included in the fit:. HCHO at 298 K (Meller & Moortgat, 2000), NO_2 at 294 K (Vandaele *et al.* , 1998), O_3 at 241 K (Bogumil *et al.* , 2003), O_4 (Greenblatt *et al.* , 1990), BrO at 228 K (Wilmouth *et al.* , 1999), as well as a Fraunhofer reference spectrum determined from averaging of every preceding and following zenith measurements, and Ring spectrum calculated from the averaged Fraunhofer reference. A polynomial of third order was included in the fitting procedure. The measured spectrum was allowed to be shifted against the reference spectrum. A gap was inserted in the fitting interval from 354.8 nm to 355.0 nm. The wavelength calibration was performed based on a high resolution solar spectrum (Kurucz *et al.* , 1984).

A typical formaldehyde fit result is shown in figure 6.40 for July 16, 2009 at 12:22 (UTC time) with an elevation angle of 22°.

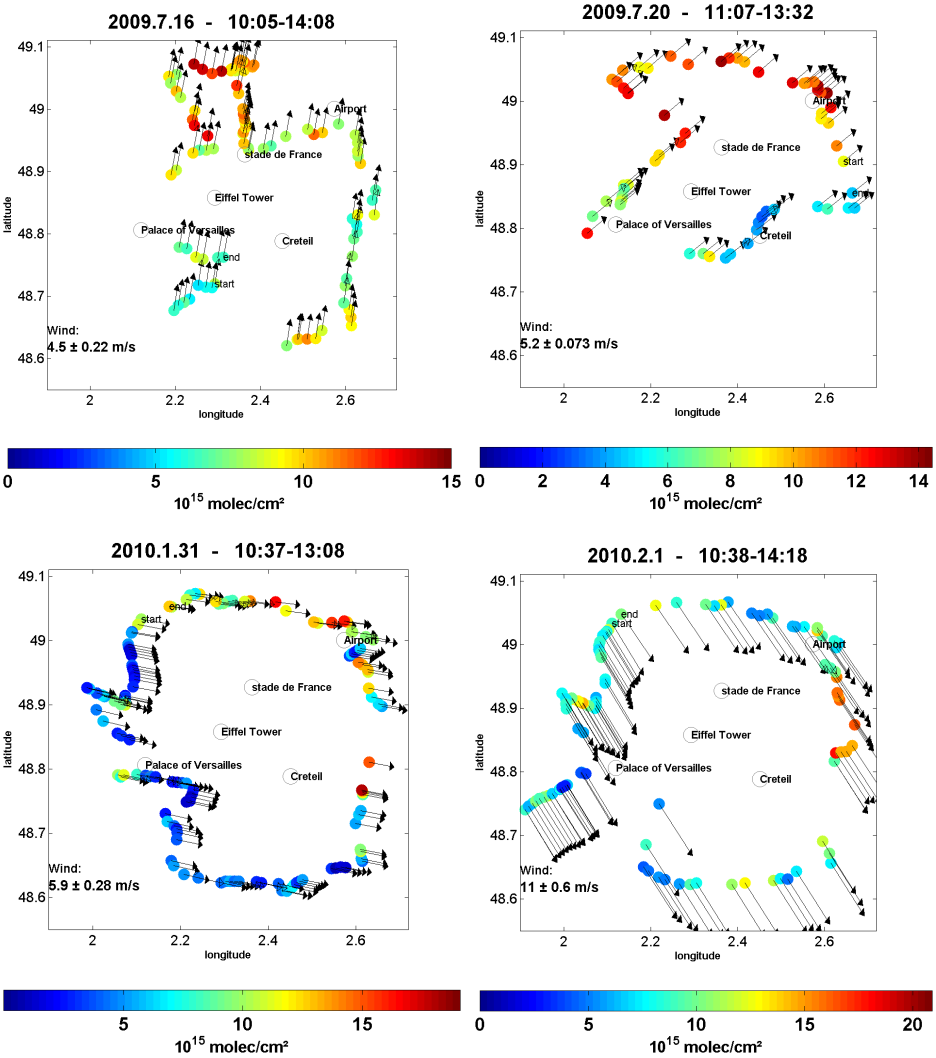

Figure 6.41: Tropospheric formaldehyde VCDs for different days with associated wind vectors, during summer and winter, Paris.

We consider here only the spectra with 22° elevation angles. The results with RMS of the residuals larger than 1.5×10^{-3} are skipped.

The tropospheric VCD can be obtained from SCD (see section 3.2.4.3) using a geometric airmass factor (AMF). The observations from July 2009 and Winter 2010 with 22° elevation angles are applied to get the tropospheric vertical column densities in figure 6.41.
An offset was determined for the vertical column density (see equation 3.27).

Generally, the high values of HCHO were found at the lee sides of the city for several days, as expected, but the high values are distributed over a larger area compared to NO_2.

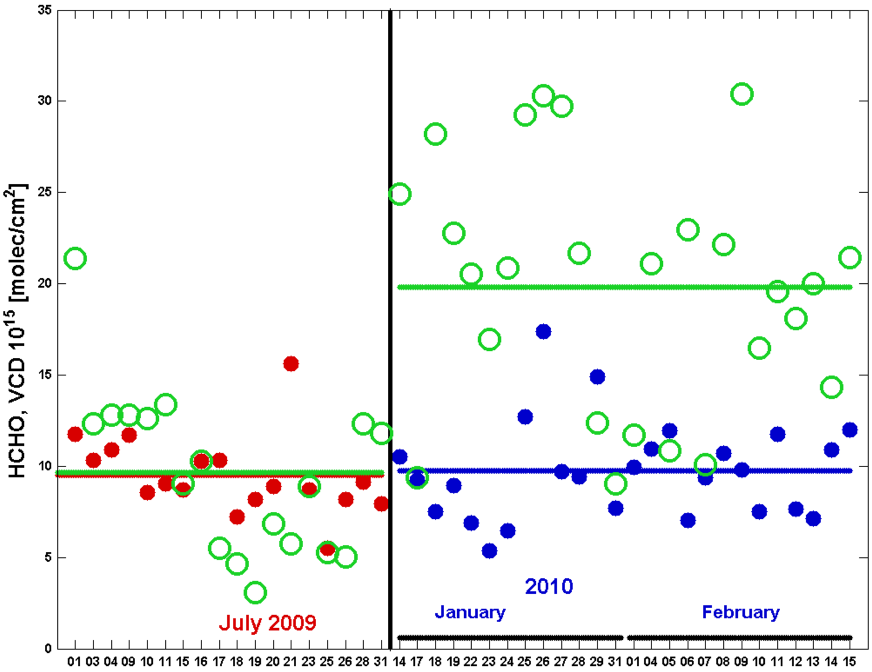

Figure 6.42: Daily averaged tropospheric formaldehyde VCDs (the red circles for summer and the blue circles for winter) and tropospheric NO_2 VCDs (green circles).

The daily averaged tropospheric formaldehyde vertical column densities are shown in figure 6.42 (the red circles for summer and the blue circles for winter). For these averaged values, all vertical column densities measured during the day are used. The green circles indicate the daily averaged tropospheric NO_2 VCDs. The colored lines are seasonal averages of the daily averages. Good agreement is found for summer data, whereas in winter NO_2 values are higher.

6.7 Summary

During two MEGAPOLI campaigns in Paris, we performed mobile MAX-DOAS measurements, which were conducted on orbits with different radii around Paris.

Total NO_x emissions from Paris were derived from mobile MAX-DOAS observations, which were compared to the emissions, obtained from OMI satellite observations. Only three days of OMI observations in summer could fulfill the conditions for the estimation of emissions, which are almost in the same range as the MAX-DOAS emissions, but bad statistic of OMI data in winter avoided the estimation of emissions.

The obtained emissions from mobile MAX-DOAS are season-dependent, the emissions for winter are 145 % higher. Also the CHIMERE model was used in this study. The derived emissions from CHIMERE for summer are only 17 % less than emissions derived from mobile MAX-DOAS, but the difference of emissions is 45 % for winter. The EDGAR inventory is almost as large as the input emissions in winter, while it is higher than the other emissions in summer.

The NO_2 vertical column densities from mobile MAX-DOAS and CHIMERE were also compared. The VCDs are in summer very similar, but in winter the NO_2 VCDs from mobile MAX-DOAS are 35% higher.

The mobile MAX-DOAS vertical column densities were compared to OMI satellite observations. There were two different versions of OMI VCDs. For summer, good agreement between the VCDs from mobile MAX-DOAS and OMI was found, whereas a bad statistic in winter avoided a meaningful comparison.

7 CINDI Campaign in 2009

During summer 2009, many different instruments (in-situ and remote sensing) participated in the Cabauw intercomparison campaign for nitrogen dioxide measuring instruments (CINDI). The campaign took place at KNMI's Cabauw meteorological observatory, a semi rural site for atmospheric research in the Netherlands, 30 km south of Utrecht. The coordinats are latitude: 51.97°N, longitude: 4.963°E at sea level. The main purpose was to intercompare a broad range of NO_2 measuring instruments, which can be applied to validate the tropospheric NO_2 column measurement from satellites. The focus was on the assessment of tropospheric NO_2 column and profile measurements using the DOAS and MAX-DOAS techniques (Van Roozendael *et al.* , 2010). In addition, some other trace gases were measured: HCHO, CHOCHO, Ozone, O_4, BrO and aerosols.
An adequate overview of the campaign and some of results are published in Piters *et al.* (2011), Roscoe *et al.* (2010) and Zieger *et al.* (2011).

The campaign focused on 2 different tasks. The first one was to determine the accuracy of ground-based NO_2 measurement techniques, to test these techniques under different atmospheric conditions, and second for validation of global satellite data retrievals.
The weather in Cabauw was usually warm and sunny during June and July 2009.

The campaign was divided in to two periods: 1. Running the instruments from June 8 to July 8 with an extensive intercomparison campaign. 2. From July 9 to July 26, the measurements were extended to different viewing geometries at different locations, for investigating the spatial variability on the scale of a typical satellite ground pixel over the measurement site (Piters *et al.* , 2011).

The participating instruments with their properties are listed in table 7.1.
We contributed with two mini MAX-DOAS instruments. The stationary one had a wavelength range 310-461 nm (included in the table 7.1). It was mounted on the first level at 20 m altitude above the ground of the Cabauw tower (213 m). The second instrument was a mini MAX-DOAS mounted on a car for mobile MAX-DOAS observations with a wavelength range 320-460 nm, which is not included in the table 7.1 (see section 9.1).

Table 7.1: Characteristics of the instruments taking part in the intercomparison campaign (Roscoe *et al.* , 2010)

Instrument	observed wavelengths (nm)	width of spectral response (nm FWHM)	field of view ° FWHM	detector type	cooled or not	fibre or not
BIRA-Vis	400 to 700	0.95	0.8	2-D CCD	yes	yes
Bremen-Vis	400 to 573	0.8	1.1	2-D CCD	yes	yes
CNRS-SAOZ[a,b]	270 to 630	1.2	h	1-D MMOS	no	no
CNRS-mobile[a]	270 to 630	1.5	h	1-D MMOS	no	no
CNRS-mini[a,c]	270 to 800	0.7	h	2-D CCD	no	yes
Heidelberg1[b]	290 to 789	0.9	0.9	1-D CCD	yes	yes
INTA-NEVA2	387 to 514	0.6	1.0	2-D CCD	yes	yes
INTA-RASAS2	393 to 510	0.45	1.0	2-D CCD	yes	yes
JAMSTEC	223 to 558	0.7	0.9	1-D CCD	no	yes
KNMI-2	400 to 600	0.9	0.4	1-D CCD	yes	yes
Leicester[e]	425 to 490	0.54	1.0	2-D CCD	yes	yes
MPI-Mainz[c]	310 to 461	0.55 to 0.87	1.2	1-D CCD	yes	yes
NASA	269 to 532	0.6	1.6	2-D CCD	no	yes
NIWA	389 to 510	0.48	0.5	2-D CCD	yes	yes
Toronto[a]	340 to 550[d]	0.5 to 2.5[d]	2.0	2-D CCD	yes	yes
Washington[f]	282 to 498	0.83	1.0v	2-D CCD	yes	*no*[g]
BIRA-UV	300 to 388	0.37	0.8	2-D CCD	yes	yes
BIRA-mini[c]	290 to 434	0.7	0.6	1-D CCD	no	yes
Bremen-UV	315 to 384	0.37	1.1	2-D CCD	yes	yes
Heidelberg2[b]	320 to 463	0.45	0.9	2-D CCD	yes	yes
GIST-Korea	290 to 430	0.7	0.5	1-D CCD	yes	yes
KNMI−1[c]	290 to 433	0.7	0.4	1-D CCD	yes	yes

[a]zenith only, [b] at the wind profiler site, [c] mounted on the tower, [d] changed on 30 June to 315 to 380 nm and 0.2 to 0.8 nm, for MAX-DOAS measurements in the UV, [e] a joint product with Leeds, who supplied the telescope and important on-site assistance, [f] Washington State University(WSU), [g] no fibre, but using a wedge depolariser, v in the vertical direction, less in the horizontal, [h] FOV not relevant as zenith sky only.

7.1 MPI Instrumental setup

The Mini-MAX-DOAS instrument is a fully automated, light weighted spectrometer ($13cm \times 19cm \times 14cm$) designed for the spectral analysis of scattered sunlight (Bobrowski *et al.* , 2003). It consists of a sealed aluminium box containing the entrance optics, a fibre coupled spectrograph and the controlling electronics. A stepper motor mounted outside the box rotates the whole instrument to control the elevation of the viewing angle (angle between the horizontal and the viewing direction). The entrance optics consists of a quartz lens of focal length f = 40 mm coupled to a quartz fibre bundle which leads the collected light into the spectrograph (field of view is 1.2°). The light is dispersed by a crossed Czerny-Turner spectrometer (USB2000, Ocean Optics Inc.) with a spectral resolution of 0.7 nm over a spectral range from 310 - 461nm. A one-dimensional CCD (Sony ILX511, 2048 individual pixels) is used as detector. Before the signal is transferred to the 12 bit analog to digital converter, an electronic offset is added. After conversion, the signal is digitally transmitted to a PC via a USB cable.

Figure 7.1: Left (top): the Cabauw site is located near Lopik in The Netherlands, in SW of Utrecht. Right (top): The Cabauw meteorological site has a tower, where the MPI instrument was located. Left (down): The Tower. Right (down): MPI mini MAX-DOAS with other mini MAX-DOAS instruments from BIRA and KNMI.

7.2 MAX-DOAS Measurements in Cabauw

Different MAX-DOAS instruments with various designs were installed at the Cabauw site. For the intercomparison and intercalibration, they required to have the same setting for the instruments.
All instruments were oriented to an azimuth of 287° (North-West). The MPI Mainz MAX-DOAS used the following elevation angles, -20°, -5°, -0.5°, 0°, 2°, 4°, 6°, 8°, 10°, 15°, 30°, 85°. Observations at negative elevation angles were used for Target DOAS. Instead of 90° (zenith), we used 85°, because we could not have free view at 90° elevation angle. The start of our measurements was June 8, 2009 with an integration time of 1 minute. The MiniMax Doas Measurements Software (version 2.0) [Udo Frieß 2007] was used for the stationary measurements.
The measured spectra are analyzed using the DOAS method (Platt & Stutz, 2008), and using the WinDOAS software (Fayt & Van Roozendael, 2001). All groups used the same trace gas cross sections. The Fraunhofer reference spectra were measured at local noon time.

7.2.1 NO_2 Results

For the NO_2 analysis, a wavelength range of 420-450 nm was selected. Several trace gas absorption cross sections (NO_2 at 295 K (Vandaele *et al.* , 1996), H_2O at 298 K (Rothman *et al.* , 2005), Glyoxal at 296 K (Volkamer *et al.* , 2005), O_3 at 243 K (Bogumil *et al.* , 2003), O_4 at 296 K (Hermans *et al.* , 1999) as well as a Fraunhofer reference spectrum (at noon time, daily), a Ring spectrum (calculated from the Fraunhofer spectrum) and a polynomial of third order) were included in the spectral fitting process, using the WinDOAS software (Fayt & Van Roozendael, 2001). The wavelength calibration was performed based on high resolution solar spectrum (Kurucz *et al.* , 1984).

The integrated trace gas concentration along the light path through the atmosphere, the so called slant column density (SCD) is the output of the WinDOAS software. From the spectral analysis, also the uncertainty of the retrieved SCD is determined, which for the NO_2 analysis is typically smaller than 15 %.
A semi-blind intercomparison was performed during 2 weeks in June.

In figure 7.2 selected comparison results for 4° elevation angle are shown. Very good agreement between the different instruments is found. A similar comparison for 15° elevation angle is shown in fig 7.3. Note that the slight understimation by the Mainz instrument is caused by the choice of the Fraunhofer reference spectrum.

The DSCDs from lower elevation angles are higher, (see figures 7.2 and 7.3).

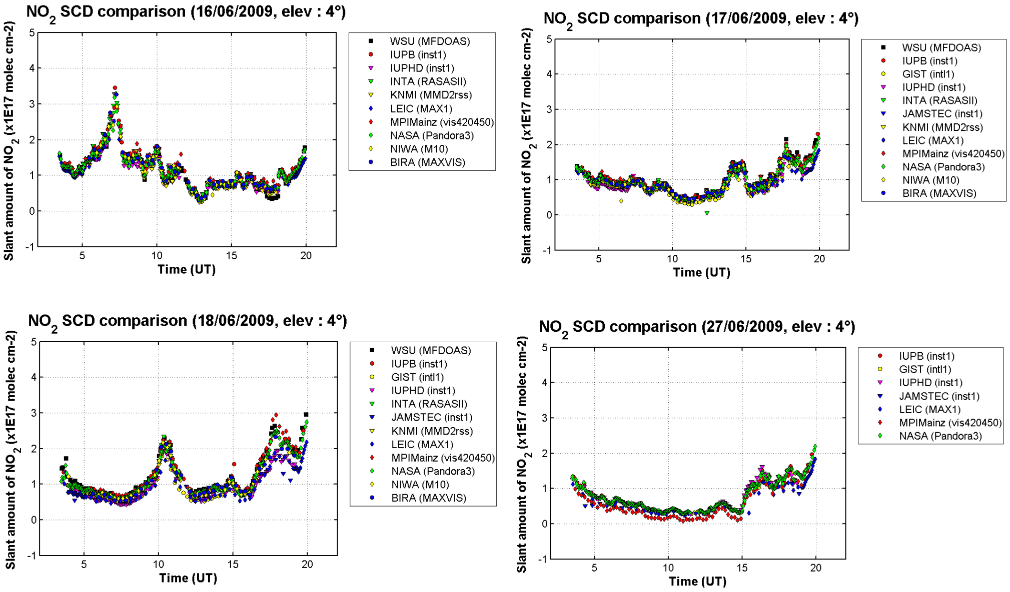

Figure 7.2: The comparison of NO_2 DSCDs from June 2009 for 4° elevation angles. [Ref: BBC.knmi.nl, by: Caroline Fayt.]

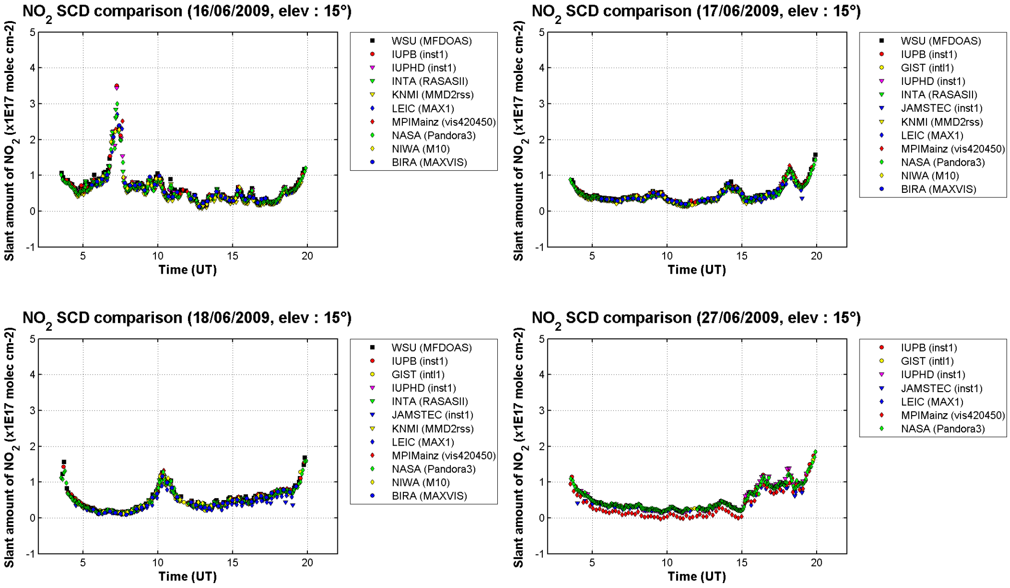

Figure 7.3: The comparison of NO_2 DSCDs from June 2009 for 15° elevation angles. [Ref: BBC.knmi.nl, by: Caroline Fayt.]

In figure 7.4, all elevation angles from 2° to 85° (instead 90°) are shown, these DSCDs are obtained from the MPI mini MAX-DOAS instrument.

The high values for the of lower elevation angles on June 18 indicate emissions from local sources, especially after 16:00 (UTC).

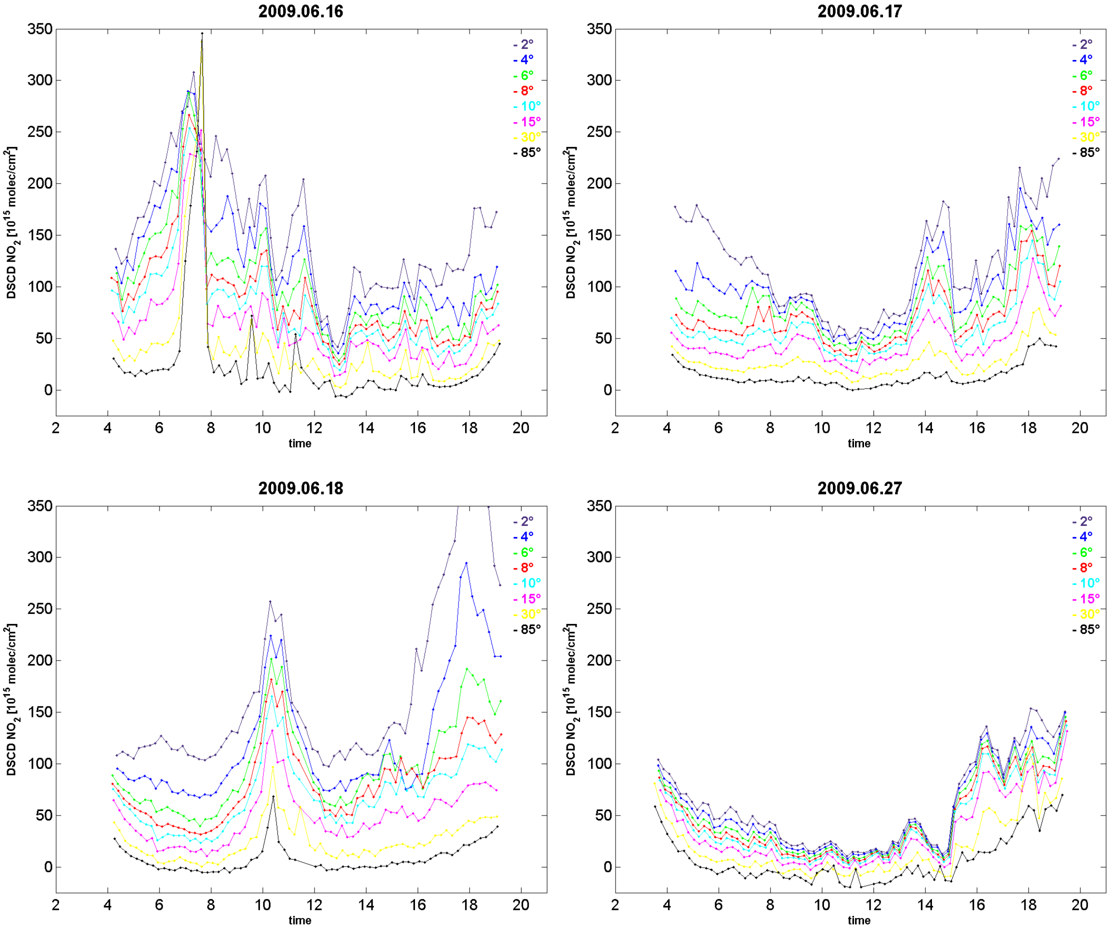

Figure 7.4: The NO_2 DSCDs from June 2009 for different elevation angles from the MPI-Mainz instrument.

Tropospheric vertical column densities were determined first by using geometric air mass factors. For elevation angles of 15° (red) and 30° (blue), the vertical column densities are determined, which are shown in figure 7.5. Tropospheric vertical column densities are calculated from equation 3.24. The values in blue are obtained from 30° elevation angle and obviously higher compared to those from 15° (see figure 7.5).

In addition, vertical column densities (in figure 7.6) are determined from a full profile retrieval.

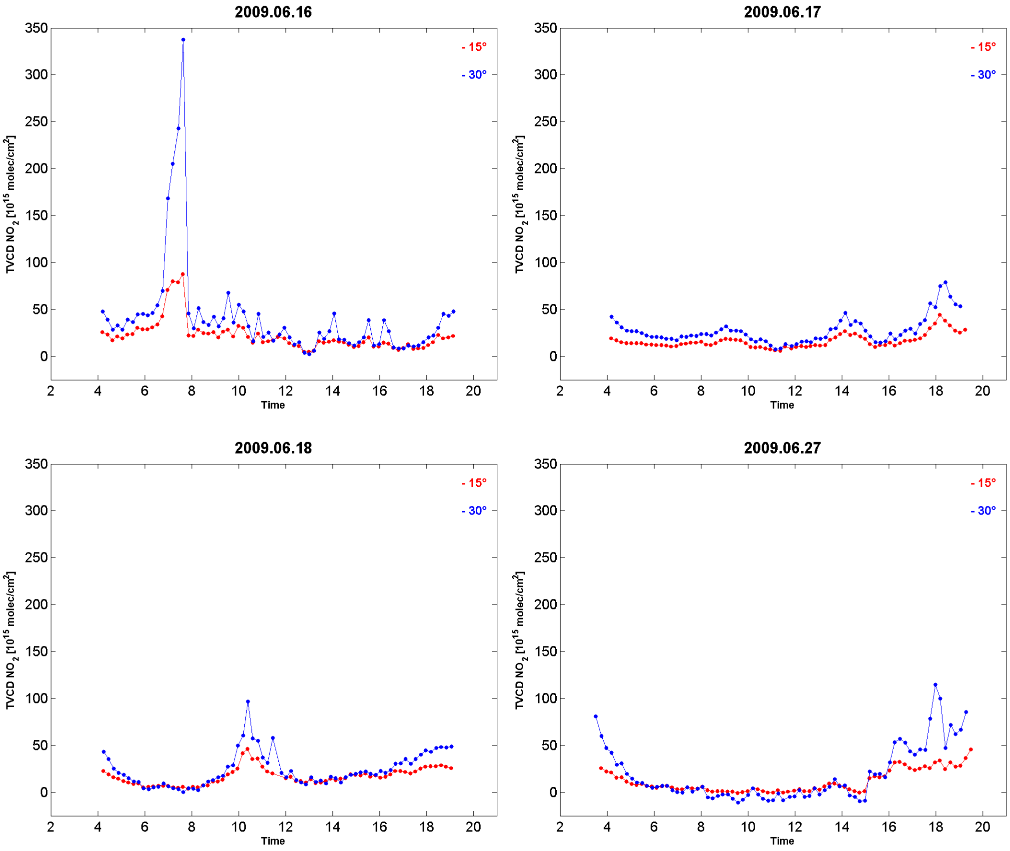

Figure 7.5: The VCD of NO_2 for four days in June 2009 for 15° and 30° elevation angles from the MPI-Mainz instrument by using a geometric airmass factor.

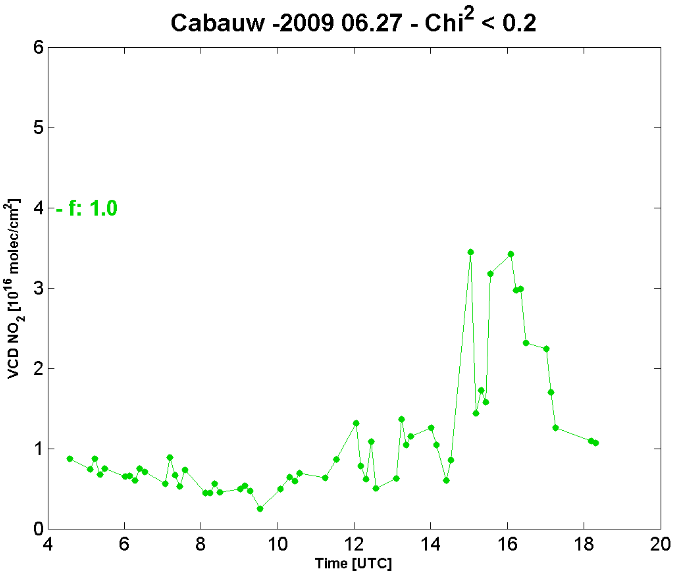

Figure 7.6: The TVCD of NO_2, obtained from a full profile retrieval.

7.2.2 Formaldehyde Results

This section focuses on formaldehyde results from mini MAX-DOAS instruments during the Cabauw-campaign. From the observed spectra also formaldehyde can be analyzed. Nine different instruments (groups) participated in this formaldehyde evaluation.

For the formaldehyde analysis, only the spectra are considered with SZA less than 75°. The fitting interval of formaldehyde is from 336.5 nm to 359 nm. Several cross sections were used: HCHO at 293 K (Meller & Moortgat, 2000), O_3 at 223 K (Bogumil *et al.* , 2003) and 243 K, I_0-corrected, NO_2 at 220°K (Vandaele *et al.* , 1998), BrO at 223 K (Fleischmann *et al.* , 2004), O_4 (Hermans *et al.* , 1999), as well as a Fraunhofer reference spectrum, a Ring spectrum (calculated from the Fraunhofer spectrum) and a polynomial of third order).

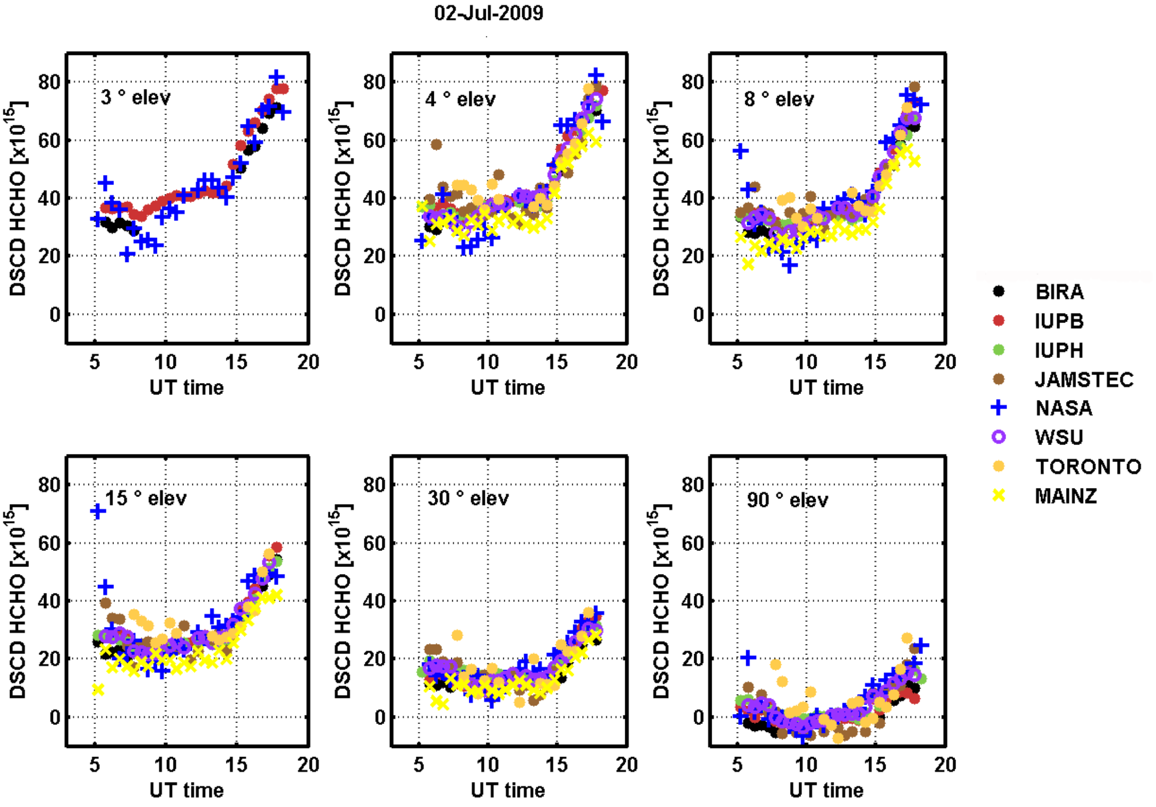

Figure 7.7: Diurnal evolution the HCHO DSCD measured on July 2, 2009 and averaged in bins of 30-minutes duration, for the different instruments involved in the inter-comparison. Units are $\frac{molec}{cm^2}$. (Pinardi *et al.* , 2012)

In figure 7.7, the slant column densities of formaldehyde are shown from different instruments with different elevation angles for July 2, 2009. In general good agreement is found between the different instruments (see also Pinardi *et al.* (2012)). At this day (July 2), all instruments could work, and the obtained formaldehyde DSCDs had a smooth variation over time. As expected higher DSCDs were found for low elevation angles.

8 MAX-DOAS observation at Greater Noida

Delhi is the largest metropolis in India, with New Delhi as the Capital of the region Delhi. New Delhi is one of the megacities with a large number of cars and some power plants in the Delhi area. Greater Noida is located about 45 km at the southeast of New Delhi (see figure 8.1). It is a fast growing region, one of the largest industrial and education hubs of India.

From the satellite observations, the Delhi area is identified as an air pollution hot-spot (see an example for tropospheric NO_2 in figure 3.2). High concentrations of various trace gases and aerosols give us the motivation to perform MAX-DOAS measurements in India. The results of mobile MAX-DOAS observations are discussed in chapter 6 with the focus on the estimation of NO_x emissions from New Delhi. In this chapter, we focus on stationary measurements at Greater Noida by a second mini MAX-DOAS instrument. From these measurements several atmospheric trace gases like NO_2, HCHO, Glyoxal, HONO, SO_2 and O_4 can be retrieved. In this chapter, a short overview of the evaluation process and some results will be shown.

8.1 Stationary MAX-DOAS Measurements

At the end of 2010, we installed a mini MAX-DOAS instrument (see section 7.1) at Sharda university, Greater Noida (see figure 8.2).
The coordinates of the installed instrument are latitude: 28.472858°N, longitude: 77.481566°E, and about 200 m altitude from sea level. The instrument is looking with an Azimuth of 215° to the southwest.

The UV/Vis spectrometer observes scattered sunlight under different elevation angles between the horizon and zenith. From these observations different trace gases can be determined. From the MAX-DOAS observations, different trace gases in the atmosphere can be determined.

The mini MAX-DOAS instrument started to measure the scattered sun light from November 2010 and the instrument is still operational. The main purpose of the measurements is to assess impacts of air pollution on regional air quality. From our observations, information

Figure 8.1: Greater Noida is located at the southeast of New Delhi. Several power plants close to Delhi are also shown in this map.

Figure 8.2: The mini MAX-DOAS instrument mounted at a window side at Sharda university in Greater Noida.

about different trace gases and aerosols is received.

Different elevation angles are used: -1°, 0°, 2°, 4°, 6°, 8°, 10°, 15°, 30°, 90°. The total integration time is 60 seconds, and the wavelength range is 310-461 nm.
Because of some logistical problems, the measurements can not be performed continuously, which means, the instrument is turned off during night.

8.1.1 Retrieval

For the measured spectra at Sharda university in India, we applied Fraunhofer reference spectra from the individual elevation angle sequences. The changing of SZA is negligible in such a sequence. The average of the previous and subsequent zenith (90°) measured spectra from the related elevation sequence is used as a Fraunhofer reference for the analysis of the spectra in this sequence.

This approach is realized by combining the WinDoas and the DOASIS software (the original script was written by Gerd Hönninger).

8.1.2 Results

To determine the trace gas DSCDs from MAX-DOAS observations, we apply the retrieval to the complete time series from the passive DOAS instrument. In the following, we present time series of slant column densities and also vertical column densities for different trace gases in the troposphere.

8.1.2.1 NO_2

The NO_2 evaluation range is from 351 to 392 nm. For the analysis in this fit window different trace gas absorption cross sections are applied: NO_2 at 294 K (Vandaele *et al.* , 1998), O_3 at 273 K (Bogumil *et al.* , 2003), O_4 (Greenblatt *et al.* , 1990), HONO (Stutz *et al.* , 2000); for the analysis in range 2, the similar NO_2, O_3 and O_4 trace gas absorption cross sections are used; for the analysis in range 3, the similar NO_2, O_3 and O_4 trace gas absorption cross sections are used, in this range also H_2O at 298 K (Rothman *et al.* , 2005), Glyoxal at 296 K (Volkamer *et al.* , 2005) trace gas absorption cross sections are added to the fit process. Fraunhofer reference spectra were determined from averaging the preceding and subsequent zenith measurements. Ring spectra were calculated from the averaged Fraunhofer reference. A polynomial of fifth order was included in the fitting procedure. The measured spectra and O_4 cross section were allowed to be shifted against the reference spectrum. The wavelength

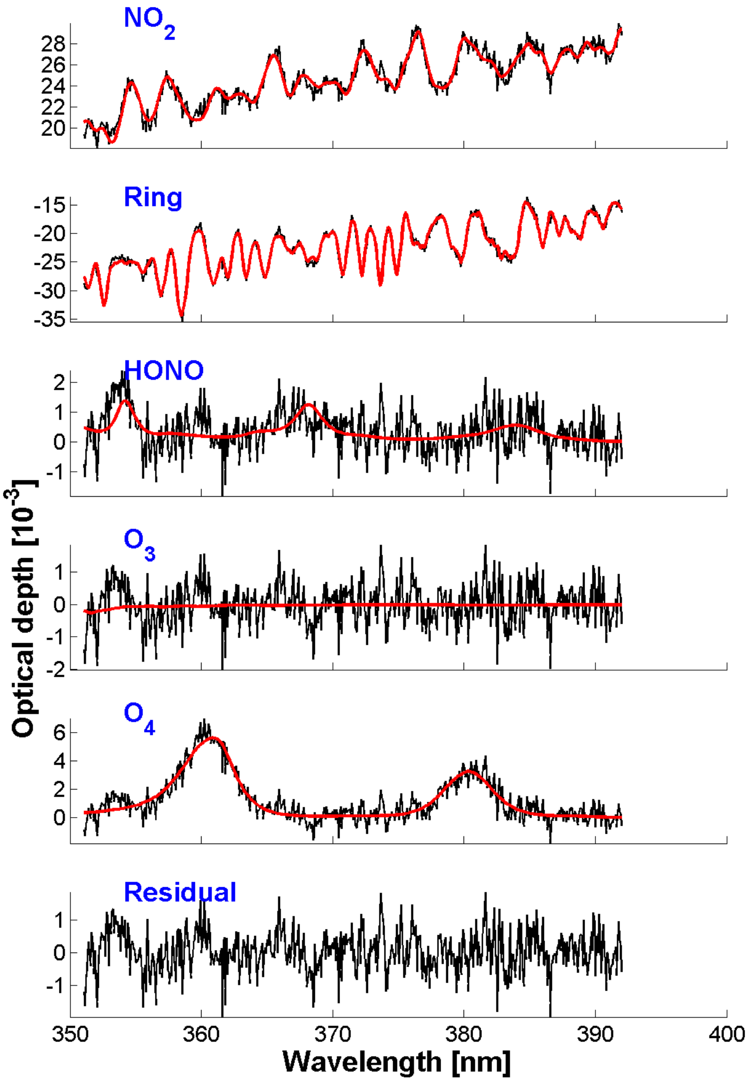

Figure 8.3: Example of the NO_2 retrieval from May 7, 2011, at 06:44 (UTC time) with an elevation angle of 10°. Shown are the fitted trace gas cross sections (red) scaled by the respective absorption of the measured spectrum (black). Fit-window: 351-392 nm.

calibration was performed based on a high resolution solar spectrum (Kurucz *et al.* , 1984).

A typical UV NO_2 fit result is shown figure 8.3 for May 7, 2011 at 06:44 (UTC time) with an elevation angle of 10°.

In figure 8.4, the time series of daily averaged NO_2 DSCDs from November 21, 2010 to June 6, 2012 are shown. The data were selected according to the following conditions:

1. RMS of the residual $< 2.5 \times 10^{-3}$.
2. Solar zenith angle $< 55°$.

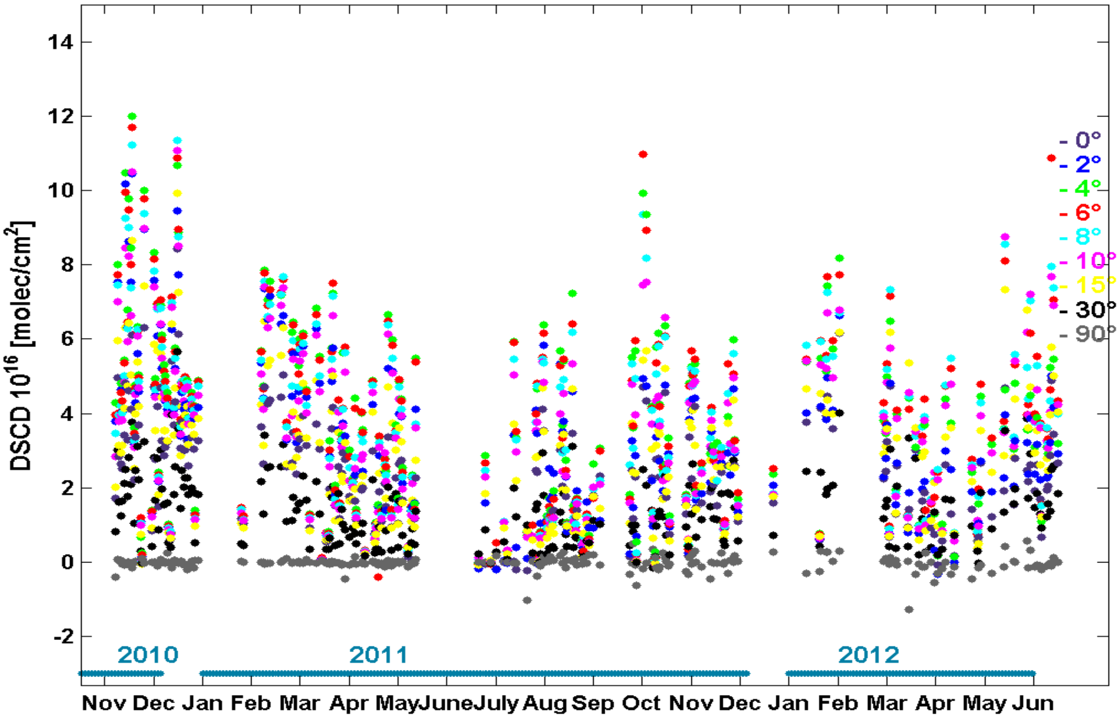

Figure 8.4: Time series of daily averaged NO_2 DSCDs from November 21, 2010 to June 6, 2012.

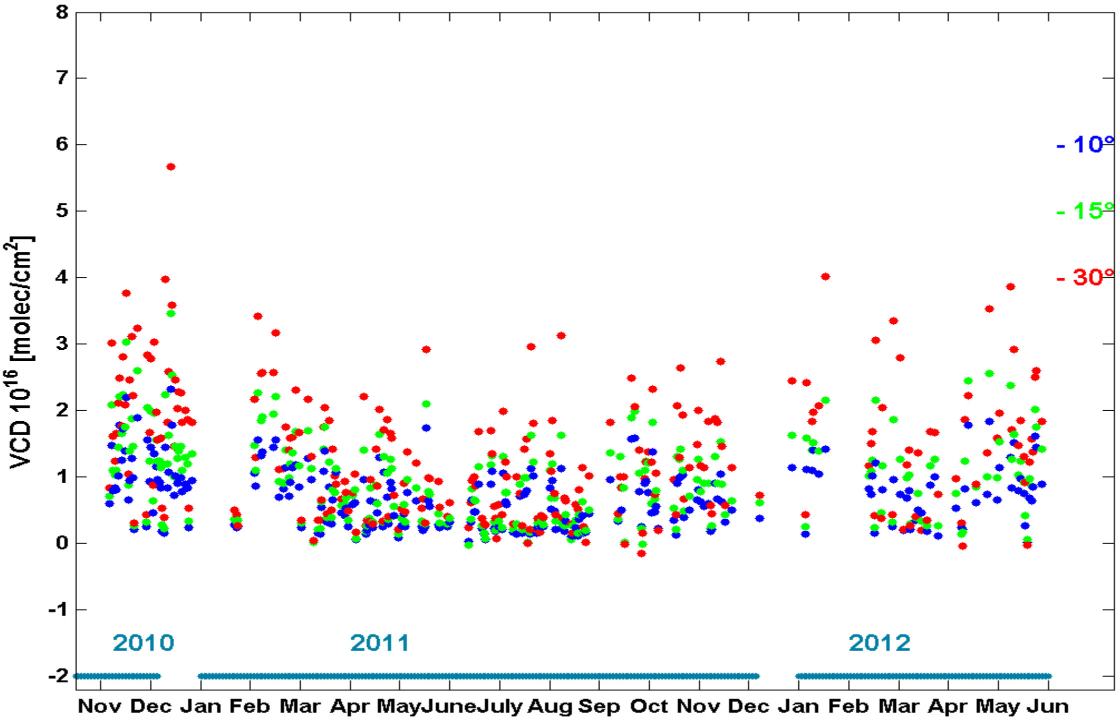

Figure 8.5: Time series of tropospheric daily averaged NO_2 VCDs.

The obtained DSCDs are found to be higher in 2010 compared to the year 2011 and 2012. In November and December 2010, the highest NO_2 DSCDs are observed; in October 2011. It should be noted that because of the buildings and other obstacles, the lowest elevation angle with a free view is 2°.

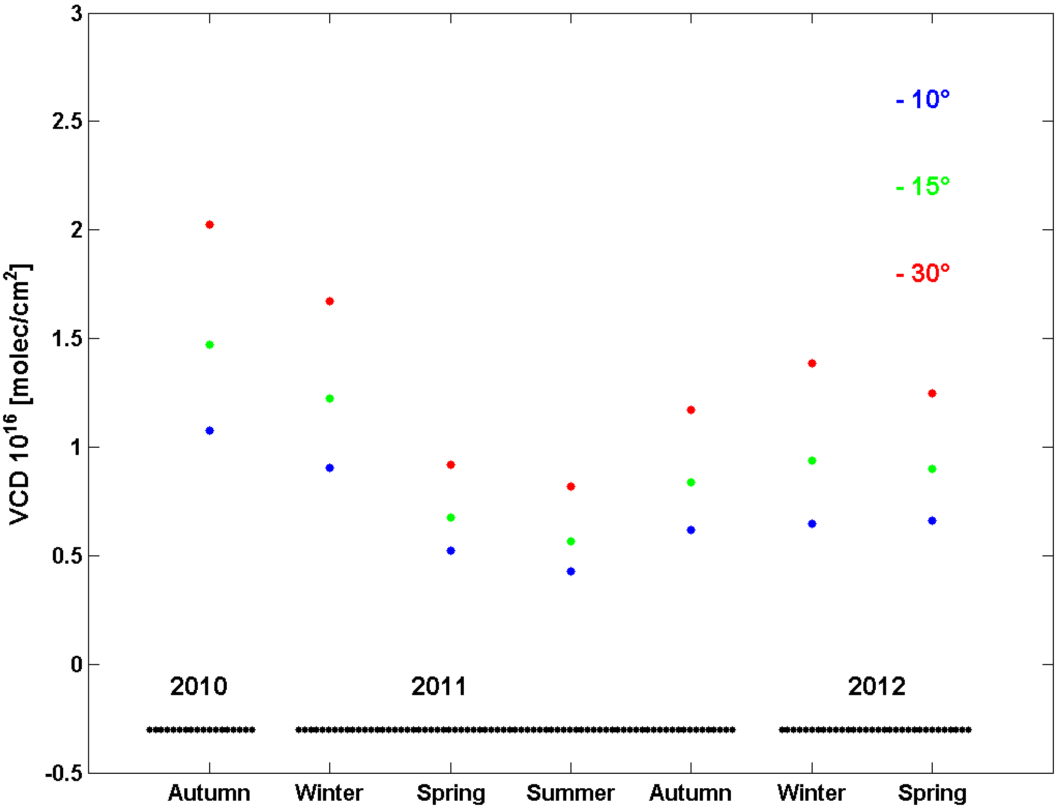

Figure 8.6: Seasonal variations of the tropospheric NO_2 VCDs analyzed for the different elevation angles.

In figure 8.5, the time series of tropospheric NO_2 VCDs are shown. Daily averaged tropospheric NO_2 VCDs for three different elevation angles (10°, 15° and 30°) from November 21, 2010 to June 6, 2012 using geometric air mass factors are shown.
The vertical column densities from 30° elevation angle are systematically higher than the VCD's from 10 and 15° elevation angles (figures 8.5). The values for 2010 are rather higher than for 2011 and 2012. In April, June and July 2011, the VCDs are lower than in the other months.

In figure 8.6, seasonal variations of the NO_2 VCDs are shown. The values for 30° are higher than for the other elevation angles. The maximum VCDs are found in autumn 2010, while in summer 2011, minimum VCDs were found.

8.1.2.2 HCHO

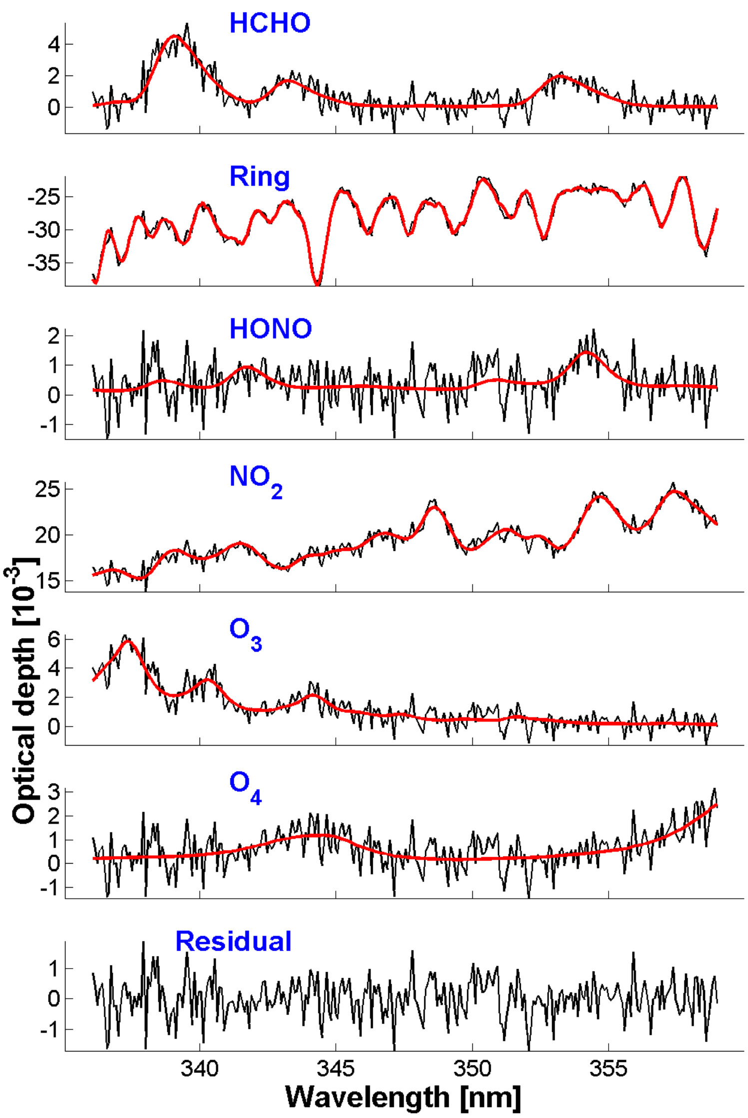

Figure 8.7: This example for the HCHO retrieval from May 7, 2011, at 06:44 (UTC time) with an elevation angle of 10°. Shown are the fitted trace gas cross sections (red) scaled by the respective absorption of the measured spectrum (black).

Like for NO_2, the evaluation of Formaldehyde was performed with the closest Fraunhofer reference to the spectrum, for the fit-window: 336-359 nm. The following trace gas absorption cross sections are applied: HCHO at 298 K (Meller & Moortgat, 2000), NO_2 at 294 K (Vandaele *et al.* , 1998), O_3 at 273 K (Bogumil *et al.* , 2003), O_4 (Greenblatt *et al.* , 1990), HONO (Stutz *et al.* , 2000), as well as a Fraunhofer reference spectrum determined from averaging of every preceding and subsequent zenith measurements. Ring spectra were calculated from the averaged Fraunhofer reference. A polynomial of fifth order was included in the fitting procedure. The measured spectra and O_4 were allowed to be shifted against the reference spectrum. The wavelength calibration was performed based on a high resolution solar spectrum (Kurucz *et al.* , 1984).

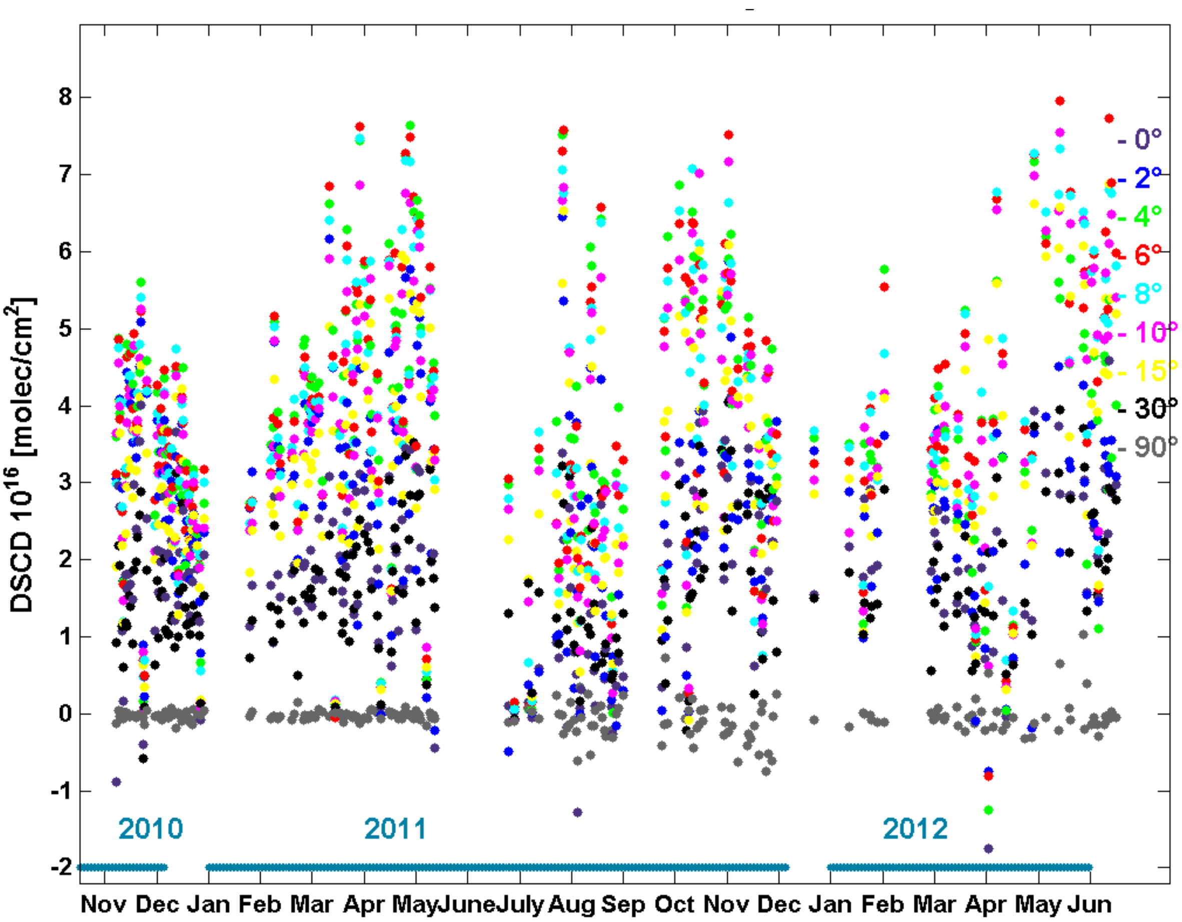

Figure 8.8: Time series of daily averaged formaldehyde slant column densities from November 21, 2010 to June 6, 2012.

A typical HCHO fit result is shown in figure 8.7 for May 7, 2011 at 06:44 (UTC time) with an elevation angle of 10°.

In figure 8.8, time series of formaldehyde slant column densities from November 21, 2010 to June 6, 2012 are shown. The values are daily averaged. The following selection criteria were applied:
1. RMS $< 1.5 \times 10^{-3}$.
2. SZA $< 55°$.
The HCHO DSCDs are increasing from 2010 to 2012 (see figure 8.8). The formaldehyde DSCDs from elevation angles 4° to 10° are higher than the values from the other elevation angles.

In figure 8.9, seasonal variations of HCHO VCDs are shown. The geometric approximation was applied for airmass factors. The values from 30° are higher than other elevation angles. The highest VCDs are obtained in autumn 2011 and spring 2012, while for summer 2011,

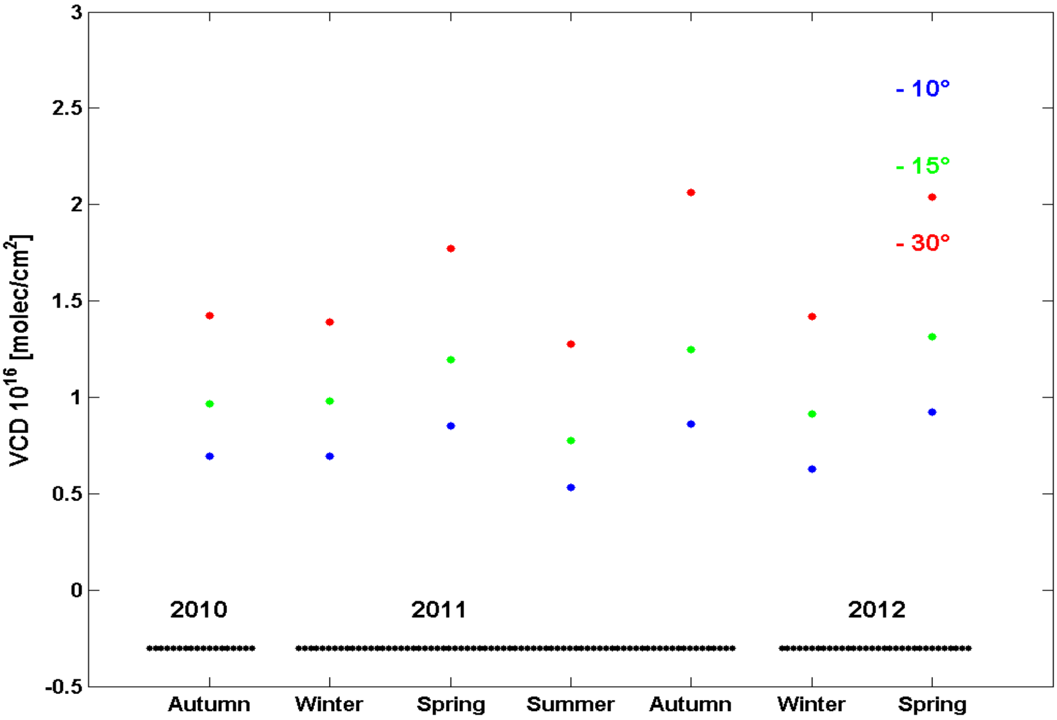

Figure 8.9: Seasonal variations of the formaldehyde vertical column densities for different elevation angles.

rather low VCDs of formaldehyde are found.

8.1.2.3 SO_2

The retrieval of SO_2 with closest Fraunhofer reference to the spectrum was performed in the fit-window: 313-328 nm. Some trace gas absorption cross sections are applied. SO_2 at 243 K (SCIA Bremen Webpage), NO_2 at 294 K (Vandaele *et al.* , 1998), O_3 at 223 K (Bogumil *et al.* , 2003), as well as a Fraunhofer reference spectrum determined from averaging of every preceding and subsequent zenith measurements. Ring spectra were calculated from the averaged Fraunhofer reference. A polynomial of fifth order was included in the fitting procedure. The measured spectra were allowed to be shifted against the reference spectrum. The wavelength calibration was performed based on a high resolution solar spectrum (Kurucz *et al.* , 1984).

A typical SO_2 fit result is shown in figure 8.10 for May 7, 2011 at 06:44 (UTC time) with an elevation angle of 10°.

In figure 8.11, daily averaged sulfur dioxide DSCDs are shown. Two selection criteria were applied:
1. RMS $< 2.5 \times 10^{-3}$.

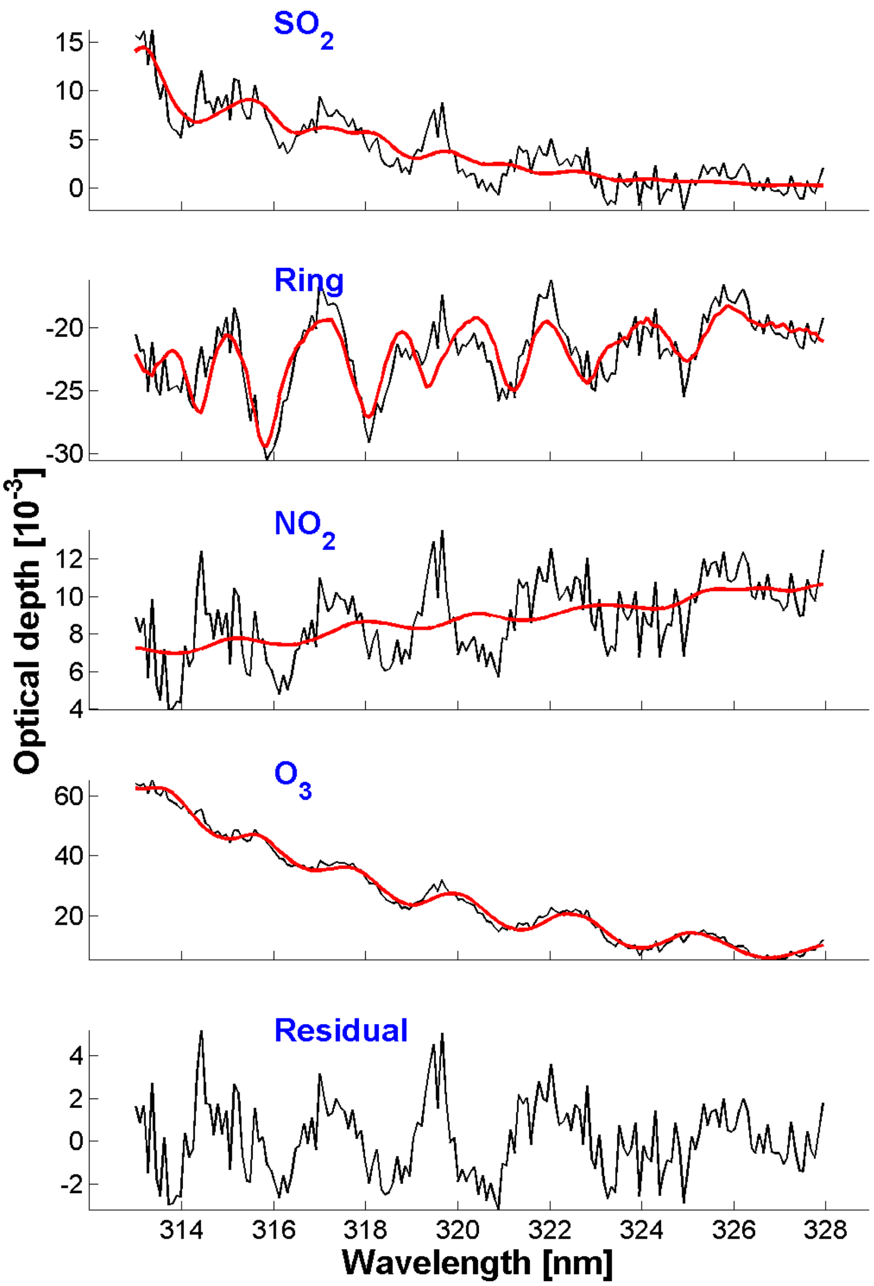

Figure 8.10: Example for the SO_2 retrieval from May 7, 2011, at 06:44 (UTC time) with an elevation angle of 10°. Shown are the fitted trace gas cross sections (red) scaled by the respective absorption of the measured spectrum (black).

2. SZA < 55°.

The time series of SO_2 DSCDs from November 21, 2010 to June 6, 2012 are shown in figure 8.11. The sulfur dioxide DSCDs (specially with 2° elevation angles) are decreasing from 2011 to 2012. In the first three months in 2012, they show minimum values.

The seasonal variation of SO_2 DSCDs is shown in figure 8.12.

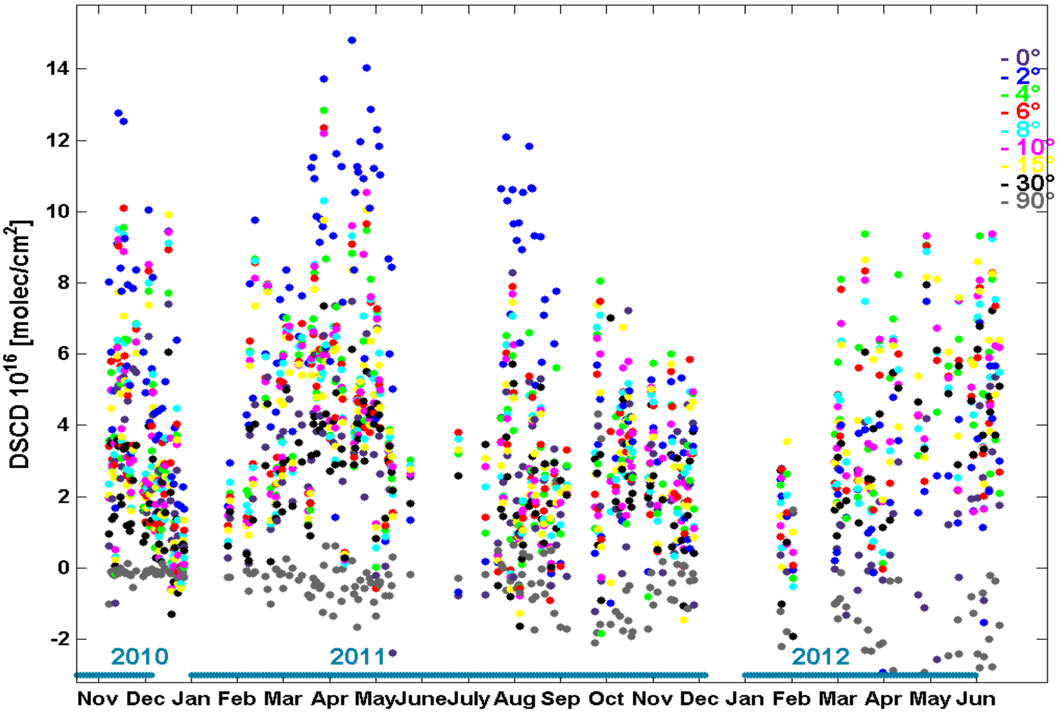

Figure 8.11: Time series of daily averaged SO_2 DSCDs from November 21, 2010 to June 6, 2012.

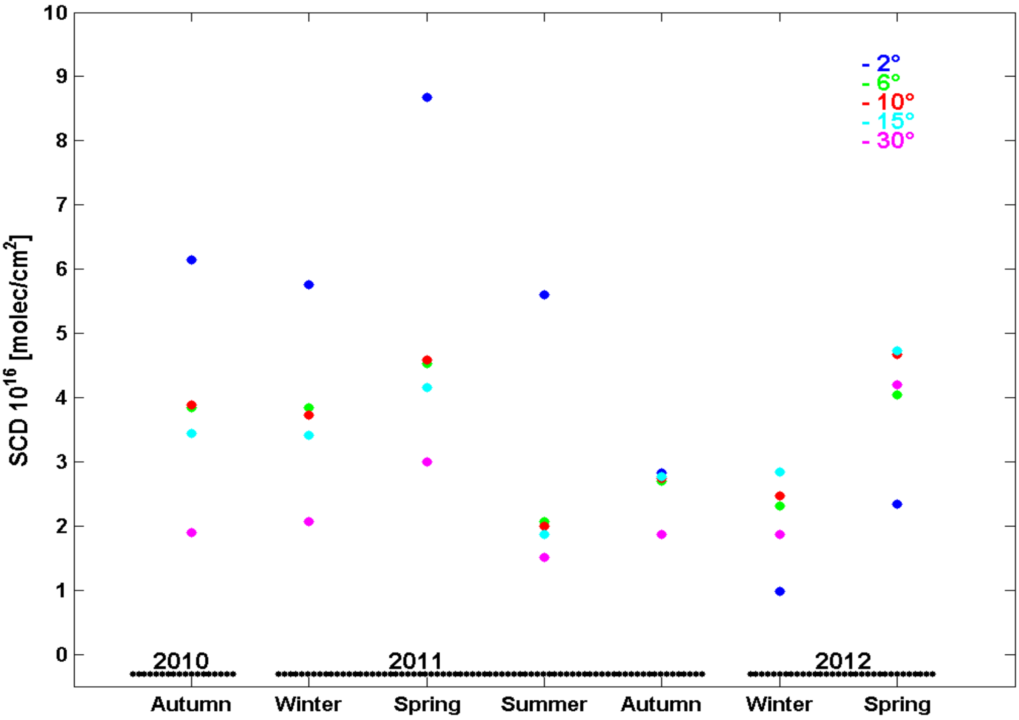

Figure 8.12: Seasonal variations of the SO_2 slant column densities for different elevation angles.

8.2 Summary

In this chapter, we showed time series of different atmospheric trace gases from the observations at Greater Noida in India. The evaluated atmospheric trace gases in this chapter show seasonal variations. These variations are rather different for the different trace gases. A general correlation can not be seen between different trace gases. However, this chapter is a short overview of these measurements. A detailed analysis is underway, but not the part of present study. In the future a detailed study of the various different gases and their relation with meteorological parameters is planned.

9 Additional mobile MAX-DOAS observations

In this chapter, we show different mobile MAX-DOAS measurements at different routes. Some of these measurements were not part of any measurement campaign.
By using a mini MAX-DOAS mounted on a car, we tried to observe scattered sun light under several elevation angles.
Most of these observations took place, when we drove with the instrument between different cities.

9.1 Mobile MAX-DOAS observations around Cabauw

During the CINDI campaign, we carried out mobile measurements around Cabauw, Utrecht and Gouda. Two successful orbits around the area on June 12 2009.
The characteristics of the instrument and the analysis method is explained in chapters 5 and 6.

Mobile MAX-DOAS results are shown in figure 9.1 for June 12, 2009.
The nitrogen dioxide plumes are at the south side of the circles in figure 9.1 (parts a and b), close to the Papendrecht. The wind direction was rather constant in this day. The nitrogen dioxide VCDs were found to be higher during morning compared to evening.

9.2 Mobile MAX-DOAS observations from Gouda to Mainz

We started the measurements on June 13, 2009 at 7:33 (UTC) in Gouda and continued the measurements until 13:59, the time we reached Mainz.
In figure 9.2, the colored circles present the tropospheric VCDs derived from the mobile MAX-DOAS, while in the background, the OMI satellite observations from the TEMIS data base are shown. The correspondence of the NO_2 plume is good between the satellite and the mobile measurements. The location during the overpass of OMI at 12:13 is marked by a white circle, which shows the position of the mobile MAX-DOAS instrument. For OMI data, we applied some conditions:

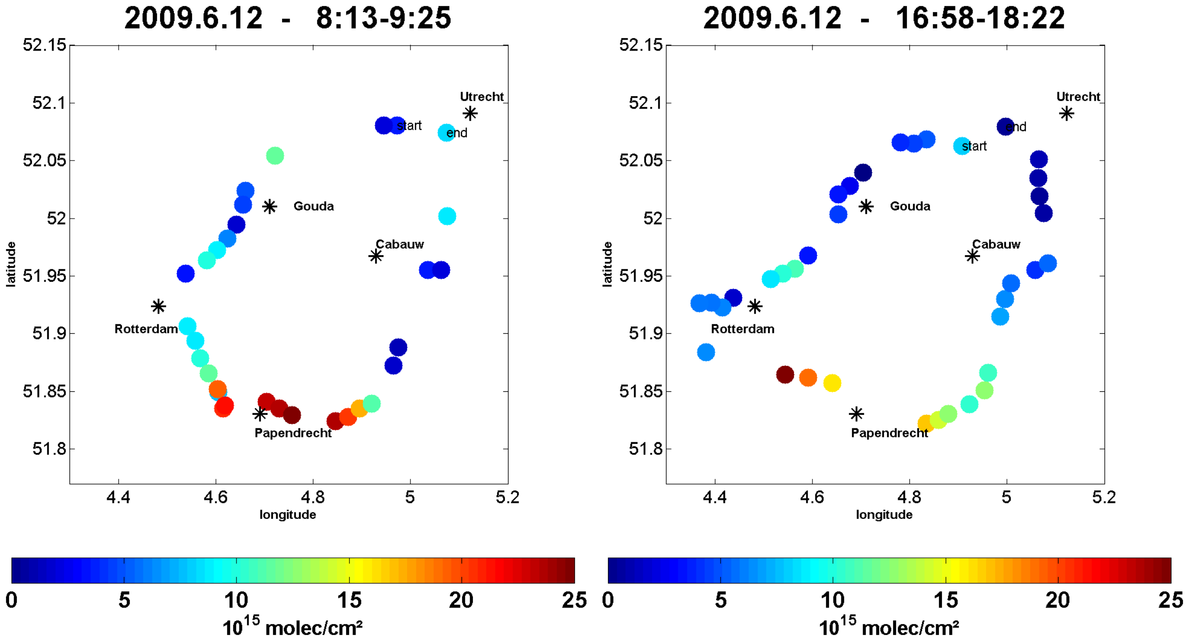

a) First orbit in the morning

b) Second orbit in the afternoon

Figure 9.1: Tropospheric NO_2 VCD measured by the mini MAX-DOAS instrument during different time intervals of June 12, 2009. The area of Cabauw, Utrecht and Gouda and Rotterdam was encircled.

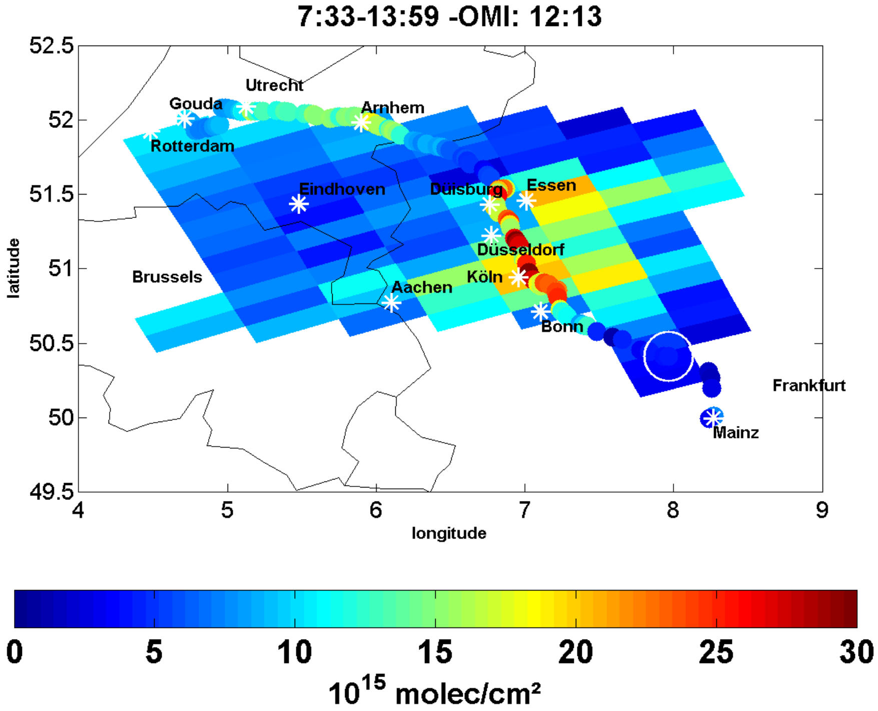

Figure 9.2: Comparison of mobile MAX-DOAS observations with OMI satellite measurements on June 13, 2009. The white circle shows the position of the mobile MAX-DOAS during the OMI overpass.

1. The OMI pixels without missing data, snow and ice are used.
2. Cloud fraction less than 30 %.

The highway, which we drove, is close to different cities in Germany, it is located in Ruhr area, showing high values of tropospheric nitrogen dioxide. Ruhr area in one of the main focusing part of MEGAPOLI project.

9.3 Mobile MAX-DOAS observations from Mainz to Paris

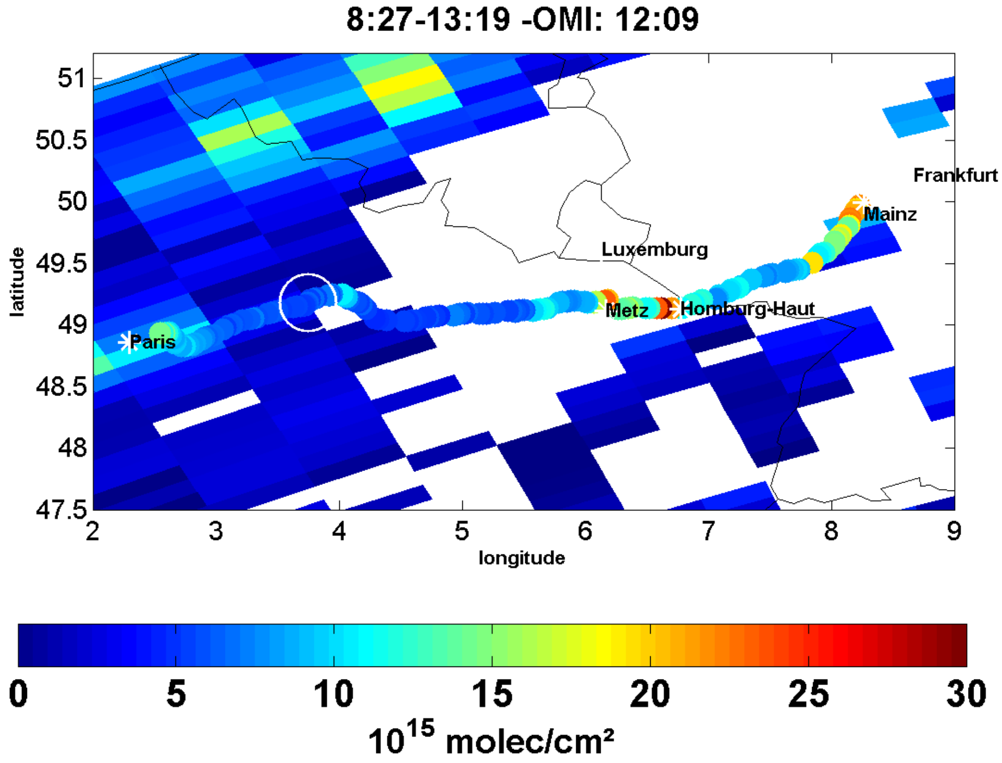

Figure 9.3: Vertical column densities from mobile MAX-DOAS and OMI (v1.0.2) observations for June 29, 2009. The white circle shows the position of the mobile MAX-DOAS at the time of the OMI overpass.

Another example of comparisons of the mobile measurements with satellite data is from June 29, 2009. At this day, we carried out the measurements from Mainz to Paris with a mounted instrument on top of a car. The tropospheric VCDs of the mobile MAX-DOAS and OMI satellite VCDs are shown in figure 9.3. Unfortunately, we do not have many OMI data to compare to our observations. Many OMI-pixels are removed by restrictions (e.g. high cloud fraction), especially where high values from mobile MAX-DOAS occur. The white circle presents the position of the mobile MAX-DOAS at the overpass time of OMI.

9.4 Mobile MAX-DOAS observations from Paris to Utrecht and back

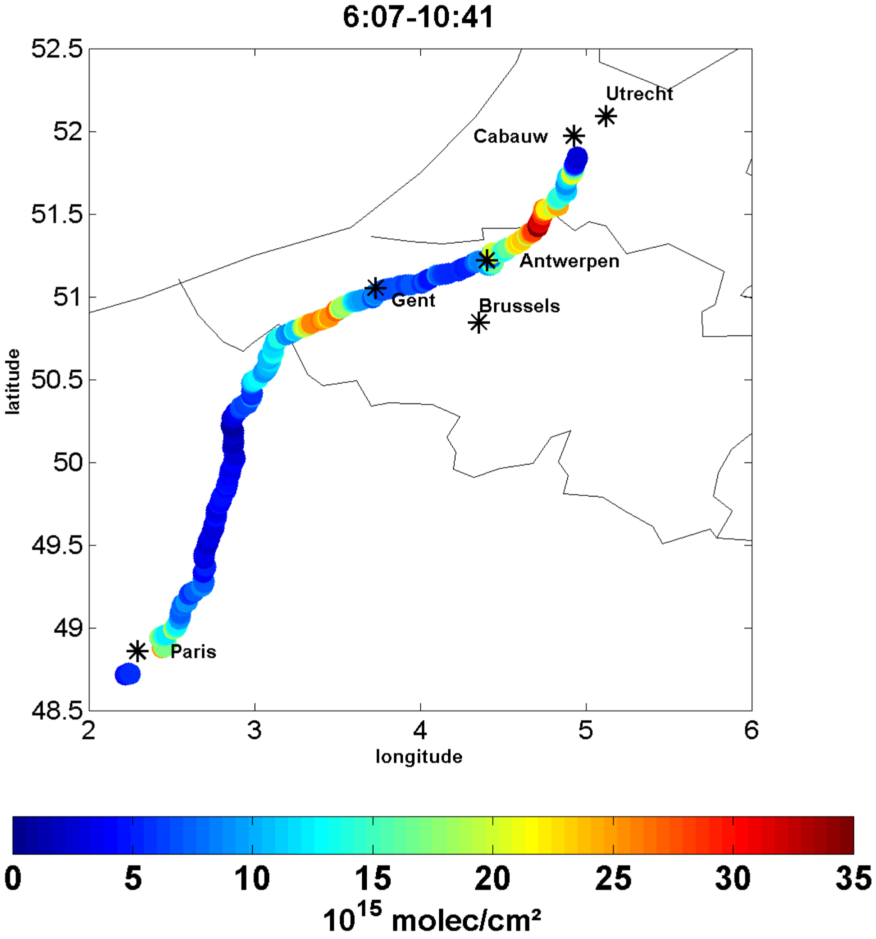

Figure 9.4: Tropospheric vertical column densities of NO_2 measured by mobile MAX-DOAS from Paris to Utrecht on July 6, 2009.

In figure 9.4, tropospheric vertical column densities of NO_2 are shown along the driving route from Paris to Utrecht on July 6, 2009. Unfortunately, no OMI data are available for this day.

The NO_2 TVCDs are missing close to Utrecht, due to some technical problems. Some high values are found at the borders of The Netherlands and Belgium.

On July 8, 2009, the mobile MAX-DOAS observations were performed from Utrecht to Paris. The TVCDs of these measurements are shown in figure 9.5. Close to Warengem in Belgium, high values of NO_2 are shown in figures 9.5 and 9.4. Due to connections problems between the instrument and computer, the measurements could not be continued until Paris .

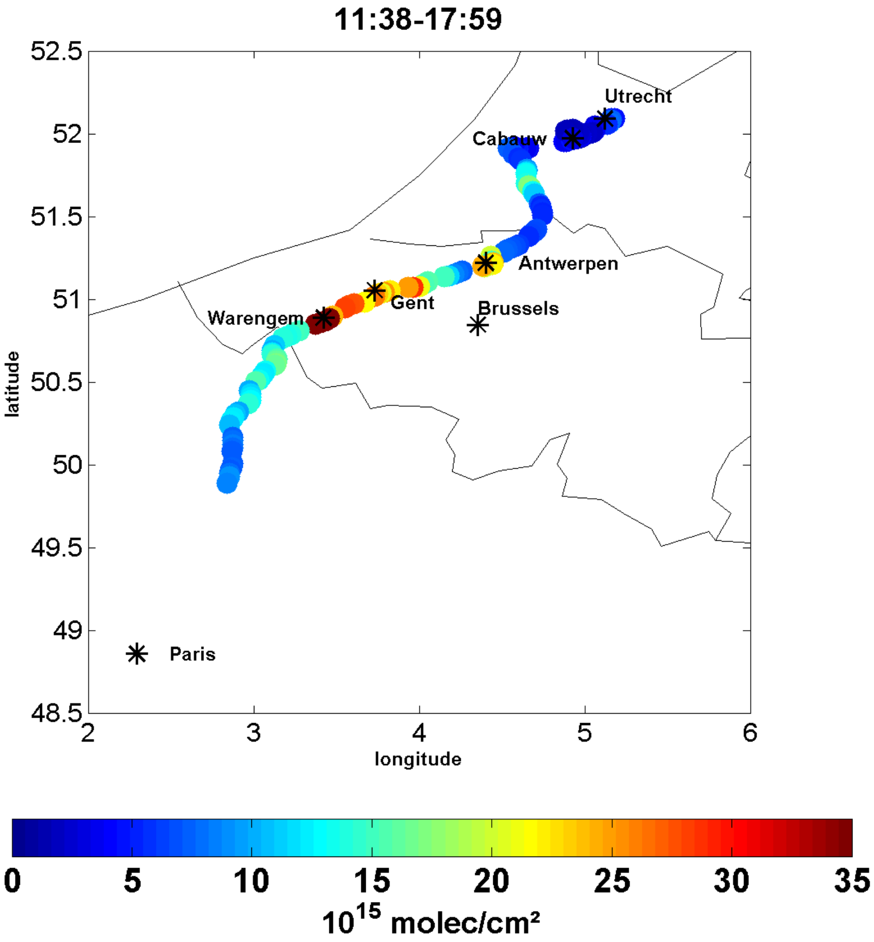

Figure 9.5: Tropospheric vertical column densities of NO_2 measured by mobile MAX-DOAS from Utrecht to Paris on July 8, 2009.

9.5 Mobile MAX-DOAS observations from Paris to Mainz

After the summer (2009) Paris campaign, we carried out MAX-DOAS observations from Paris to Mainz on July 31.

Tropospheric vertical column densities of NO_2 from mobile MAX-DOAS (colored circles) and the OMI satellite (background) are shown in figure 9.6. The white circle presents the position of mobile MAX-DOAS at the overpass time of OMI (12:11 UTC). High values of NO_2 were observed in Mainz and in the vicinity.

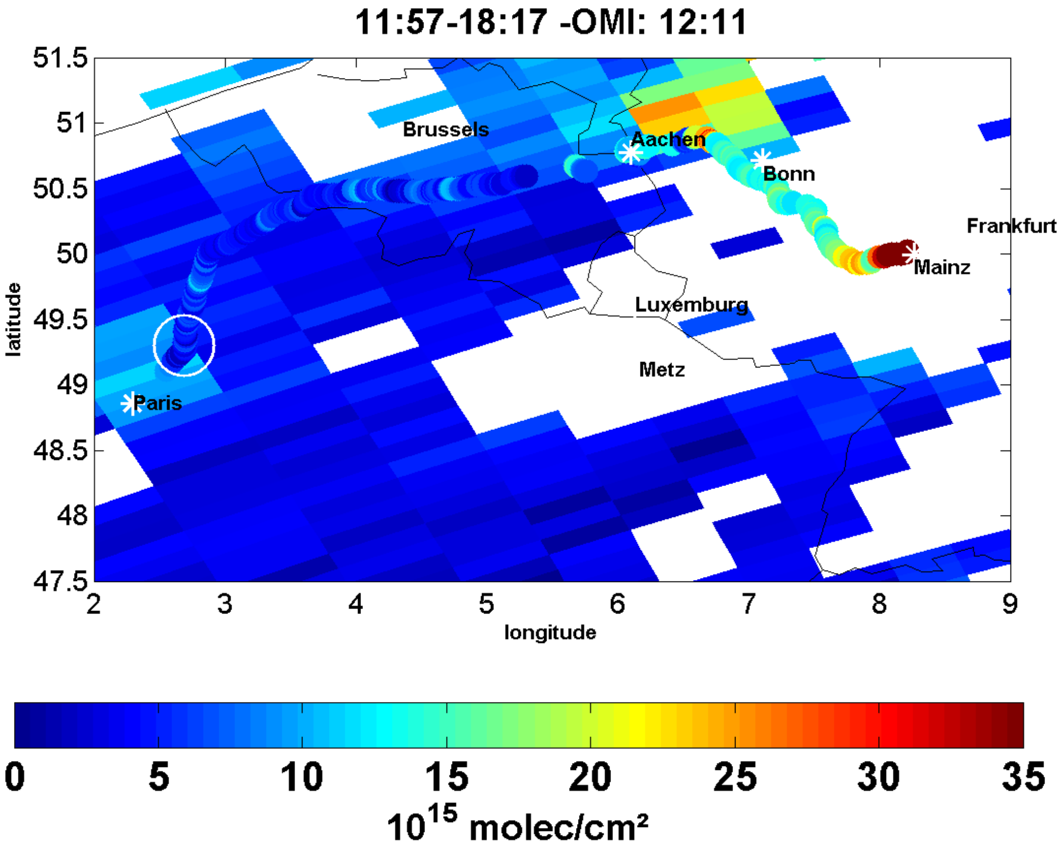

Figure 9.6: Comparison of tropospheric vertical column densities from mobile MAX-DOAS and OMI observations on July 31, 2009 along the route from Paris to Mainz. The white circle shows the position of the mobile MAX-DOAS at the OMI overpass time.

9.6 Summary

In this chapter, we showed various mobile MAX-DOAS observations. From these measurements highly resolved spatial patterns of the NO_2 VCD in many parts of Europe could be measured. Enhanced values were always observed close to strong emission sources like large cities as power plants. In general good agreement with OMI satellite observations is found.

Literature

Babu, S.S., Moorthy, K.K., Manchanda, R.K., Sinha, P.R., Satheesh, SK, Vajja, D.P., Srinivasan, S., & Kumar, V.H.A. 2011. Free tropospheric black carbon aerosol measurements using high altitude balloon: Do bc layers build "their own homes" up in the atmosphere? *Geophysical research letters*, **38**(8), L08803.

Beirle, S. 2004. *Estimating source strengths and lifetime of nitrogen oxides from satellite data*. Ph.D. thesis, Universitätsbibliothek.

Beirle, S., Boersma, K.F., Platt, U., Lawrence, M.G., & Wagner, T. 2011. Megacity emissions and lifetimes of nitrogen oxides probed from space. *Science*, **333**(6050), 1737–1739.

Bobrowski, N., Hönninger, G., Galle, B., & Platt, U. 2003. Detection of bromine monoxide in a volcanic plume. *Nature*, **423**(6937), 273–276.

Boersma, K. F., Eskes, H. J., Dirksen, R. J., van der A, R. J., Veefkind, J. P., Stammes, P., Huijnen, V., Kleipool, Q. L., Sneep, M., Claas, J., Leitão, J., Richter, A., Zhou, Y., & Brunner, D. 2011. An improved tropospheric no_2 column retrieval algorithm for the ozone monitoring instrument. *Atmospheric measurement techniques*, **4**(9), 1905–1928.

Boersma, KF, Eskes, HJ, Veefkind, J.P., Brinksma, EJ, van der A, RJ, Sneep, M., Van Den Oord, GHJ, Levelt, PF, Stammes, P., Gleason, JF, *et al.* . 2007. Near-real time retrieval of tropospheric no2 from omi. *Atmospheric chemistry & physics*, **7**, 2103–2118.

Boersma, KF, Jacob, DJ, Trainic, M., Rudich, Y., DeSmedt, I., Dirksen, R., & Eskes, HJ. 2009. Validation of urban no2 concentrations and their diurnal and seasonal variations observed from the sciamachy and omi sensors using in situ surface measurements in israeli cities. *Atmos. chem. phys*, **9**, 3867–3879.

Bogumil, K., Orphal, J., Homann, T., Voigt, S., Spietz, P., Fleischmann, OC, Vogel, A., Hartmann, M., Kromminga, H., Bovensmann, H., *et al.* . 2003. Measurements of molecular absorption spectra with the sciamachy pre-flight model: instrument characterization and reference data for atmospheric remote-sensing in the 230-2380 nm region. *Journal of photochemistry and photobiology a: Chemistry*, **157**(2-3), 167–184.

Bovensmann, H., Burrows, JP, Buchwitz, M., Frerick, J., Noël, S., Rozanov, VV, Chance, KV, & Goede, APH. 1999. Sciamachy: Mission objectives and measurement modes. *Journal of the atmospheric sciences*, **56**(2), 127–150.

Brinksma, EJ, Pinardi, G., Volten, H., Braak, R., Richter, A., Schönhardt, A., Van Roozendael, M., Fayt, C., Hermans, C., Dirksen, RJ, *et al.* . 2008. The 2005 and 2006 dandelions no2 and aerosol intercomparison campaigns. *J. geophys. res*, **113**, D16S46.

Burrows, J.P., Weber, M., Buchwitz, M., Rozanov, V., Ladstätter-Weissenmayer, A., Richter, A., DeBeek, R., Hoogen, R., Bramstedt, K., Eichmann, K.U., *et al.* . 1999. The global ozone monitoring experiment (gome): Mission concept and first scientific results. *Journal of the atmospheric sciences*, **56**(2), 151–175.

Cantrell, C. A. 2008. Technical note: Review of methods for linear least-squares fitting of data and application to atmospheric chemistry problems. *Atmospheric chemistry and physics*, **8**(17), 5477–5487.

Celarier, EA, Brinksma, EJ, Gleason, JF, Veefkind, JP, Cede, A., Herman, JR, Ionov, D., Goutail, F., Pommereau, JP, Lambert, JC, *et al.* . 2008. Validation of ozone monitoring instrument nitrogen dioxide columns. *J. geophys. res*, **113**, D15S15.

Chen, D., Zhou, B., Beirle, S., Chen, LM, & Wagner, T. 2009. Tropospheric no2 column densities deduced from zenith-sky doas measurements in shanghai, china, and their application to satellite validation. *Atmos. chem. phys*, **9**(11), 3641–3662.

Deutschmann, T., Beirle, S., Grzegorski, M., Kern, C., Kritten, L., Platt, U., Prados-Roman, C., Puki-te, J., Wagner, T., Werner, B., *et al.* . 2010. The monte carlo atmospheric radiative transfer model mcartim: Introduction and validation of jacobians and 3d features. *Journal of quantitative spectroscopy and radiative transfer.*

Dobber, M.R., Dirksen, R.J., Levelt, P.F., Van Den Oord, GHJ, Voors, R.H.M., Kleipool, Q., Jaross, G., Kowalewski, M., Hilsenrath, E., Leppelmeier, G.W., *et al.* . 2006. Ozone monitoring instrument calibration. *Geoscience and remote sensing, ieee transactions on*, **44**(5), 1209–1238.

Dubovik, O., Holben, B., Eck, T.F., Smirnov, A., Kaufman, Y.J., King, M.D., Tanré, D., & Slutsker, I. 2002. Variability of absorption and optical properties of key aerosol types observed in worldwide locations. *Journal of the atmospheric sciences*, **59**(3), 590–608.

Fayt, C., & Van Roozendael, M. 2001. Windoas 2.1–software user manual. *Uccle, belgium, bira-iasb.*

Fleischmann, O.C., Hartmann, M., Burrows, J.P., & Orphal, J. 2004. New ultraviolet absorption cross-sections of bro at atmospheric temperatures measured by time-windowing fourier transform spectroscopy. *Journal of photochemistry and photobiology a: Chemistry*, **168**(1), 117–132.

Gautam, R., Hsu, N.C., Kafatos, M., & Tsay, S.C. 2007. Influences of winter haze on fog/low cloud over the indo-gangetic plains. *J. geophys. res*, **112**, D05207.

Goyal, SK, Ghatge, SV, Nema, P., & M. Tamhane, S. 2006. Understanding urban vehicular pollution problem vis-a-vis ambient air quality–case study of a megacity (delhi, india). *Environmental monitoring and assessment*, **119**(1), 557–569.

Greenblatt, G.D., Orlando, J.J., Burkholder, J.B., & Ravishankara, AR. 1990. Absorption measurements of oxygen between 330 and 1140 nm. *Journal of geophysical research*, **95**(D11), 18577–18.

Gurjar, BR, Van Aardenne, JA, Lelieveld, J., & Mohan, M. 2004. Emission estimates and trends (1990-2000) for megacity delhi and implications. *Atmospheric environment*, **38**(33), 5663–5681.

Guttikunda, S. 2009. A review of the impact of biofuels on local, regional, and global air quality.

Hains, J.C., Boersma, K.F., Kroon, M., Dirksen, R.J., Cohen, R.C., Perring, A.E., Bucsela, E., Volten, H., Swart, D.P.J., Richter, A., *et al.* . 2010. Testing and improving omi domino tropospheric no_2 using observations from the dandelions and intex-b validation campaigns. *J. geophys. res*, **115**, D05301.

Heckel, A., Kim, S.-W., Frost, G. J., Richter, A., Trainer, M., & Burrows, J. P. 2011. Influence of low spatial resolution a priori data on tropospheric no_2 satellite retrievals. *Atmospheric measurement techniques*, **4**(9), 1805–1820.

HELAND, J., SCHLAGER, H., RICHTER, A., & BURROWS, J.P. 2002. First comparison of tropospheric no_2 column densities retrieved from gome measurements and in situ aircraft profile measurements. *Geophysical research letters*, **29**(20), 1983.

HERMANS, C., VANDAELE, A.C., CARLEER, M., FALLY, S., COLIN, R., JENOUVRIER, A., COQUART, B., & MÉRIENNE, M.F. 1999. Absorption cross-sections of atmospheric constituents: No 2, o 2, and h 2 o. *Environmental science and pollution research*, **6**(3), 151–158.

HÖNNINGER, G., & PLATT, U. 2002. Observations of bro and its vertical distribution during surface ozone depletion at alert. *Atmospheric environment*, **36**(15-16), 2481–2489.

HÖNNINGER, G., VON FRIEDEBURG, C., & PLATT, U. 2004. Multi axis differential optical absorption spectroscopy (max-doas). *Atmos. chem. phys*, **4**, 231–254.

IBRAHIM, O., SHAIGANFAR, R., SINREICH, R., STEIN, T., PLATT, U., & WAGNER, T. 2010. Car max-doas measurements around entire cities: quantification of no_x emissions from the cities of mannheim and ludwigshafen (germany). *Meas. tech*, **3**, 709–721.

JACOB, D.J. 1999. *Introduction to atmospheric chemistry.*

JENKIN, ME, WATSON, LA, UTEMBE, SR, & SHALLCROSS, DE. 2008. A common representative intermediates (cri) mechanism for voc degradation. part 1: Gas phase mechanism development. *Atmospheric environment*, **42**(31), 7185–7195.

KUENEN, J., VAN DER GON, H.D., VISSCHEDIJK, A., VAN DER BRUGH, H., FINARDI, S., RADICE, P., D'ALLURA, A., BEEVERS, S., THELOKE, J., UZ-BASICH, M., *et al.* . 2010. A base year (2005) megapoli european gridded emission inventory (final version). deliverable d1. 6. *Megapoli scientific report 10-17, megapoli-20-rep-2010-10, 37p, isbn: 978-87-993898-8-9 http://megapoli. dmi. dk/publ/megapoli_sr10-17. pdf.*

KURUCZ, R.L., FURENLID, I., BRAULT, J., & TESTERMAN, L. 1984. Solar flux atlas from 296 to 1300 nm. *National solar observatory atlas, sunspot, new mexico: National solar observatory, 1984*, **1**.

LESER, H., HÖNNINGER, G., & PLATT, U. 2003. Max-doas measurements of bro and no_2 in the marine boundary layer. *Geophys. res. lett*, **30**(10), 1537.

LEUE, C., WENIG, M., WAGNER, T., KLIMM, O., PLATT, U., & JÄHNE, B. 2001. Quantitative analysis of no_x emissions from global ozone monitoring experiment satellite image sequences. *Journal of geophysical research*, **106**(D6), 5493–5505.

LEVELT, PF, & NOORDHOEK, R. 2002. *Omi algorithm theoretical basis document volume i: Omi instrument, level 0-1b processor, calibration & operations.* Tech. rept. Tech. Rep. ATBD-OMI-01, Version 1.1.

LEVELT, P.F., VAN DEN OORD, G.H.J., DOBBER, M.R., MALKKI, A., VISSER, H., DE VRIES, J., STAMMES, P., LUNDELL, J.O.V., & SAARI, H. 2006. The ozone monitoring instrument. *Geoscience and remote sensing, ieee transactions on*, **44**(5), 1093–1101.

LEVENBERG, K. 1944. A method for the solution of certain problems in least squares. *Quarterly of applied mathematics*, **2**, 164–168.

LORD RAYLEIGH, R. 1899. On the transmission of light through an atmosphere containing small particles in suspension, and on the origin of the blue of the sky. *Philos mag*, **47**, 375–384.

MAHURA, A., & BAKLANOV, A. 2011. Megapoli; newsletters. *Megapoli project; isbn: 978-87-92731-27-2; megapoli-01-mnl-11-09.*

MARTIN, R.V., JACOB, D.J., CHANCE, K., KUROSU, T.P., PALMER, P.I., & EVANS, M.J. 2003. Global inventory of nitrogen oxide emissions constrained by space-based observations of no2 columns. *J. geophys. res*, **108**(453710.1029).

MELLER, R., & MOORTGAT, G.K. 2000. Temperature dependence of the absorption cross sections of formaldehyde between 223 and 323 k in the wavelength range 225-375 nm. *Journal of geophysical research*, **105**(6), 7089–7101.

MIE, G. 1908. Beiträge zur optik trübcr mcdien, spcziell kolloidalcn mctallösungen. *Ann. physik*, **25**, 377.

OLIVIER, JGJ, BOUWMAN, AF, VAN DER HOEK, KW, & BERDOWSKI, JJM. 1998. Global air emission inventories for anthropogenic sources of no_x, nh_3 and n_2o in 1990. *Environmental pollution*, **102**(1), 135–148.

PETETIN, H., BEEKMANN, M., MICHOUD, V., BORBON, A., DOUSSIN, JF, COLOMB, A., SCHWARZENBOECK, A., VAN DER GON, H.D., HONORE, C., WIEDENSOHLER, A., *et al.* . 2011. the megapoli campaign team (2011): Effective emission factors for oc and bc for urban type emissions. deliverable d3. 3. *Megapoli scientific report 11-08, megapoli-34-rep-2011-06, 30p, isbn: 978-87-92731-12-8 http://megapoli. dmi. dk/publ/megapoli_sr11-08. pdf.*

Pinardi, G., Van Roozendael, M., N. Abuhassan, C. Adams, A. Cede K. Clémer C. Fayt U. Friess M. Gil J. Herman C. Hermans F. Hendrick H. Irie A. Merlaud M. Navarro Comas E. Peters A.J.M. Piters O. Puentedura A. Richter A. Schönhardt R. Shaiganfar E. Spinei K. Strong H. Takashima M. Vrekoussis T. Wagner F. Wittrock, & Yilmaz, S. 2012. Maxdoas formaldehyde slant column measurements during cindi: intercomparison and analysis improvement. *Atmospheric measurement techniques discussions*, **5**(5), 6679–6732.

Piters, AJM, Boersma, KF, Kroon, M., Hains, JC, Van Roozendael, M., Wittrock, F., Abuhassan, N., Adams, C., Akrami, M., Allaart, MAF, *et al.* . 2011. The cabauw intercomparison campaign for nitrogen dioxide measuring instruments (cindi): design, execution, and early results. *Atmospheric measurement techniques discussions*, **4**, 5935–6005.

Platt, U., & Stutz, J. 2008. *Differential optical absorption spectroscopy: Principles and applications.* Springer Verlag.

Ramanathan, V., & Ramana, MV. 2005. Persistent, widespread, and strongly absorbing haze over the himalayan foothills and the indo-gangetic plains. *Pure and applied geophysics*, **162**(8), 1609–1626.

Ramanathan, V., Chung, C., Kim, D., Bettge, T., Buja, L., Kiehl, JT, Washington, WM, Fu, Q., Sikka, DR, & Wild, M. 2005. Atmospheric brown clouds: Impacts on south asian climate and hydrological cycle. *Proceedings of the national academy of sciences of the united states of america*, **102**(15), 5326.

Rehman, IH, Ahmed, T., Praveen, PS, Kar, A., & Ramanathan, V. 2011. Black carbon emissions from biomass and fossil fuels in rural india. *Atmos. chem. phys*, **11**, 7289–7299.

Roscoe, H.K., Van Roozendael, M., Fayt, C., Du Piesanie, A., Abuhassan, N., Adams, C., Akrami, M., Cede, A., Chong, J., Clémer, K., *et al.* . 2010. Intercomparison of slant column measurements of no_2 and o_4 by max-doas and zenith-sky uv and visible spectrometers. *Atmospheric measurement techniques discussions*, **3**, 3383–3423.

Rothman, L.S., Jacquemart, D., Barbe, A., Chris Benner, D., Birk, M., Brown, LR, Carleer, MR, Chackerian, C., Chance, K., Coudert, L.H., *et al.* . 2005. The hitran 2004 molecular spectroscopic database. *Journal of quantitative spectroscopy and radiative transfer*, **96**(2), 139–204.

Satheesh, SK, Vinoj, V., & Moorthy, K.K. 2011. Weekly periodicities of aerosol properties observed at an urban location in india. *Atmospheric research.*

Schmidt, H., Derognat, C., Vautard, R., & Beekmann, M. 2001. A comparison of simulated and observed ozone mixing ratios for the summer of 1998 in western europe. *Atmospheric environment*, **35**(36), 6277–6297.

Schoeberl, MR, Douglass, AR, Hilsenrath, E., Bhartia, PK, Barnett, J., Gille, J., Beer, R., Gunson, M., Waters, J., Levelt, PF, *et al.* . 2004. Earth observing system missions benefit atmospheric research. *Eos*, **85**(18), 177–178.

Seinfeld, J.H., & Pandis, S.N. 2006. From air pollution to climate change, 2nd edition. *Atmospheric chemistry and physics, john wiley & sons, new york.*

Shaiganfar, R., Beirle, S., Sharma, M., Chauhan, A., Singh, RP, & Wagner, T. 2011. Estimation of no x emissions from delhi using car max-doas observations and comparison with omi satellite data. *Atmos. chem. phys*, **11**, 10871–10887.

Singh, RP, Dey, S., Tripathi, SN, Tare, V., & Holben, B. 2004. Variability of aerosol parameters over kanpur, northern india. *J. geophys. res*, **109**, D23206.

Singh, RP, Prasad, AK, Chauhan, SS, & Singh, S. 2005. Impact of growing urbanization and air pollution on the regional climate over india. *International association for urban climate newsletter, issue*, 5–10.

Sluis, WW, Allaart, MAF, Piters, AJM, & Gast, LFL. 2010. The development of a nitrogen dioxide sonde, atmos. *Meas. tech. discuss*, **3**, 2805–2832.

Solomon, S., Schmeltekopf, A.L., & Sanders, R.W. 1987. On the interpretation of zenith sky absorption measurements. *Journal of geophysical research*, **92**(D7), 8311–8319.

Spicer, C.W. 1982. Nitrogen oxide reactions in the urban plume of boston. *Science*, **215**(4536), 1095.

Stutz, J., Kim, ES, Platt, U., Bruno, P., Perrino, C., & Febo, A. 2000. Uv-visible absorption cross sections of nitrous acid. *Journal of geophysical research*, **105**, 14.

Van Roozendael, M., Fayt, C., Post, P., Hermans, C., & Lambert, JC. 2003. Retrieval of bro and no_2 from uv-visible observations. *Sounding the troposphere from space: a new era for atmospheric chemistry, springer-verlag, isbn*, 3–540.

Van Roozendael, M., Piters, A., Boersma, F., Wittrock, F., Hains, J., Kroon, M., & Roscoe, H. 2010. Overview of the cindi campaign. *Egu general assembly 2010, held 2-7 may, 2010 in vienna, austria, p. 8240*, **12**, 8240.

VANDAELE, AC, HERMANS, C., SIMON, PC, ROOZENDAEL, M., GUILMOT, JM, CARLEER, M., & COLIN, R. 1996. Fourier transform measurement of no_2 absorption cross-section in the visible range at room temperature. *Journal of atmospheric chemistry*, **25**(3), 289–305.

VANDAELE, AC, HERMANS, C., SIMON, PC, CARLEER, M., COLIN, R., FALLY, S., MERIENNE, MF, JENOUVRIER, A., & COQUART, B. 1998. Measurements of the no_2 absorption cross-section from 42 000 cm^{-1} to 10 000 cm^{-1} (238-1000 nm) at 220 k and 294 k. *Journal of quantitative spectroscopy and radiative transfer*, **59**(3), 171–184.

VOLKAMER, R., SPIETZ, P., BURROWS, J., & PLATT, U. 2005. High-resolution absorption cross-section of glyoxal in the uv-vis and ir spectral ranges. *Journal of photochemistry and photobiology a: Chemistry*, **172**(1), 35–46.

VOLKAMER, R., KUROSU, TP, CHANCE, K., LI, Z., ZHANG, Y., BRAUERS, T., & WAHNER, A. 2006. Spatial variability of glyoxal, hcho and no_2 during prd-2006: Comparison of mobile mini-max-doas and omi satellite data in the pearl river delta, china. *Eos trans. agu*, **87**, 52.

WAGNER, T., DIX, B., FRIEDEBURG, C., FRIESS, U., SANGHAVI, S., SINREICH, R., & PLATT, U. 2004. Max-doas o4 measurements: A new technique to derive information on atmospheric aerosols–principles and information content. *J. geophys. res*, **109**, D22205.

WAGNER, T., BURROWS, JP, DEUTSCHMANN, T., DIX, B., VON FRIEDEBURG, C., FRIESS, U., HENDRICK, F., HEUE, K.P., IRIE, H., IWABUCHI, H., *et al.* . 2007. Comparison of box-air-mass-factors and radiances for multiple-axis differential optical absorption spectroscopy (max-doas) geometries calculated from different uv/visible radiative transfer models. *Atmospheric chemistry and physics*, **7**(7), 1809–1833.

WAGNER, T., IBRAHIM, O., SHAIGANFAR, R., & PLATT, U. 2010. Mobile max-doas observations of tropospheric trace gases. *Atmospheric measurement techniques*, **3**, 129–140.

WAGNER, T., BEIRLE, S., BRAUERS, T., DEUTSCHMANN, T., FRIESS, U., HAK, C., HALLA, JD, HEUE, KP, JUNKERMANN, W., LI, X., *et al.* . 2011. Inversion of tropospheric profiles of aerosol extinction and hcho and no.

WILMOUTH, D.M., HANISCO, T.F., DONAHUE, N.M., & ANDERSON, J.G. 1999. Fourier transform ultraviolet spectroscopy of the a $2\pi 3/2 \leftarrow$ x $2\pi 3/2$ transition of bro. *The journal of physical chemistry a*, **103**(45), 8935–8945.

Zieger, P., Weingartner, E., Henzing, J., Moerman, M., de Leeuw, G., Mikkilä, J., Ehn, M., Petäjä, T., Clémer, K., van Roozendael, M., *et al.* . 2011. Comparison of ambient aerosol extinction coefficients obtained from in-situ, max-doas and lidar measurements at cabauw. *Atmos. chem. phys*, **11**, 2603–2624.

Ziskin, D., Baugh, K., Hsu, F.C., Ghosh, T., & Elvidge, C. 2010. Methods used for the 2006 radiance lights. *Pages 131–142 of: Proceedings of the 30th asia-pacific advanced network meeting.*

Appendix A

A.1 The tropospheric NO_2 VCDs from mobile MAX-DOAS

Here we present the tropospheric NO_2 vertical column densities (TVCDs) from mobile MAX-DOAS in the Paris for summer and winter campaigns.

A.1.1 Summer campaign, 2009

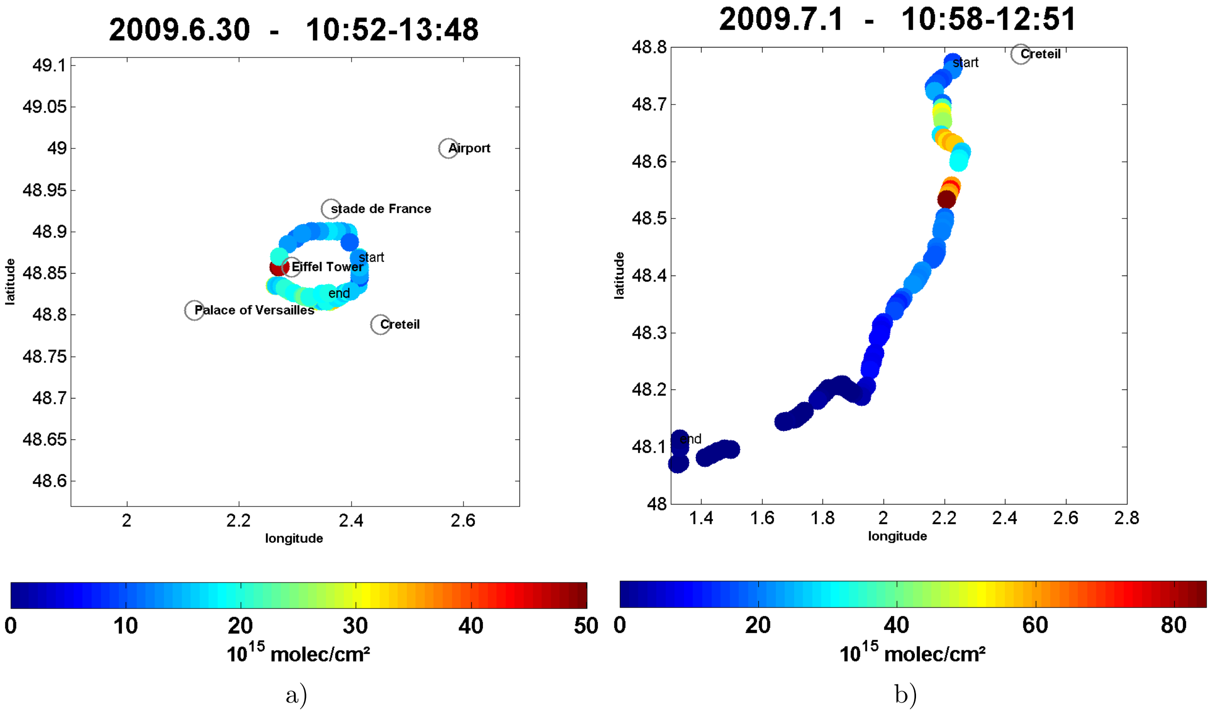

a)

b)

Figure A.1: The TVCDs of NO_2 in Paris on June 30 (a) and July 1 (b), 2009.

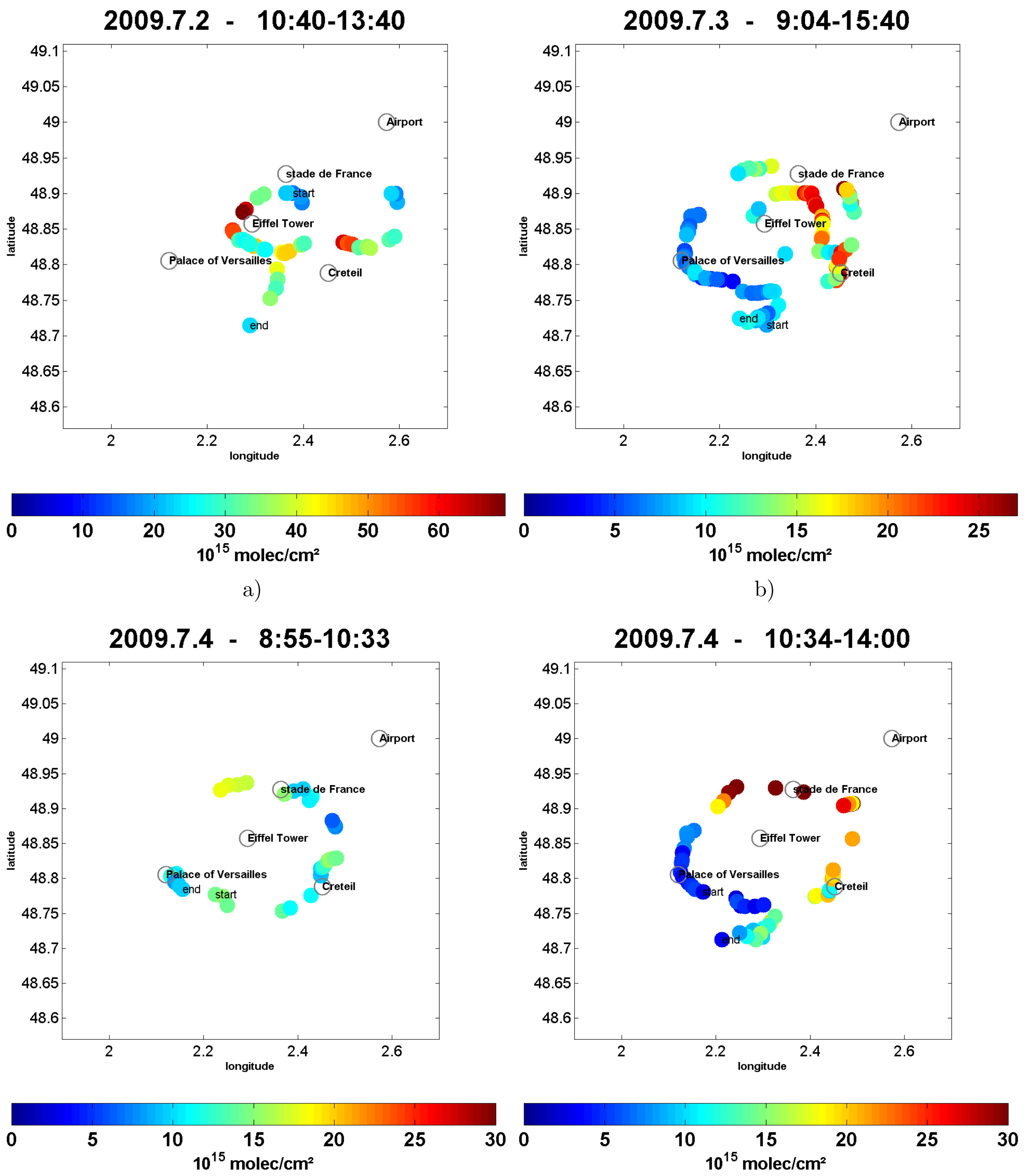

a) b) c) d)

Figure A.2: The TVCDs of NO_2 in Paris on July 2 (a), July 3 (b), July 4 (c) and July 4 (d), 2009.

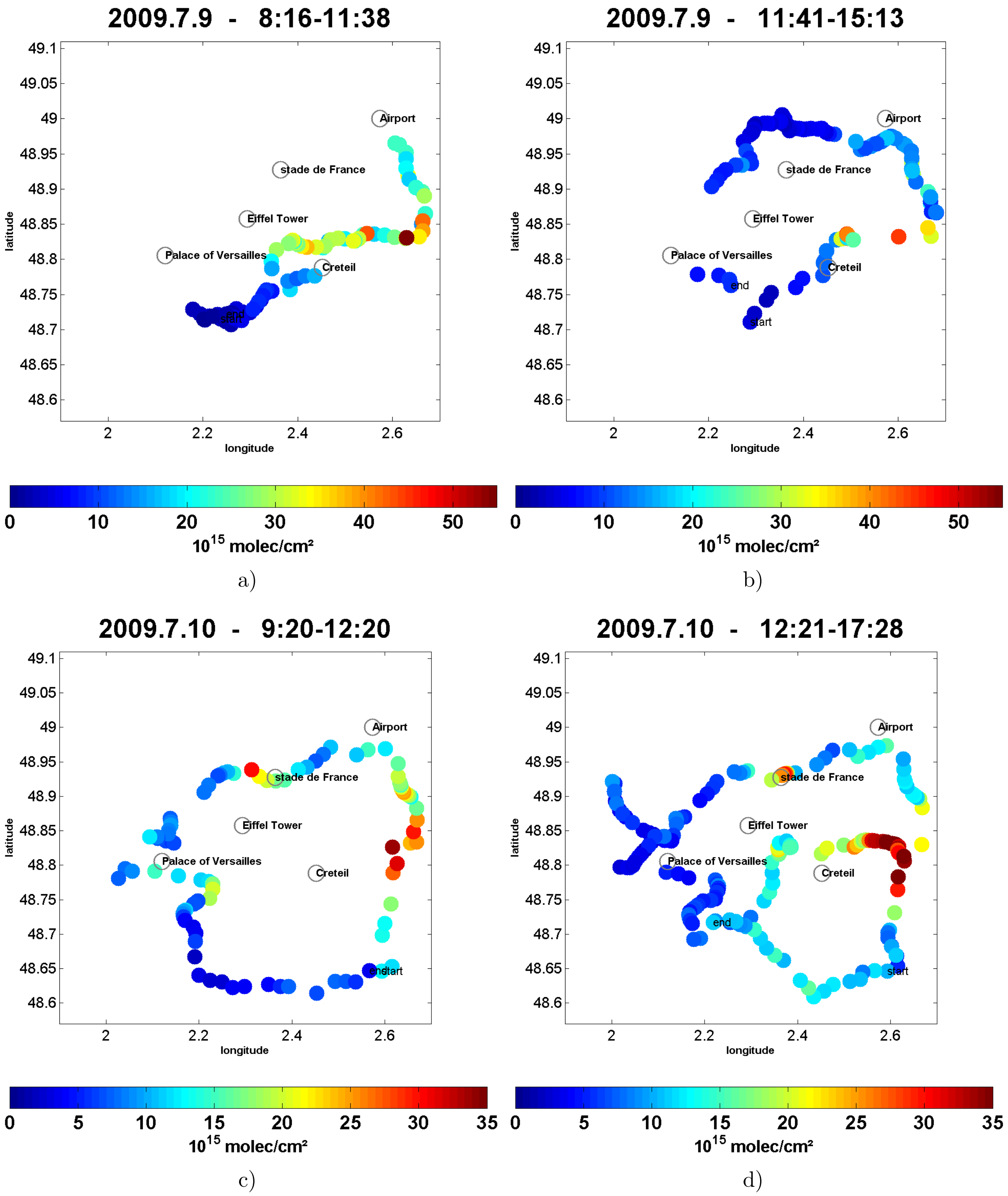

a) b) c) d)

Figure A.3: The TVCDs of NO_2 in Paris on July 9 (a), July 9 (b), July 10 (c) and July 10 (d), 2009.

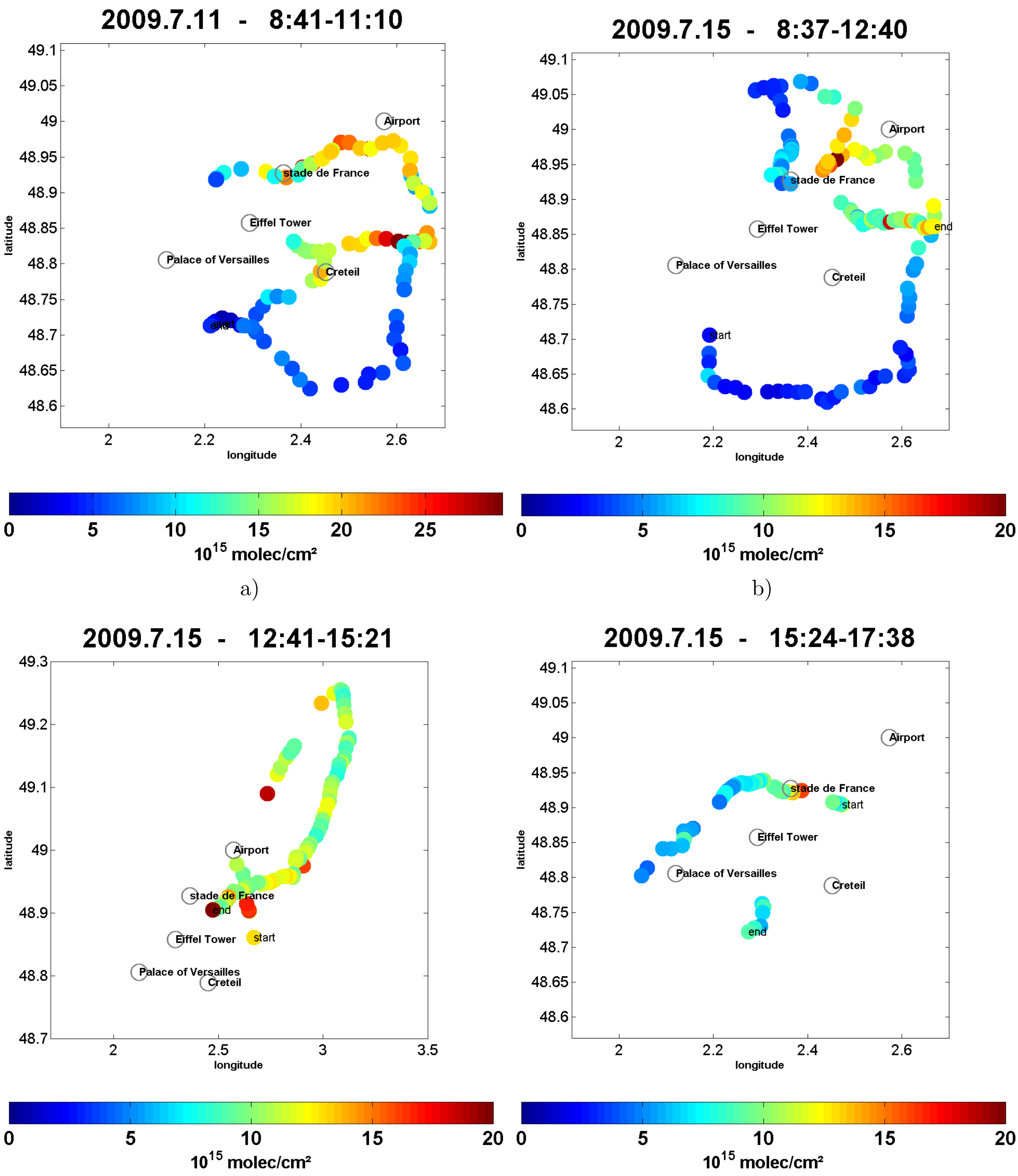

a)

b)

c)

d)

Figure A.4: The TVCDs of NO_2 in Paris on July 11 (a), July 15 (b), July 15 (c) and July 15 (d), 2009.

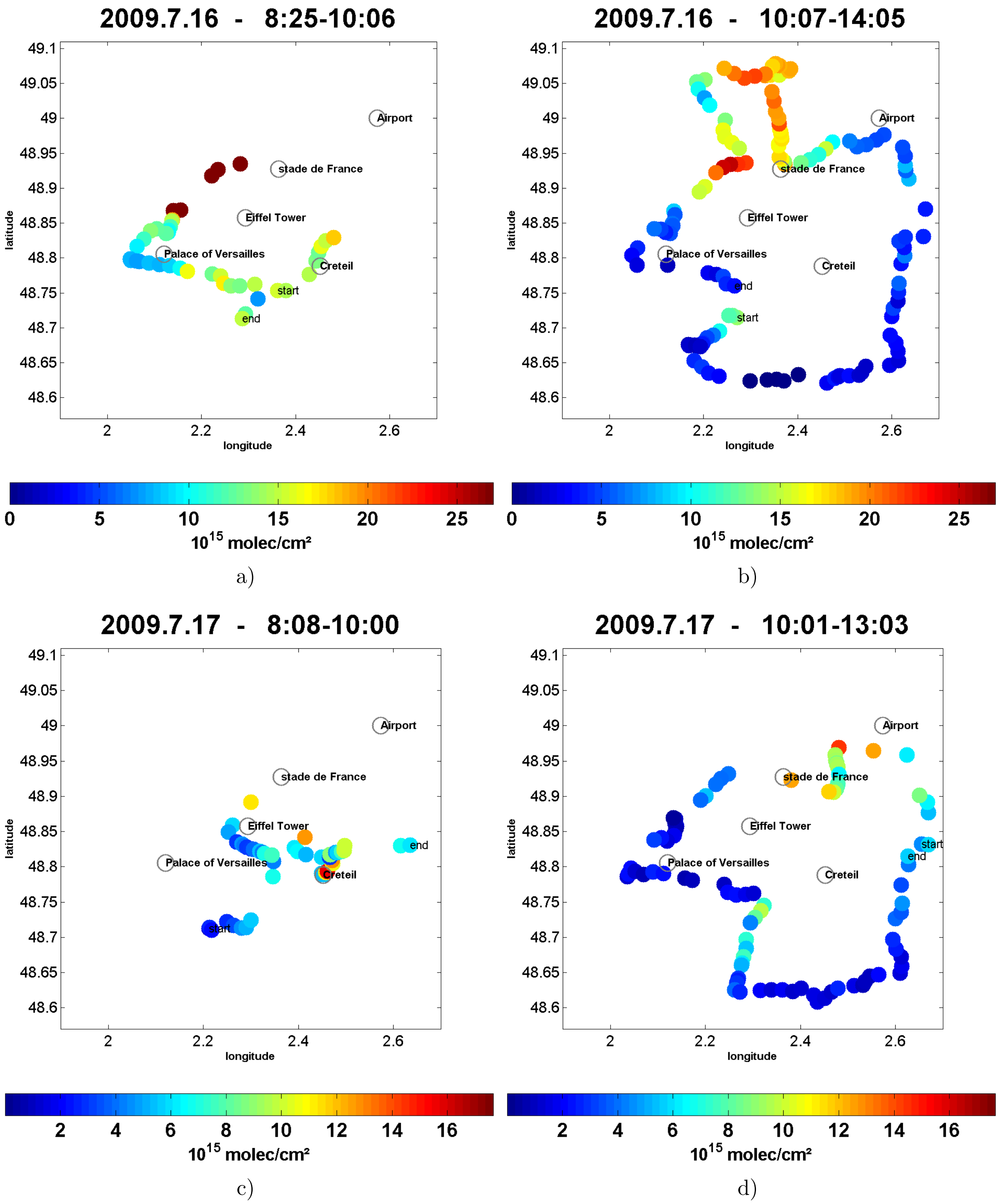

Figure A.5: The TVCDs of NO_2 in Paris on July 16 (a), July 16 (b), July 17 (c) and July 17 (d), 2009.

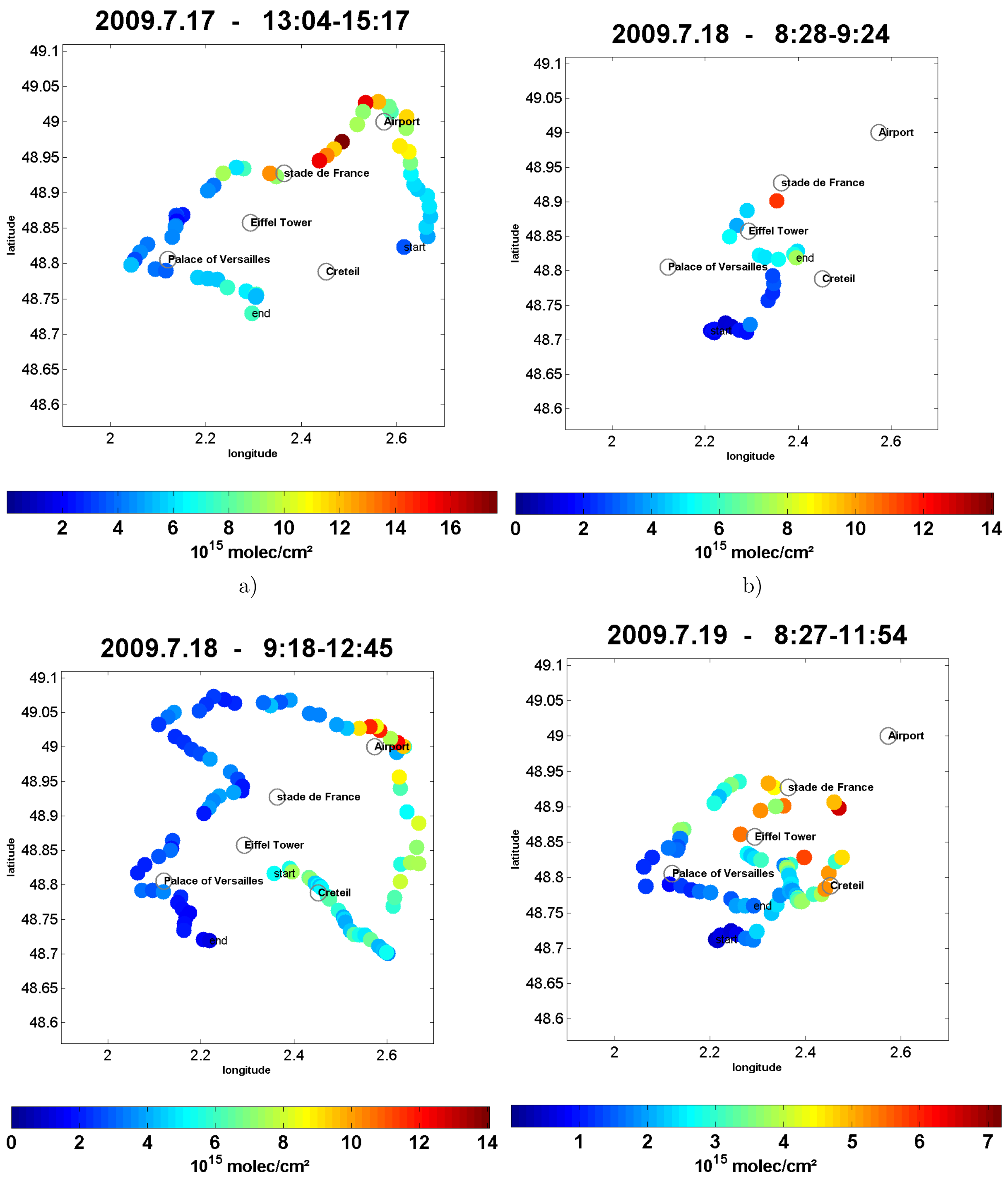

a) b) c) d)

Figure A.6: The TVCDs of NO_2 in Paris on July 17 (a), July 18 (b), July 18 (c) and July 19 (d), 2009.

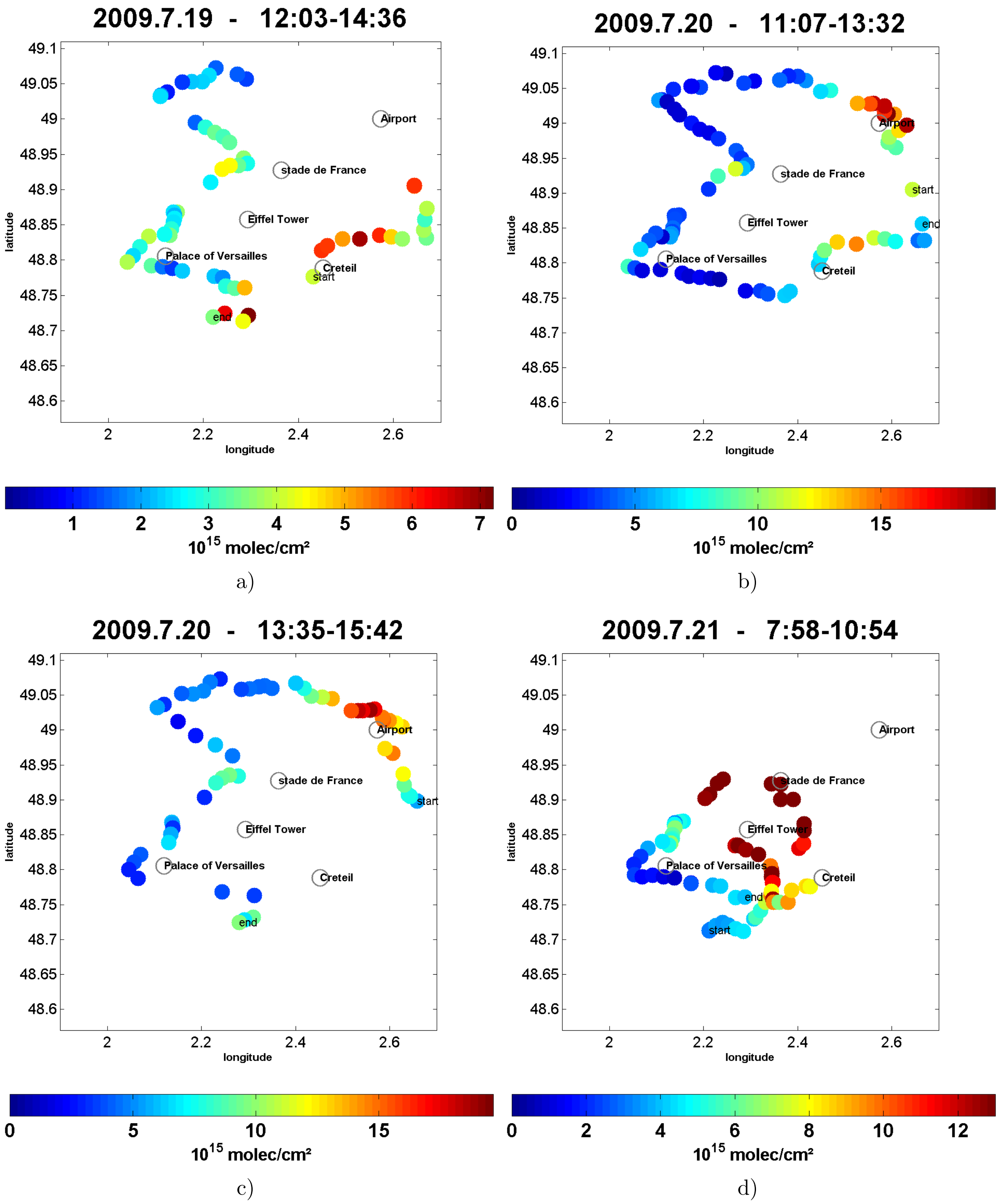

a) b) c) d)

Figure A.7: The TVCDs of NO_2 in Paris on July 19 (a), July 20 (b), July 20 (c) and July 21 (d), 2009.

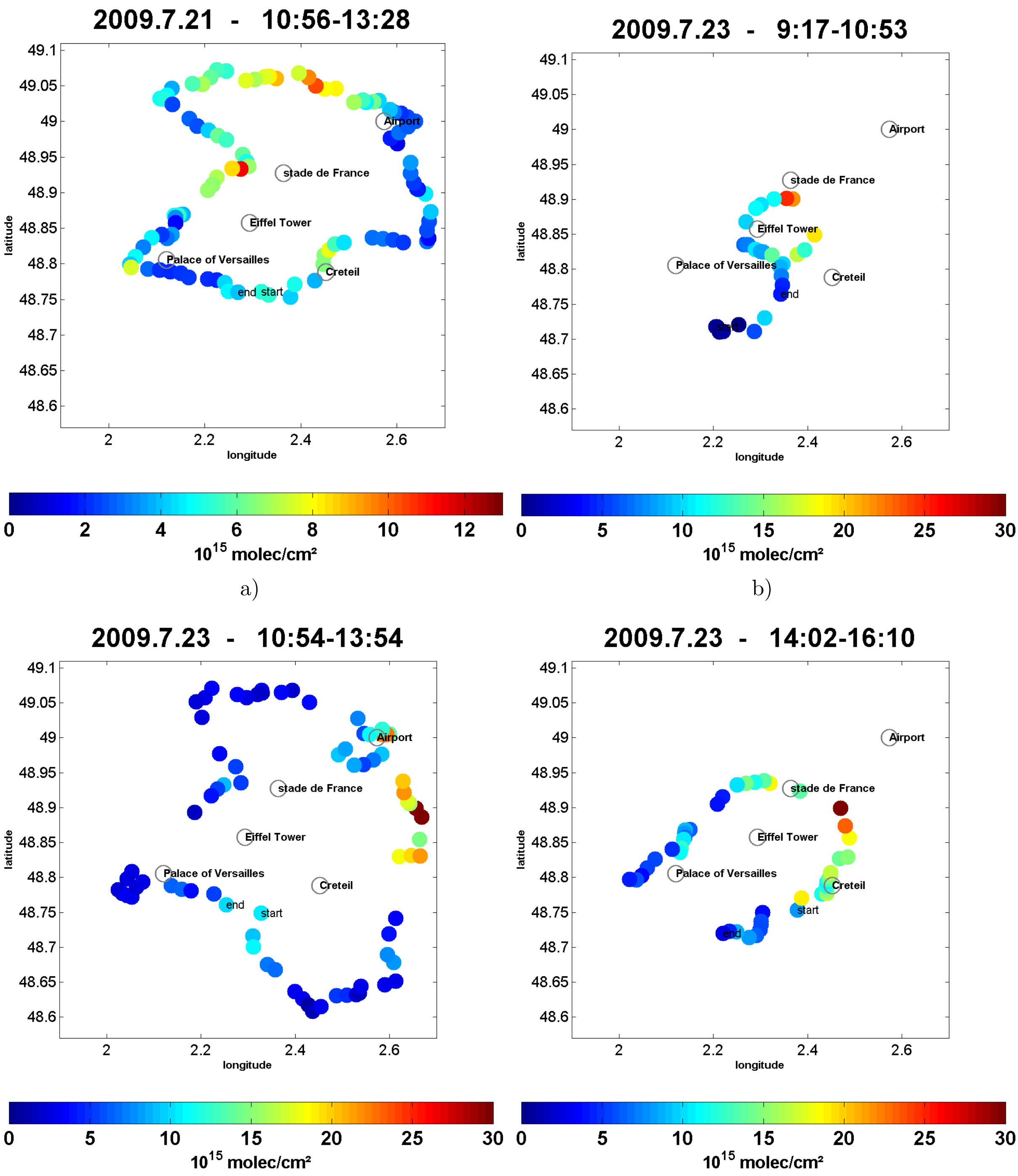

a) b) c) d)

Figure A.8: The TVCDs of NO_2 in Paris on July 21 (a), July 23 (b), July 23 (c) and July 23 (d), 2009.

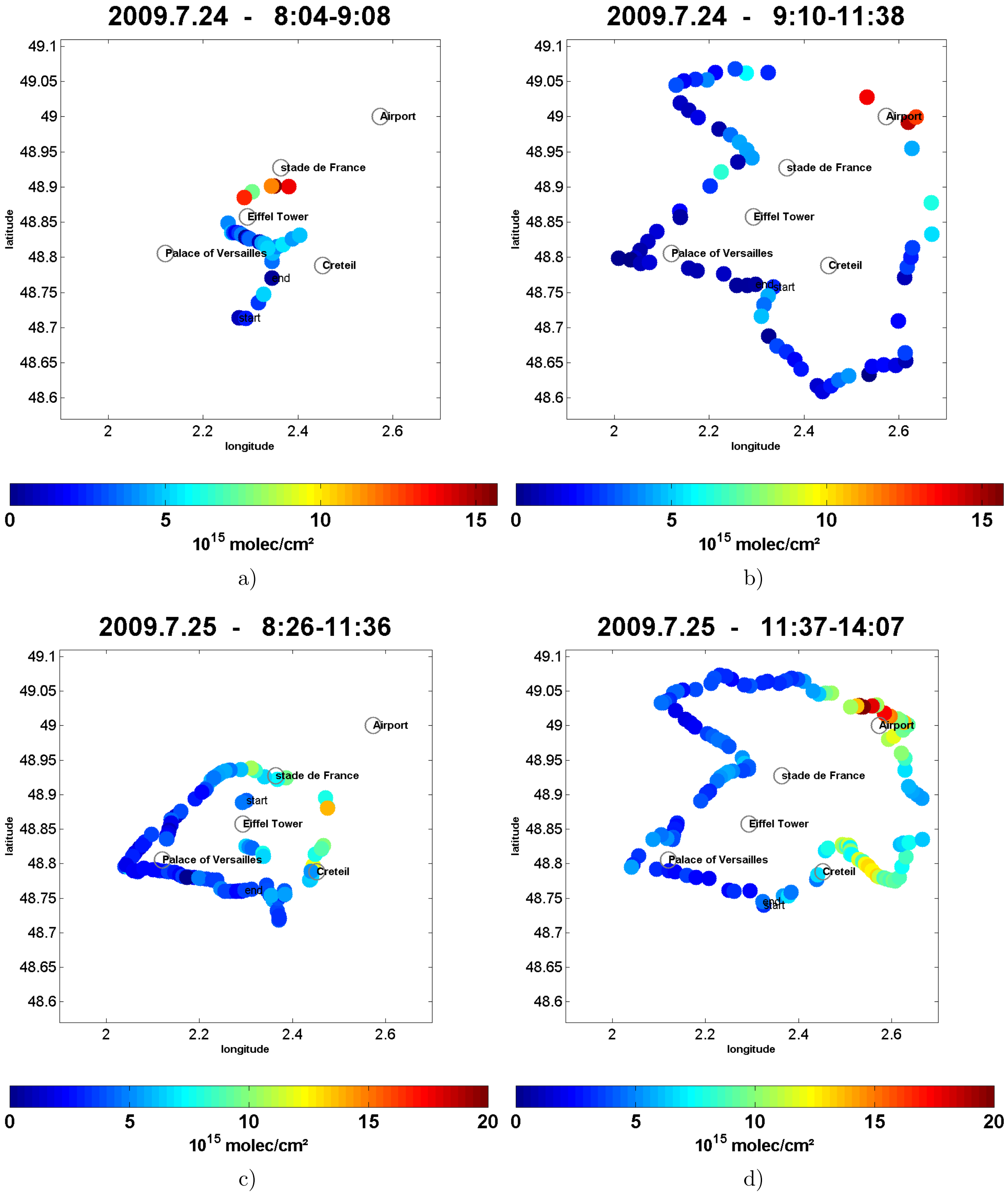

a) b) c) d)

Figure A.9: The TVCDs of NO_2 in Paris on July 24 (a), July 24 (b), July 25 (c) and July 25 (d), 2009.

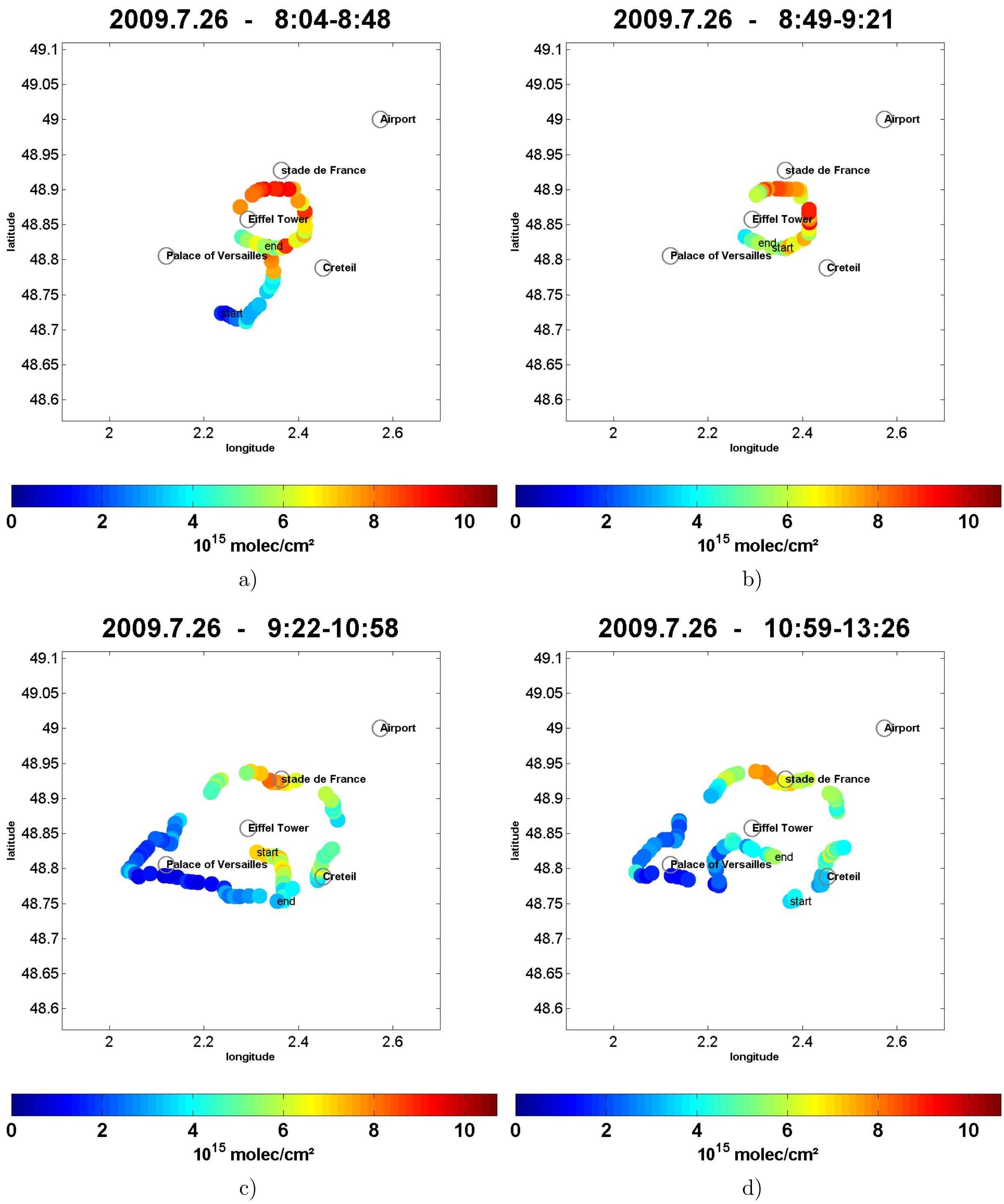

a) b) c) d)

Figure A.10: The TVCDs of NO_2 in Paris on July 26 (a), July 26 (b), July 26 (c) and July 26 (d), 2009.

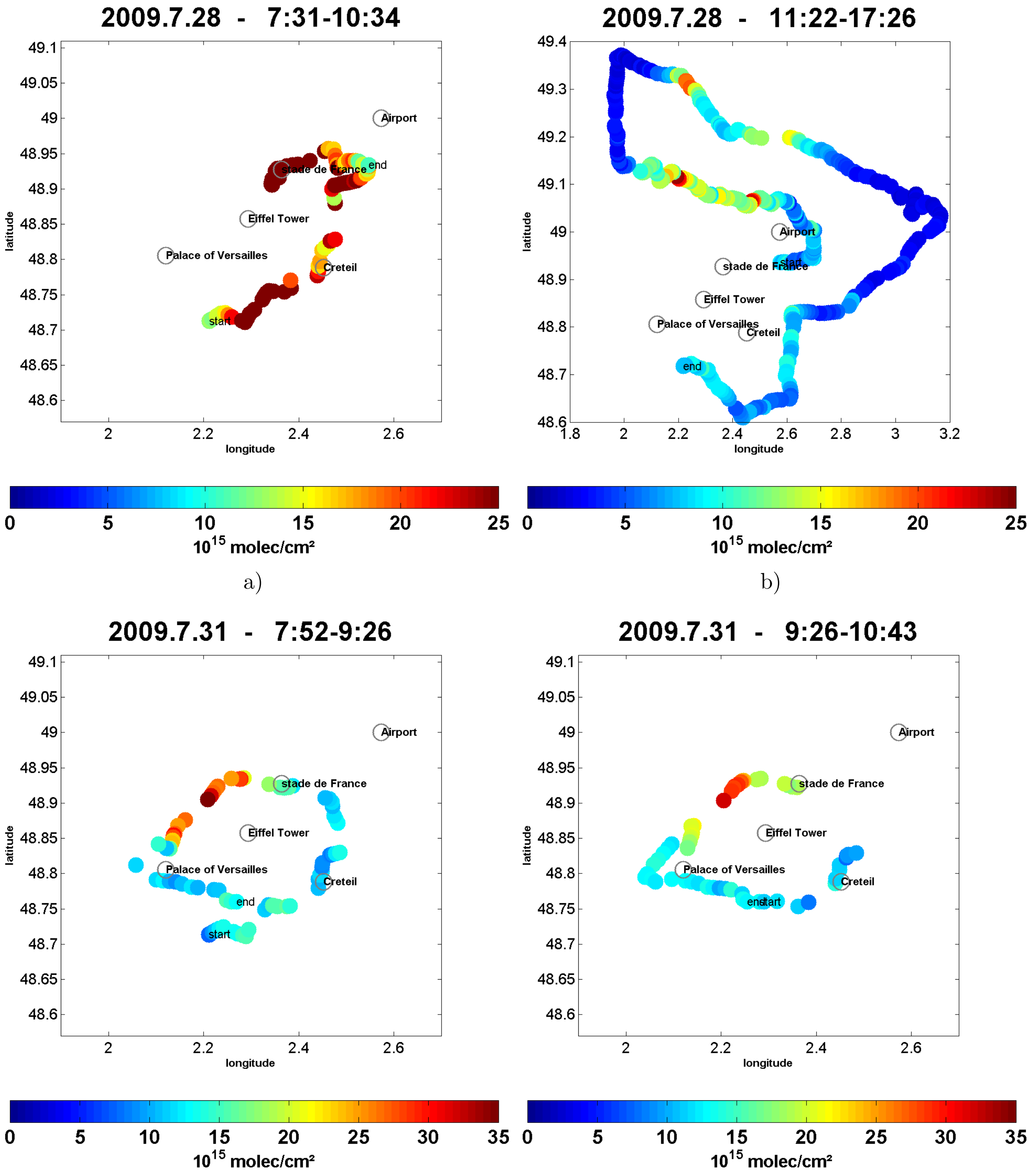

a) b)

c) d)

Figure A.11: The TVCDs of NO_2 in Paris on July 28 (a), July 28 (b), July 31 (c) and July 31 (d), 2009.

A.1.2 Winter campaign, 2010

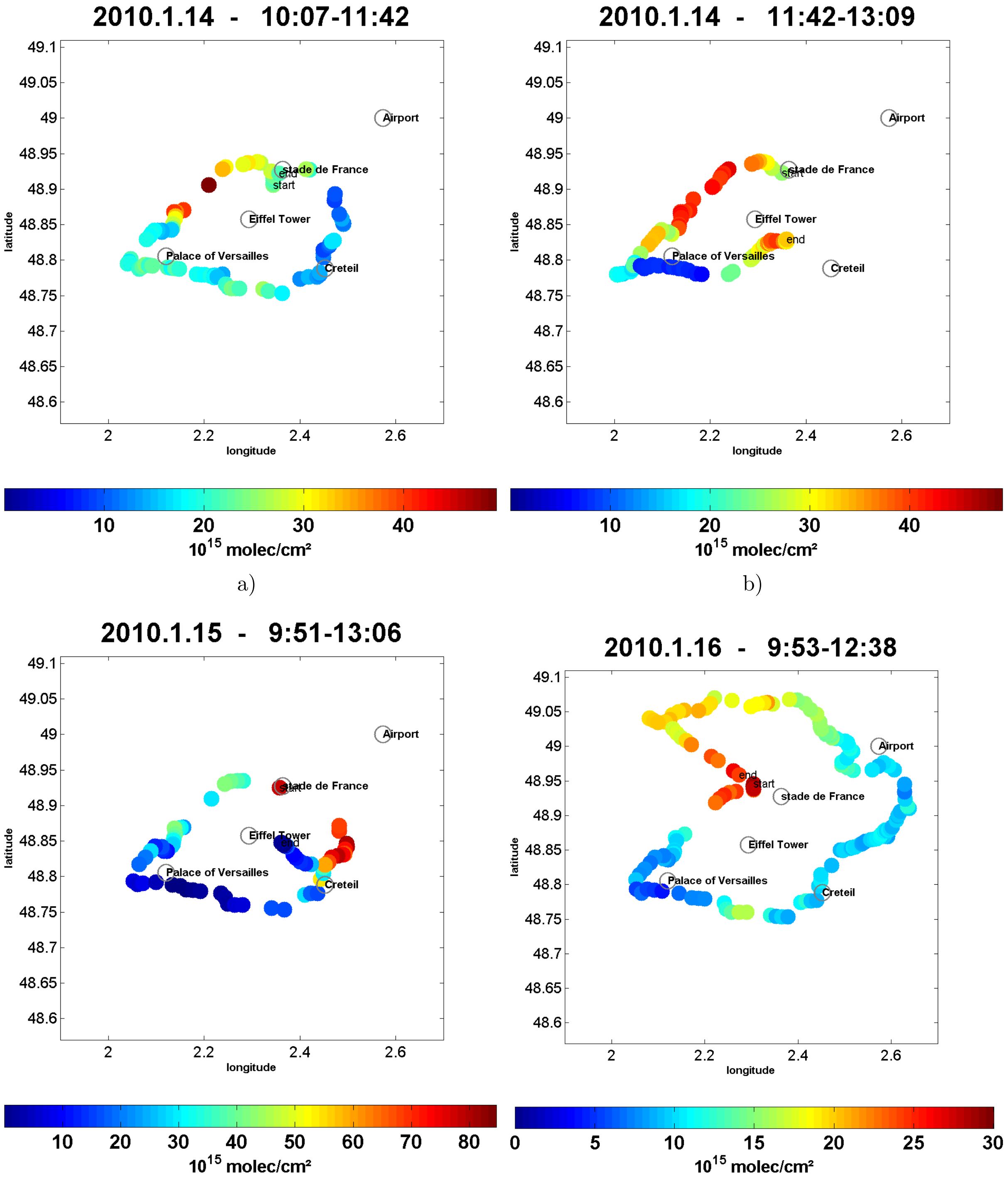

a)

b)

c)

d)

Figure A.12: The TVCDs of NO_2 in Paris on January 14 (a), January 14 (b), January 15 (c) and January 16 (d), 2010.

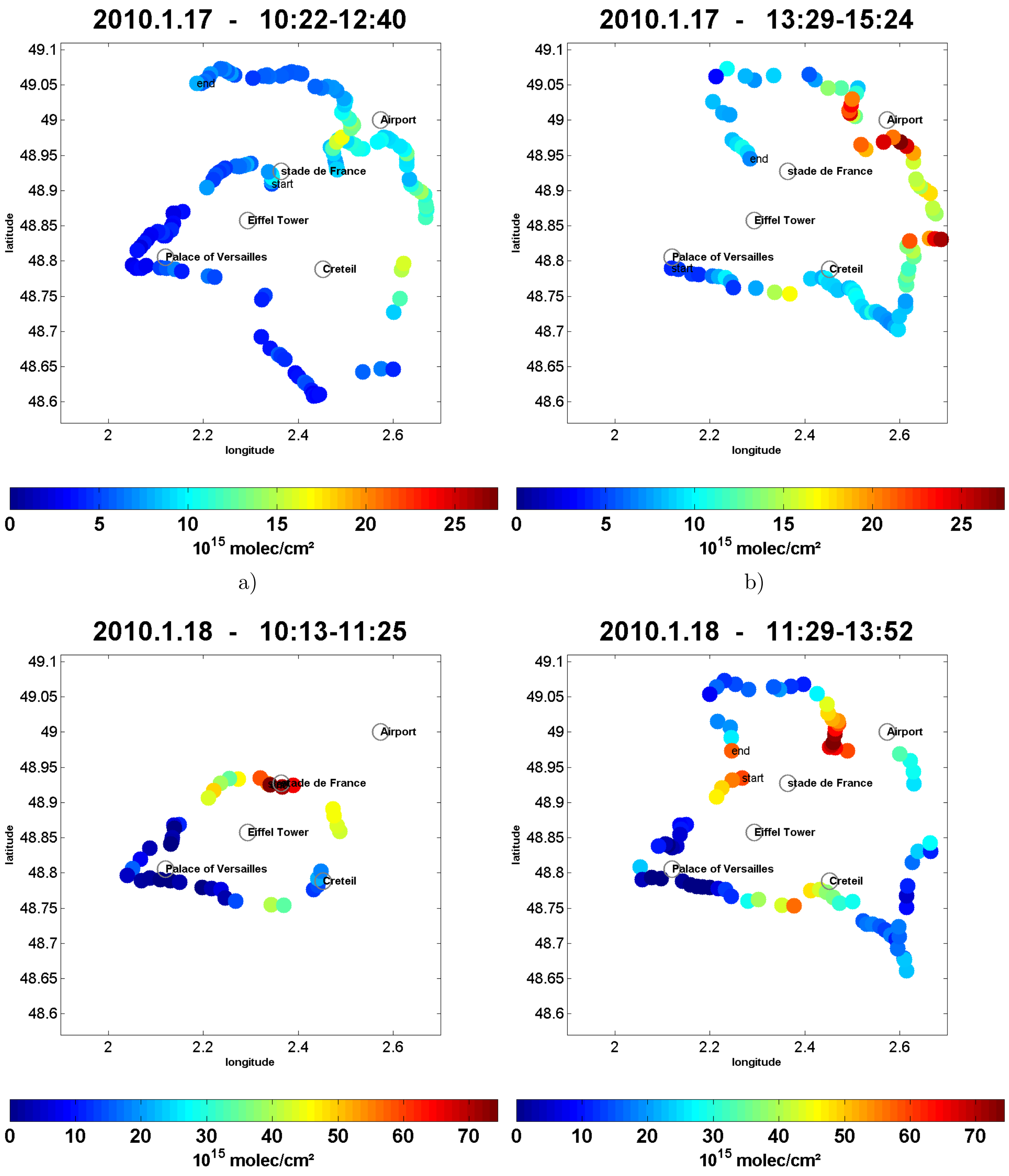

a) b) c) d)

Figure A.13: The TVCDs of NO_2 in Paris on January 17 (a), January 17 (b), January 18 (c) and January 18 (d), 2010.

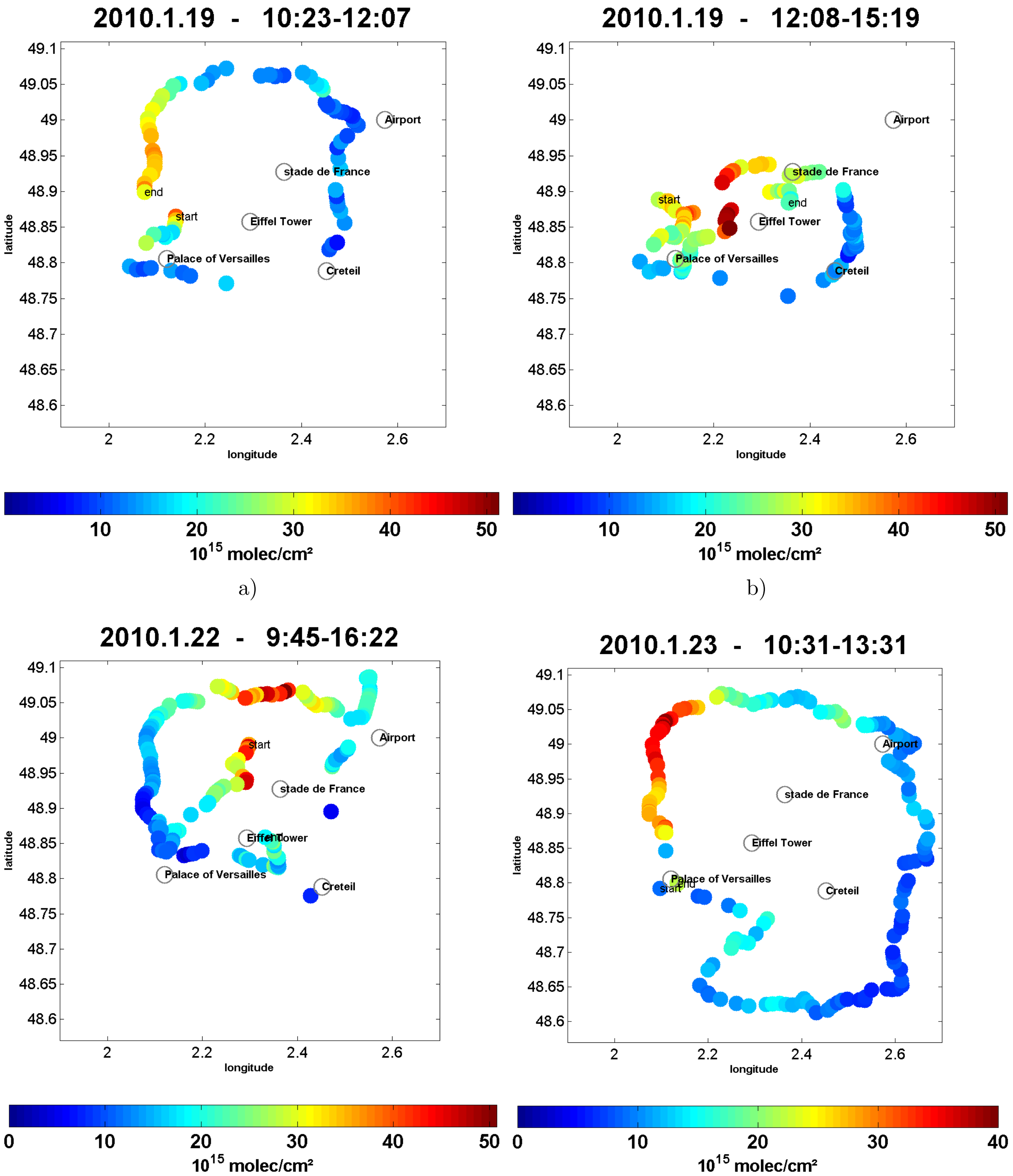

a)

b)

c)

d)

Figure A.14: The TVCDs of NO_2 in Paris on January 19 (a), January 19 (b), January 22 (c) and January 23 (d), 2010.

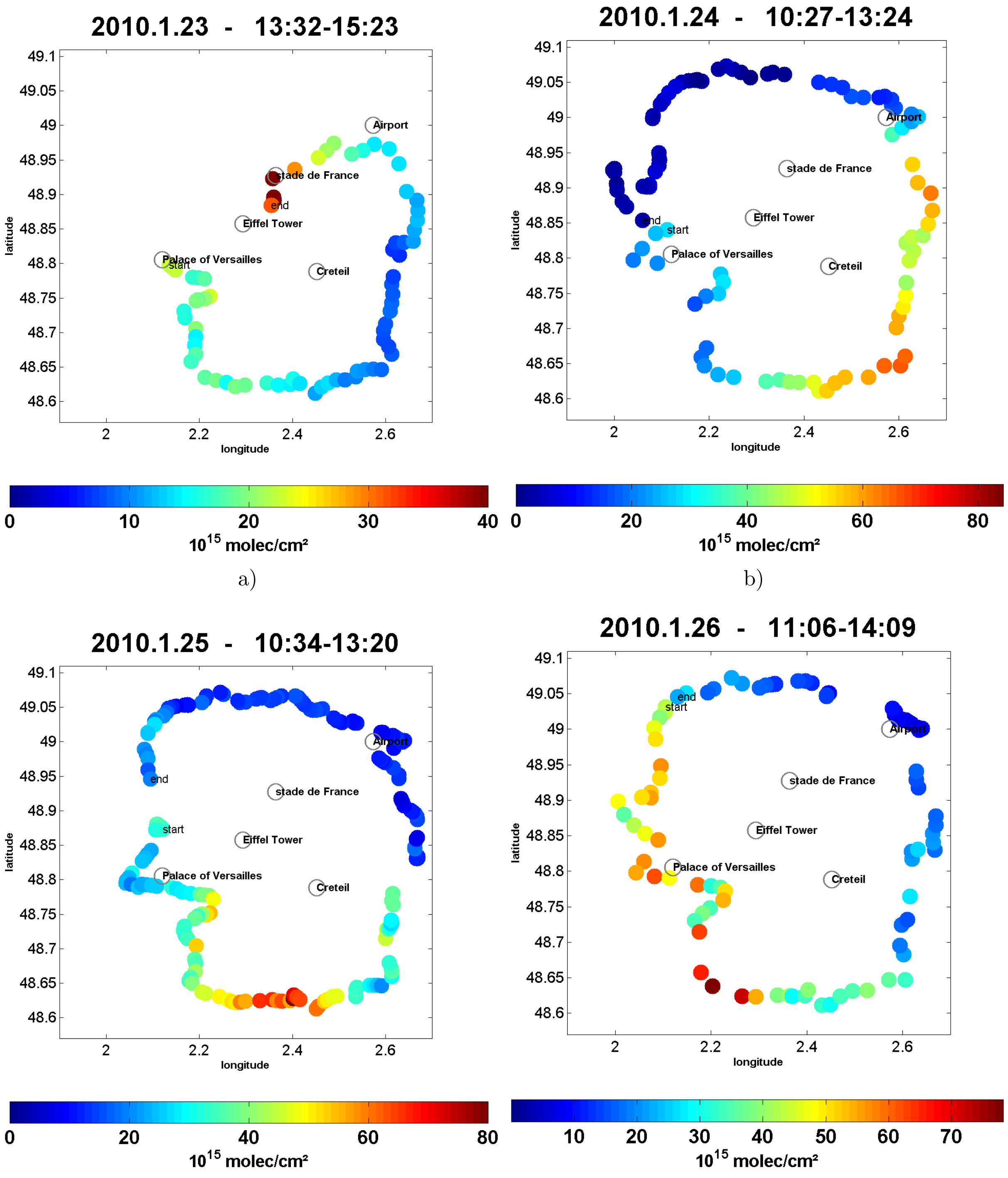

a) b)

c) d)

Figure A.15: The TVCDs of NO_2 in Paris on January 23 (a), January 24 (b), January 25 (c) and January 26 (d), 2010.

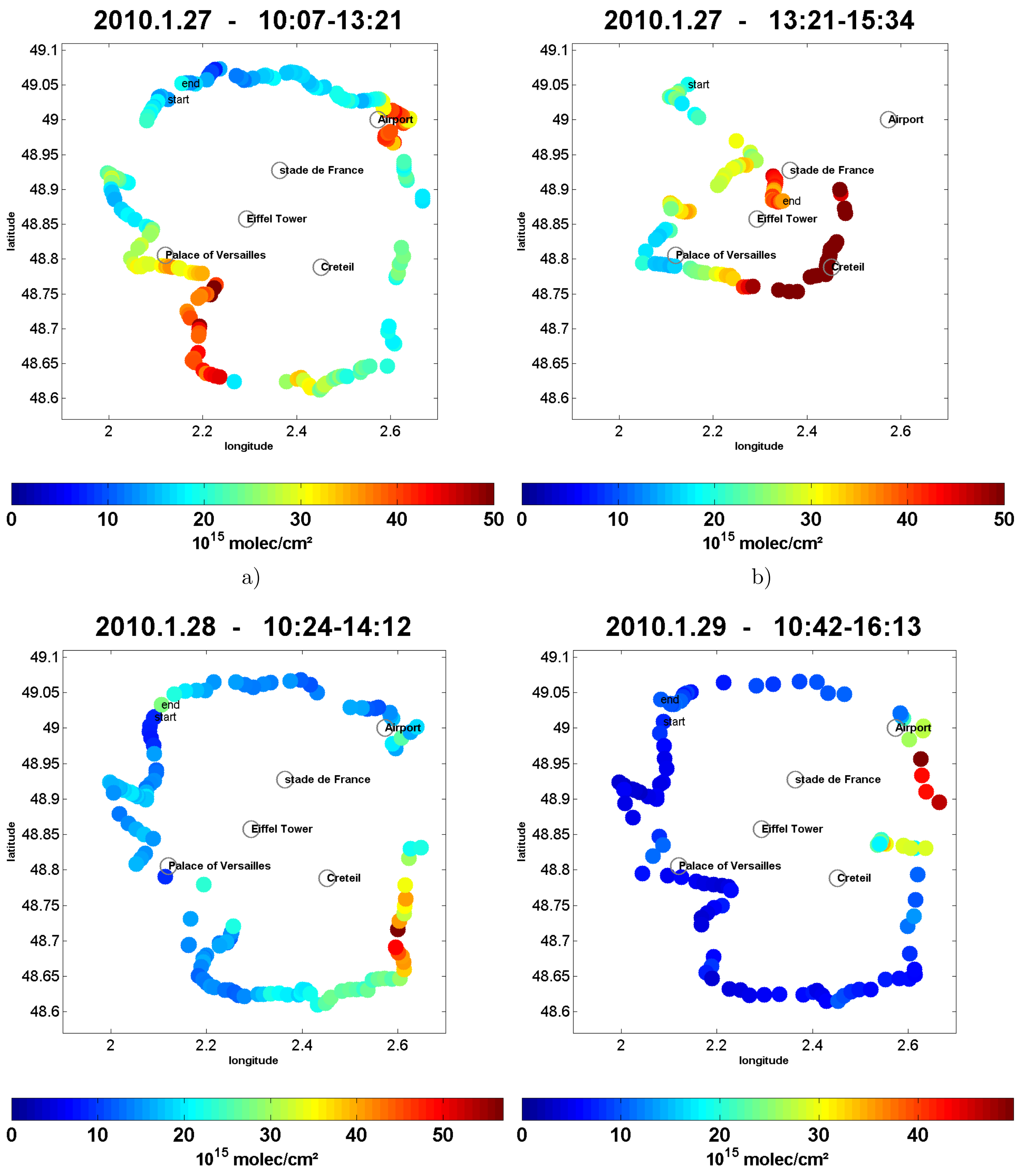

a) b) c) d)

Figure A.16: The TVCDs of NO_2 in Paris on January 27 (a), January 27 (b), January 28 (c) and January 29 (d), 2010.

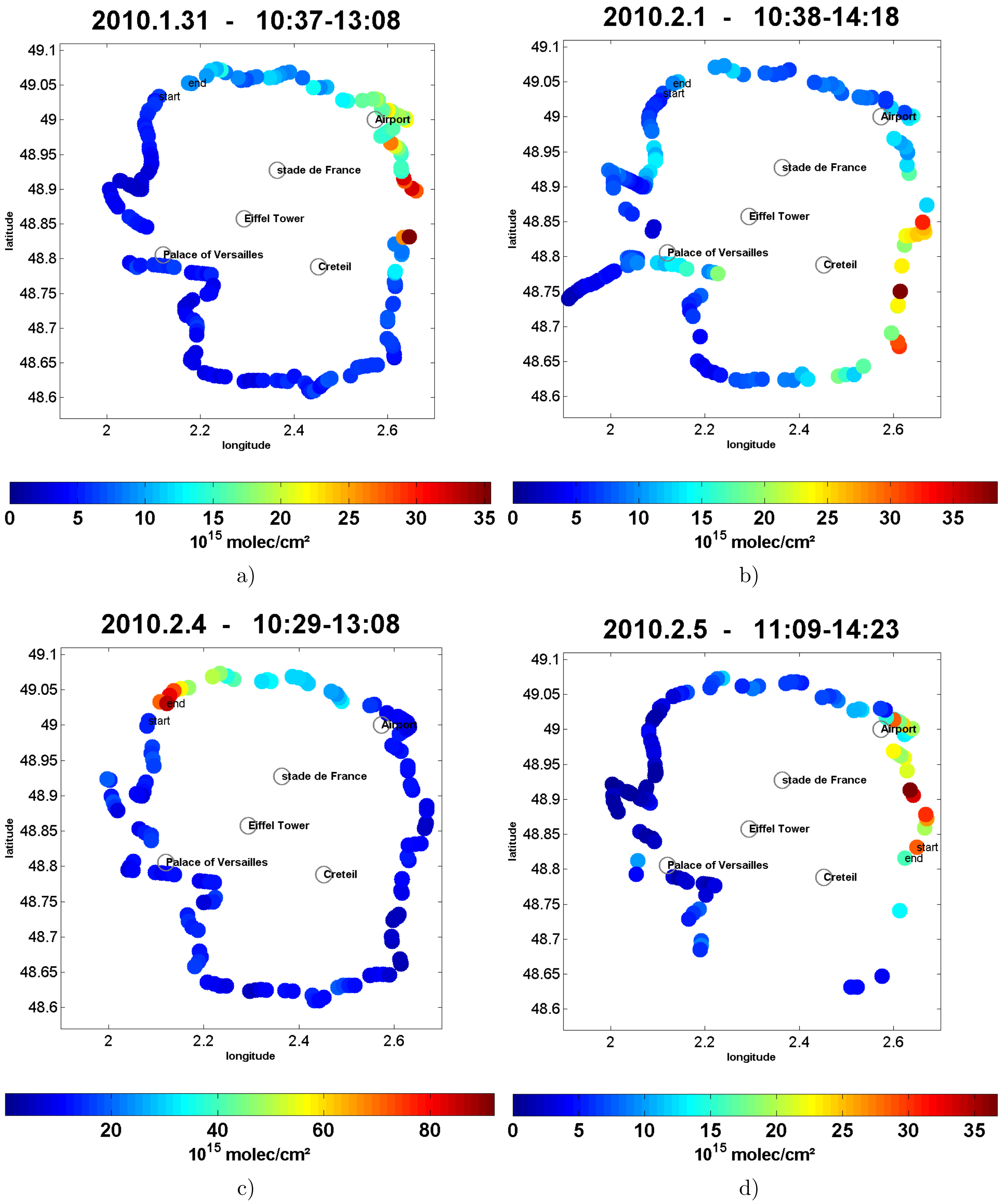

a)

b)

c)

d)

Figure A.17: The TVCDs of NO_2 in Paris on January 31 (a), February 1 (b), February 4 (c) and February 5 (d), 2010.

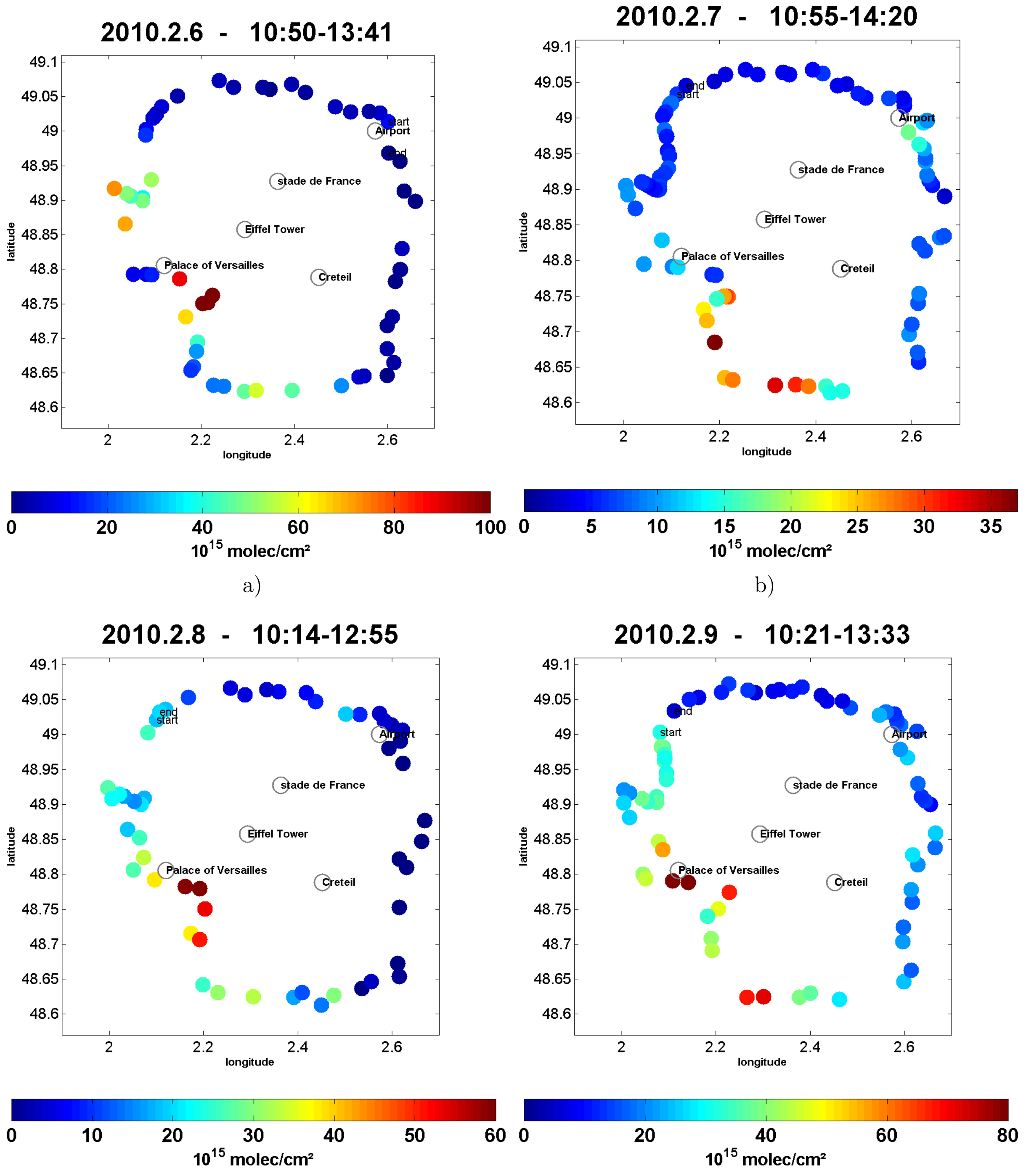

a)

b)

c)

d)

Figure A.18: The TVCDs of NO_2 in Paris on February 6 (a), February 7 (b), February 8 (c) and February 9 (d), 2010.

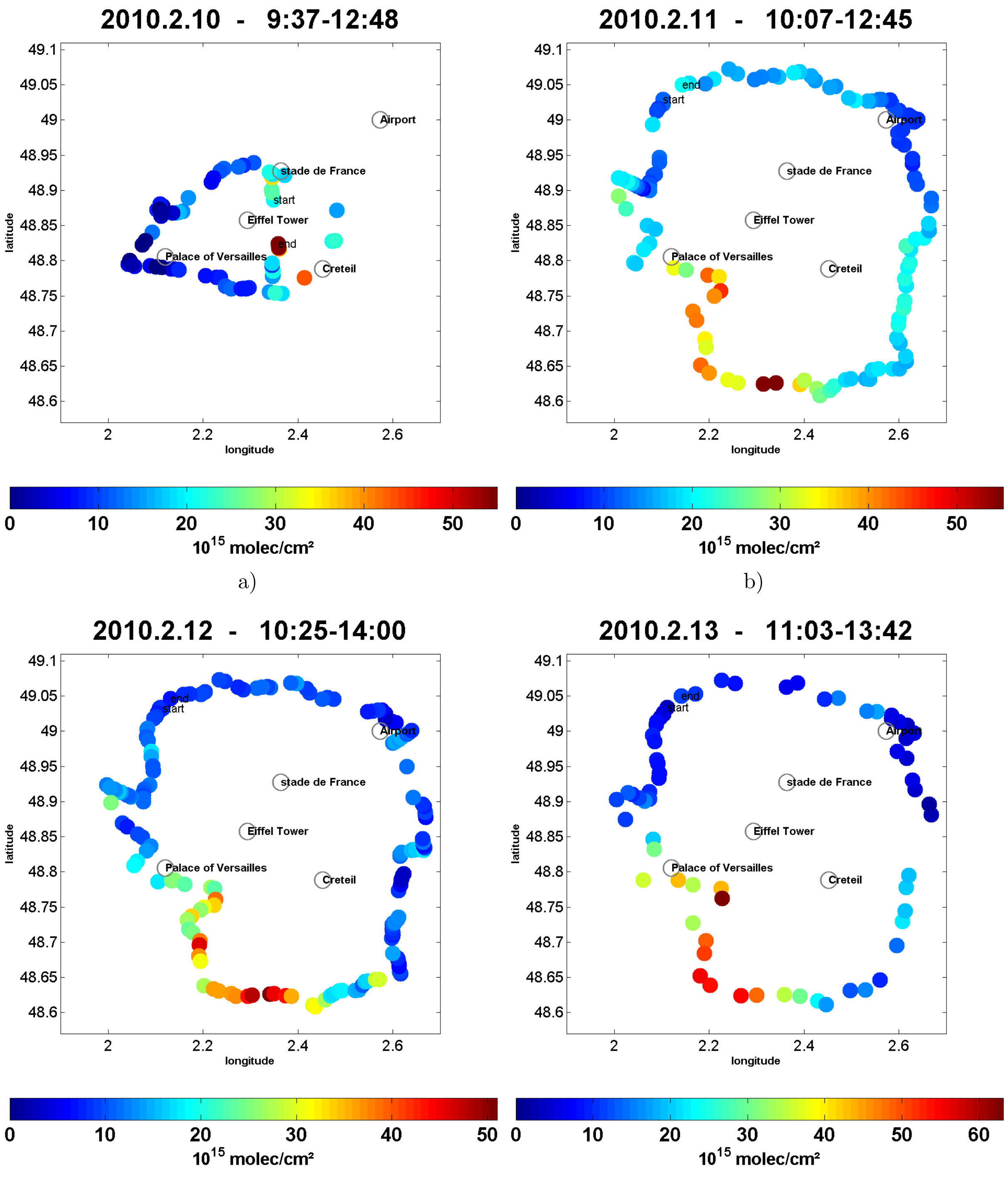

a)

b)

c)

d)

Figure A.19: The TVCDs of NO_2 in Paris on February 10 (a), February 11 (b), February 12 (c) and February 13 (d), 2010.

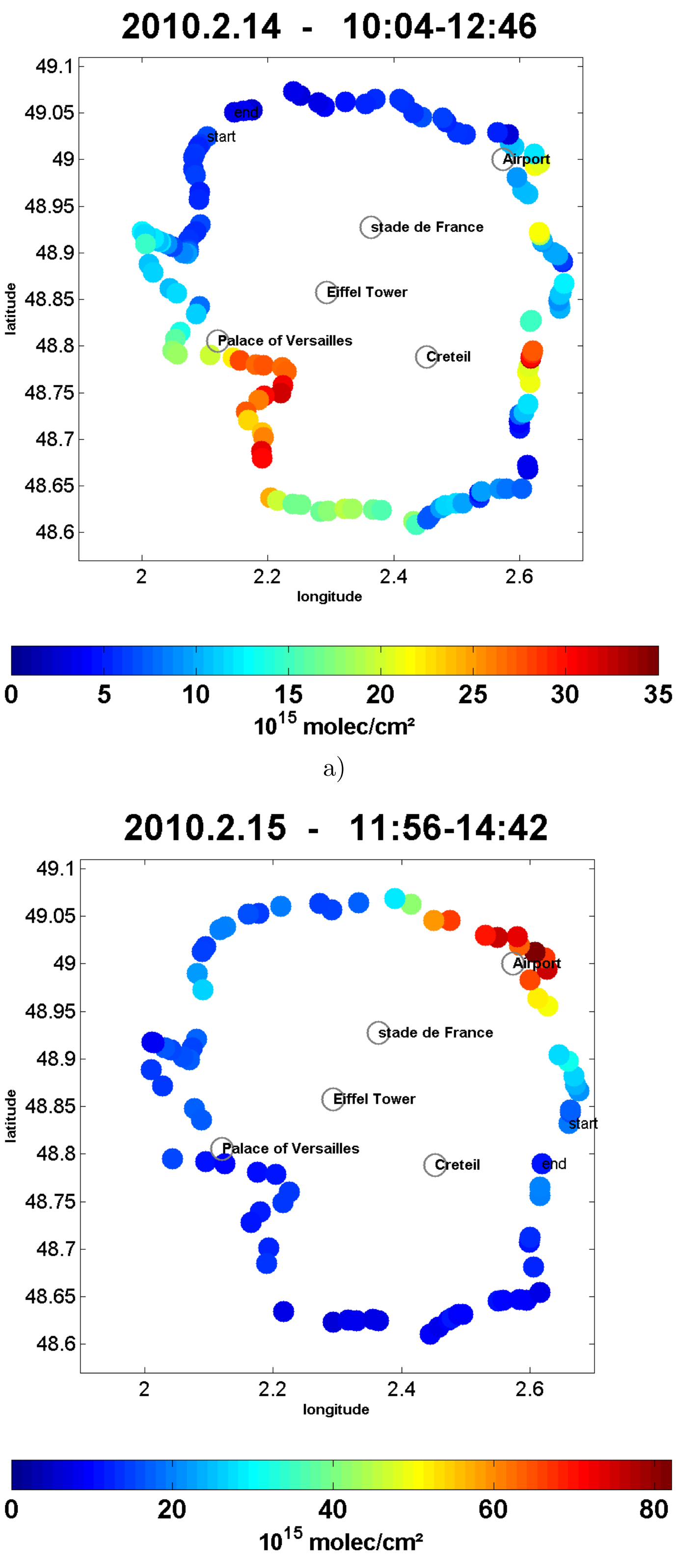

a)

b)

Figure A.20: The TVCDs of NO_2 in Paris on February 14 (a) and February 15 (b), 2010.

Appendix B

B.1 The selected days from the Paris campaigns for estimation of NO_x emissions

Here we present the tropospheric vertical column densities (TVCDs) of nitrogen dioxide from mobile MAX-DOAS in Paris together with associated wind vectors for the days, which were selected to determine the NO_x emissions.

B.1.1 Summer campaign, 2009

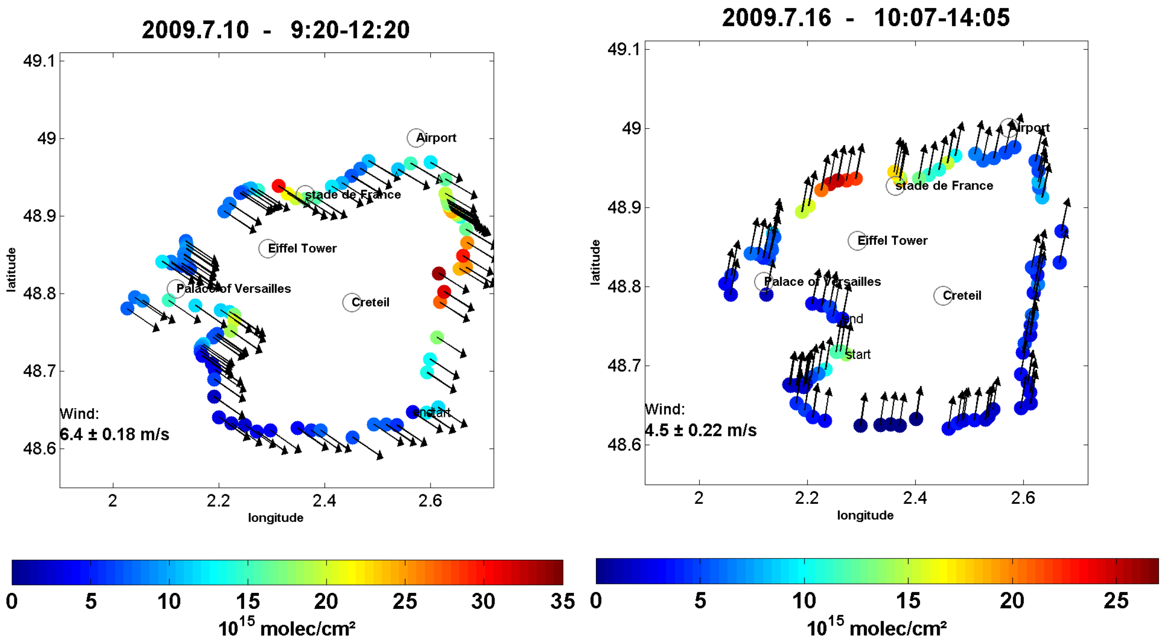

a) b)

Figure B.1: TVCDs of NO_2 in Paris with associated wind vectors for July 10 (a) and July 16 (b), 2009.

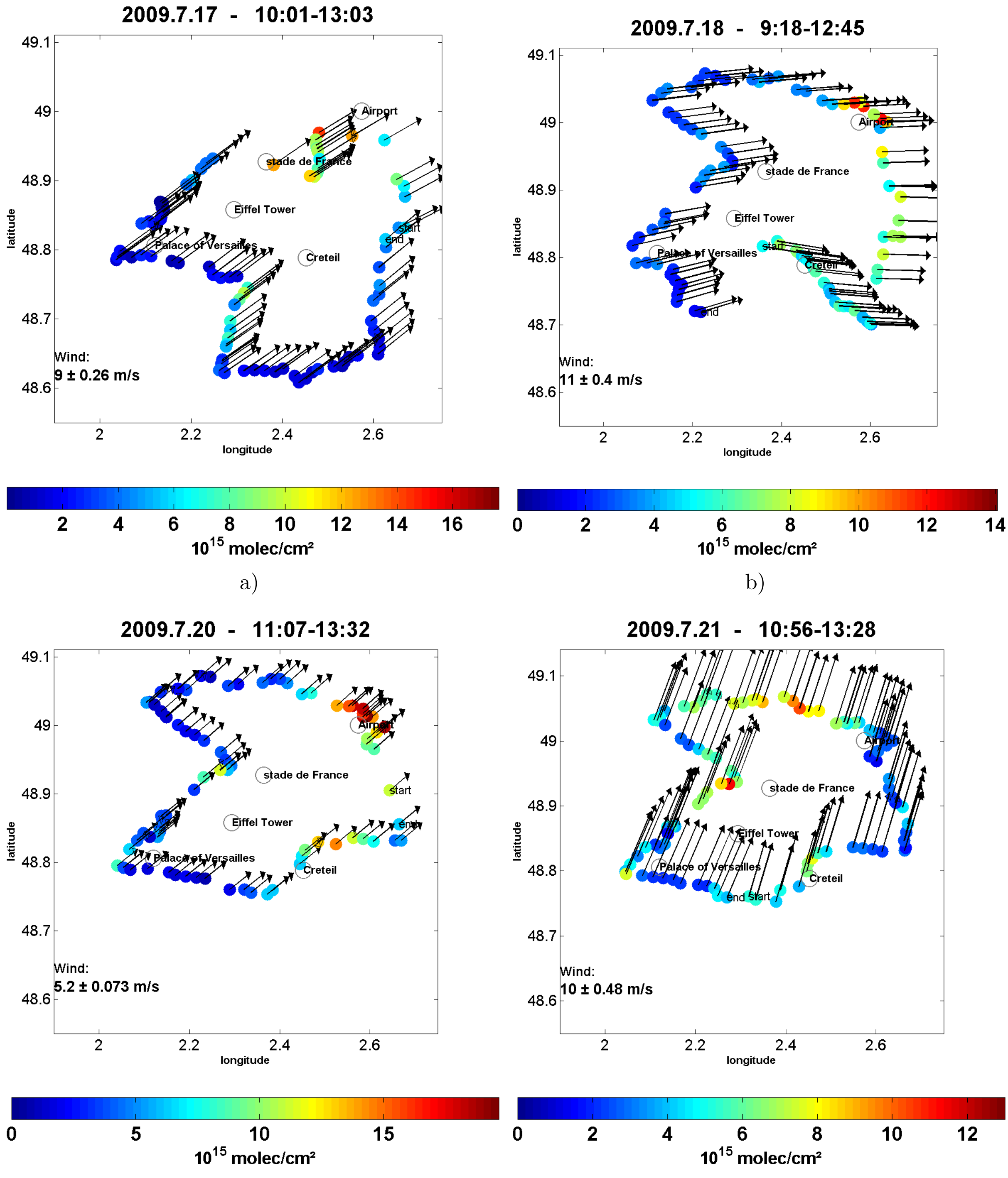

a)

b)

c)

d)

Figure B.2: TVCDs of NO_2 in Paris with associated wind vectors for July 17 (a), July 18 (b), July 20 (c) and July 21 (d), 2009.

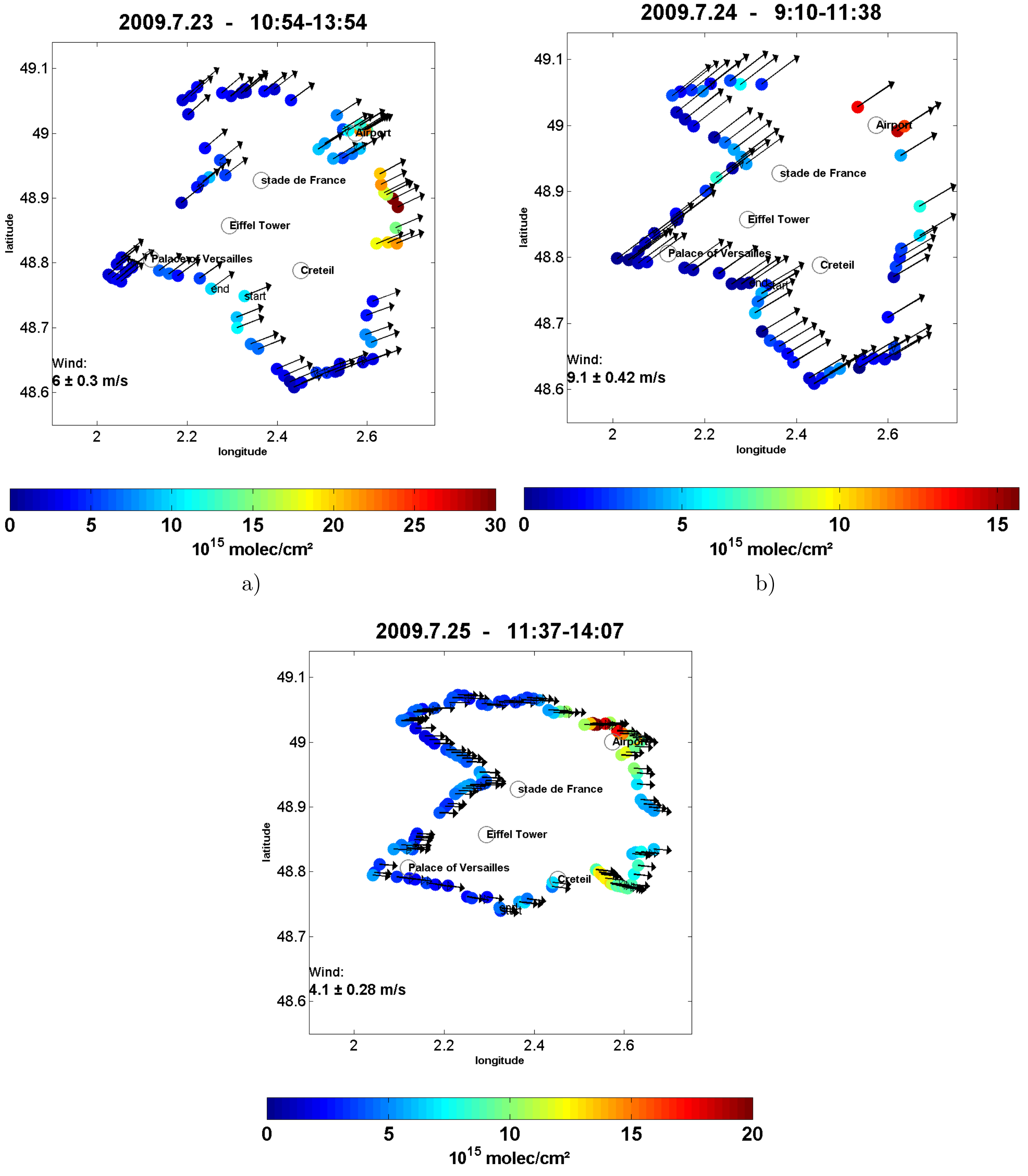

a) b)

c)

Figure B.3: TVCDs of NO_2 in Paris with associated wind vectors for July 23 (a), July 24 (b) and July 25 (c), 2009.

B.1.2 Winter campaign, 2010

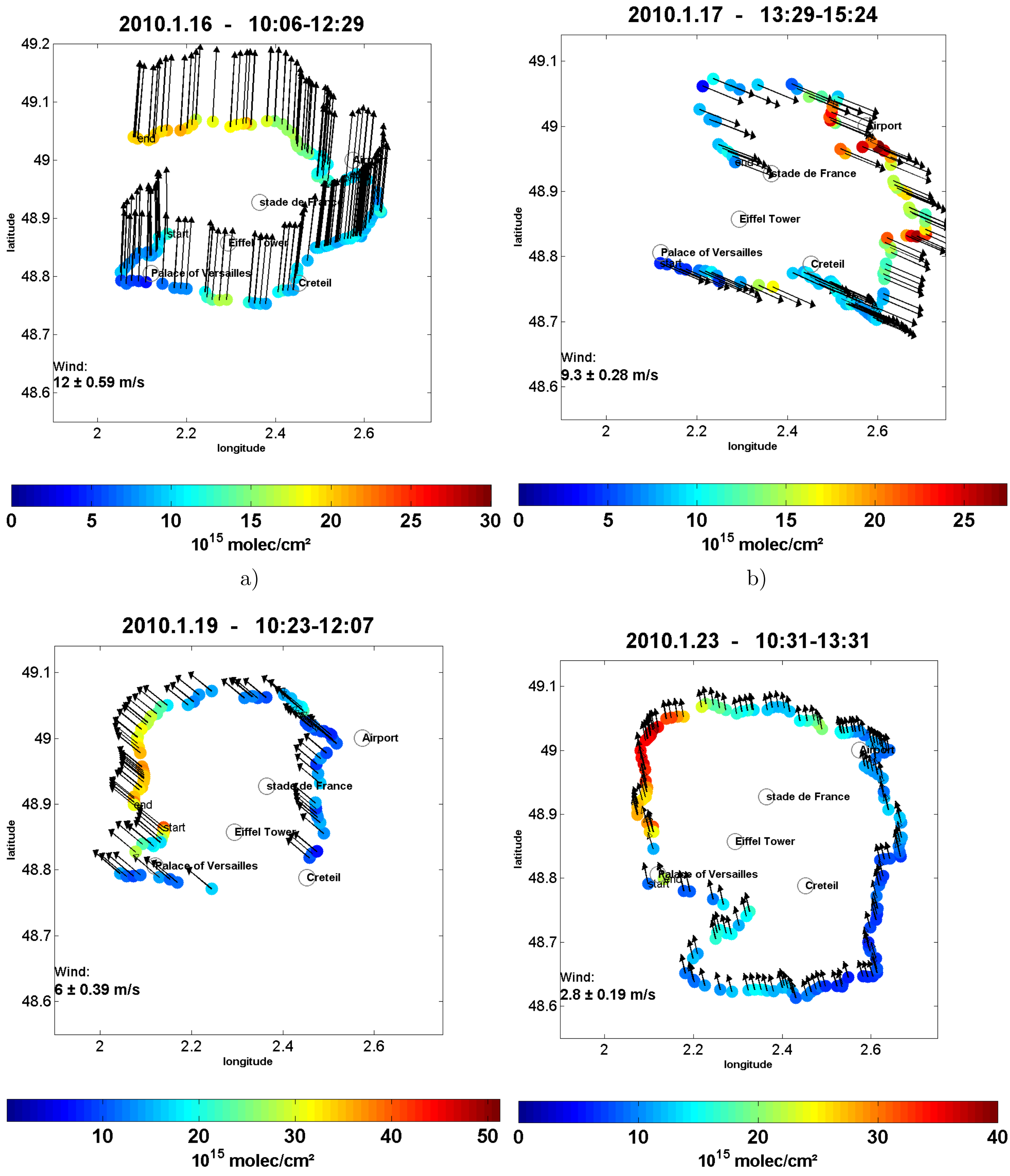

a)

b)

c)

d)

Figure B.4: TVCDs of NO_2 in Paris with associated wind vectors for January 16 (a), January 17 (b), January 19 (c) and January 23 (d), 2010.

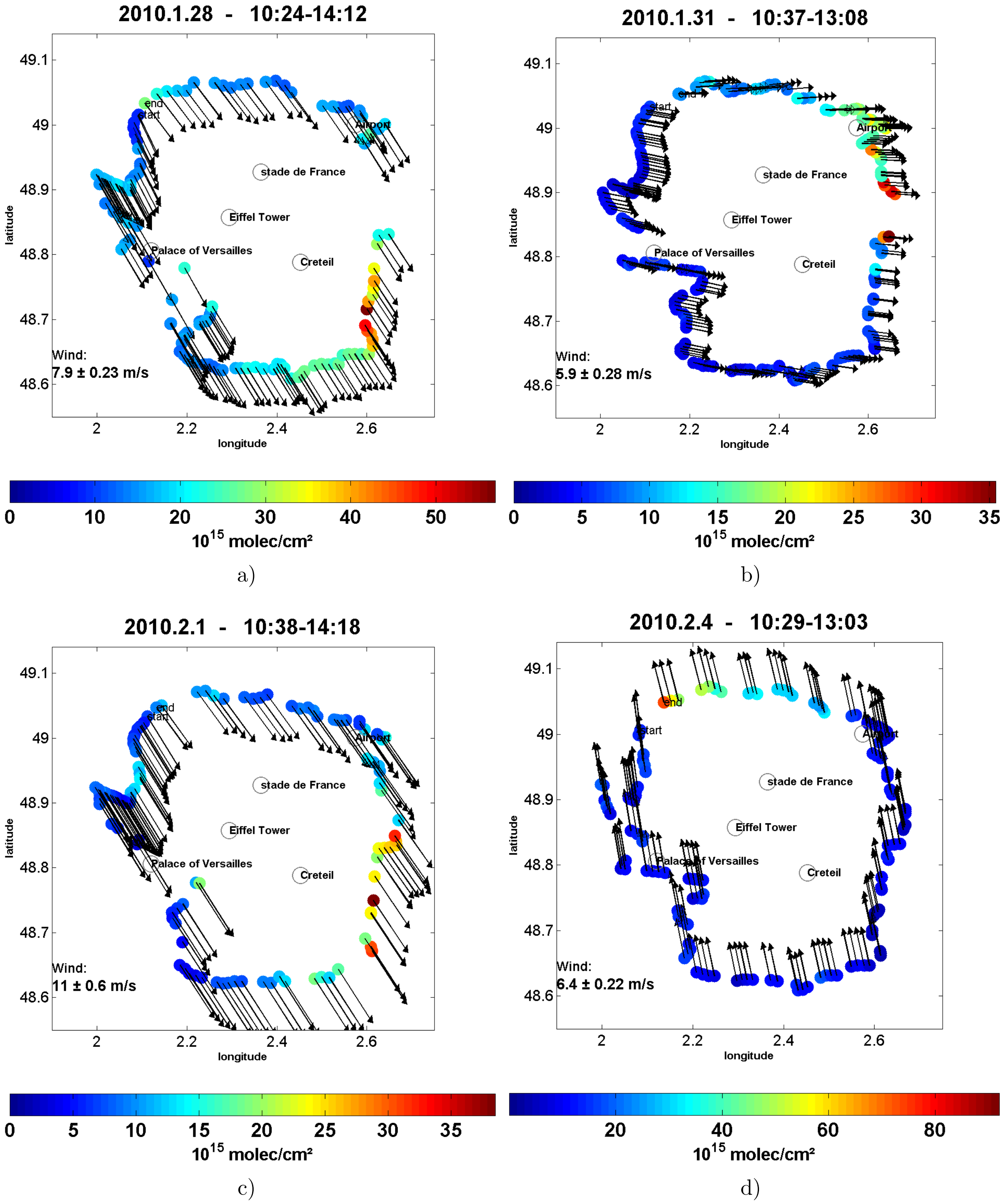

a)

b)

c)

d)

Figure B.5: TVCDs of NO_2 in Paris with associated wind vectors for January 28 (a), January 31 (b), February 1 (c) and February 4 (d), 2010.

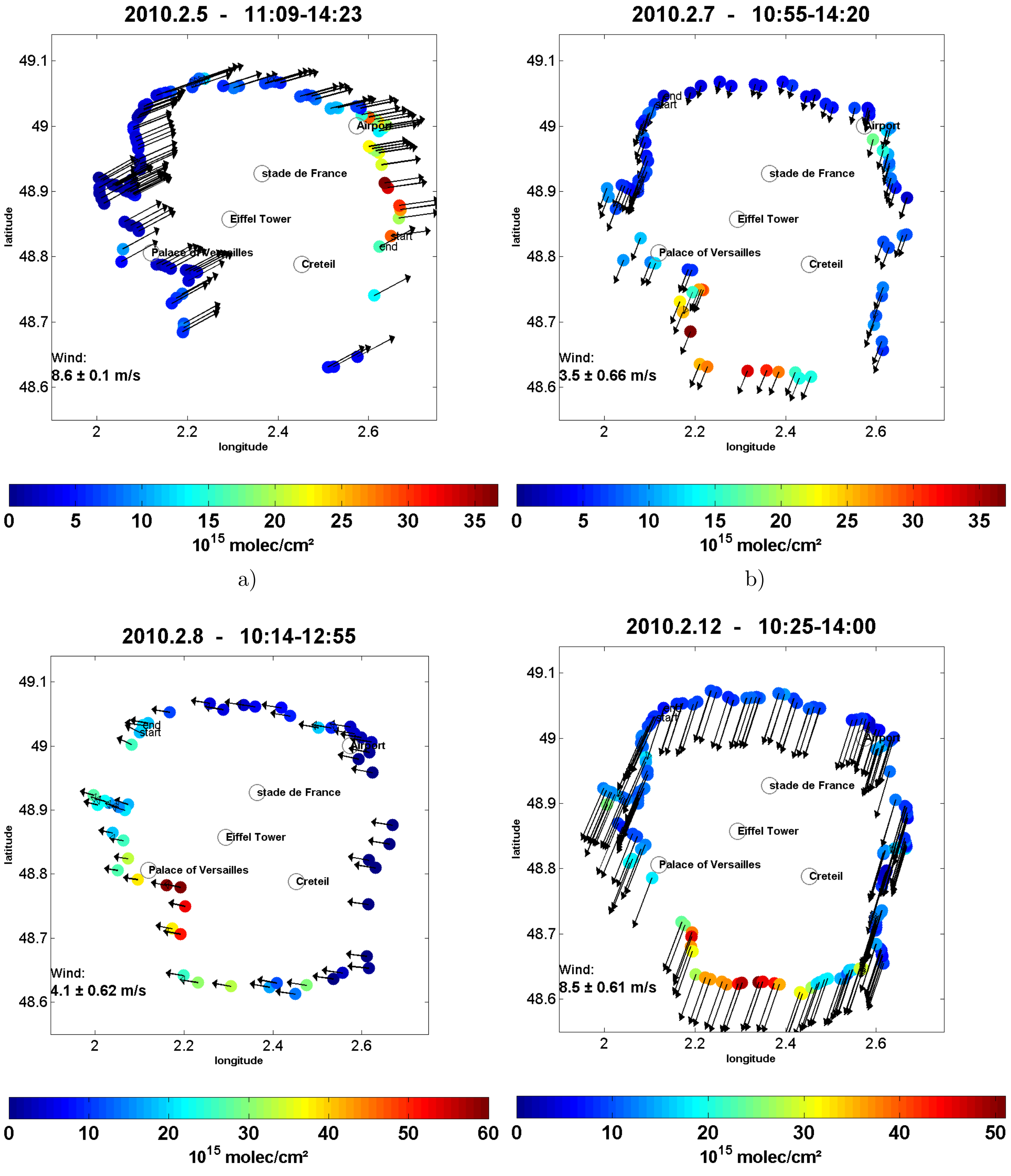

a)

b)

c)

d)

Figure B.6: TVCDs of NO_2 in Paris with associated wind vectors for February 5 (a), February 7 (b), February 8 (c) and February 12 (d), 2010.

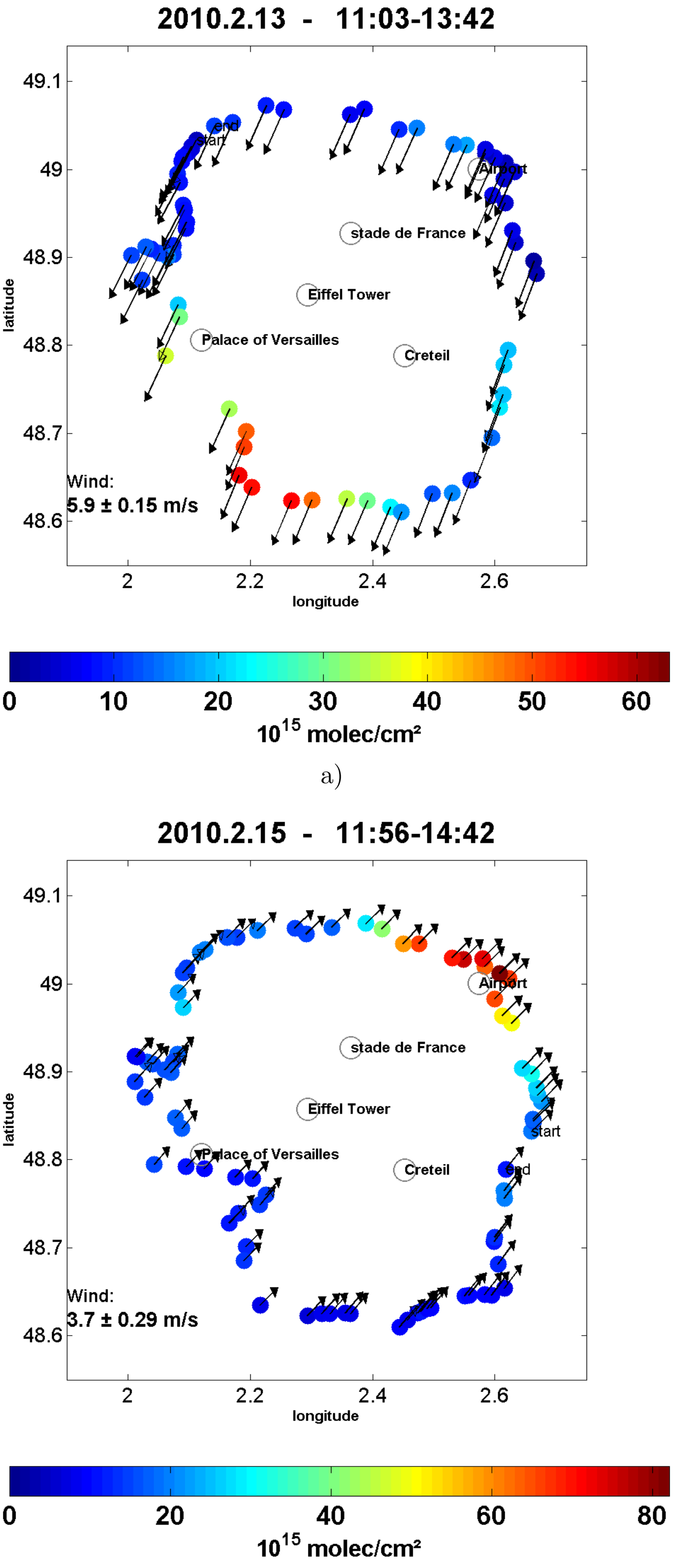

a)

b)

Figure B.7: TVCDs of NO_2 in Paris with associated wind vectors for February 13 (a) and February 15 (b), 2010.

Appendix C

C.1 Tropospheric NO_2 VCDs from OMI observations

Here we present the tropospheric vertical column densities (TVCDs) of nitrogen dioxide from OMI observations over Paris for the summer and winter campaigns.

C.1.1 Summer 2009

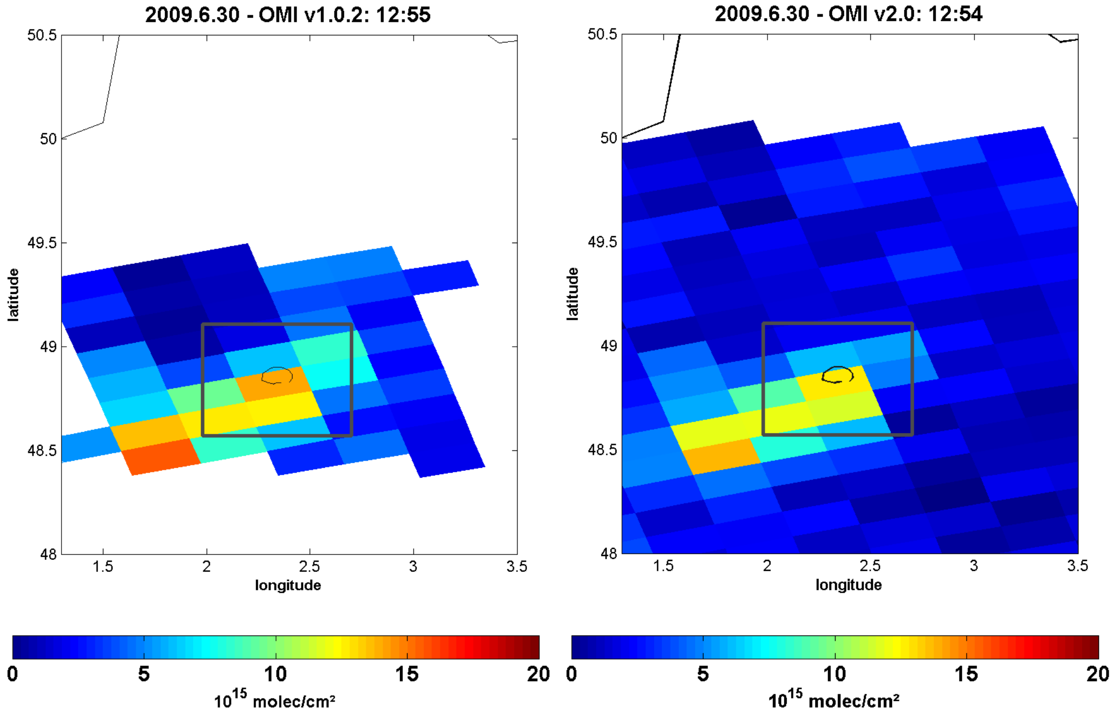

a)

b)

Figure C.1: TVCDs of NO_2 from OMI over Paris with two different versions on June 30, 2009.

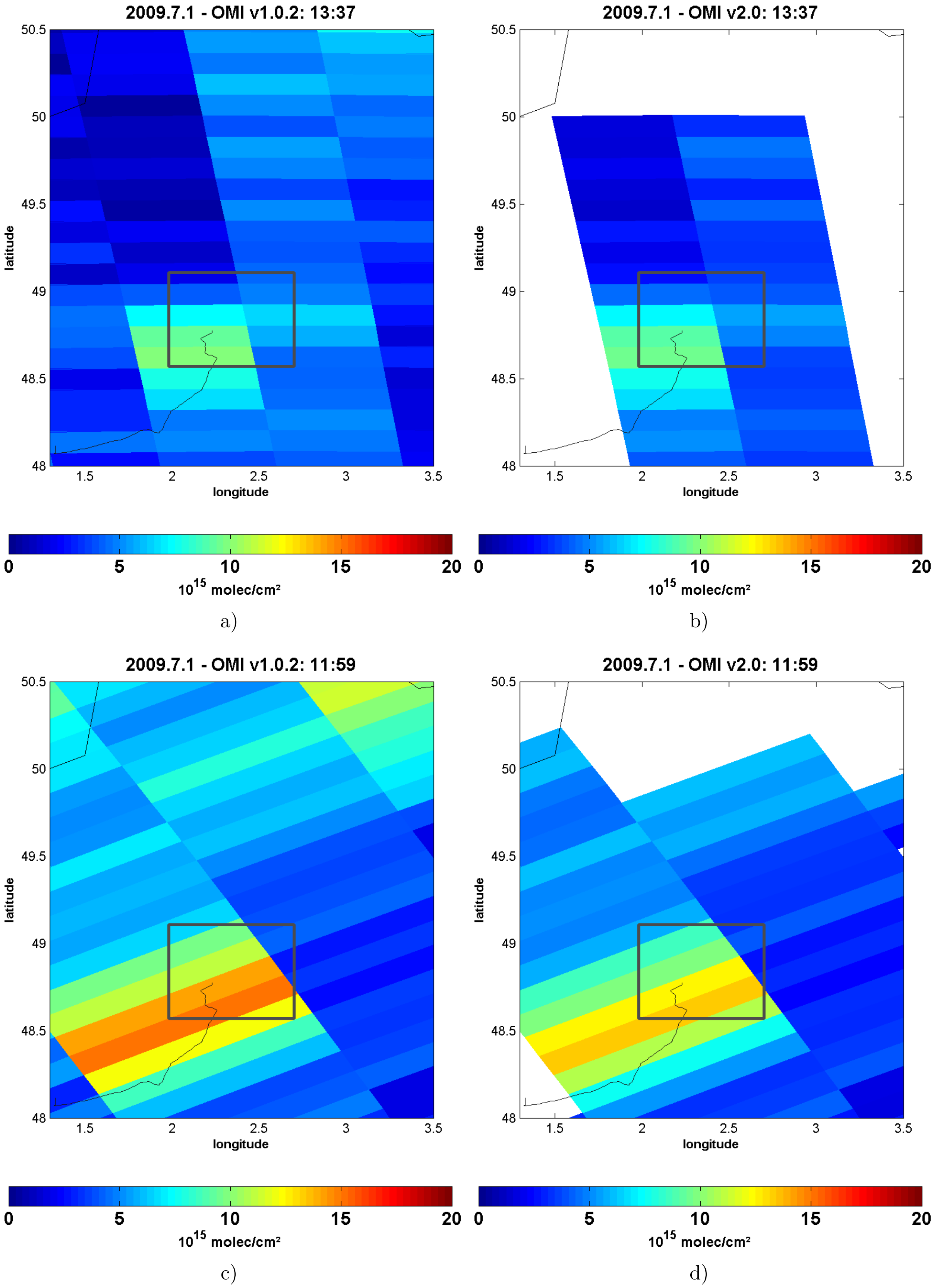

a) b) c) d)

Figure C.2: TVCDs of NO_2 from OMI over Paris with two different versions on July 1, 2009.

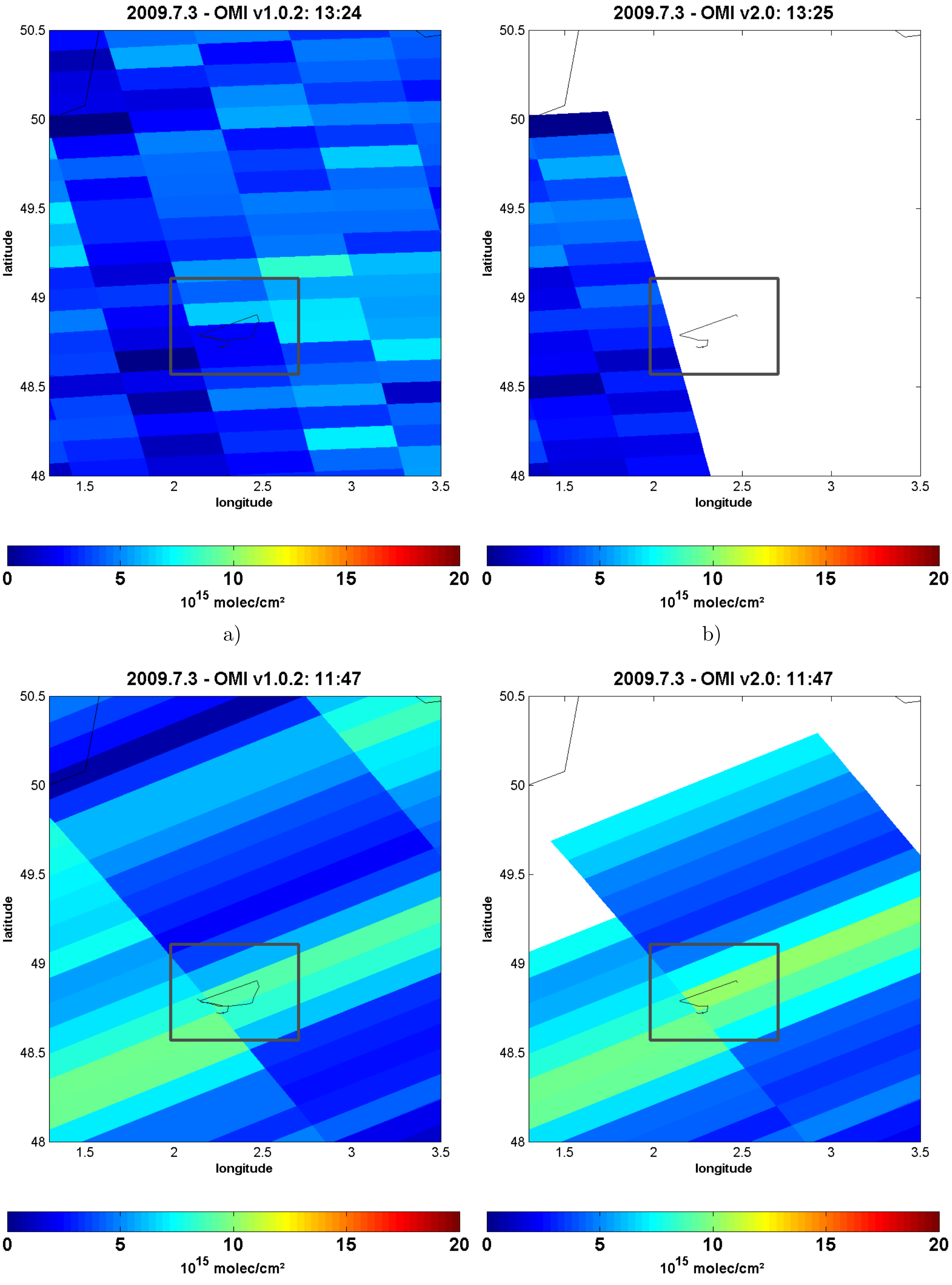

a)

b)

c)

d)

Figure C.3: TVCDs of NO_2 from OMI over Paris with two different versions on July 3, 2009.

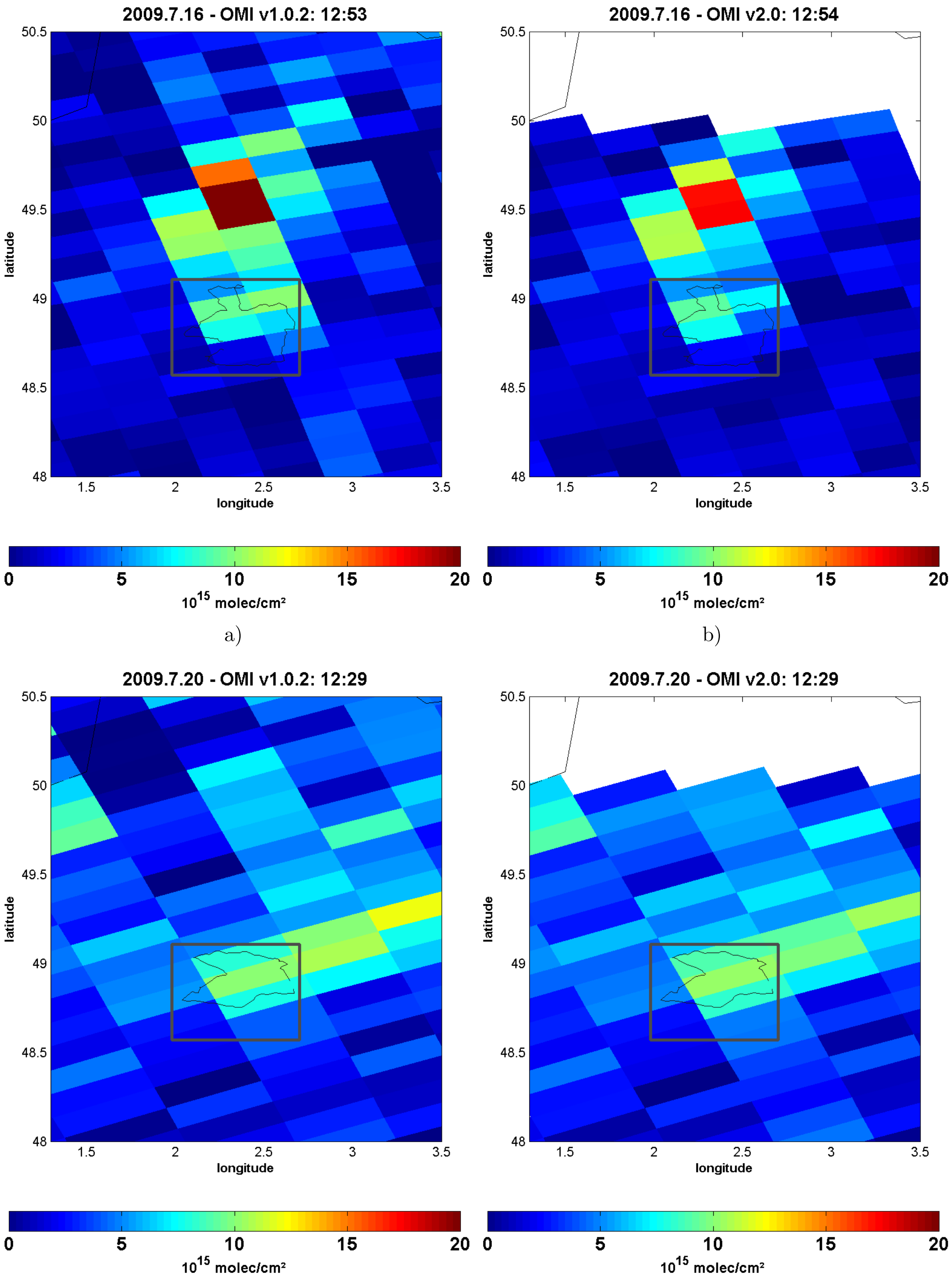

a) b) c) d)

Figure C.4: TVCDs of NO_2 from OMI over Paris with two different versions on July 16 (a and b) and July 20 (c and d), 2009.

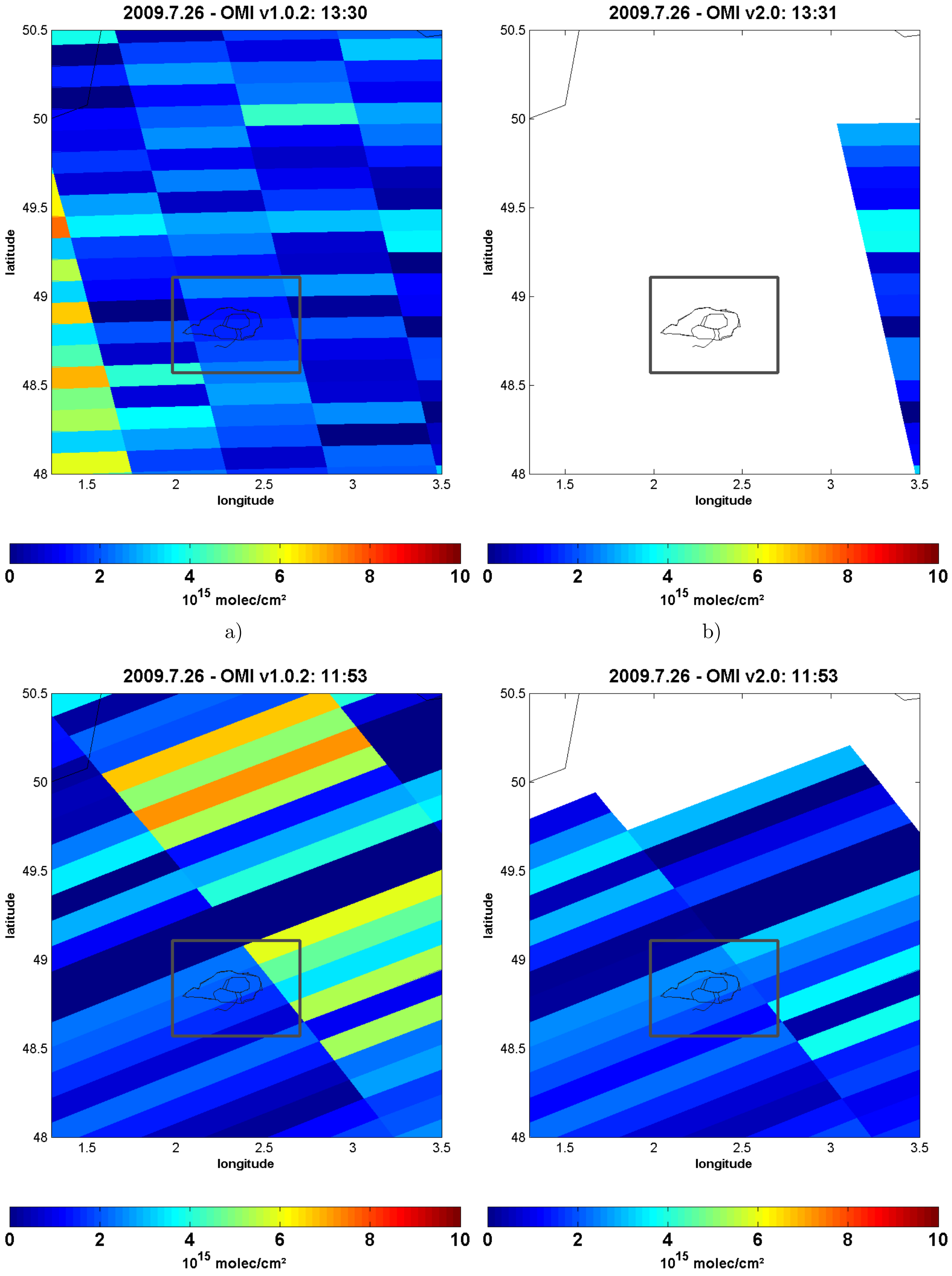

a)

b)

c)

d)

Figure C.5: TVCDs of NO_2 from OMI over Paris with two different versions on July 26, 2009.

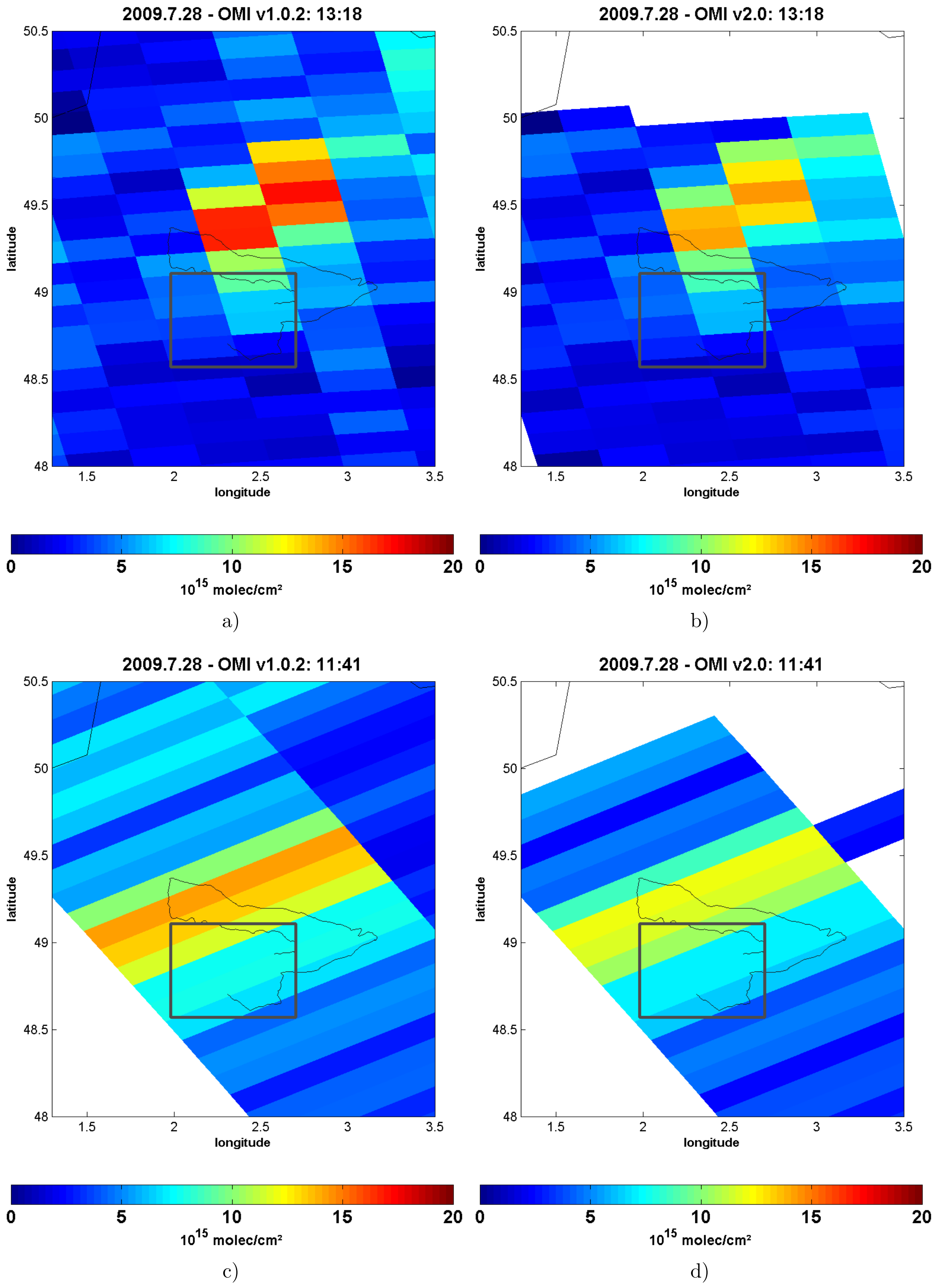

a)

b)

c)

d)

Figure C.6: TVCDs of NO_2 from OMI over Paris with two different versions on July 28, 2009.

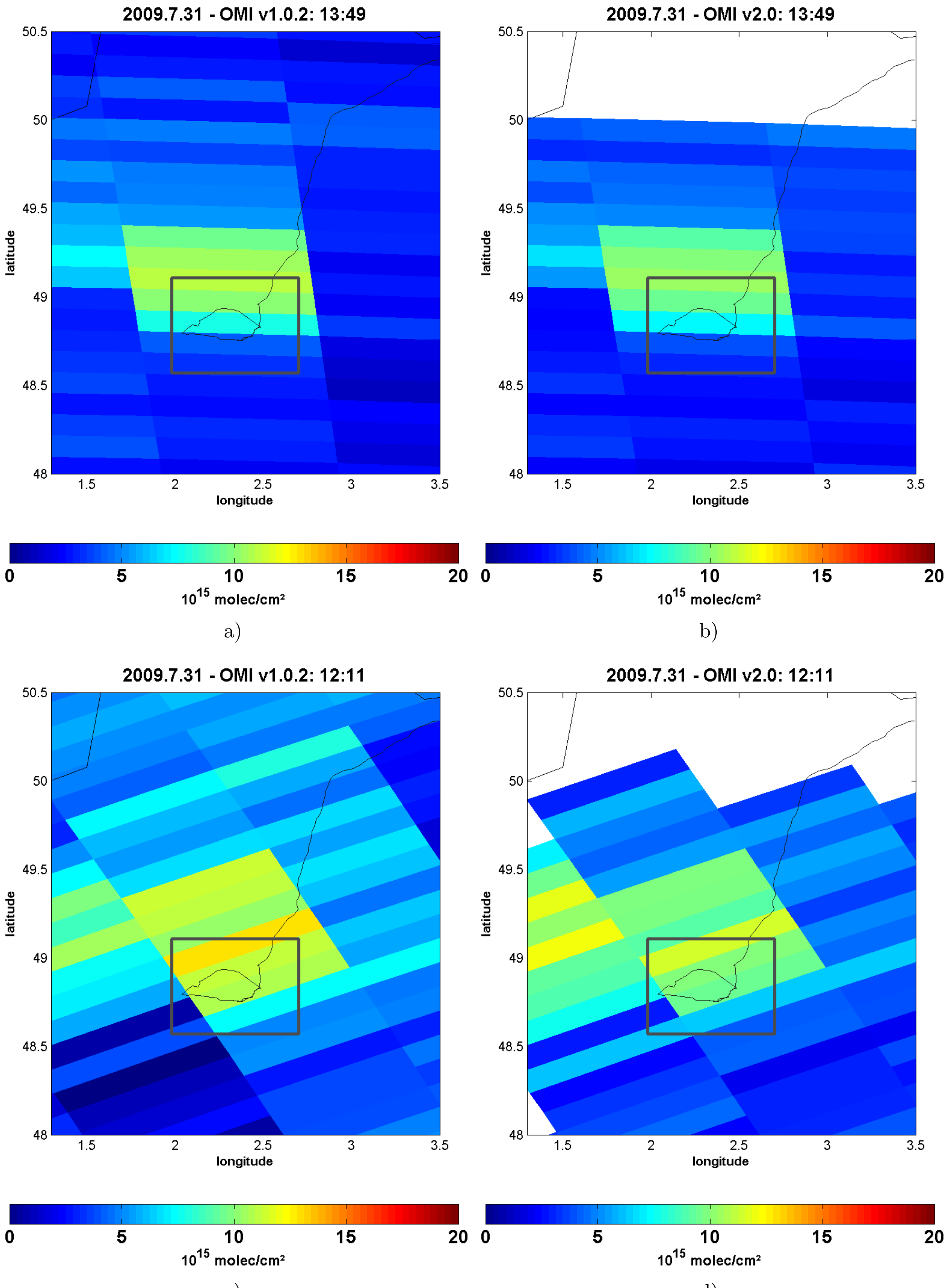

a) b) c) d)

Figure C.7: TVCDs of NO_2 from OMI over Paris with two different versions on July 31, 2009.

C.1.2 Winter 2010

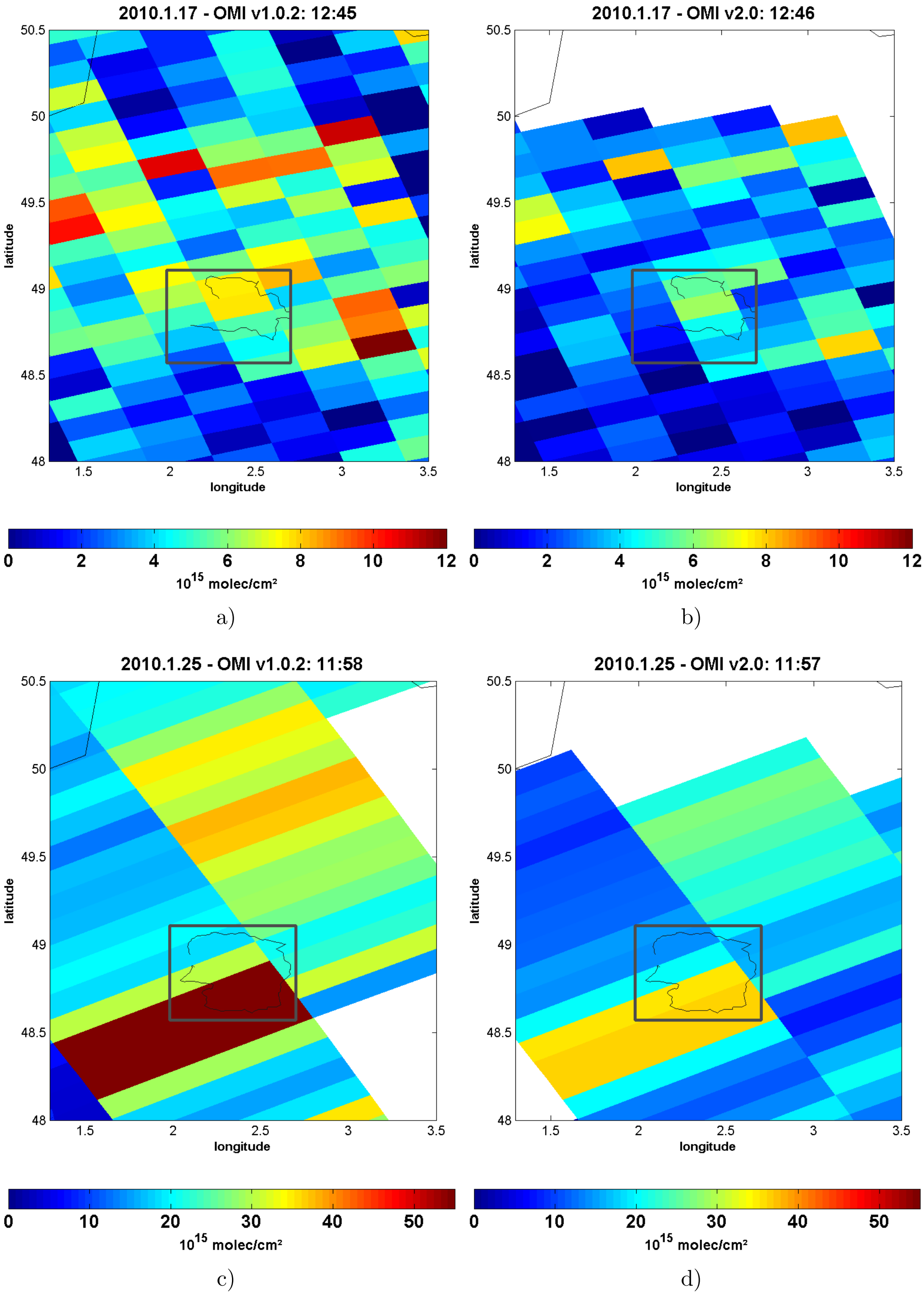

a) b)

c) d)

Figure C.8: TVCDs of NO_2 from OMI over Paris with two different versions on January 17 (a and b) and January 25 (c and d), 2010.

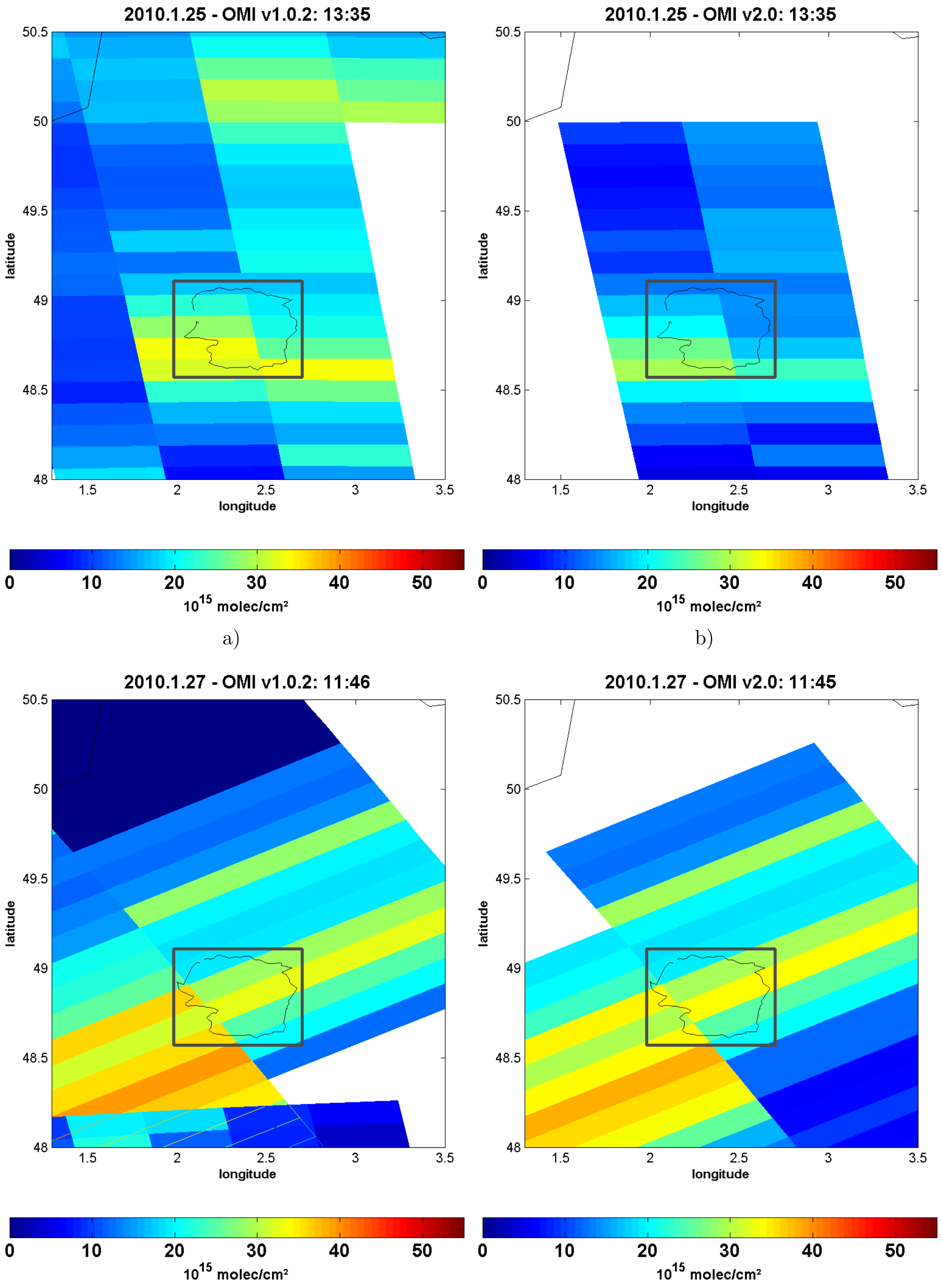

a) b) c) d)

Figure C.9: TVCDs of NO_2 from OMI over Paris with two different versions on January 25 (a and b) and January 27 (c and d), 2010.

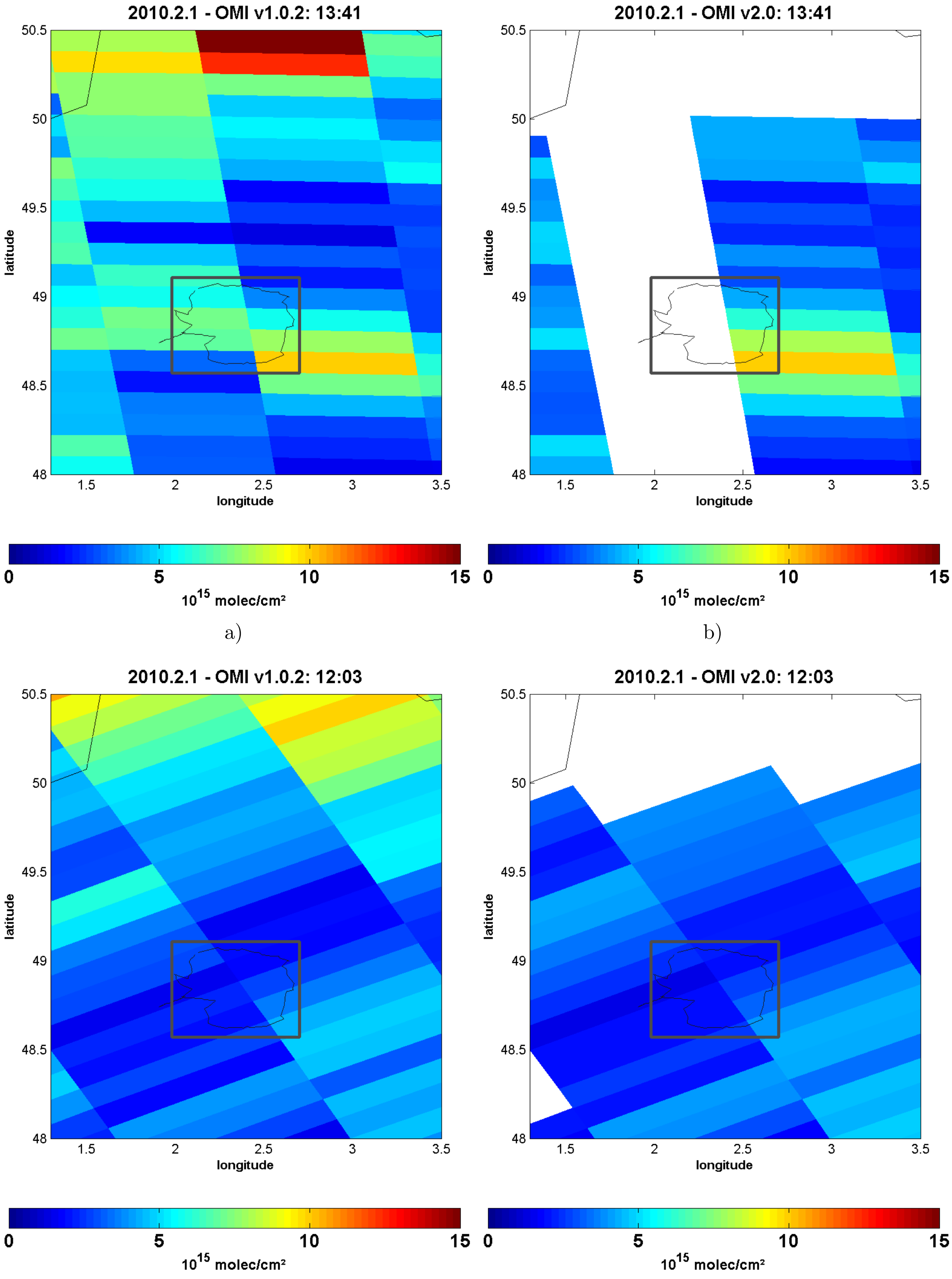

a) b)

c) d)

Figure C.10: TVCDs of NO_2 from OMI over Paris with two different versions on February 1, 2010.

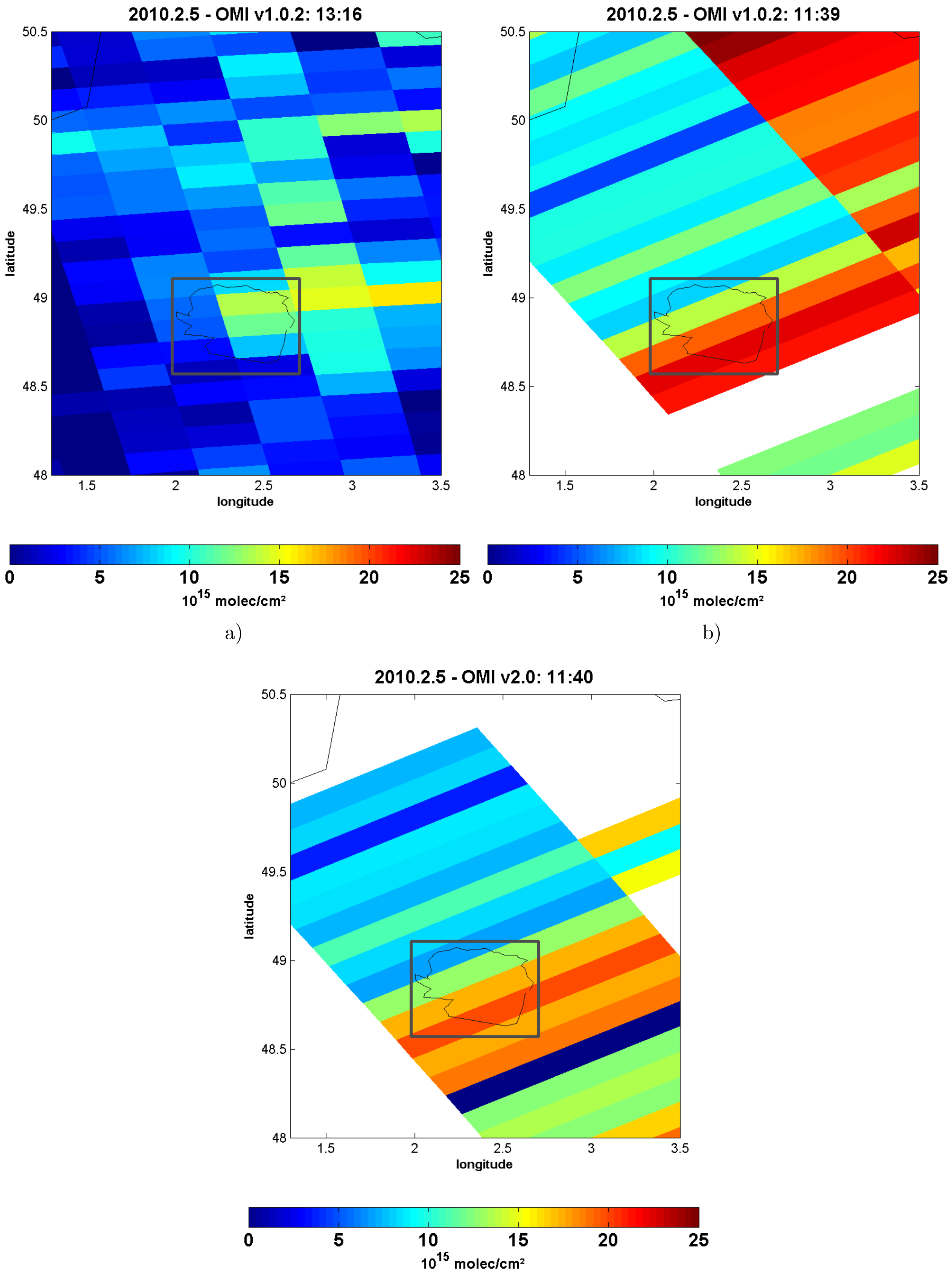

a) b)

c)

Figure C.11: TVCDs of NO_2 from OMI over Paris with two different versions on February 5, 2010.

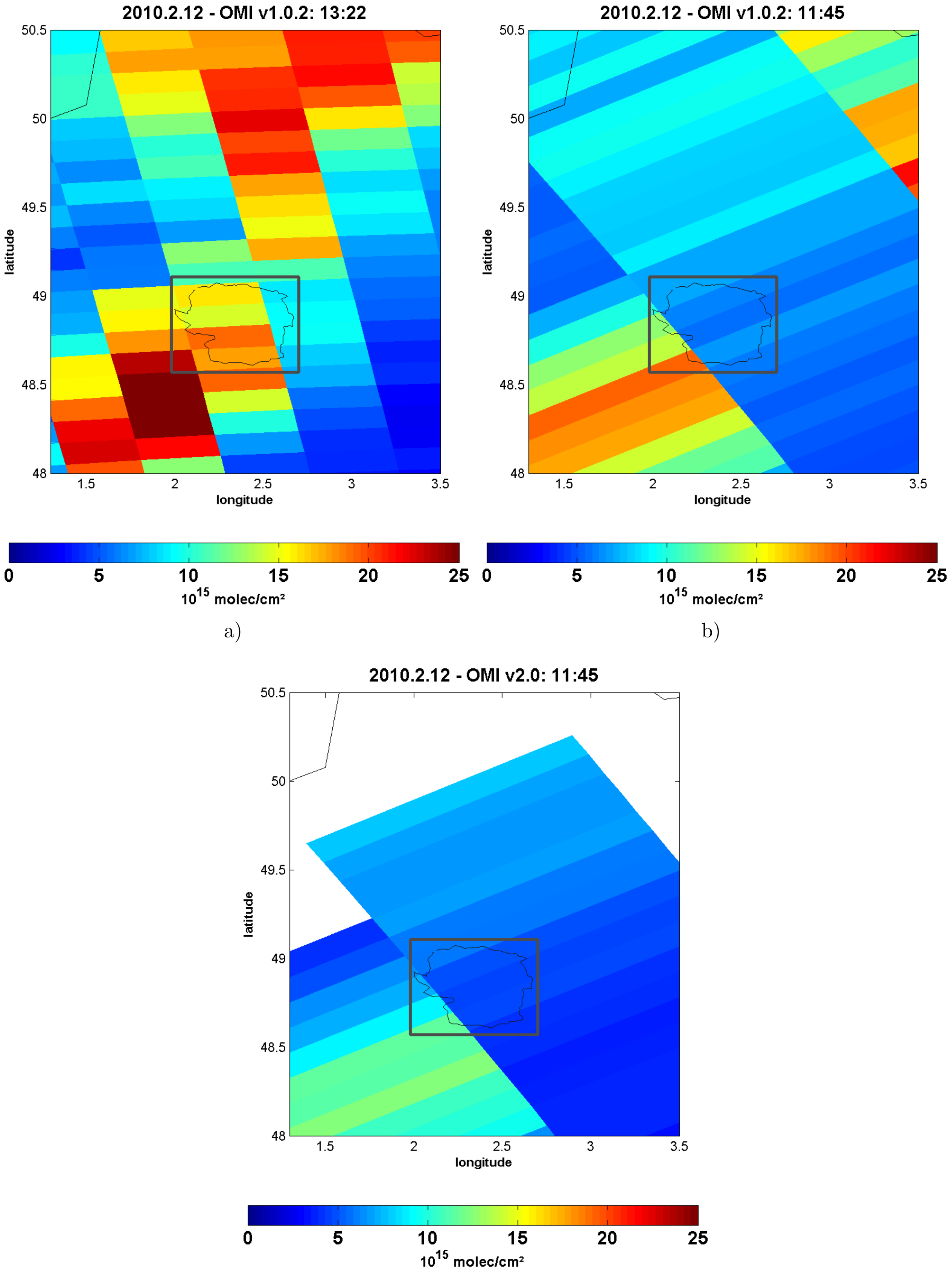

a)

b)

c)

Figure C.12: TVCDs of NO_2 from OMI over Paris with two different versions on February 12, 2010.

Appendix D

D.1 The tropospheric HCHO VCDs from mobile MAX-DOAS

Here we present the tropospheric vertical column densities (TVCDs) of formaldehyde from mobile MAX-DOAS in Paris for the summer and winter campaigns.

D.1.1 Summer campaign, 2009

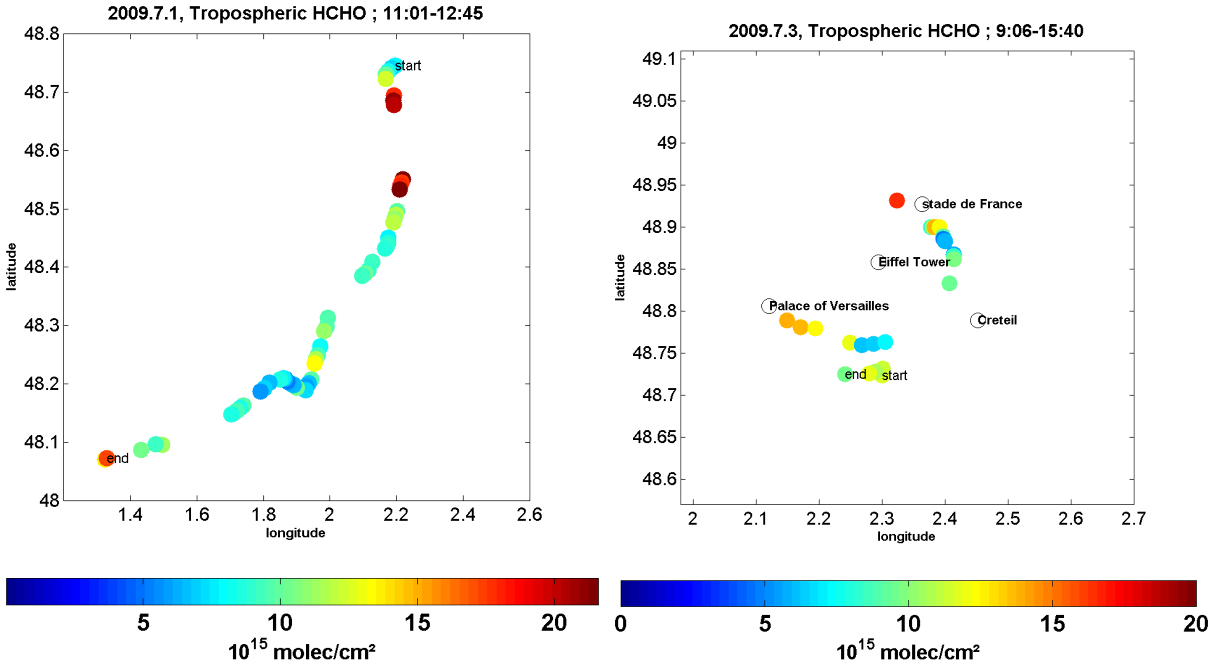

a) b)

Figure D.1: TVCDs of HCHO in Paris on July 1 (a) and July 3 (b), 2009.

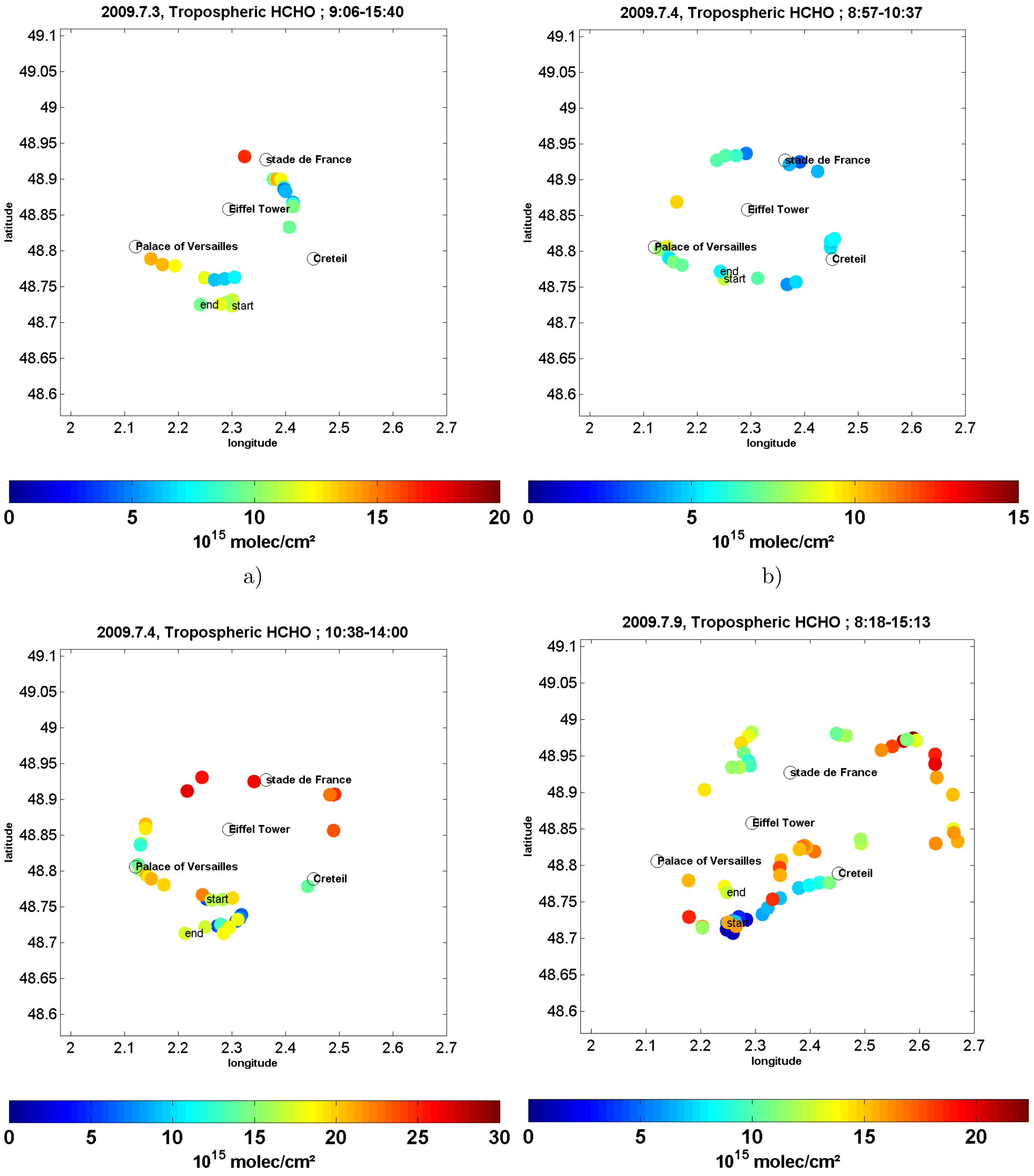

a) b)

c) d)

Figure D.2: TVCDs of HCHO in Paris on July 3 (a), July 4 (b and c) and July 9 (d), 2009.

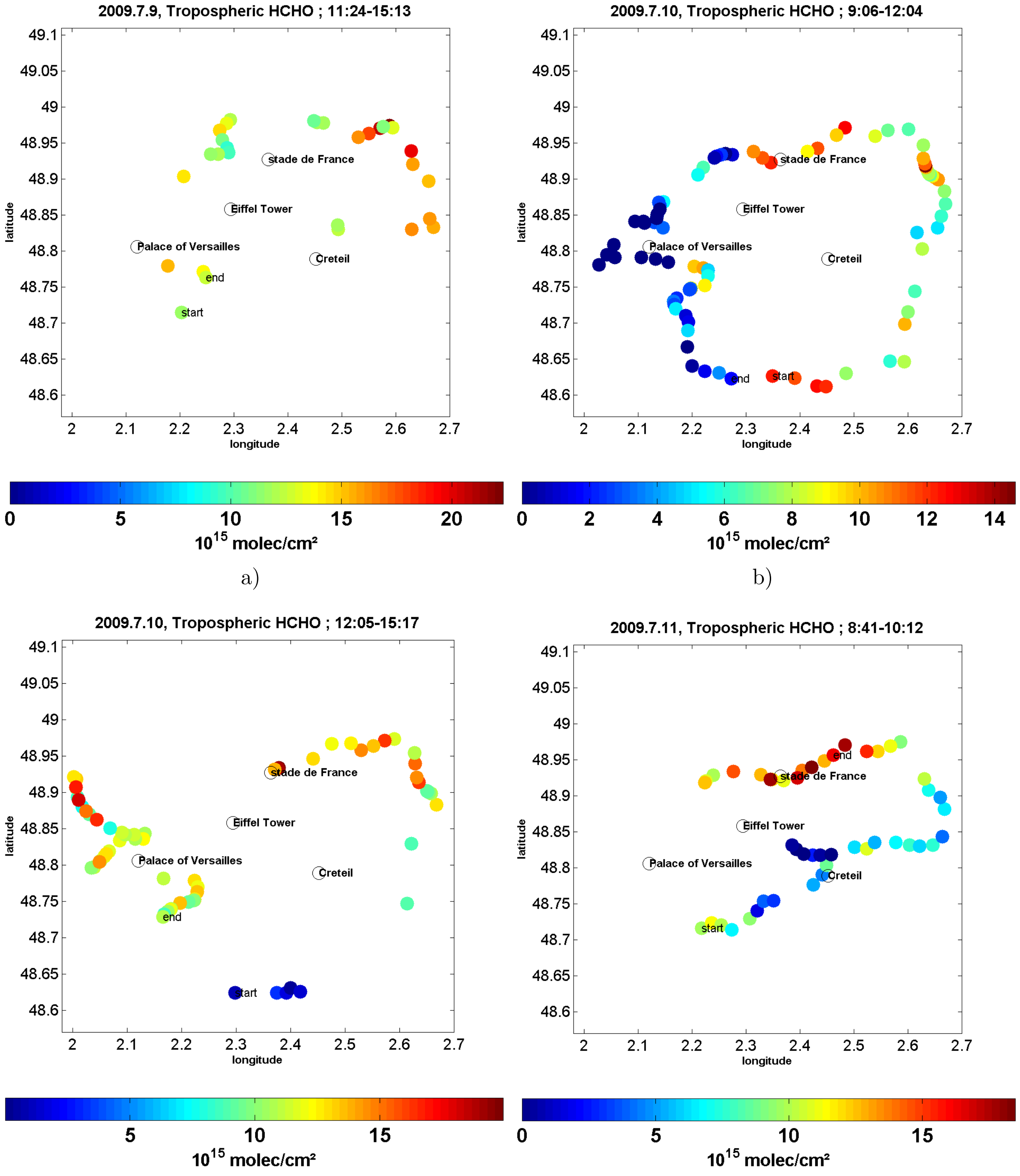

a)

b)

c)

d)

Figure D.3: TVCDs of HCHO in Paris on July 9 (a), July 10 (b and c) and July 11 (d), 2009.

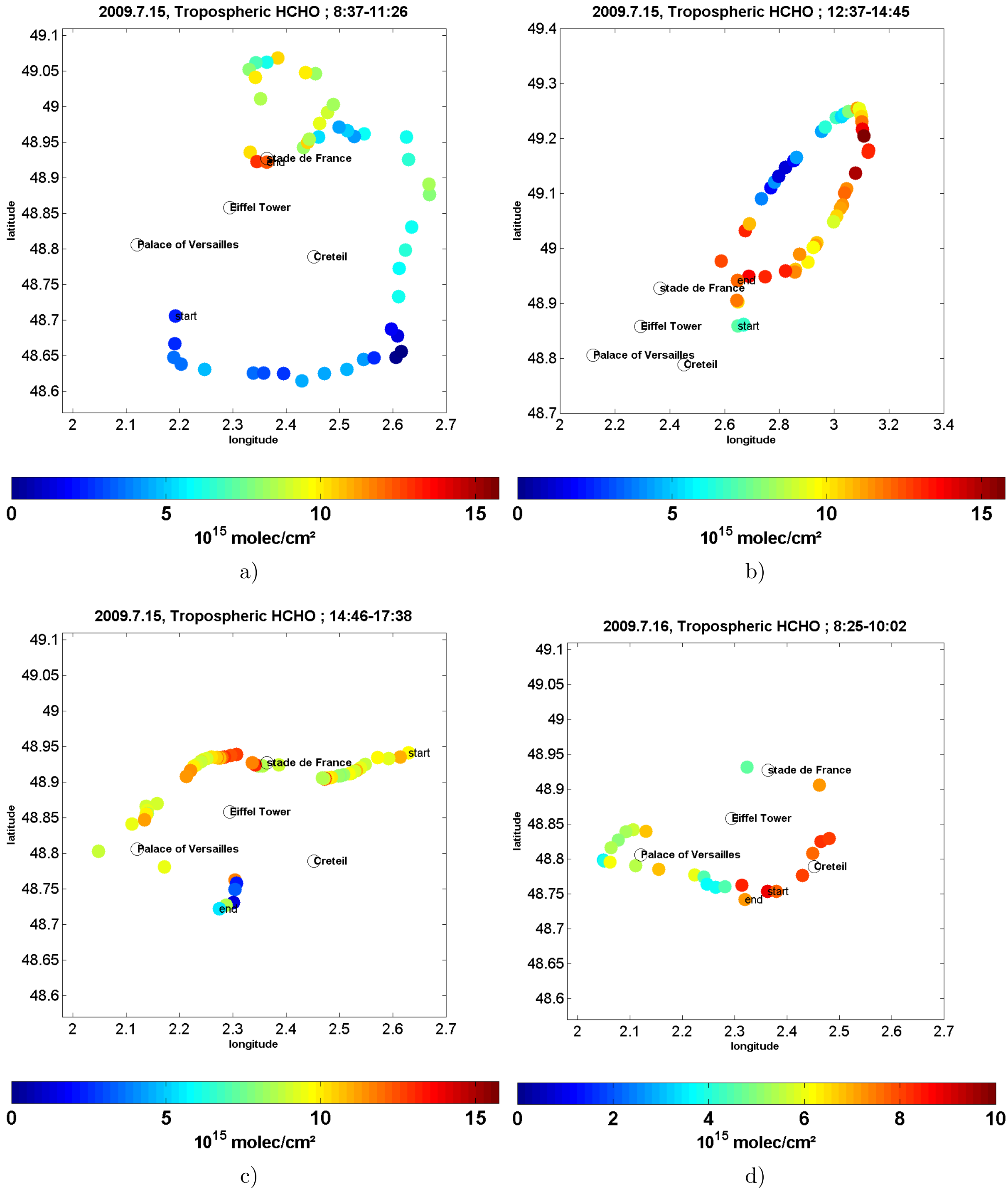

a)

b)

c)

d)

Figure D.4: TVCDs of HCHO in Paris on July 15 (a, b and c) and July 16 (d), 2009.

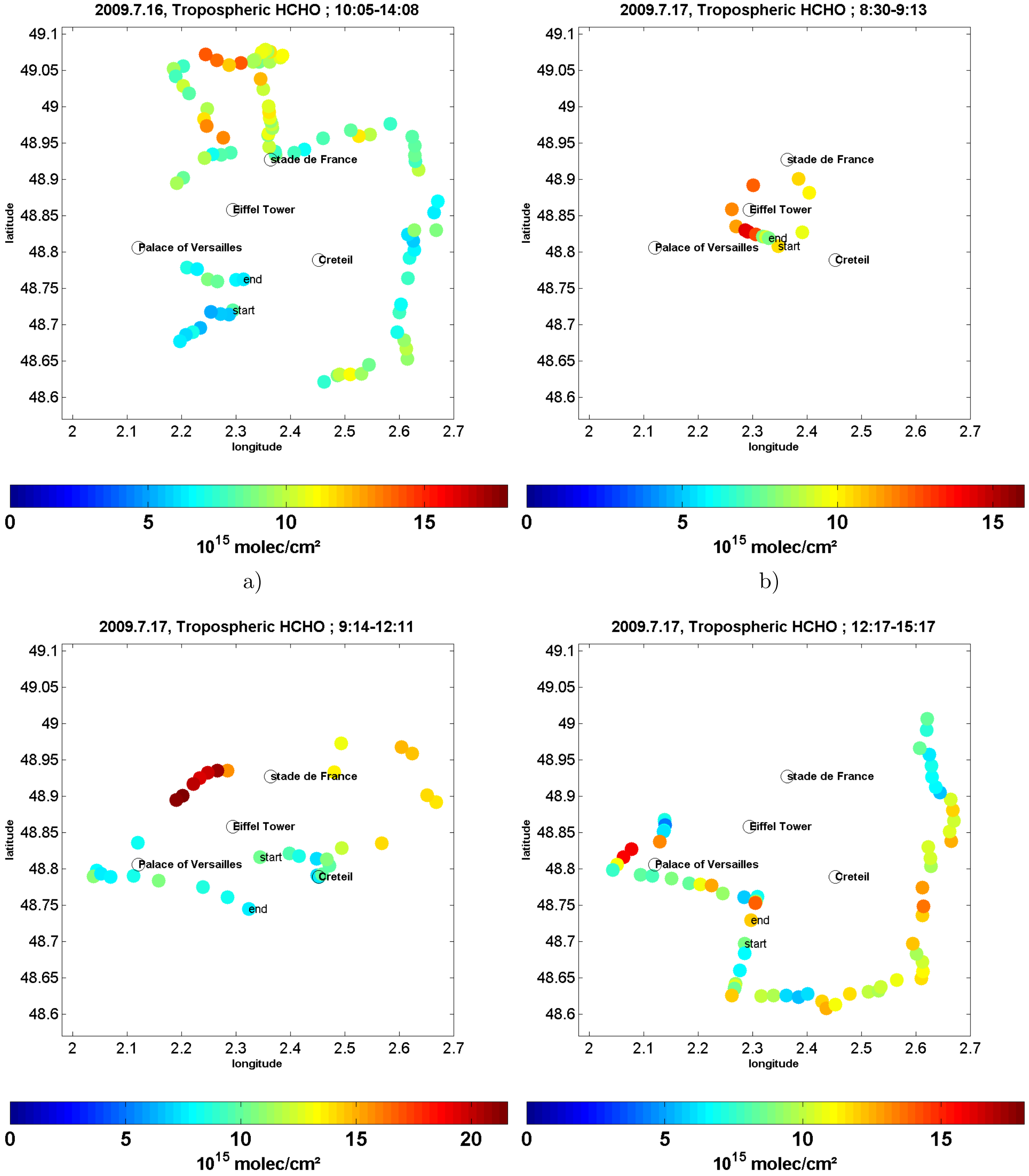

a)

b)

c)

d)

Figure D.5: TVCDs of HCHO in Paris on July 16 (a) and July 17 (b, c and d), 2009.

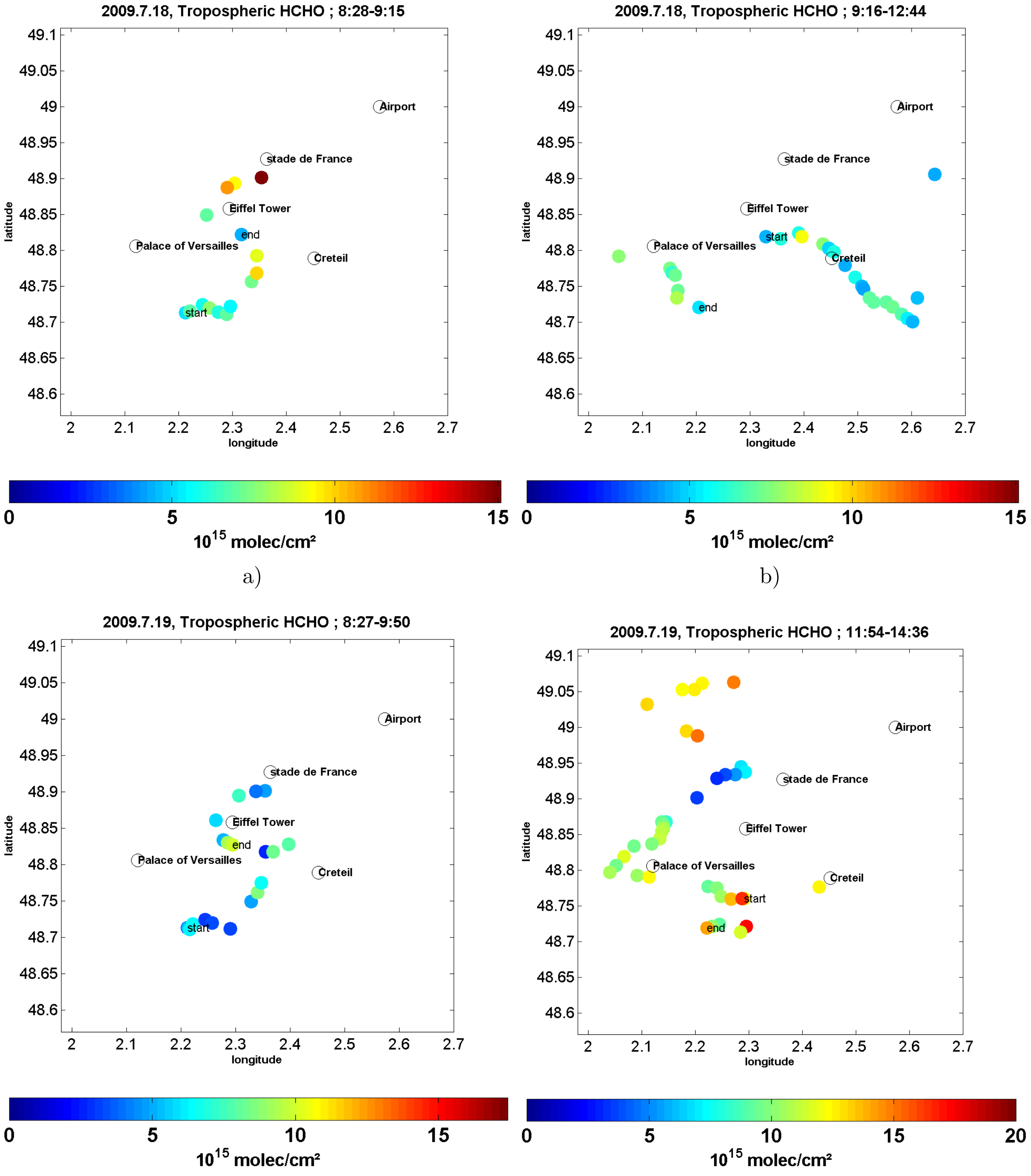

a) b) c) d)

Figure D.6: TVCDs of HCHO in Paris on July 18 (a and b) and July 19 (c and d), 2009.

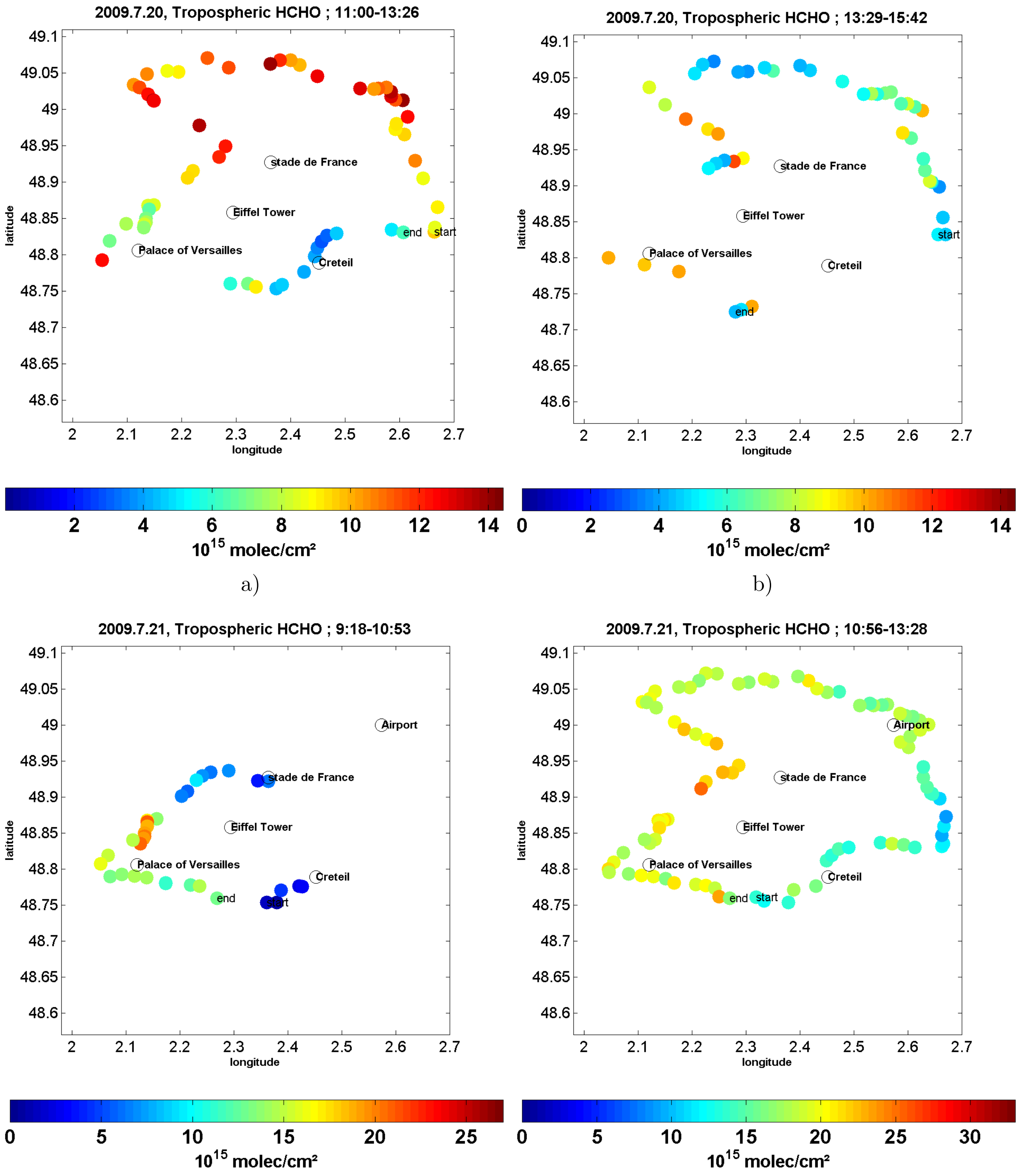

a)

b)

c)

d)

Figure D.7: TVCDs of HCHO in Paris on July 20 (a and b) and July 21 (c and d), 2009.

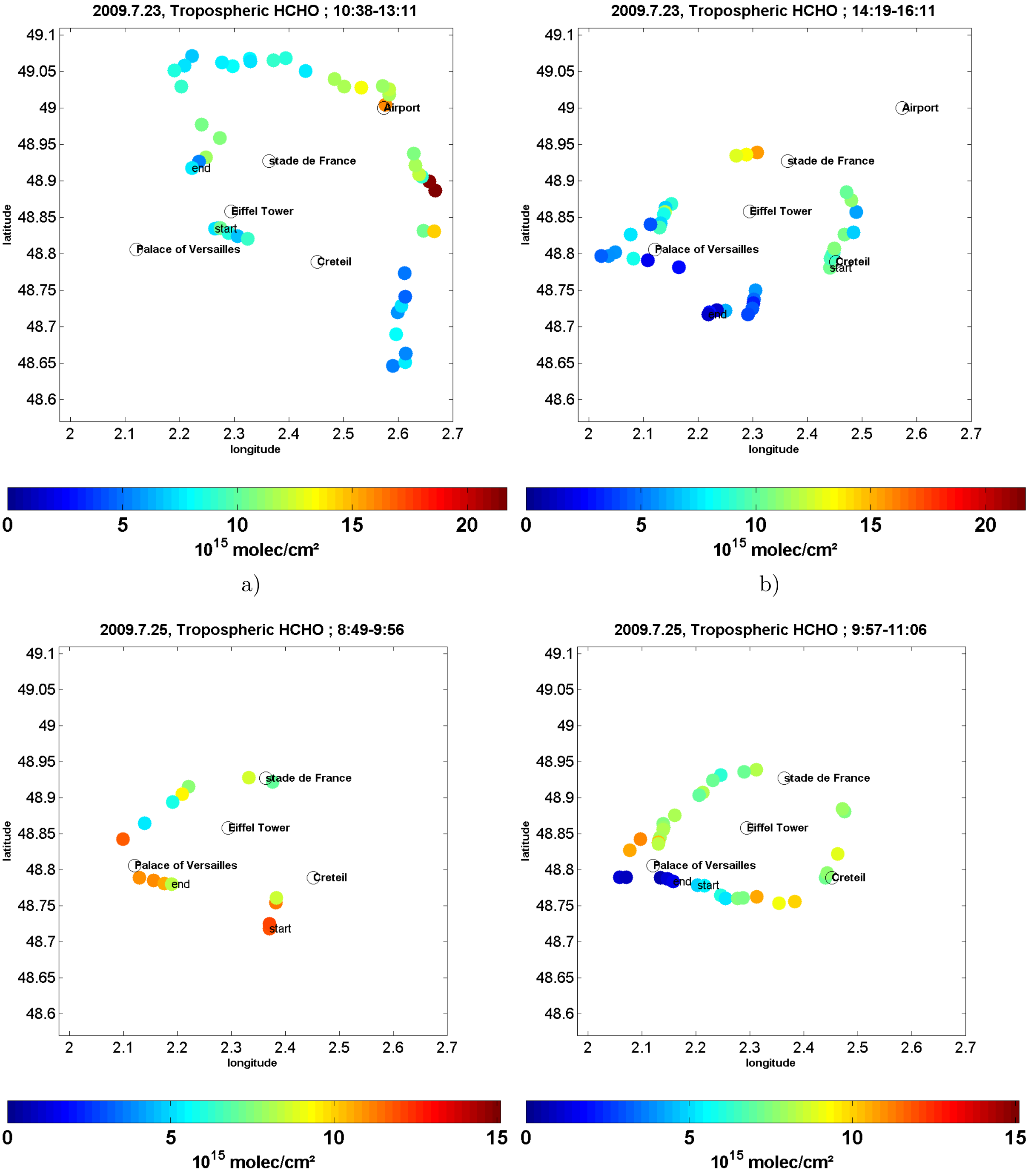

a) b) c) d)

Figure D.8: TVCDs of HCHO in Paris on July 23 (a and b) and July 25 (c and d), 2009.

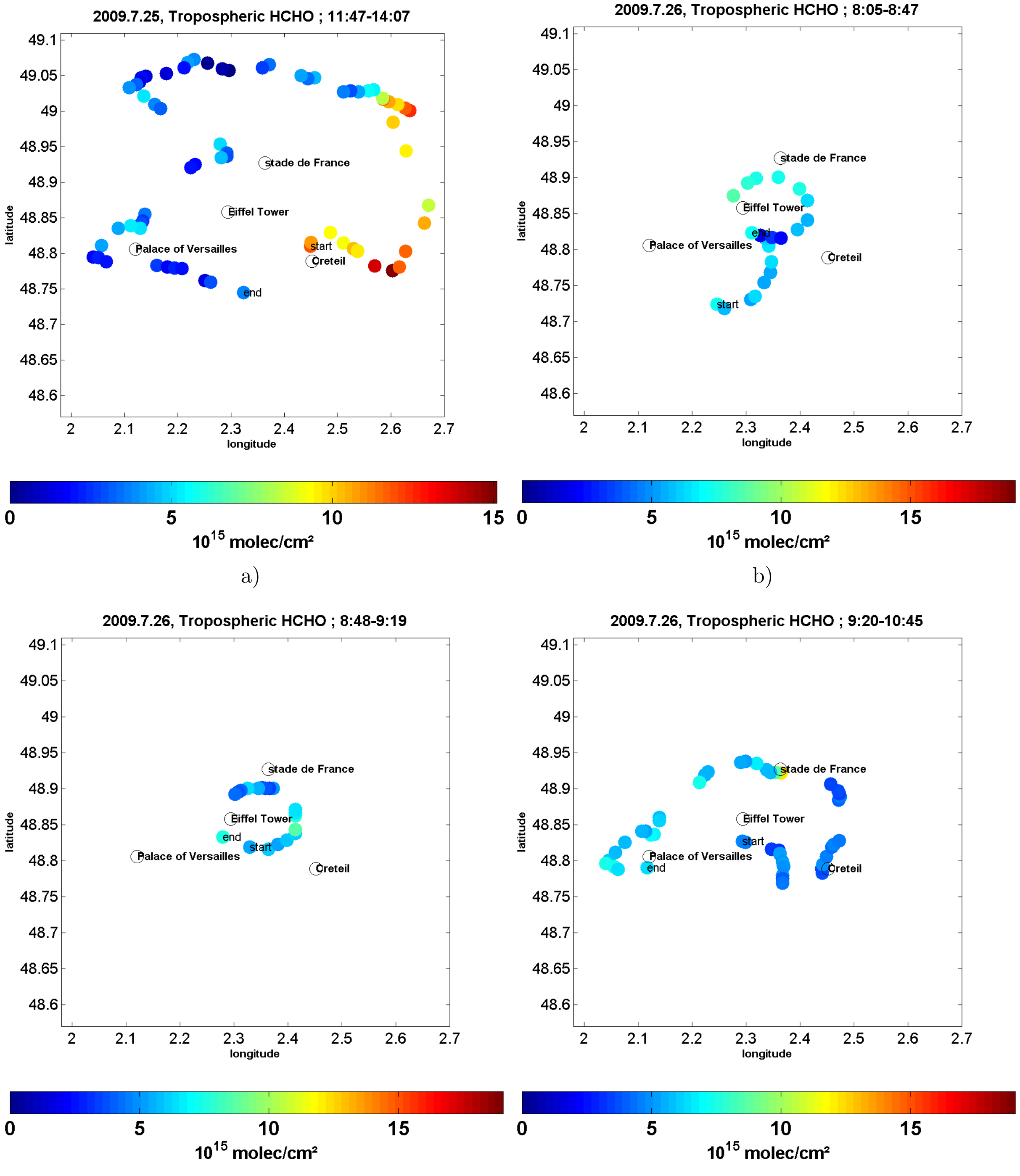

a) b) c) d)

Figure D.9: TVCDs of HCHO in Paris on July 25 (a) and July 26 (b, c and d), 2009.

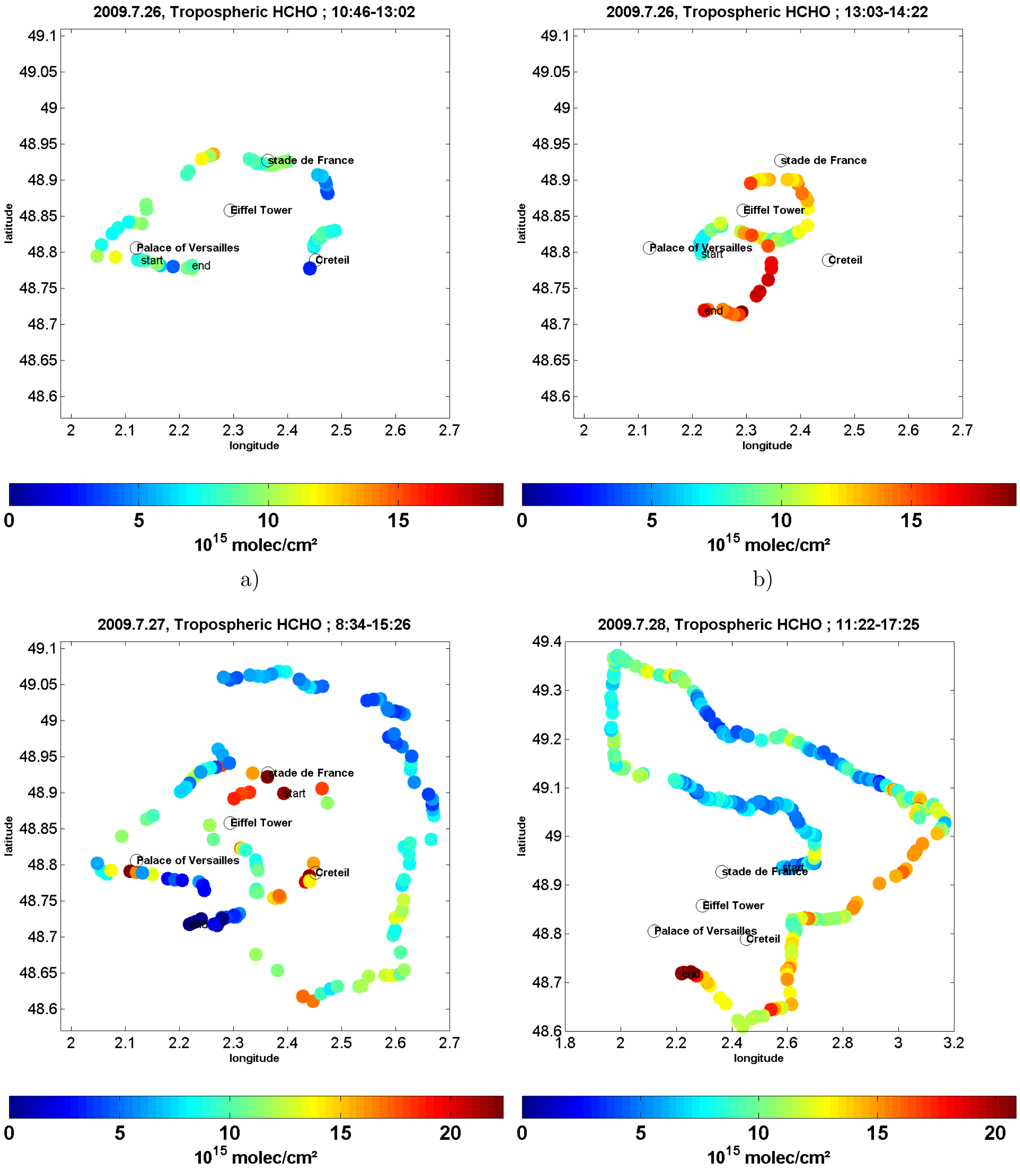

a)

b)

c)

d)

Figure D.10: TVCDs of HCHO in Paris on July 26 (a and b), July 27 (c) and July 28 (d), 2009.

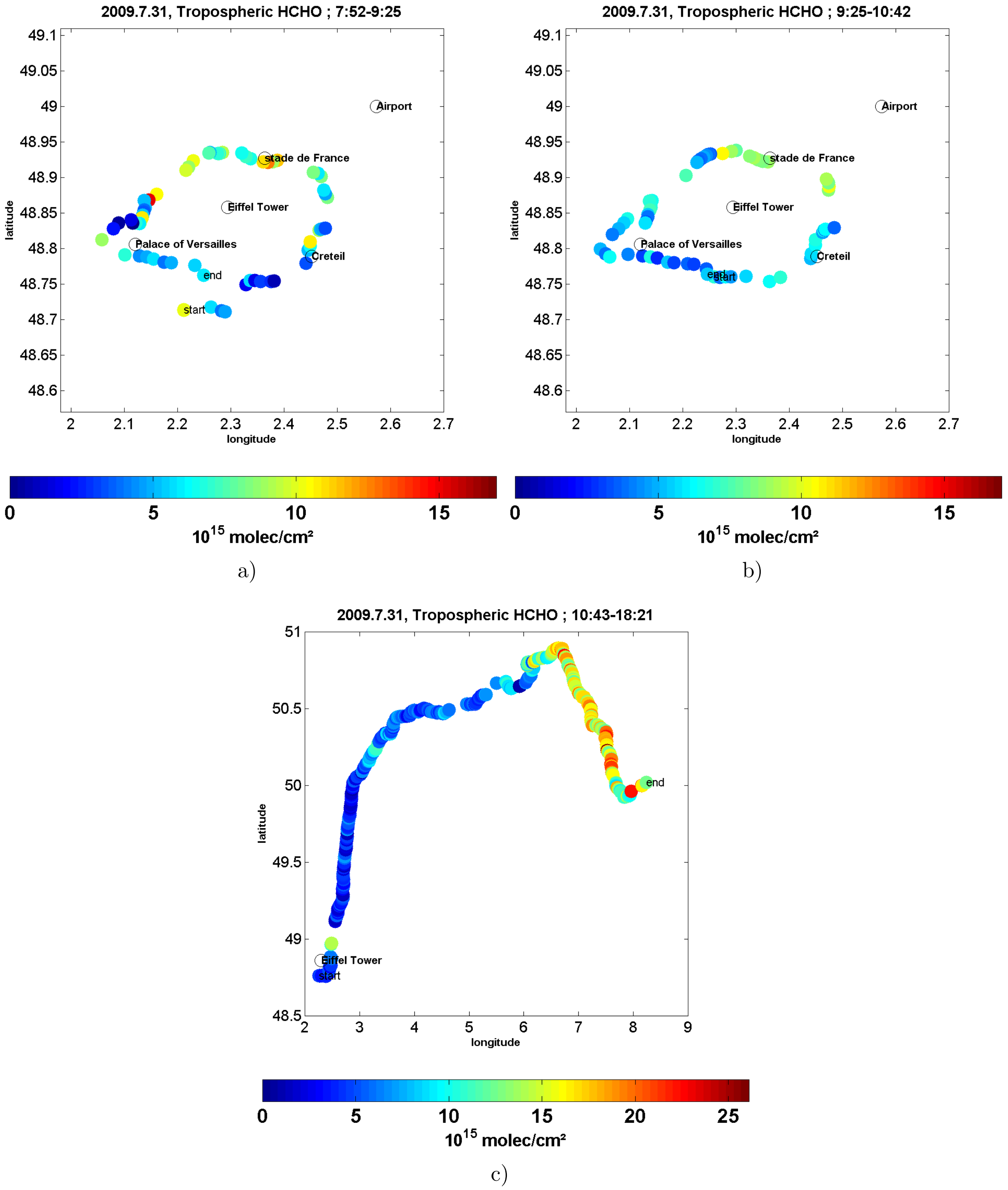

a)

b)

c)

Figure D.11: TVCDs of HCHO in Paris on July 31, 2009.

D.1.2 Winter campaign, 2010

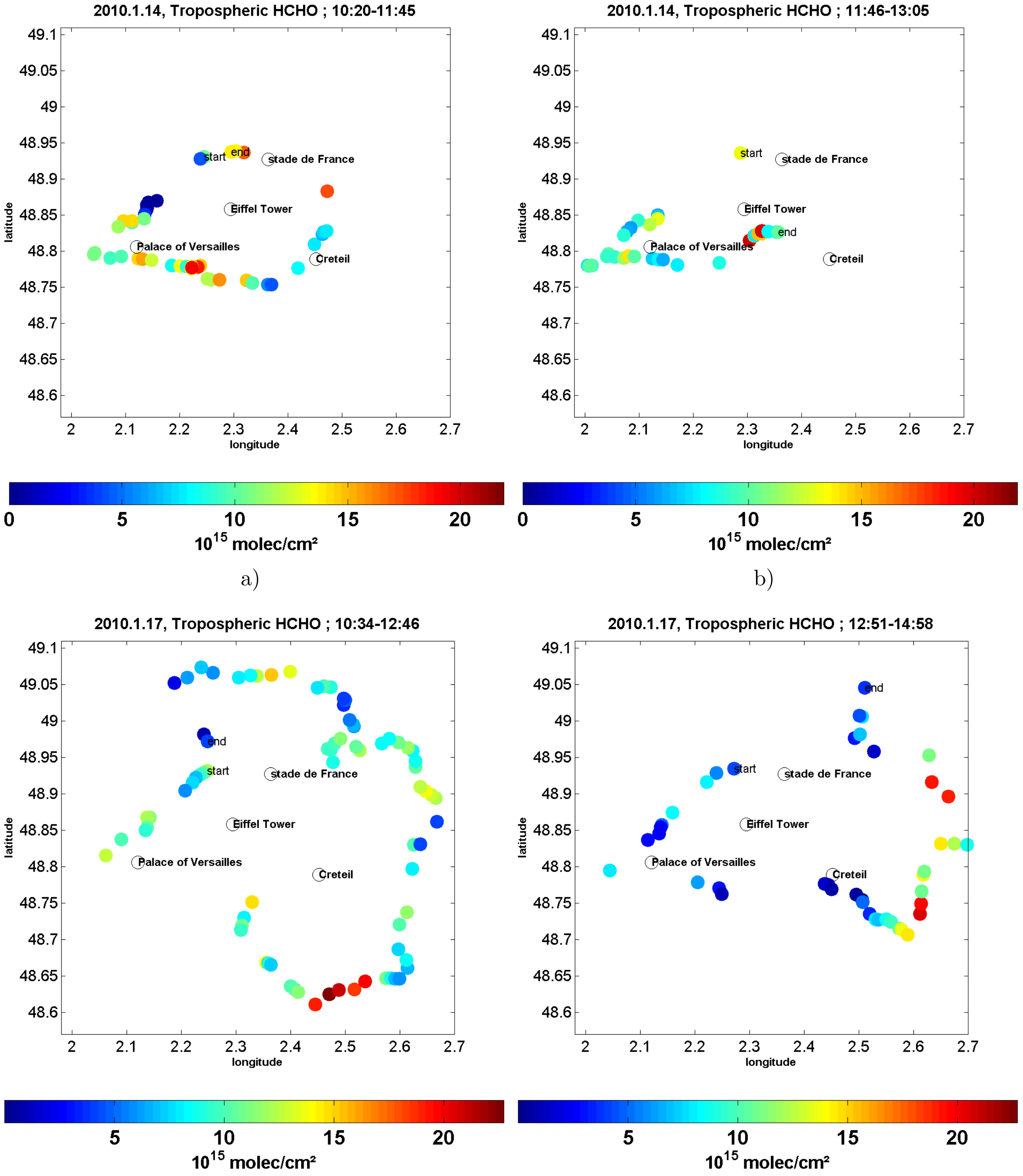

a) b)

c) d)

Figure D.12: TVCDs of HCHO in Paris on January 14 (a and b) and January 17 (c and d), 2010.

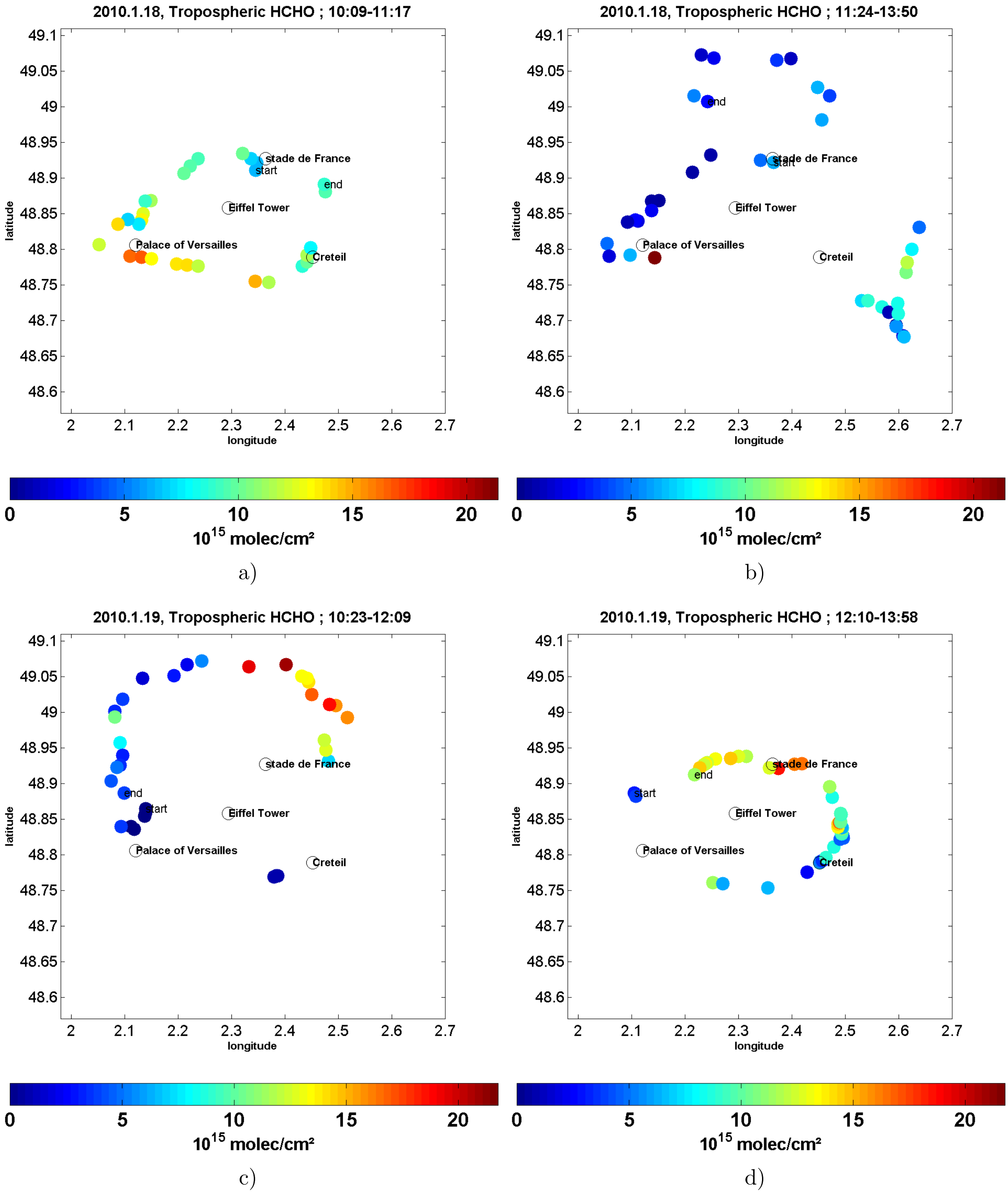

a)

b)

c)

d)

Figure D.13: TVCDs of HCHO in Paris on January 18 (a and b) and January 19 (c and d), 2010.

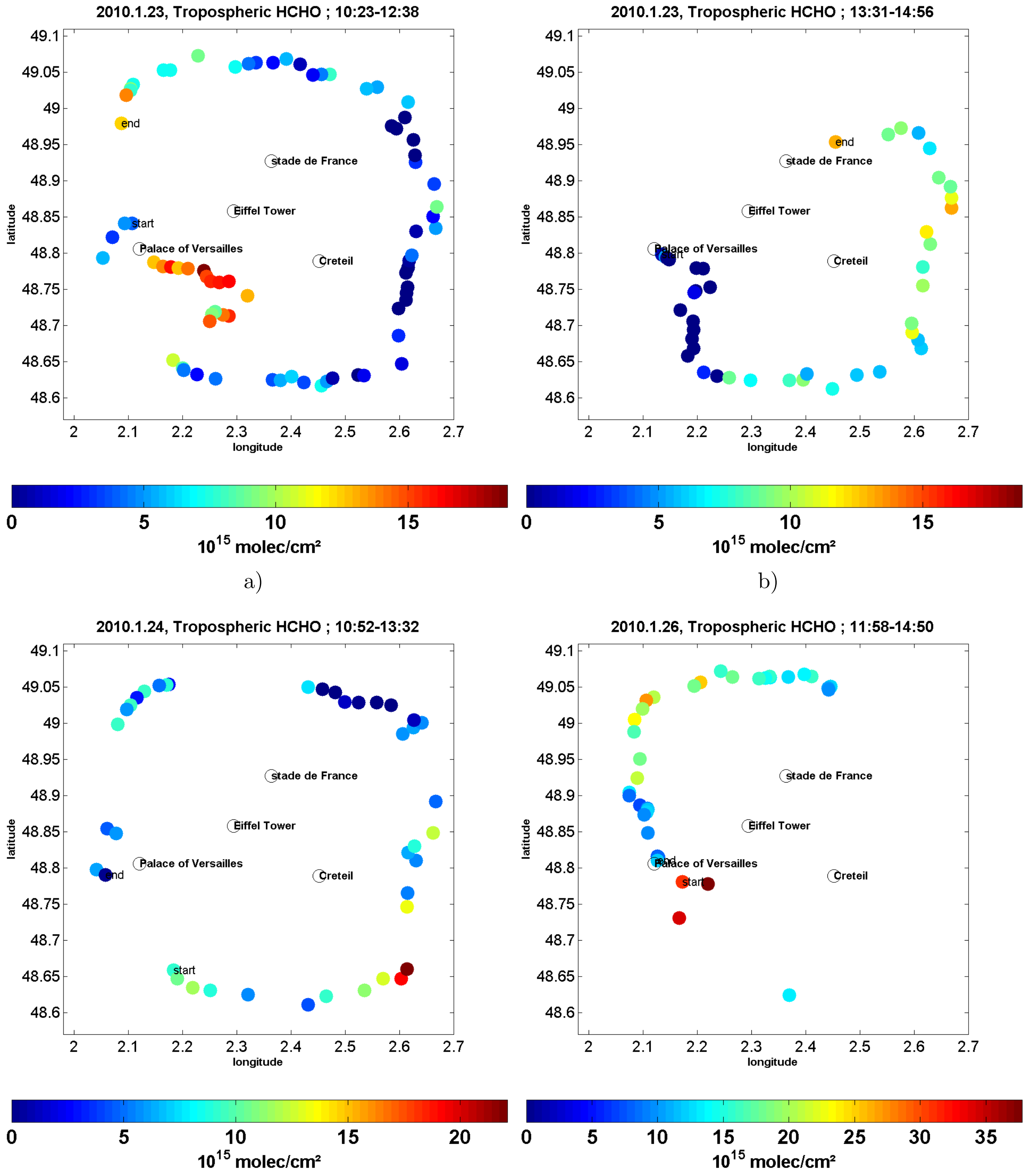

2010.1.23, Tropospheric HCHO ; 10:23-12:38

2010.1.23, Tropospheric HCHO ; 13:31-14:56

2010.1.24, Tropospheric HCHO ; 10:52-13:32

2010.1.26, Tropospheric HCHO ; 11:58-14:50

a)

b)

c)

d)

Figure D.14: TVCDs of HCHO in Paris on January 23 (a and b), January 24 (c) and January 26 (d), 2010.

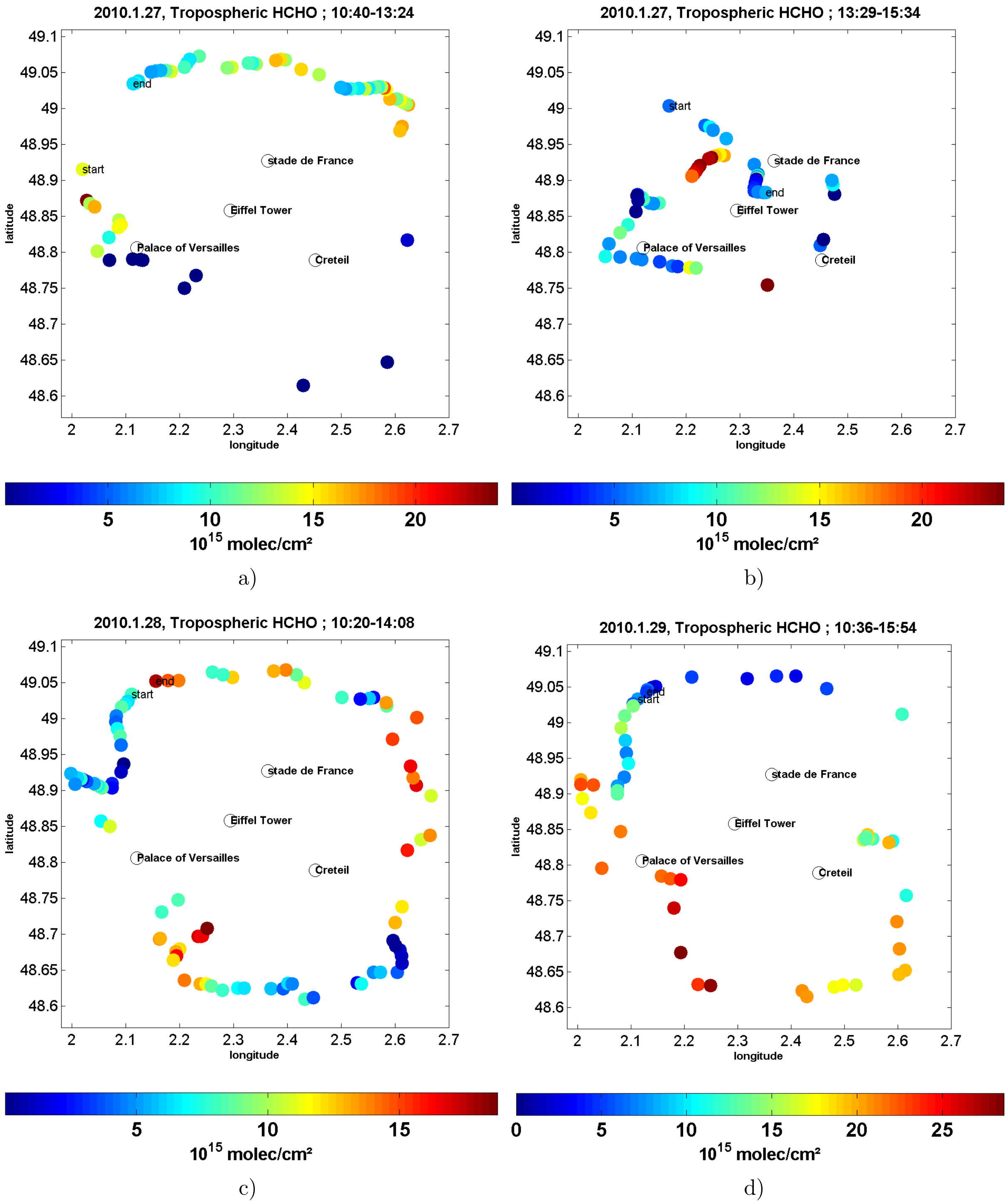

a) b) c) d)

Figure D.15: TVCDs of HCHO in Paris on January 27 (a and b), January 28 (c) and January 29 (d), 2010.

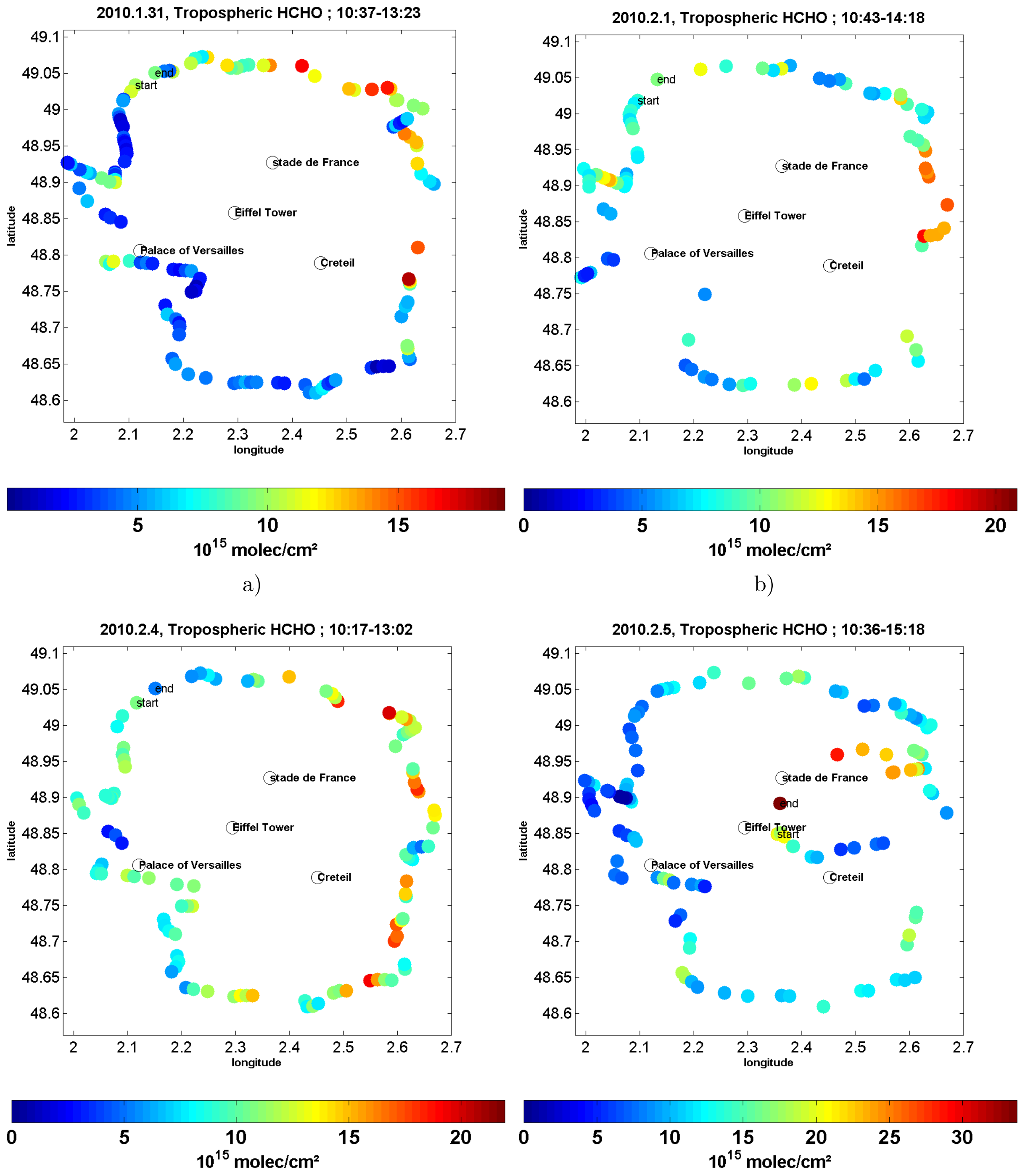

a) b) c) d)

Figure D.16: TVCDs of HCHO in Paris on January 31 (a), February 1 (b), February 4 (c) and February 5 (d), 2010.

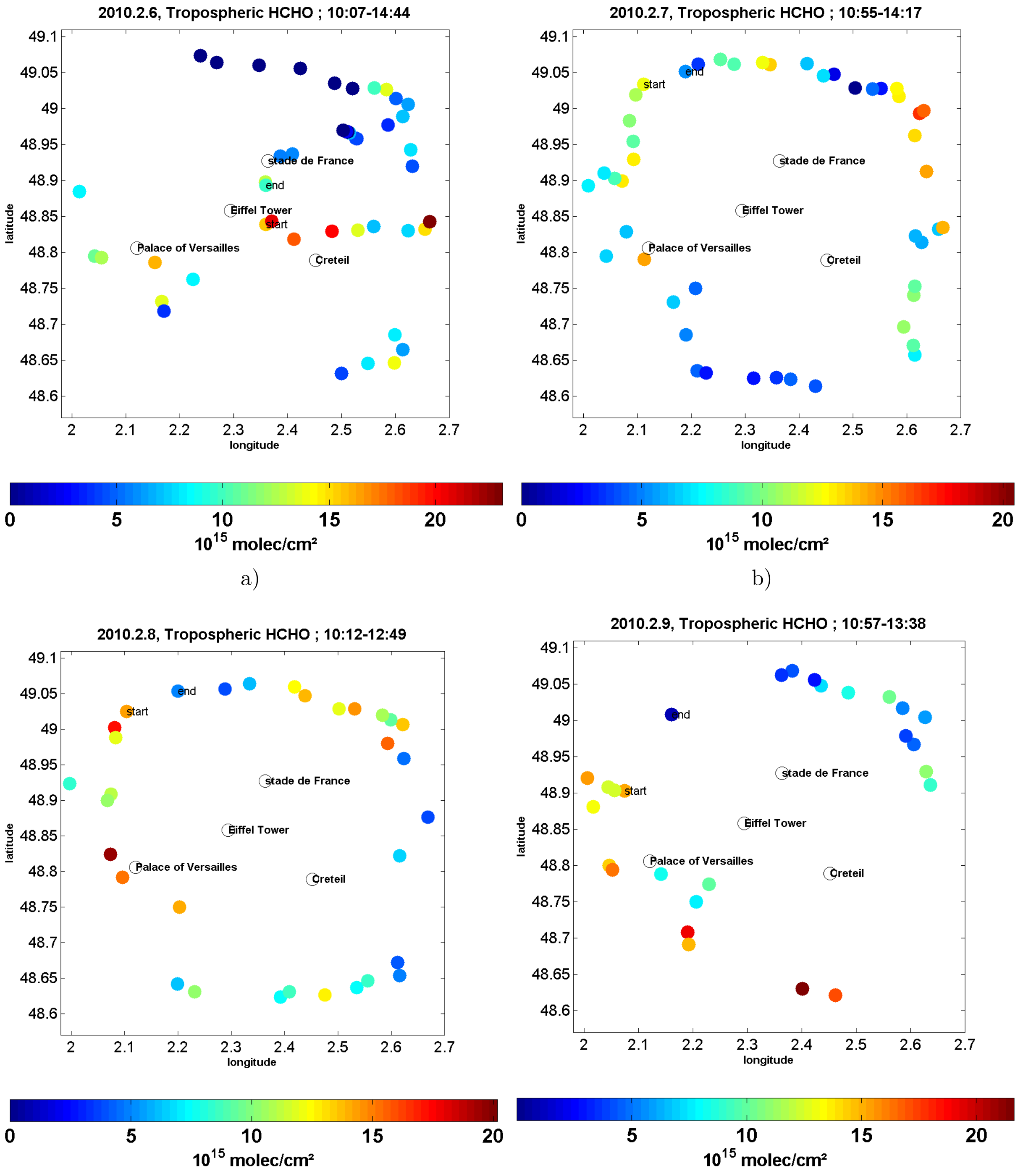

a)

b)

c)

d)

Figure D.17: TVCDs of HCHO in Paris on February 6 (a), February 7 (b), February 8 (c) and February 9 (d), 2010.

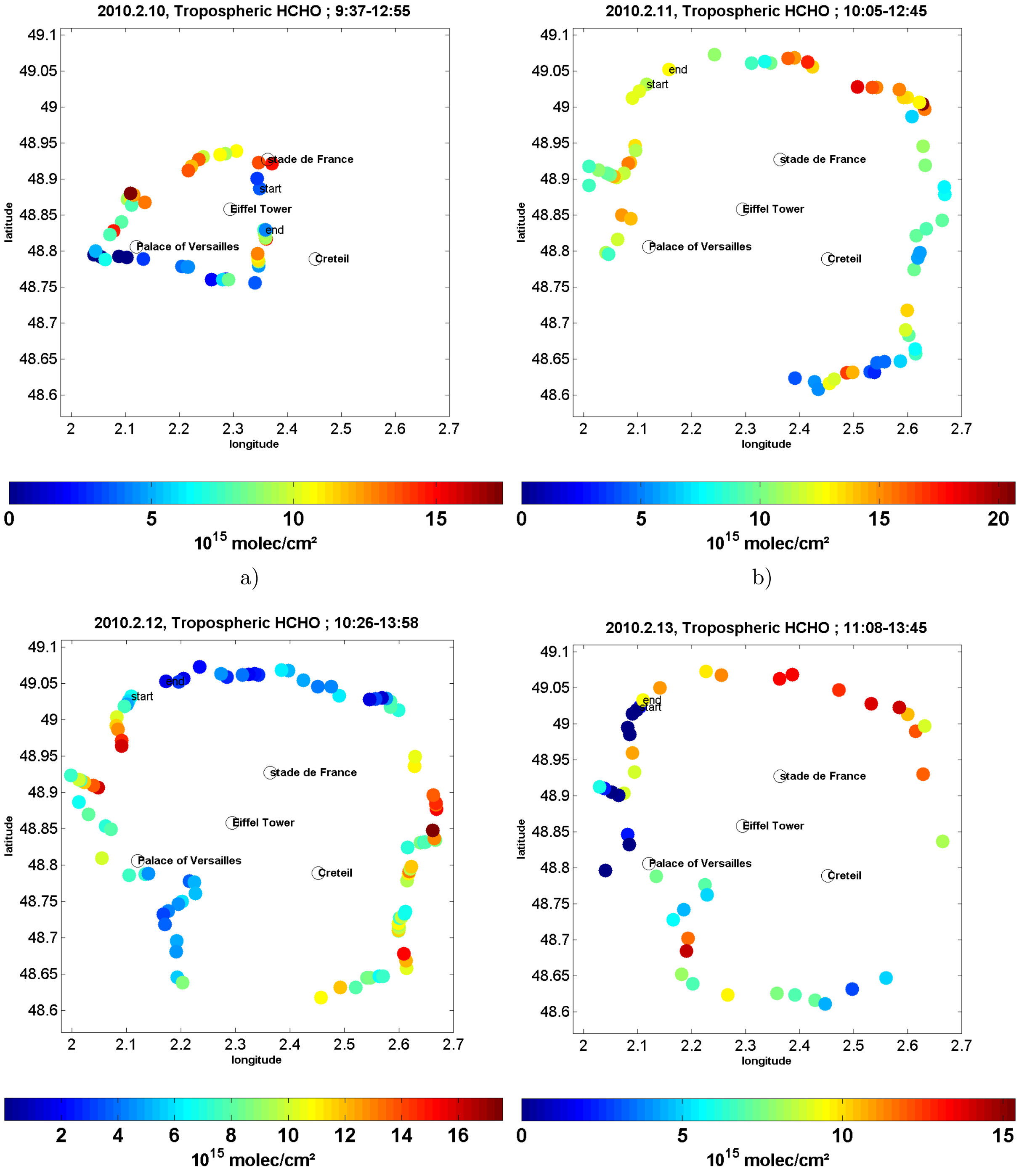

a)

b)

c)

d)

Figure D.18: TVCDs of HCHO in Paris on February 10 (a), February 11 (b), February 12 (c) and February 13 (d), 2010.

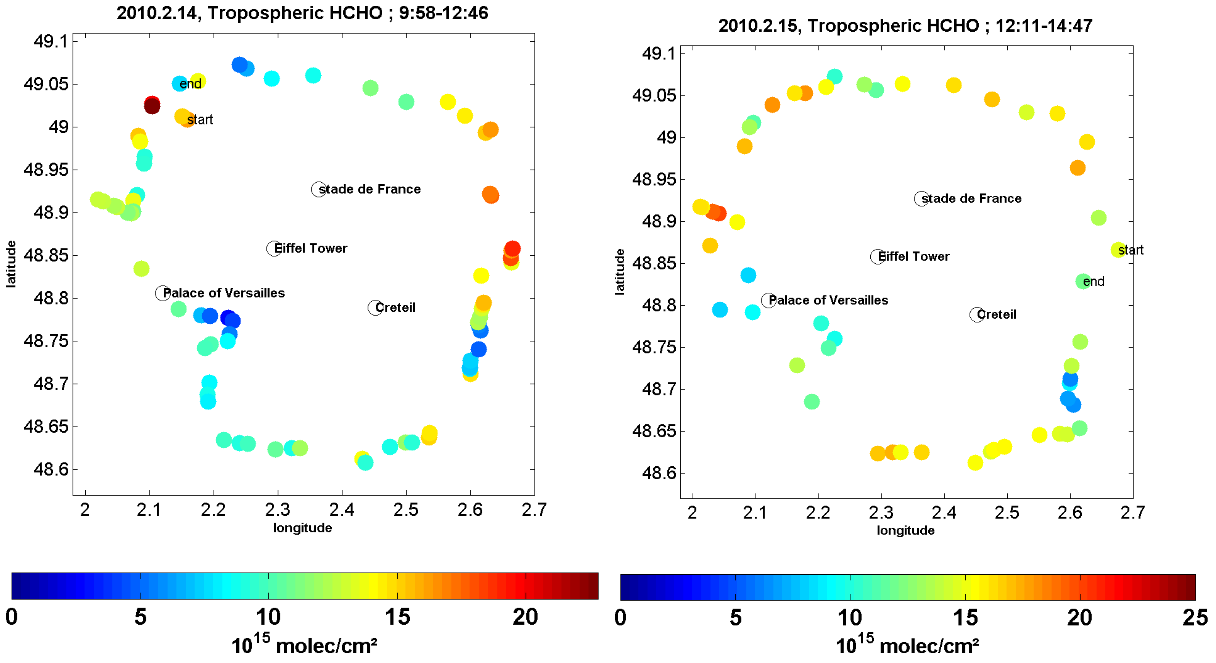

a) b)

Figure D.19: TVCDs of HCHO in Paris on February 14 (a) and February 15 (b), 2010.

Appendix E

E.1 Investigating the effects of aerosols on the mobile MAXDOAS measurements

As shown in the main text of the chapter 4 (section 4.1.1), aerosols cause modifications of the atmospheric radiation field compared to clear sky. These modifications lead to deviations from the assumptions of geometric light paths through the trace gas layers of interest. In figure 5.3 of the main text the relative differences to the so called geometric approximation are shown for various NO_2 and aerosol profiles and aerosol optical properties. The differences become particularly large for cases of strong aerosol optical depth and high trace gas layer height. The results shown in figure 5.3 represent aerosols with asymmetry parameter of 0.68 and single scattering albedo of 0.95 which are typical for polluted urban regions (see Dubovik *et al.* (2002)). In this appendix we explore the effects of variations of aerosol optical properties. In addition, we also investigate the effects of elevated aerosol layers.

In figures E.1 to E.4 the optical properties of the aerosol are changed. The single scattering albedo is varied from 0.9 to 1.0, and the asymmetry parameter is varied from 0.6 to 0.75. Both variations have additional systematic effects on the sensitivity of the measurements but compared to the main effects (aerosol optical depth and trace gas layer height) these changes are small.

In figure E.5 we investigate the effect of elevated aerosol layers (between 2 and 3km and between 8 and 9km), which were e.g. observed by (Babu *et al.* , 2011). We used the same NO_2 profiles as in figure 5.3 and figures E.1 to E.4. Compared to aerosol layers close to the surface, elevated aerosol layers lead only to rather small deviations from the geometric approximation. This finding indicates that elevated aerosols have only small influence on the light paths in the line of sight of the instrument close to the surface. We conclude that the possible presence of elevated aerosol layers can be neglected for the interpretation of our measurements.

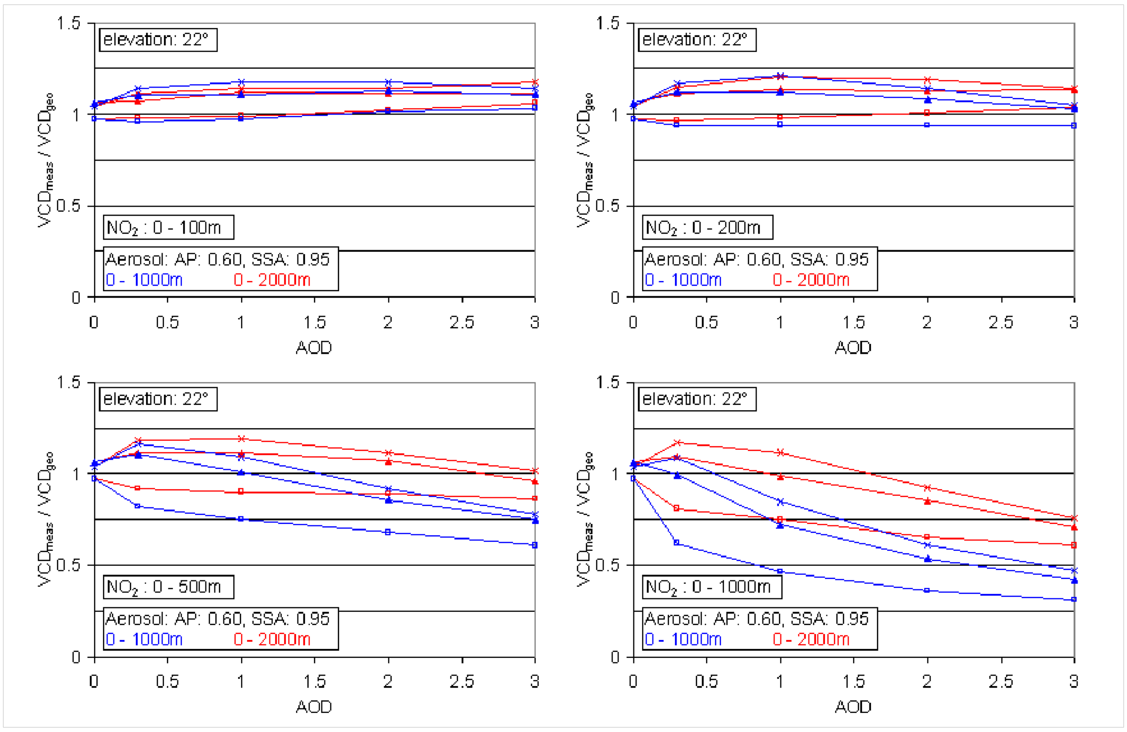

Figure E.1: Relative deviation of the true tropospheric VCDs (derived from radiative transfer simulations) from the geometric VCD for different trace gas layer heights, aerosol optical depth, aerosol layer heights and relative azimuth angles. Asymmetry parameter: 0.6, Single scattering albdo: 0.95

In figure E.6 we present similar data as shown in figure 5.3, but they are shown now as function of the relative azimuth angle or SZA. For small SZA, the geometric approximation generally leads to an overestimation of the trace gas VCD, while for large SZA also an underestimation is found. This underestimation is especially strong for high trace gas layers, relative azimuth angles and SZA around 50° - 60°.

The azimuth dependence is shown in more detail in figure E.7. While for an aerosol-free atmosphere the azimuth dependence is weak, it increases with aerosol optical depth and aerosol layer height.

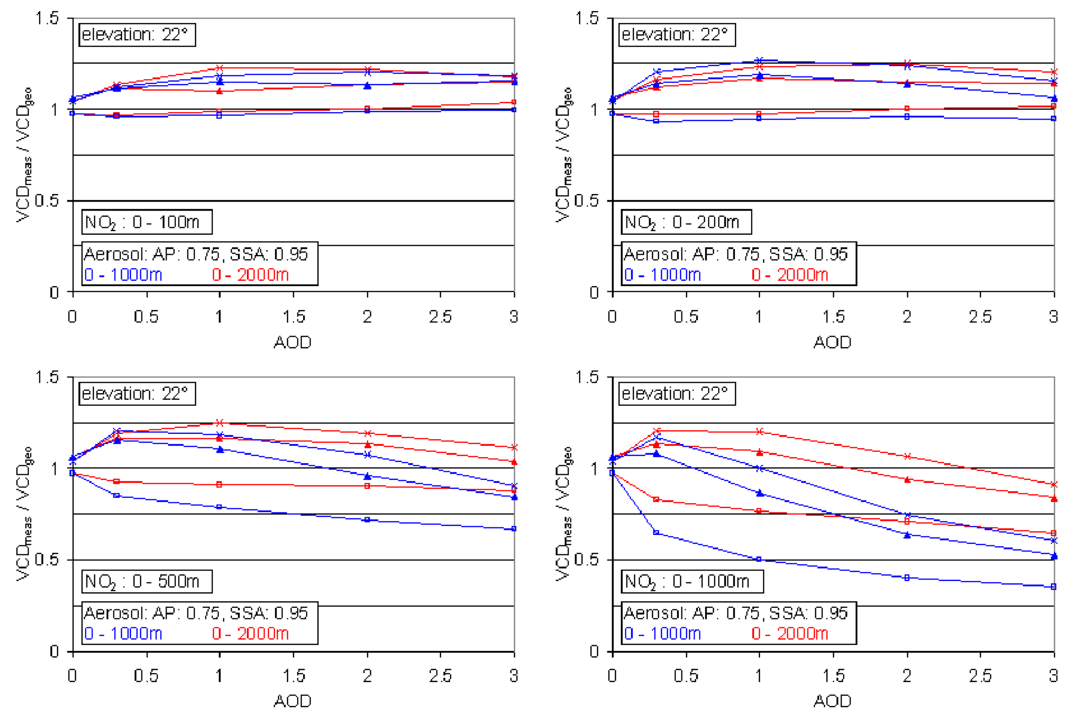

Figure E.2: Similar as figure E.1. Asymmetry parameter: 0.75, Single scattering albdo: 0.95

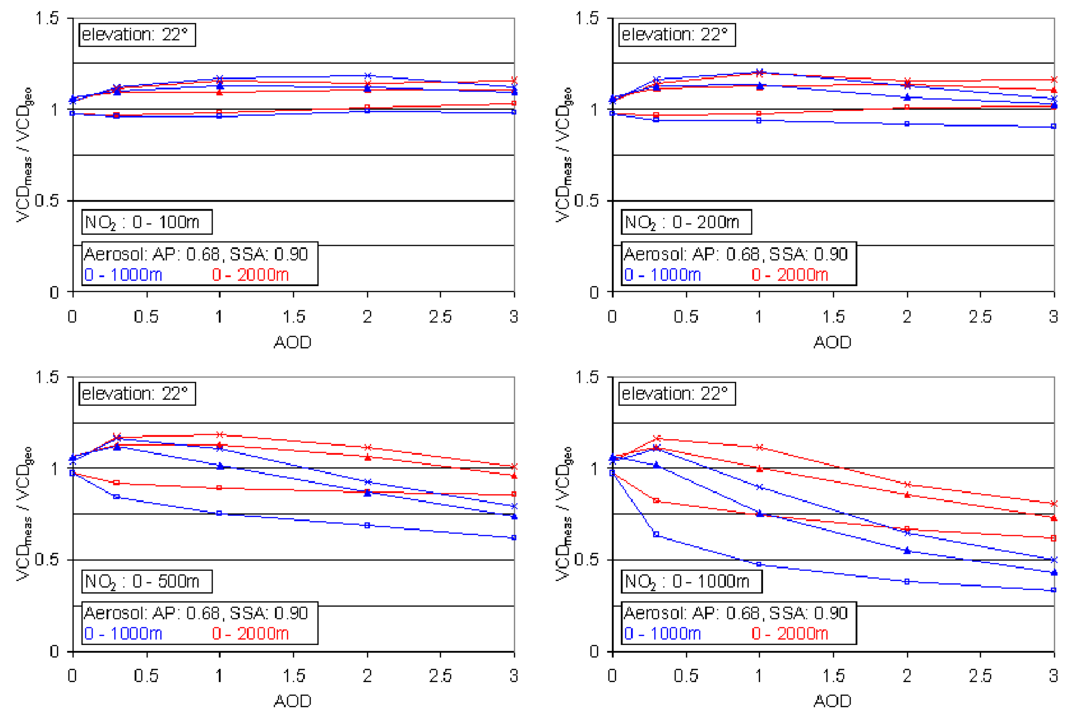

Figure E.3: Similar as figure E.1. Asymmetry parameter: 0.68, Single scattering albdo: 0.9

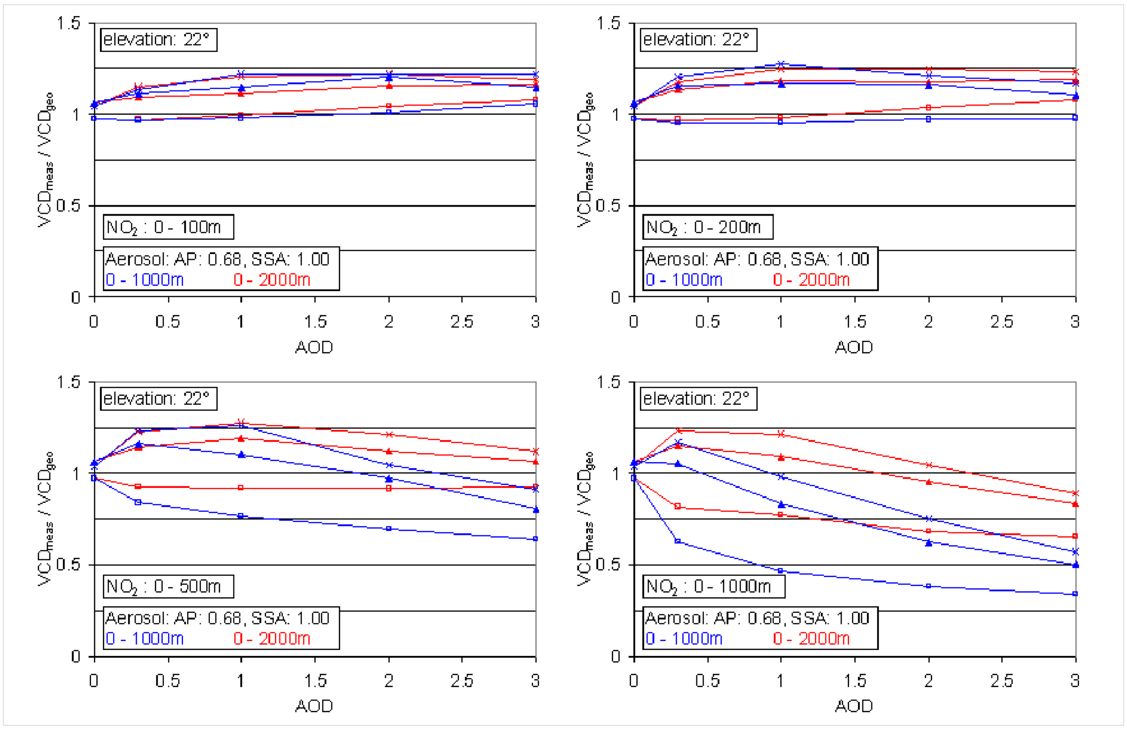

Figure E.4: Similar as figure E.1. Asymmetry parameter: 0.68, Single scattering albdo: 1

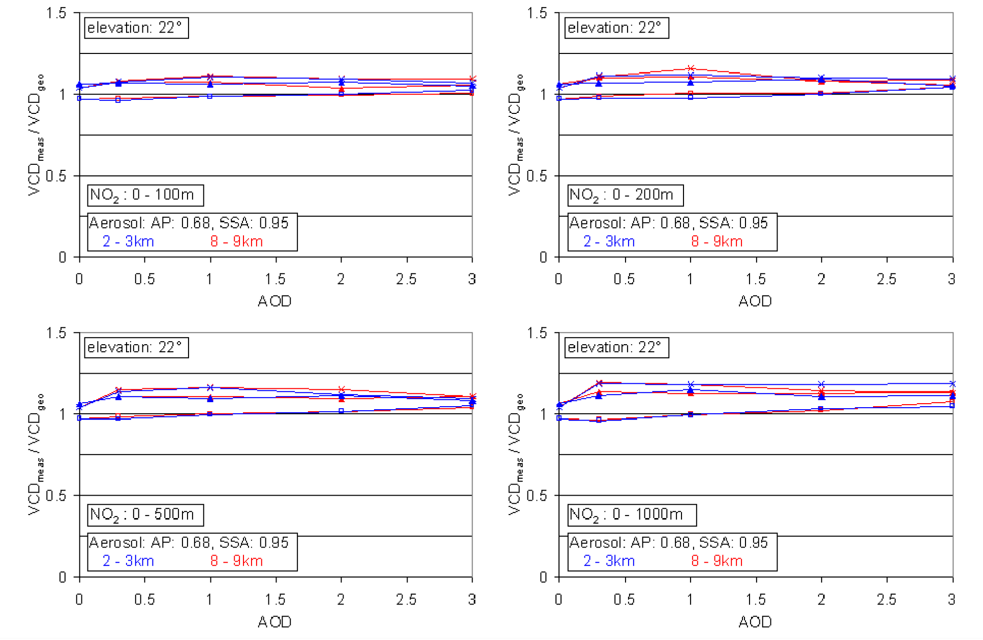

Figure E.5: like last figure, but for elevated aerosol layers (2 - 3km, blue; 8 - 9km, red).

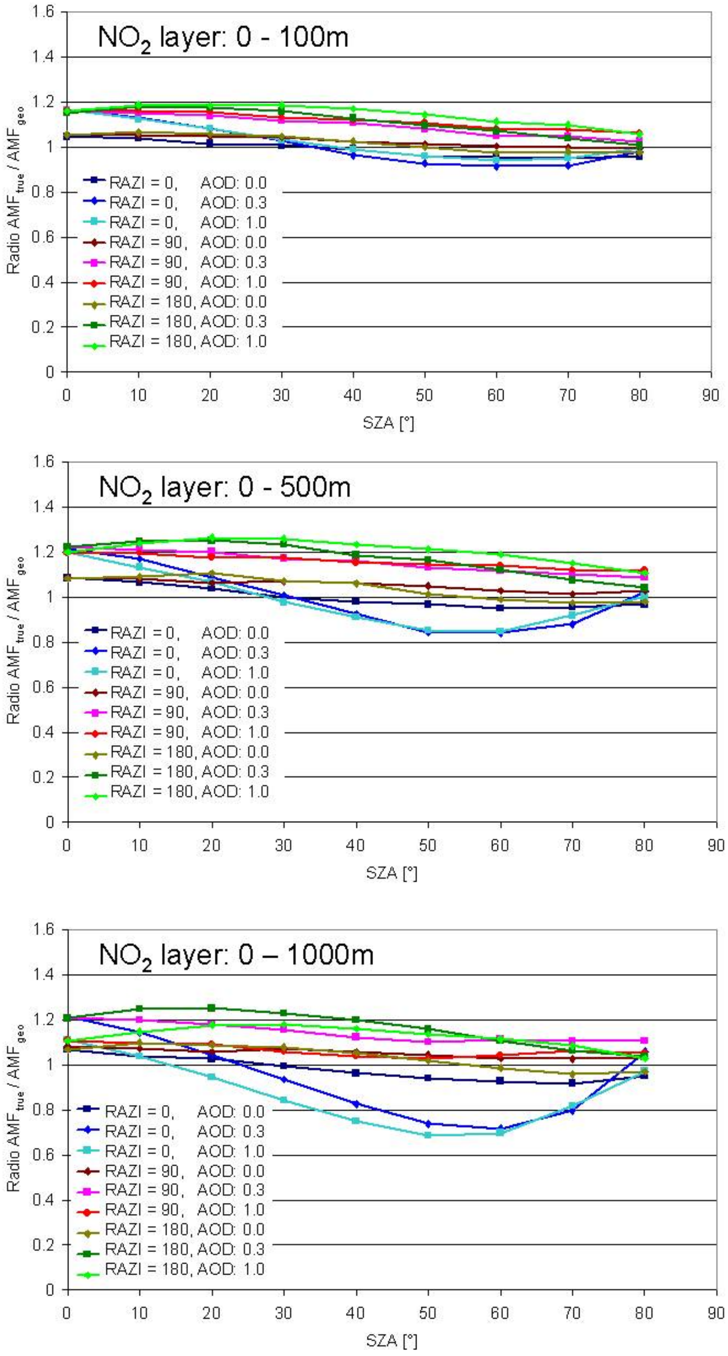

Figure E.6: Relative deviation of the true tropospheric VCDs (derived from radiative transfer simulations) from the geometric VCD for aerosol optical depth, aerosol layer heights and relative azimuth angles as a function of the solar zenith angle. Panels a) to c) show the results for different NO_2 layer heights.

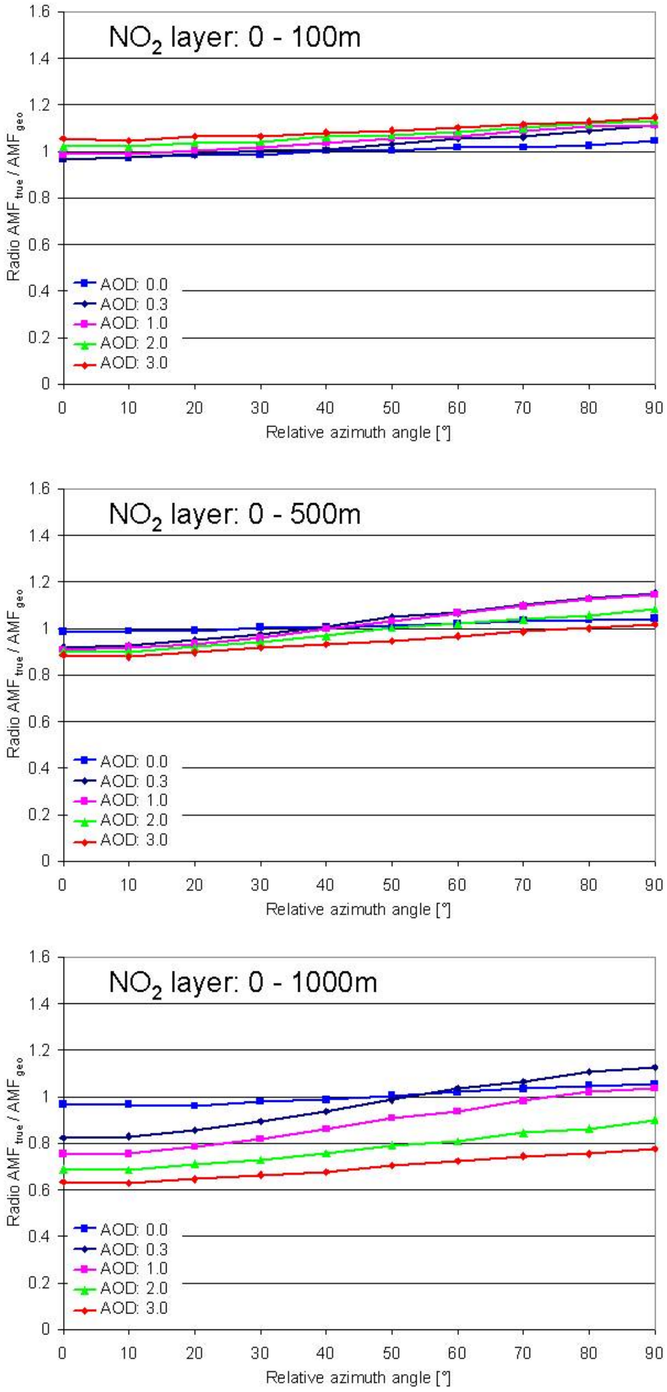

Figure E.7: Relative deviation of the true tropospheric VCDs (derived from radiative transfer simulations) from the geometric VCD for aerosol optical depth, aerosol layer heights and relative azimuth angles as a function of the relative azimuth angle. Panels a) to c) show the results for different NO_2 layer heights.

Acknowledgments

Finally, I would like to thank people, who supported me and helped me during the course of this thesis.

First of all, I would like to thank Prof. Dr. Thomas Wagner for the warm welcome in the group, supervising my work, scientific support and opportunity to do different experiences during the PHD.

Prof. Dr. Ulrich Platt: for his supervising and the opportunity to do this work. His comments were very useful for me and helped to realize the PHD step by step.

Prof. Dr. Heinz Friedrich Schöler, for the interested assessment this work, and his help and comments about the atmospheric chemistry.

Steffen Beirle, who was one of my PHD Advisory Committee (PAC). His scientific experience helped me very much, especially at the beginning the thesis.

All member the satellite group (also former members in last 4 years).

The people, who helped me during different field campaigns: Tim Vlemmix, Thirry Marbach, Thomas Wagner, Tobias Tröndle, Steffen Dörner, Bastian Jäcker, Christoph Hörmann, Sven Krautwurst, Matthias Beekmann, Ramesh Singh, Manish Sharma, Akshansha Chauhan and Sarah Alznauer.

Matthias Beekmann, Herve Petetin, Qiji Zhang; for CHIMERE model data.

MEGAPOLI: the first three years of this work was financed from MEGAPOLI project. MEGAPOLI team. I would like to thank Mark Laurence, who gave me the opportunity to be in MEGAPOLI team, and also his scientific comments.

Katja Grossmann, who helped me about an evaluation algorithm.

IMPRS office, for the support, Elmar Uherek and Agnes Heinemann.

Max Planck institute for chemistry in Mainz.

Zeinab Beigi, for the English proofreading of three chapters.

My parents and sister.